

# Active nanophotonic antenna arrays for effective light-matter interactions

**Kaminski, Piotr Marek**

*Publication date:*
2019

*Document Version*
Publisher's PDF, also known as Version of record

Technical University of Denmark

# Active nanophotonic antenna arrays for effective light-matter interactions

Ph.D. thesis

*Piotr Marek Kamiński*

March 2019

DTU Electrical Engineering
Department of Electrical Engineering

DTU Fotonik
Department of Photonics Engineering

VILLUM FONDEN

# Active nanophotonic antenna arrays for effective light-matter interactions

Piotr Marek Kamiński

Ph.D. Thesis

March 2019

DTU Electrical Engineering
Department of Electrical Engineering

DTU Fotonik
Department of Photonics Engineering

VILLUM FONDEN

**Thesis title:**
Active nanophotonic antenna arrays for effective light-matter interactions

**Ph.D. Student:**
Piotr Marek Kamiński
piotr.marek.kaminski@gmail.com

**Supervisors:**
Associate Professor Samel Arslanagić, Ph.D.[1]
Professor Olav Breinbjerg, Ph.D.[1]
Professor Jesper Mørk, Ph.D.[2]

[1]**Electromagnetic Systems**
DTU Electrical Engineering
Ørsteds Plads, building 348
DK-2800 Kgs. Lyngby
www.ems.elektro.dtu.dk
ob@elektro.dtu.dk

[2]**Quantum and Laser Photonics**
Department of Photonics Engineering
Ørsteds Plads, building 345A
DK-2800 Kgs. Lyngby
http://www.fotonik.dtu.dk/
jesm@fotonik.dtu.dk

**Submission date:**
14 March 2019

**Remarks:**
The present version was adapted for printing after the thesis defence.

# Abstract

*Active nanophotonic antenna arrays for effective light-matter interactions*

We have investigated novel phenomena such as bound state in the continuums (BICs), Dirac cones and exceptional points in photonic crystal (PhC)-based lasers.

We found that the extent of the ring of exceptional points can be controlled with thickness of the PhC slab. For a specific thickness, the extent of the ring can be reduced almost to a point. Then, large Q-factor values are found over the broad region of the Brillouin zone (BZ). These results were used in the design of high Q-factor, small footprint PhC-based resonators that could be used in photonic crystal surface-emitting lasers (PCSELs). Furthermore, we found that elliptical air-holes introduce frequency separation between the two large Q-factor bands leading to the uniform field profile without field localization effects. The dispersion of the PhC with elliptical air-holes is radically different along the high symmetry directions and is significantly altered by a sheer rotation of the air-hole. This may allow to easily control band curvature along specific directions and thus control mode spacing in finite size structures.

Moreover, we have investigated the dynamic model of the self-pulsing Fano laser. We observed that the laser dynamics are confined to the curved surface after the initial transition stage. We proved that after the initial transition stage, the original five-dimensional (5D) model can be reduced to only one-dimensional (1D) in the limited region of the parameter space and that the system evolves into two-dimensional (2D) beyond the exceptional point when the steady-state eigenvalues transition from being purely real to a complex conjugate pair.

We have used the simplified 2D model to associate the unknown origin of instability with a new unstable periodic orbit separating the stable steady-state from the stable periodic orbit. We have classified the bifurcation standing behind the two orbits and an equilibrium point (steady-state) as a Bautin bifurcation. Furthermore, the instantaneous eigenvalues have been found to form a complex conjugate pair within the pulse, which is bounded by two exceptional points. In total, four exceptional points are found to be crossed within a single loop in the phase space.

Finally, we have demonstrated that the intervals of the solution following the adiabatic prediction are interrupted by abrupt nonadiabatic transitions when the state is at the periodic orbit. These transitions have been observed in close vicinity of the pulse. To the best of author's knowledge, this is the first time when the nonadiabatic phenomena are observed in the complex Fano laser system in which the exceptional points are crossed due to the self-modifying behaviour, without any need for an external parameter variation.

# Resumé (in Danish)

*Aktive nanofotoniske antennearrays til effektiv lys-materiale interaktion*

Vi har undersøgt nye fænomener, så som bundne tilstande i kontinuummet (BICs), Dirackegler og exceptionelle punkter fotonisk krystal (PhC)-baserede lasere.

Vi har fundet, at udstrækningen af ringen af exceptionelle punkter kan justeres gennem tykkelsen af PhC-pladen. Med en specifik tykkelse af pladen kan ringen stort set reduceres til et punkt. I dette tilfælde er der store værdier af Q-faktoren over hele den brede Brillouin-zone (BZ). Disse resultater er blevet brugt til at designe høj Q-faktor, lille areal PhC-baserede resonatorer, som ville kunne bruges i fotonisk krystal overfladeudstrålende lasere (PCSELs). Ydermere fandt vi ud af, at elliptiske lufthuller introducerer en frekvensseparation mellem de to store Q-faktorbånd, hvilket fører til en uniform feltprofil uden lokaliseringseffekter i feltet. Dispersionen af PhC'en med elliptiske lufthuller er radikalt forskellig langs retningerne med høj symmetri, og den ændres signifikant ved en ren og skær rotation af lufthullet. Dette kan muliggøre nem justering af båndets krumning langs specifikke retninger og dermed mode-afstanden i strukturer af endelig størrelse.

Vi har ydermere undersøgt den dynamiske model for selvpulserende Fano-lasere. Vi observerede, at laserdynamikkerne er begrænsede til den krumme overflade efter det indledende overgangsstadie. Vi beviste, at den originale femdimensionelle (5D) model kan reduceres til en endimensionel model (1D) efter det indledende overgangsstadie i et begrænset område af parameterrummet, og at systemet udvikler sig til en todimensionel (2D) model på den anden side af det exceptionelle punkt, når steady-state egenværdierne overgår fra at være rent reelle til et komplekst konjugeret par.

Vi har brugt den simplificerede 2D-model til at kæde den ukendte oprindelse af ustabilitet sammen med et nyt, ustabilt periodisk kredsløb, som adskiller det stabile steady-state fra det stabile periodiske kredsløb. Vi har klassificeret bifurkationen bag de to kredsløb og et ligevægtspunkt (steady-state) som en Bautin bifurkation. Ydermere konstateres det, at de øjeblikkelige egenværdier danner et komplekst konjugeret par i løbet af pulsen, som er afgrænset af to exceptionelle punkter. I alt fire exceptionelle punkter krydses i løbet af en enkel sløjfe i faserummet.

Slutteligt har vi demonstreret, at intervallerne af løsningen i forlængelse af den adiabatiske forudsigelse er afbrudt af bratte ikke-adiabatiske overgange, når tilstanden er ved det periodiske kredsløb. Disse overgange er blevet observeret i umiddelbar nærhed af pulsen. Dette er, efter forfatterens bedste overbevisning, første gang ikke-adiabatiske fænomener observeres i det komplekse Fano-laser system, hvor de exceptionelle punkter krydses ved hjælp af selvmodificerende adfærd uden behov for ekstern parametervariation.

# Preface

The work presented in this thesis was carried out by the author at the Electrical Engineering department of the Technical University of Denmark (DTU) between August 2015 and January 2019. The thesis is submitted as a requirement for obtaining the PhD degree from the Technical University of Denmark. The study was funded by Villum Fonden via the Centre of Excellence NATEC (grant 8692).

### Acknowledgements

I would like to thank my supervisors Samel Arslanagić, Olav Breinbjerg and Jesper Mørk for their continuous encouragement, guidance and trust in me throughout the project. My interest in electromagnetics, and in science in general, has been resurrected by Samel Arslanagić and Olav Breinbjerg lectures given 7.5 years ago during my Erasmus exchange. Their inspiring teaching attitude, engagement and encouragement have been a continuous source of motivation. Moreover, Jesper Mørk ability to guide, engage and stimulate curiosity has been exceptional. I am grateful for our discussions on the Fano laser and that I could have worked on it.

I would like to express my gratitude to Prof. Jensen Li. I consider myself very fortunate that our roads have crossed and we could work together during my project. His immense passion, determination, openness to new ideas and drive were truly inspiring and motivating. Our discussions have benefited me immensely and pushed my limits each time we met.

I am also very grateful to Alireza Taghizadeh, Yi Yu and Thorsten Rasmussen for all the discussion we have had, willingness to discuss all the crazy, not always successful ideas and help in introducing me to various photonic crystal laser concepts.

My sincere gratitude also goes to all the fellow PhD students that have been sharing my fate and the research crew of the EMS group at DTU. Special mention goes to Kyriakos Kaslis, Ugur Meriç Gür, Michael Palvig, Nikolaj Kammersgaard for the enjoyable discussions we have had. Also a great thank you to Michael Palvig for helping me with the Danish translation of the abstract.

I would like to sincerely thank all my friends that are still in touch with me despite me rejecting most of their invitations due to lack of time. I am deeply grateful to my girlfriend for constant support and reminding me each day about beauty and complexity of life beyond science. Finally, I would like to thank my parents for all the efforts and sacrifices they made to ensure that I can become the person I am today.

Piotr Marek Kamiński
March 2019

# Contents

# List of Publications

The conference papers [P1, P2] and the journal papers [P3, P4] have been prepared during this study. They are included in Appendix C as part of this thesis. The journal paper [P4] is currently in review.


[P1] P. M. Kamiński, O. Breinbjerg, J. Mørk, and S. Arslanagic. "Control of the rings of exceptional points in photonic crystal slabs". In: *2017 Conference on Lasers and Electro-Optics Europe European Quantum Electronics Conference (CLEO/Europe-EQEC)*. June 2017, pp. 1–1.

[P2] P. M. Kamiński, A. Taghizadeh, O. Breinbjerg, J. Mørk, and S. Arslanagić. "Quality factor enhancement in photonic crystal slabs by manipulation of the ring of exceptional points". In: *2017 International Conference on Numerical Simulation of Optoelectronic Devices (NUSOD)*. July 2017, pp. 11–12.

[P3] P. M. Kamiński, A. Taghizadeh, O. Breinbjerg, J. Mørk, and S. Arslanagić. "Control of exceptional points in photonic crystal slabs". In: *Optics Letters* 42.15 (Aug. 1, 2017), pp. 2866–2869.

[P4] P. M. Kamiński, J. Mørk, S. Arslanagić, O. Breinbjerg, and J. Li. "A two-dimensional phase-space picture of the photonic crystal Fano laser". In: *Physical Review A* ().

# Chapter 1

# Introduction

As a matter of fact, an excited electron decaying to a lower energy level is a source of all light in our lives. There are three possible radiative processes, absorption, spontaneous emission and stimulated emission. Spontaneous emission does not require a photon, instead the electron spontaneously decays to the lower energy state emitting a photon. This process is responsible for most of the light around us. On the other hand, both, absorption and stimulated emission, are dependent on the presence of a photon. Absorption excites an electron to a higher energy state, while stimulated emission stimulates an excited electron to decay to a lower energy state creating a new photon of the same properties as the incident one. If there are more electrons in the higher energy level than in the lower energy level, the medium exhibits population inversion. Then, the stimulated emission dominates and the medium provides net amplification of light. The process of stimulated emission, first described by Einstein in 1917 [1], led to the invention of the first laser 40 years later [2]. The gain medium together with a resonating cavity constitute the core of a laser. The name *laser* is in fact an acronym standing for "light amplification by stimulated emission of radiation". At first, named as "the solution looking for a problem", nowadays, laser applications span from barcode scanners [3] and hair/wrinkle removal [4] through cutting, welding [5] and additive manufacturing [6] to lidar systems [7], laser surgery [8], data storage [9] and optical communication [10]. Laser owes its popularity to the properties of light that it generates such as monochromaticity, directionality, intensity and coherence. The very first laser was a solid-state laser, ruby laser [11]. The gain medium was made out of the ruby crystal and pumped by the flashlamps, the laser cavity was made by silver coating both ends of the ruby rod, one end was completely coated, the other one only partially to allow for light propagation. It produced light pulses at 694nm wavelength. Since then many laser types have been conceived, e.g. chemical, gas, dye, metal-vapor, solid-state and semiconductor lasers. They are usually classified based on the material used as the gain medium which also affects the operating wavelength.

Since the Ph.D. project is a part of NATEC (Nanophotonics for TErabit Communications) project, here, we focus on semiconductor lasers as they are used for high-speed optical communication and integrated photonic chips in the future. Commercial semiconductor lasers are fabricated with III-V chemical compounds, the most common families of semiconductor lasers are those using GaAs and those using InP as a substrate. Lasers using GaAs operate at wavelengths in the range from 630nm to 1100nm. InP-based lasers operate at longer wavelengths in the rage of 1100nm

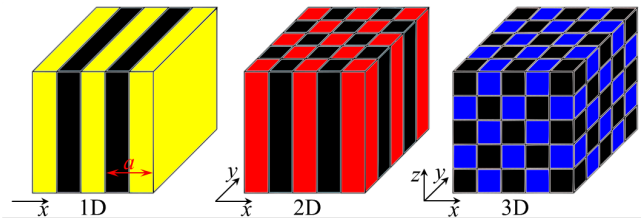


*Figure 1.1: Examples of 1D, 2D and 3D PhCs. Colours indicate different materials. Dimension of the PhC is defined by the periodicity of the material along one or more axes.*

to 2000nm, among them is the telecommunication wavelength 1550nm at which the silica optical fibers have a low loss window. This is also the operational wavelength in our case so that the potential new devices could be integrated with already existing optical communication systems. Thus, we will be working with InP-based lasers and the gain medium will consist of several layers of an active material made out of InAs.

The simplest semiconductor lasers have been using Fabry-Perot resonator as an optical cavity which is usually obtained by cleaving or coating the ends of the laser and the gain material is placed along the cavity. This kind of laser is called an edge-emitting laser due to its emission from the side. It usually exhibits output powers on the level of several hundreds of milliwatts when accompanied by high beam quality. However, these lasers will usually support multiple longitudinal modes within the gain bandwidth of the active material. This leads to laser instabilities as the number of lasing modes can vary with temperature and pumping power. Moreover, the constantly increasing demand for capacity in optical fiber transmission requires lasers with very narrow frequency spectra. This and single frequency operation can be met by lasers using distributed Bragg reflectors (DBRs), which are made of alternating layers of dielectric materials with different permittivities. DBRs can be used in edge-emitting lasers, but also in vertical-cavity surface-emitting lasers (VCSELs) which are one of the most novel commercially available semiconductor lasers. In contrast to edge-emitting lasers, in VCSELs light propagates perpendicularly to the gain medium and is emitted vertically. This significantly shortens the path of light in the gain medium and puts strict requirements on reflectivities of top and bottom mirrors. However, the very high reflectivities limit the output power of VCSELs to only several milliwatts [12]. Despite this disadvantage, VCSELs possess numerous advantages over edge-emitting lasers such as catastrophic damage free operation [13–15], convenient integration in 2D multi-wavelength array [15–17], circularly symmetric Gaussian beam [18] and due to very short cavity length they emit only single longitudinal mode. Currently, VCSELs have replaced edge-emitting lasers in short-range optical fiber communication. DBR is the simplest possible, 1D, type of PhC, see Fig. 1.1. When one wants to increase output power a VCSEL she/he should increase its area. However, as simple reflector as DBR grating does not provide enough opportunities to sufficiently control mode distribution in the cavity and when the area of a VCSEL increases, its beam quality degrades very quickly due to competition from higher order modes [18, 19].

Over the years, the concept of DBR has evolved towards 2D and three-dimensional (3D) PhCs, see Fig. 1.1. Particularly, 2D PhCs are an attractive solution as they are relatively easily fabricated and are very flexible in their design providing access to rich physics. PCSELs have recently grabbed considerable attention due to their large-area single-mode lasing, which led to watt-class high-power, high-beam-quality PhC lasers [20–22]. The square lattice PhC is shown in Fig. 1.2(a) with the corresponding reciprocal space (b), BZ (c) and the photonic band structure (d). PCSELs operate at the Γ-point of the PhC band structure and take advantage of the very low group velocity at this point [23, 24]. At the Γ-point, rotationally symmetric mode can be

found. It does not radiate due to perfect destructive interference. It enables lower lasing threshold of large-area surface-emitting lasers [25–28]. Some of the designs have on purpose broken in-plane rotational symmetry [29] and vertical symmetry of air-holes [30, 31] to extract more power in the vertical direction while maintaining relatively low lasing threshold [21]. Moreover, flexibility in the design of PhCs has allowed to include numerous additional functionalities in PCSELs such as beam steering [22, 32, 33], polarization and beam pattern control [34–39], to mention a few.

The rotationally symmetric mode at the Γ-point is called the symmetry-protected BIC and it exhibits an infinite quality factor (Q-factor). There is also another type of BIC that is particularly important for PCSELs, it is a trapped BIC which arises due to destructive inference of radiating modes with the guided resonance in the PhC slab [27, 40, 41]. Strong confinement of light offered by quasi-BICs in finite structures allows the field to be stored longer in the structure and leads to strong enhancement of electromagnetic fields [42–44]. This finds application in e.g., surface-enhanced Raman spectroscopy [45, 46], four-wave mixing [47] and optical sensing [48].

In order to increase the output power of PCSELs, their area can be increased. However, it cannot be done indefinitely since as the PhC area increases, the spacing between the modes decreases. Because of the broad spectrum of the active material, at one point this will lead to multi-mode lasing which quickly degrades the quality of the beam. Several solutions have been proposed to mitigate these issues. The solutions include double-hole unit cell structure [20], vertically asymmetric air-holes [49, 50], external reflection [51] and Dirac-like cone dispersion [52]. Particularly, the last solution has been shown to be not only very effective in alleviating these issues, but also very interesting from the physical stand-point [53–59].

Moreover, it has been demonstrated that Dirac cone dispersion can be deformed when losses are present in the structure and a ring of exceptional points is spawned [60]. In photonic band structure, exceptional point is a point at which two modes

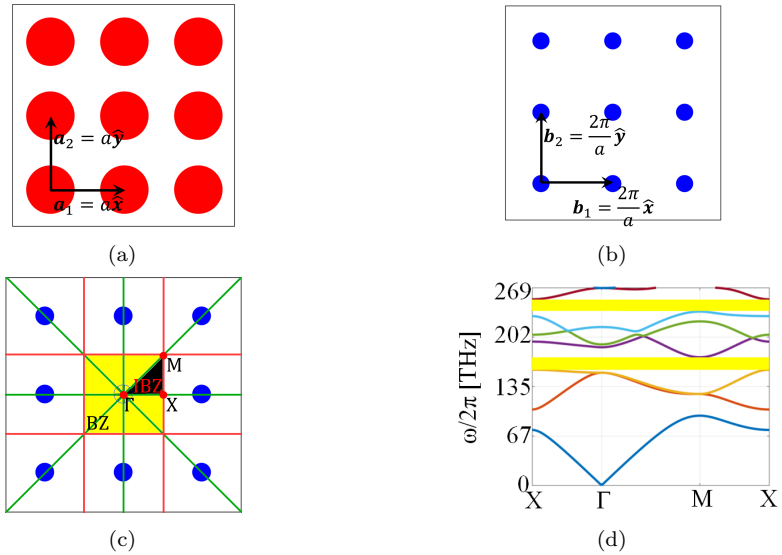


*Figure 1.2: (a) Square lattice PhC in physical space, white and red colours indicate different materials. (b) The square lattice in the k-space. (c) The k-space lattice showing the construction of the BZ, marked in yellow, and the irreducible Brillouin zone (IBZ), marked in black. The centre is treated as the origin, the lines connecting the origin and other lattice points are drawn together with the lines bisecting them. The BZ is the area closer to the origin than any other point. The IBZ is part of the BZ not satisfying any symmetries. (d) Photonic band structure of the PhC consisting of dielectric cylinders ($\epsilon$=8.9) in air with radius of the cylinders $r = 0.38a$, where $a$ is the lattice constant. The band structure is plotted along edges of the IBZ. Two photonic band gaps are marked in yellow.*

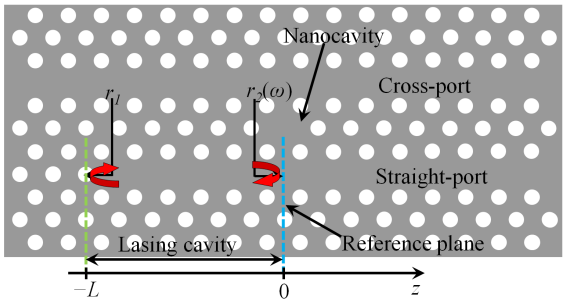


*Figure 1.3: Schematic of PhC-based Fano laser. The gain medium is uniformly distributed in the PhC slab. The lasing cavity is defined between the PhC mirror (marked with green dashed line) and the right mirror due to Fano resonance (marked with blue dashed line).*

exhibit not only the same radiation losses and resonating frequencies, eigenvalues, but also the same mode profiles, eigenvectors [61–64]. Observation of exceptional point in PhC slabs has sparked broad interest due to their intriguing properties, e.g., unidirectional zero reflection/transmission [65, 66], inverse pump dependence of lasers [67] and single-mode operation lasers [68, 69]. Moreover, exceptional point physics offers access to new directions in system control and may provide new, exciting opportunities for the design of novel nanophotonic devices that can find applications in photonic switches and isolators [70–72].

Dirac cones, exceptional points and BICs have opened a new page in the nanophotonics research [71, 73–79]. However, there are still many unknowns concerning future applications of these phenomena, and even their presence is sometimes uncertain. Particularly, the question arises whether the BIC persists when the size of the PhC decreases to several unit cells. Recently, some efforts have been made towards realization of BIC-based ultracompact resonators [80]. However, in this case, a high contrast grating, which is a 1D PhC slab of bars, was investigated. It is not known to what extent the effect would persist in 2D PhCs. Moreover, it is of importance to investigate the influence of BICs on the ring of exceptional point which, to the best of author's knowledge, has not been given enough space in the literature thus far. This could lead to the development of a new class of ultracompact lasers that could combine advantages of multimode cavities with stable single mode emission [68, 69].

Furthermore, the icon of the NATEC project is a PhC-based laser that utilizes Fano resonance to form a narrow-band mirror of the lasing cavity, the second mirror of the lasing cavity is due to PhC. The configuration of the so-called Fano laser is shown in Fig. 1.3. Fano resonance arises as a consequence of interference between the continuum of PhC waveguide modes and the discrete resonance of the nanocavity side-coupled to the waveguide [81]. The spectral width of the resonance is determined by the Q-factor of the side-coupled nanocavity. One of the features of the Fano resonance is the highly asymmetric lineshape which has been shown to significantly reduce energy consumption in optical switches [82]. Moreover, the PhC Fano laser has been recently demonstrated to be the first nanolaser generating a self-sustained train of pulses at gigahertz frequencies [83]. Self-sustained pulsing occurs due to the laser becoming unstable and does not require any external intervention except of the continuous pumping. However, there is a region in the parameter space in which, if the laser is perturbed strongly enough, it becomes unstable despite the employed analysis indicating the stable steady-state which normally should lead to continuous wave operation. The origin of laser instability is unknown in this region.

In [84–87], it has been shown that single mode self-pulsing in distributed feedback lasers is strongly related to complete mode degeneracy (exceptional point) of a pair of longitudinal modes. In this case as well as in the Fano laser, the self-pulsing was

attributed to dispersive Q-factor self-switching and the repetition rate was on the order of several GHz [83]. Thus far, it has not been investigated whether exceptional points play a role in the self-pulsing Fano laser. Furthermore, the nonlinear interaction between the carrier density and the electromagnetic field in the laser cavity changes the internal state of the laser in a periodic manner without any need for external modulation. Thus, this kind of self-adopting interaction could potentially be used to sweep across or encircle an exceptional point.

The purpose of this study is to further investigate novel phenomena such as BICs, Dirac cones and exceptional points in PhC-based lasers. The research activities are identified with motivation to work on fundamental scientific challenges that may lead to new discoveries and technologies, not necessarily immediate applications. In the first part, we examined the relation between the rings of exceptional points and BICs. We found that by varying thickness of the PhC slab, we can control the extent of the ring of exceptional points by moving trapped BICs in the BZ. We have shown that for a specific thickness, the extent of the ring can be reduced almost to a point. Then, large Q-factor values are found over the broad region of the BZ. These results were used in the design of large Q-factor, small footprint PhC-based resonators. In the second part, we investigated the dynamic model of the self-pulsing Fano laser. We demonstrated that after the initial transition stage, the original 5D model can be reduced to only 1D in the limited region of the parameter space and that the system evolves into 2D beyond the exceptional point when the steady-state eigenvalues transition from being purely real to a complex conjugate pair. We used the simplified 2D model to associate the unknown origin of instability with a new unstable periodic orbit separating the stable steady-state from the stable periodic orbit. Furthermore, the pulse was found to be bounded by two exceptional points and four exceptional points were found to be crossed within one period of the laser operation. Finally, the simplified model has been used to investigate the non-Hermitian dynamics. Using the general framework of [88], we demonstrated that the intervals of the solution following the adiabatic prediction are interrupted by abrupt nonadiabatic transitions in close vicinity of the pulse.

## Reading Guide

Chapter 2 introduces the topics of PhCs, BICs, Dirac cones and exceptional points. It is discussed how the extent of the ring of exceptional points can be controlled. The primary goal of this investigation is to find the connection between the extent of the ring of exceptional points and presence of the BICs in the vicinity of the Γ-point and examine potential application in PhC based lasers. It is shown that these results can be used in the design of high Q-factor PhC cavity of small footprint.

Chapter 3 investigates the steady-state as well as the instantaneous eigenvalues of the stability matrix of the dynamic model of the Fano laser. We demonstrate that the original dynamic model can be replaced by the 'minimal' model after the initial transition stage, which lasts only a few picoseconds. Then the simplified model is used to investigate the origin of the laser instability when the steady state eigenvalues are negative suggesting stable steady-state operation. Finally, the pulsing behaviour is linked to the nonadiabatic transition occurring in the vicinity of the instantaneous exceptional points bounding the pulse.

Chapter 4 presents the summary, conclusion and future directions of this work. Chapters 2 and 3 can be read independently.

Throughout the present report, the time factor $e^{-i\omega t}$, with $\omega$ being the angular frequency, $t$ being the time and $i$ being the imaginary unit, is assumed and suppressed.

# Chapter 2

# Photonic Crystal Based Lasers

This chapter investigates phenomena such as bound states in the continuum, Dirac cones and exceptional points with the aim of further improvement of PhC-based lasers. These phenomena are described based on the literature in the following three sections 2.1, 2.2 and 2.3, respectively. We began with a brief introduction of the basic concepts in PhCs and discuss the models of the PhC slab used in the study, see section 2.1. Subsequently, section 2.2 discusses the concept of BICs based on the literature and in relation to the configurations considered in the project. In section 2.3, we review the literature on Dirac-like cone dispersion in PhCs using our own examples.

In the following sections, we exploit these discussions and present our results. Particularly, in section 2.4, we demonstrate that by varying thickness of the PhC slab, we can control the extent of the ring of exceptional points. We show that for a specific thickness, the extent of the ring can be reduced almost to a point. Then, large Q-factor values are found over the broad region of the BZ. These results are used in section 2.5 to design small footprint PhC slabs with total Q-factor values rapidly increasing with an in-plane size of the structure. Moreover, in sections 2.4.2 and 2.5, we found that elliptical air-holes introduce frequency separation between the two large Q-factor bands leading to the uniform field profile without field localization effects. The dispersion of the PhC with elliptical air-holes differs radically along the high symmetry directions and can be significantly altered by a sheer rotation of the air-hole. Finally, section 2.6 introduces configuration of the Fano laser and demonstrates that introduction of the second side-coupled nanocavity can significantly increase accessible Q-factor values of the 3D PhC Fano structure.

## 2.1 Introduction - configuration and its properties

Modern information society is fueled by discoveries coming from laser research. Particularly, semiconductor lasers contribute significantly to the field of optical storage and fiber-optic communication. Thus far, the researchers working on semiconductor lasers have been mainly focused towards widening their range of accessible wavelengths and increasing their modulation speed. Surface-emitting semiconductor lasers such as VCSELs were especially successful. These devices possess fundamental advantages over edge-emitting lasers, such as easily obtained circularly symmetric Gaussian beams [18], 2D integration [13] and catastrophic optical damage free operation [15]. The mode confinement is achieved using refractive phenomena in case of the lateral con-

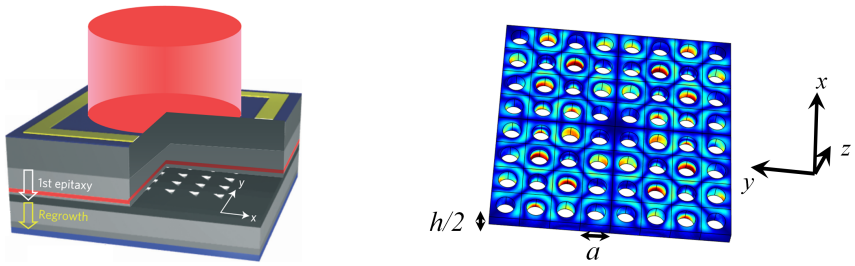


(a) (b)

*Figure 2.1: (a) Schematic of the watt-class, high-beam quality PCSEL [21], (b) 3D model of a PhC membrane of finite thickness h with square lattice of circular air-holes with dimensions of* $8a \times 8a$.

finement, while the diffractive mechanism is responsible for the vertical confinement. The mechanism is based on a 1D periodic structure, which causes Bragg diffraction resulting in coupling between forward and backward propagating waves leading to an enhancement of the modes which satisfy the Bragg condition. Unfortunately, these lasers usually suffer when high output power is simultaneously required with high beam quality, which, in this case, is considerably degraded by the competition from higher-order modes [18]. Moreover, in order to introduce capabilities such as on-chip beam steering and polarization pattern control, external devices have to be used together with the laser. This eliminates the most notable advantage of semiconductor lasers which is their compactness.

The concept of 1D Bragg grating can be extended into 2D PhCs [23]. This allows to obtain a multidirectional Bragg diffraction making it possible to control the lasing field over the large 2D area of PhC-based lasers. This control allows for a lot of flexibility in their design, particularly BICs are natural sources of beams of different shapes [36, 37], they are highly sought in the fields of high resolution microscopy [89], optical trapping [90] and ultra-high-density optical memory [91].

The recently realized watt-class, high-beam-quality PCSEL consists of a PhC and an active layer sandwiched between two cladding layers, see Fig. 2.1(a) [21]. The active layer is formed from multi quantum-wells and is electronically pumped by electrodes placed at the top and bottom of the device. The light is amplified in the active layer and is confined to the region in its close vicinity. Since the PhC layer is positioned very close to the active layer, evanescent wave leaks into the PhC, the lattice constant, $a$, of which is designed to match the wavelength of the light inside the active layer. The lasing principle is based on multidirectional Bragg diffraction, due to which a 2D standing wave is formed over a large area of the PhC. This keeps the light wave for a long time in proximity of the active medium leading to further enhancement of the radiated field. However, for research purposes, PCSELs usually consist of a PhC membrane made of semiconductor material suspended in air, see Fig. 2.1(b). An active material is incorporated in the PhC membrane and usually consists of several layers of quantum wells or dots. The positive net material gain in these configurations is achieved by optical pumping and emission takes place perpendicular to the membrane, below and above the membrane in the case of symmetric vertical profiles of the air-holes [83, 92].

Figure 2.1(b) shows a 3D model of a PhC membrane which is finite in all directions; this model will be investigated in section 2.5. Before that, we introduce a model of a 2D unit cell of a PhC together with the corresponding BZ and IBZ, see Fig. 2.2(a). The PhC in Fig. 2.2 is composed of a square lattice of circularly shaped air holes with symmetric vertical profiles introduced in a material with dielectric constant $\epsilon_d = 10.05$. The PhC is periodic in the $x$ and $y$ directions and infinitely long in the $z$ direction. The radius of the air-hole is set to $0.28a$, where $a$ is the lattice constant. Due to PhC

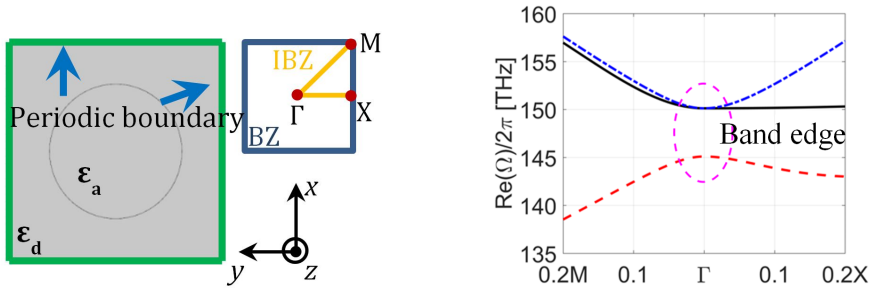


(a) (b)

*Figure 2.2: (a) 2D unit cell of a PhC together with the corresponding BZ and IBZ, (b) Band diagram in the Γ-M and Γ-X directions of a 2D PhC. The blue, black and red curves correspond to different bands. The band edges is marked with a dashed pink ellipse.*

resemblance to solid-state crystals, it is often described in terms of a photonic band structure. In our case, the photonic band structure is computed with an eigenfrequency solver [93] using the finite element method [93]. Eigenvalues are defined as $\Omega = \omega - i\delta$, where $\omega$ is the angular frequency and $\delta$ represents losses. Here and in the following sections the structures are investigated under the transverse-electric (TE) polarization; only in-plane electric field intensity components $(E_x, E_y)$ and out-of-plane magnetic field intensity component $(H_z)$ are present. Figure 2.2(b) shows the detailed structure of the bands in the vicinity of the Γ point plotted over 20% of the BZ versus in-plane wavenumber $k$ along the two principal directions Γ-X and Γ-M. Configuration is infinite along each direction, thus it does not exhibit any radiation losses and the eigenvalues are purely real. Usually, there is a frequency range within which none of the optical modes exists in the entire BZ, this frequency range is called a photonic band gap. Importantly, at the band edge of a photonic band structure the group velocity of light waves slows down and ultimately vanishes. The group velocity is defined as $\vec{v}_g = \partial\omega/\partial\vec{k}$, thus it can be estimated directly from the band structure. Vanishing group velocity results in a standing-wave over the whole area of the PhC.

However, in order to form a laser cavity which would exploit the standing-wave over the whole area of the PhC, the PhC has to be of finite thickness $h$. Fig. 2.3(a) shows a model of a 3D unit cell of a PhC. The configuration has an open boundary in the $z$ direction and is periodic in the $x$ and $y$ directions. The computational domain of the model shown in Fig. 2.3 is terminated with perfectly matched layers at the top of the model and with periodic boundary conditions along the $x$ and $y$ directions. At the bottom of the model, the computational domain is terminated with perfect magnetic conductor in order to enforce the TE-like polarization in the middle of the PhC slab thickness. In this case, the configuration exhibits out-of-plane radiation losses which vary as a function of wavevector $\vec{k}$. Therefore, the eigenvalues are complex. The Q-factor is defined as $Q = \mathrm{Re}(\Omega)/2\mathrm{Im}(\Omega)$ and is plotted in Fig. 2.3(b). It is seen that the black and blue modes exhibit rather low Q-factors, on the other hand the mode marked in red exhibits a diverging quality factor at the Γ-point. This is a known case from the literature; this mode is a symmetry-protected BIC [27] and it usually appears at high symmetry points in the BZ. It is characterized by an infinite Q-factor, see Fig. 2.3(b) and it arises due to symmetry mismatch of the given mode with radiation modes. This can be explained by looking at the mode profiles. Figure 2.4 shows magnitudes of $H_z$ at the Γ-point together with the corresponding components of the electric field intensity shown as arrows.

It is seen that the black and blue modes at the Γ-point, Fig. 2.4(b),(c), have a symmetric $(E_x, E_y)$ distributions with respect to the axis crossing the unit cell in the middle, perpendicularly to the $x$ and $y$ axes. This leads to the strong coupling

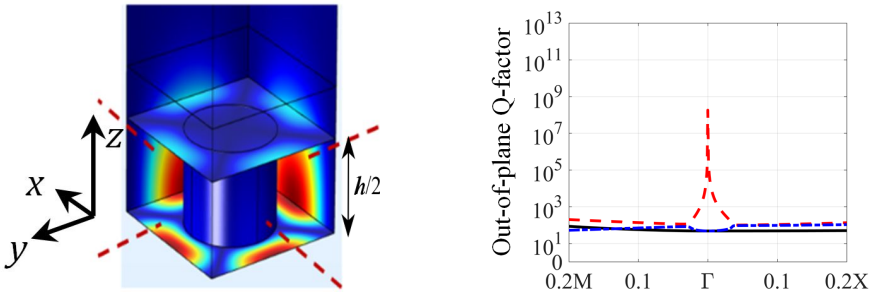


(a) (b)

*Figure 2.3: (a) 3D unit cell of a PhC, (b) Out-of-plane Q-factors of the PhC slab with finite thickness $h = 250nm$ versus in-plane wavenumber $k$ along the Γ-$M$ and Γ-$X$ directions. Q-factors are plotted over 20% of the considered directions. The PhC parameters are the same as in Fig. 2.2.*

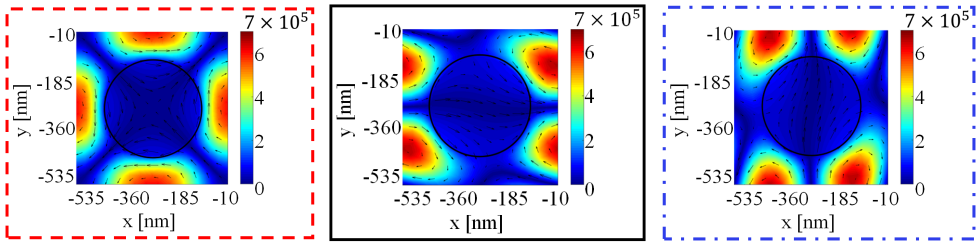


(a) (b) (c)

*Figure 2.4: Field profiles of the three modes at the Γ-point evaluated in the middle of the PhC slab thickness in the case of the configuration shown in Fig. 2.3. Magnitudes of $H_z$ for (a) the lower band (red), (b) the middle, flat band (black) and (c) the upper band (blue) shown in 2.2, respectively. Colors of the frames correspond to colors of the bands in Fig. 2.2. The arrows show $E_x$ and $E_y$.*

to the radiation modes and, thus, larger out-of-plane losses. Consequently, the threshold gain of these modes is so high that none of them would be able to compete with the third mode at the Γ-point; the red curve in Fig. 2.2(b). This is because the $(E_x, E_y)$ distribution is antisymmetric in this case. The system preserves 180° rotational symmetry, thus the mode in-plane components offset each other. It results in destructive interference between the $E_x, E_y$ field components, increases the out-of-plane Q-factor and decreases threshold gain required for lasing [24]. That is why the antisymmetric mode, the red mode at the Γ-point in Fig. 2.2, is selected as the lasing mode. Furthermore, in Fig. 2.3(b) it is seen that the mode is symmetry-protected only in very close vicinity of the Γ-point and as soon as we move away from the Γ-point the Q-factor drops rapidly. The symmetry-protected BICs is very sensitive to perturbations breaking the symmetry while the perturbations that preserve the symmetry, such as modifications of the radius, have no influence on the Q-factor.

Thus far PCSELs have been exploiting symmetry-protected BICs as the lasing mode, mainly because of the low threshold gain that they ensure. However, large Q-factor of the lasing cavity limits output power of the laser. That is why the recent realization of the watt-class PCSEL has 'broken' the symmetry-protected BIC by breaking symmetry of the structure, while maintaining relatively large Q-factor, and thus small lasing threshold [21]. The high output power has been obtained by utilization of asymmetric in-plane profiles of air-holes [29], asymmetric vertical profiles of air-holes [30, 31] and backside reflection from the bottom of the PCSEL [20, 94]. All of these effects rely on suppression of the destructive interference and exploitation of constructive interference in order to extract more power from the configuration.

There is also another type of BICs that exist in PhC slabs, it is called a trapped BIC. It arises as a result of total destructive interference, thus its origin is fundamentally

different from the symmetry-protected BIC [27]. Trapped BICs have been shown to be more versatile because perturbations such as air-hole radius variation only displace the trapped BIC in $k$-space, while they are less sensitive to symmetry-breaking perturbations than the symmetry-protected BIC [26, 92]. This characteristic might be crucial in the design of future PCSELs making it more robust towards fabrication tolerances. Trapped BICs are discussed in more details in section 2.2.

Naturally, the broader the laser area, the higher the output power and the better beam quality can be obtained. Unfortunately, the area of the laser cannot be increased indefinitely. There are two fundamental constraints that limit the lasing area of PCSELs. Firstly, the frequency spacing between the modes is inversely proportional to the size of the cavity, i.e. as the laser cavity becomes larger, the frequency spacing between the modes becomes smaller. Since the gain spectrum of the active material is usually very broad compared to the width of the resonance, it results in a very similar gain experienced by the fundamental and the competing modes leading to the multi-mode lasing. Secondly, as the lasing area increases, an in-plane feedback leads to field localization. Consequently, the carrier density in these areas is depleted resulting in the reduction of the gain experienced by the lasing mode. This modified spatial gain distribution might overlap more effectively with the field distribution of one of the competing modes. This might lead to instability of the lasing mode and multi-area lasing [50]. There are several possible solutions that have been recently proposed: double-hole unit cell structure [20], vertically asymmetric air-holes [31, 49, 50], external reflection to increase threshold margin between the modes [51] and photonic band structure exhibiting Dirac-like cone dispersion close to the Γ-point [52].

Particularly interesting is the solution based on the Dirac-like cone dispersion which allows not only to significantly reduce the in-plane feedback, but also to increase mode-spacing by orders of magnitude. Dirac-like cone is characterized by linear dispersion in contrast to the quadratic dispersion that is usually used to create band-edge modes in PCSELs. When the photonic band structure is plotted in 3D $\omega(k_x, k_y)$, then the Dirac-like dispersion will be formed by two bands exhibiting linear dispersion and meeting at a single point, i.e. Dirac point. In this way a general conical surface will be formed. Application of Dirac-like cones in PhC slabs not only overcomes two fundamental limitations, but is also very interesting from the physical standpoint as it is expected that many fascinating phenomena will arise in analogy to the similar band structure exhibited by graphene [53].

Furthermore, it has been shown that when the PhC is designed to exhibit Dirac-like cone dispersion and is accompanied by radiation losses, the Dirac-like cone is deformed and the ring of exceptional points is created [60]. Exceptional point in PhCs is the point in the complex band structure at which two individual resonances have the same resonating frequencies and spectral widths (i.e., the real and imaginary parts of the eigenvalues are the same) as well as the same mode profiles (i.e., the eigenvectors are also the same). It is a very general and peculiar phenomenon observed in optical waveguides [95], unstable laser resonators [96], self-pulsing lasers [84–87], coupled nanolasers [97], quantum systems [98], metasurfaces [99, 100], electronic circuits [101] and mechanical resonators [71]. Moreover, exceptional points possess many intriguing properties such as unidirectional zero reflection or transmission [65, 66], inverse pump dependence [67] and single-mode operation [68, 69]. Therefore, the application of Dirac-like cone dispersion not only can further increase single-mode output power in PCSELs, but it is also a very rich field which is currently at the forefront of the scientific research. Dirac cones and exceptional points in PhCs constitute considerable part of the current chapter and will be discussed in more details in section 2.3, while section 2.4 will present new results and discuss possibility of controlling extent of the ring of exceptional point and its relation to BICs.

## 2.2 Bound states in the continuum in photonic crystals

This section is based on the literature and introduces theoretical background of BICs as well as nomenclature used in the following sections. BICs offer a perfect confinement despite being inside the continuous spectrum of radiating waves. They are a general wave phenomenon. They have been firstly identified in quantum mechanics [102], but since then they have also been experimentally observed for electromagnetic [25], elastic [103], water and acoustic waves [104].

BICs in compact single particle structures are very difficult to realize [27, 105, 106], that is why most of the investigations are conducted with structures either extending to infinity or periodic at least in one direction. Thus, PhC slabs are an ideal candidate for studying BICs, also because of their fabrication ease. They are periodic in the $x$, $y$ directions and light can be perfectly confined in the out-of-plane $z$ direction.

Subsequently, the concept of BICs in PhC slabs is defined. Figure 2.5 shows the band structure for the configuration in Fig. 2.2, but the PhC is of finite thickness $h = 250$nm. The gray region in Fig. 2.5 marks the continuum of radiation modes. The continuum is bounded by the light line (black dot-dashed line) which is defined as $\omega = c_0 k_{\|}$, where $c_0$ is speed of light in free space and $k_{||}$ is magnitude of an in-plane components $(k_x, k_y)$ of wavevector $\vec{k}$. Light cone can be understood by considering that radiating waves in the far-field closely resemble free-space plane waves satisfying $\omega = c_0\sqrt{k_{\|}^2 + k_{\perp}^2}$ for some value of $k_{\perp}$ which is a component of wavevector $\vec{k}$ perpendicular to the PhC slab [107]. As long as $k_{\|}$ is smaller than $\omega/c_0$, $k_{\perp}$ can take any value resulting in a mode of a frequency $\omega$ greater than $c_0 k_{\|}$. These modes create continuum of modes. The BIC is the mode at the same $k_{\|}$ as the continuum of modes. Despite this the BIC is not coupled to the continuum of modes and thus does not radiate. On the other hand, when $k_{\|}$ is larger than $\omega/c_0$ i.e. it lies below the light line, a solution decays exponentially away from the PhC slab. This is a guided mode in the PhC slab and for a given $k_{\|}$ we will have a discrete set of $\omega$ at which these modes will appear. They are characterized by infinite Q-factors. However, guided modes above the light line couple to radiation modes, and thus no longer have infinite Q-factors. Then, they are called guided resonances [108]. BIC is a guided resonance that is perfectly confined to the slab despite being among the radiating modes. Subsequently, different types of BICs, that are of relevance for PhC slabs, will be described together with the mechanisms standing behind them.

The most basic BIC is due to symmetry of the structure [25–27, 108, 109]. In this case, a state of a given symmetry class is decoupled from a continuous spectrum of another symmetry class. In a PhC slab, it often appears at high symmetry points of the BZ such as the Γ-point, $k_{||} = (0, 0)$; then the system preserves 180° rotational

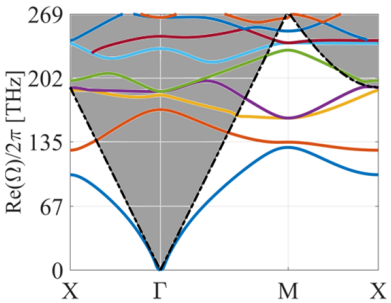


*Figure 2.5: Band structure of the PhC slab of finite thickness $h = 250nm$ for the TE-like polarization. Parameters of the PhC slab are the same as in Fig. 2.2. The gray region indicates the continuum of radiation modes. Its boundary is marked with the black line indicating the light line.*

symmetry. The even and odd modes with respect to the rotational symmetry are decoupled from each other [27]. The even modes with respect to the rotational symmetry have an infinite Q-factor because their in-plane components of the electric field offset each other, as found in Fig. 2.4(a). This perfect destructive interference of the in-plane components $E_x, E_y$ results in no field being radiated. However, these modes are no longer symmetry-protected away from the Γ-point because the destructive inference of the $E_x, E_y$ is not perfect anymore. This leads to coupling to the continuum of radiation modes and rapid drop in their Q-factors as we move away from the Γ-point, as found in Fig. 2.3(b). Symmetry-protected BICs are sensitive to perturbations breaking symmetry, however they are robust towards any variation of the parameters preserving the symmetry, e.g. variation of the air-hole radius [27].

Recently, other type of BICs have been proposed and experimentally demonstrated. These BICs are called trapped BICs and they do not arise due to symmetry, but as a result of destructive interference obtained by proper parameter tuning [27, 40, 74, 110, 111]. We distinguish between three kinds of trapped BICs [27] appearing when:

1. two identical resonant structures interact through a radiation channel,
2. two different resonances in the same cavity are coupled to a radiation channel,
3. the radiation amplitude of the single resonance is suppressed.

The trapped BIC in the 1$^{\text{st}}$ point is also called a Fabry-Perot BIC and it stands behind the formation of the lasing cavity in the self-pulsing Fano laser fabricated within the NATEC project [83, 112]. When a cavity is side-coupled to an open PhC waveguide, then at the resonating frequency of the cavity the transmission through the waveguide will drop to zero due to destructive interference of the wave travelling through the waveguide and radiation from the cavity [81]. When the two cavities are at a distance $d = n\lambda/2$, then the resonating Fabry-Perot cavity can be formed in the waveguide trapping the light between the two narrow band mirrors, Fig. 2.6(a). One of the cavities could be replaced by termination of the PhC waveguide with a PhC exhibiting photonic band gap and creating a broad band mirror, Fig. 2.6(b). The unique property of the Fabry-Perot BIC is that the two cavities can interact through the waveguide even over long distances. This long-range interaction has been studied not only in PhC cavities, but also in qubits coupled through the waveguide [113, 114].

The 2$^{\text{nd}}$ point BIC can be obtained by careful design of the resonance frequencies and radiation rates from the cavity to the radiation channel, e.g. a waveguide. The radiation from both resonances can interfere destructively leading to the trapped BIC [115]. These BICs are obtainable when number of resonances is larger than the number of radiation channels [116].

The 3$^{\text{rd}}$ point BIC requires only a single resonance and is associated with simultaneous suppression of the radiation amplitudes $\vec{c}(\vec{k})$. The radiation amplitude can be

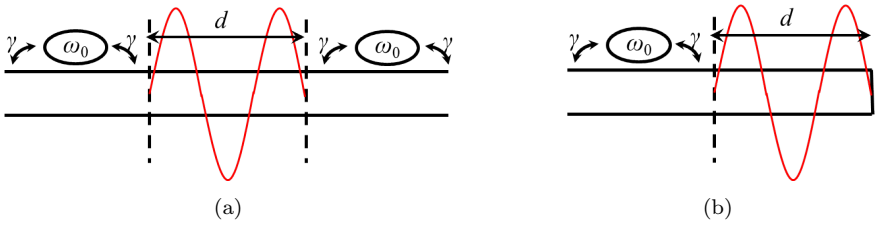


*Figure 2.6: Schematics illustrating Fabry-Perot BICs. (a) Cavities form narrow-band mirrors in the waveguide at the resonance frequency. Then, the waves are trapped between them if distance between the cavities is $d = n\lambda/2$. (b) Similarly, Fabry-Perot BIC can be realized when instead of the narrow-band mirror, a hard boundary is placed on one side, e.g. a PhC exhibiting photonic band gap.*

determined using the Bloch theorem for PhCs [107]. The electric field of a resonance in the PhC slab can be expanded as

$$\overrightarrow{E_{\vec{k}}}(\vec{\rho}, z) = e^{i\,\vec{k}\cdot\vec{\rho}}\,\overrightarrow{u_{\vec{k}}}(\vec{\rho}, z), \tag{2.1}$$

where $\vec{k} = k_x\hat{x} + k_y\hat{y}$ is the 2D wavevector restricted to the BZ describing the wave propagation in the plane of the PhC slab, $\vec{\rho} = x\hat{x} + y\hat{y}$ is the in-plane position vector and $\overrightarrow{u_k}$ is a periodic function in $\vec{\rho}$. For frequencies below the diffraction limit, the only propagating wave amplitudes are $c_{x,y} = \hat{x}, \hat{y} \cdot \langle \vec{u}(\vec{k}) \rangle$, where $\langle\rangle$ indicates a spatial average [74]. When both $c_{x,y}$ are zero, then no power will be radiated into the farfield, thus a guided resonance is turned into a BIC. Generally, $c_{x,y}$ are complex numbers, thus it is unlikely that both $c_{x,y}$ will become zero at any point of the BZ by variation of the two parameters $k_x$ and $k_y$. However, if the PhC slab exhibits some symmetries then the degrees of freedom of $c_{x,y}$ can be reduced. In fact, the PhC slab considered in the following sections exhibit several symmetries:

1. it is invariant under 180° rotation around the $z$-axis ($\epsilon(\vec{r}) = \epsilon(-\vec{r})$),
2. it exhibits time-reversal symmetry ($\epsilon(\vec{r}) = \epsilon^*(\vec{r})$)
3. it is vertically symmetric satisfying mirror symmetry with respect to the $z$-plane.

In this case, both $c_{x,y}$ are simultaneously purely real or imaginary [74]. Thus, there are only two degrees of freedom left and by varying $k_x$ and $k_y$ in the BZ, both radiation amplitudes can be suppressed resulting in the robust BIC. It is noted that simultaneous suppression of $c_{x,y}$ is accidental as it arises due to parameter tuning and is considerably distinct from the symmetry-protected BICs as it is not related to symmetry incompatibility of the guided resonance with the radiation continuum.

The trapped BIC is robust towards small perturbations of the system parameters; any variation of them will result in a shift of the BIC in the BZ, and not in its destruction. Moreover, it has been shown that the Q-factor of trapped BICs decays more slowly away from the design point in the BZ compared to symmetry-protected BICs [92]. This allows to design a mode with a large out-of-plane Q-factor value over the large region of the BZ. This property is crucial in the design of real life devices based on PhC slabs which are always of finite sizes and thus their total Q-factor depends on the finite samples of the dispersion relation in the vicinity of the BIC. The formation of trapped BICs can also be understood as the interband coupling [117] between the higher order bands [37, 40]. When the PhC slab is infinitely thick, there is no coupling between the bands due to the orthogonality of the modes. However, when the PhC slab thickness is finite, then the system exhibits radiation loss and the modes are not orthogonal anymore. The bands can be coupled through the radiation continuum and if they interfere destructively a trapped BICs can be created [40].

Due to coupling of guided resonance with radiation continuum, BICs are closely related to Fano resonances [26, 106, 108, 110, 118, 119]. As the BIC is approached, the Fano lineshape in the reflectivity spectrum will become sharper and eventually disappear completely at the BIC. Thus, Fano lineshapes are a birthmark of BICs.

High confinement of light offered by BICs is ideal for applications such as sensors [120], filters [121] and lasers [21, 122]. Particularly, PCSELs usually operate at the symmetry-protected BICs ensuring low lasing threshold. Moreover, trapped BICs enable creation of modes with large Q-factor over the large region of $k$-space. This might enable creation of very large Q-factor, small footprint PhC slab resonators as discussed in section 2.5. BIC is also the phenomenon standing behind the lasing cavity in the self-pulsing Fano laser designed and fabricated within the NATEC project. Thus, BIC play a crucial rule in the discussion presented in the following sections.

## 2.3 Dirac cones and exceptional points in photonic crystals

### 2.3.1 Two-dimensional photonic crystals - Dirac cones

In this section, we discuss phenomena of Dirac cones, exceptional points and their potential applications based on the current state-of the art literature. We do this using our own examples strictly relevant for the investigations in sections 2.4 and 2.5. Scientific interest in Dirac-like cone dispersion has been sparked when the first photonic analog of graphene has been demonstrated [123–125]. In the photonic analogs of graphene, the Dirac cone has been found in a hexagonal lattice PhC at the edge of the BZ as a result of double degeneracy of two bands forming a conical dispersion. It has robustly emerged due to hexagonal symmetry of the lattice without any need for parameter tuning [126]. However, this Dirac cone lies below the light cone, thus does not allow for surface-emission.

Dirac cone can also emerge accidentally at the centre of the BZ as result of fine tuning of the structural parameters, e.g. radius of the air-holes [54–58]. In this case, a pair of doubly degenerate bands can meet at the Γ-point with a singly degenerate band creating a triple degeneracy. Then two of the bands form a linear conical dispersion touching at the Dirac point, whereas the third band also crosses a Dirac point, but it exhibits a quadratic dispersion. This kind of dispersion is not truly a Dirac cone dispersion, which was found in graphene, thus because of the third quadratic band, it is called a Dirac-like dispersion [127]. It does not lead to the properties that graphene is famous for, however it provides a linear and isotropic dispersion that can be very useful for PCSELs and can spawn rings of exceptional points opening door to novel non-Hermitian physical phenomena in photonics regime [60].

We start by investigating the dispersion diagrams of a 2D PhC of square lattice with circular air-holes, see Fig. 2.7(a) and (c). The dielectric material of the PhC does not have any losses or gain, there is also no radiation loss as the configuration is periodic in the $x$ and $y$ directions, and is infinite along the $z$ direction. Thus, the system is Hermitian and the eigenfrequencies, $\Omega$, are purely real. Fig. 2.7 shows a standard quadratic dispersion in a square lattice 2D PhC with a doubly degenerate bands at the Γ-point and a third band separated in frequency. When radius of the air-holes in the PhC is tuned, all three bands become accidentally degenerate at the Γ-point forming a Dirac-like cone dispersion, see Fig. 2.7(b) and (d). It is found in Fig. 2.7(b) and (d) that isotropic Dirac-like cone dispersion is only an approximation in the vicinity of the Dirac point at the center of the BZ. It is also noted that at the Dirac point, the eigenfrequencies become degenerate, but not the eigenmodes what is further confirmed in Fig. 2.8 [61, 78]. It is seen that at the Γ-point, the bands creating the Dirac cone exhibit a dipole-like and a quadrupole-like modes, while the third quadratic band exhibits a dipole-like mode which is degenerate with one of the bands of the Dirac cone at the Γ-point.

Moreover, the quadratic dispersion surface crossing a Dirac point is almost completely flat along the Γ-$X$ direction, and the electric field is mostly parallel to the $k$-vector for the modes in this band, see Fig. 2.8(b). Thus, the modes in this band are quasi-longitudinal, whereas the modes in the other two bands have wavevectors mostly perpendicular to the electric field. The surface of quasi-longitudinal modes crossing the Dirac point corresponds to the longitudinal solution of the Maxwell equations when $\epsilon_x = 0$ and $\epsilon_y = 0$ for the TE polarization [56]. Unfortunately, the effective medium theory can only be applied to extract $\epsilon_{eff}$ and $\mu_{eff}$ when the triple degeneracy at the Γ-point is formed by low order modes such as monopole and dipole [128]. Therefore, it has been shown to work satisfactorily when the PhC is formed from dielectric cylinders immersed in air, [56], however, when the structure is inverted, as in our case, the eigenmodes have considerable projections on higher order modes, see Fig. 2.8. It is

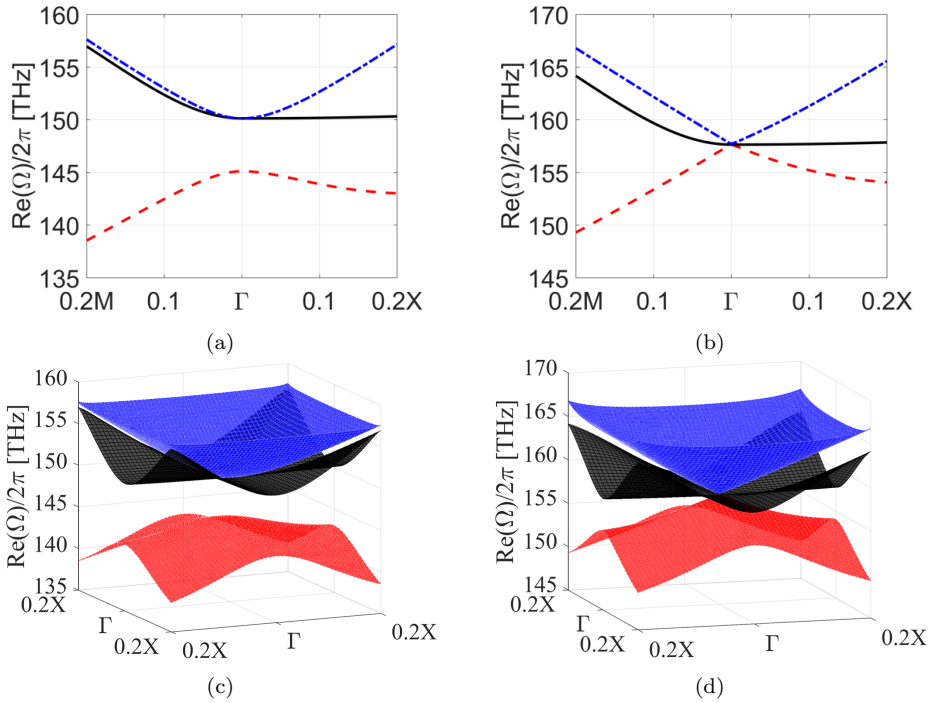


*Figure 2.7: (a),(b) Band diagrams in the Γ-M, Γ-X directions of a 2D PhC ($\epsilon_r = 10.05$) of square lattice ($a = 780nm$) of circular air-holes (a) $r = 0.28a$, (b) $r = 0.3136a$. (c),(d) are the 3D band diagrams in all directions over 20% of the BZ. The results obtained for the TE polarization.*

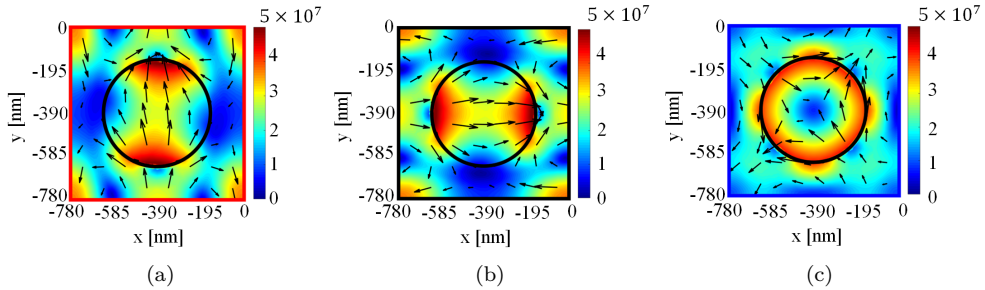


*Figure 2.8: Magnitudes of the electric field of the three modes close to the Γ-point plotted for small $k_{||}$ along the Γ-X direction. Obtained for the configuration in Fig. 2.7(b),(d). Colors of the frames correspond to colors of the bands in Fig. 2.7. The arrows show $(E_x, E_y)$.*

seen that the modes have dipole-like and quadrupole-like character. However, these are not the clear modes, but mixtures of higher order modes. Thus, the effective medium theory cannot be used. If the configuration was a homogeneous isotropic medium, then the flat surface of quasi-longitudinal modes would be completely flat. However, due to spatial dispersion of the PhC with circular air-holes, the surface exhibits quadratic dispersion for directions other than Γ-$K$ direction, Γ-$M$ direction being the most extreme case as seen in Fig. 2.7(d).

It has been shown that Dirac-like cone dispersion in PhCs can be used to ensure single-mode operation in large-area surface-emitting lasers and avoid localization of the fields in these lasers [52, 129]. It can be understood by:

1. Taylor expanding the frequency up to the first order around the Γ-point, $\omega(k_{||}) = \omega(0) + \frac{\partial\omega}{\partial k_{||}} k_{||}$, $k_{||}\big|_\Gamma = 0$

2. calculating mode spacing as a difference between the frequencies of the modes at the wavevectors $k_1 = \pi/L$, $k_2 = 2\pi/L$, $L$ is the largest dimension of the PhC

Then, we can arrive at the two equations, which were presented in [52], for the mode spacing in the case of linear, $\Delta\omega = \alpha\pi/L$, and quadratic, $\Delta\omega = 3\beta\pi^2/L^2$, dispersions. Thus, it is seen that the mode spacing decreases much more rapidly in the case of the quadratic dispersion leading to multi-mode lasing. Furthermore, large area PCSELs can take advantage from one more consequence of the linear dispersion. In this case, localization effects are significantly reduced as the group velocity is not only larger than in the case of the quadratic dispersion, but also constant for all the modes. Thus, the lasing cavity can be interpreted as a 2D Fabry-Perot cavity where the in-plane feedback is almost completely eliminated and comes only from the sides of the finite size PhC [52]. Then, the lasing mode is selected based on the lowest out-of-plane losses which differ for each mode.

### 2.3.2 Photonic crystal slabs - exceptional points

Dirac-like cone dispersion has been shown not only to be mapped into near zero index materials and allow an increased lasing area while maintaining single mode operation, but also to spawn a ring of exceptional points [60]. Exceptional point is the point at which two or more eigenvalues and eigenvectors coalesce upon variation of the parameter on which a considered matrix depends [61, 130]. In the case of PhCs, exceptional point is the point in the dispersion diagram where two resonances have the same resonating frequency and spectral widths, and identical mode profiles. This is in direct contrast to the eigenvalue degeneracy at the Dirac point discussed above as at the exceptional point there are no two independent eigenvectors, there is only one, resulting in impossibility of obtaining a diagonal matrix at this point [62, 131]. In order to highlight this difference the term 'coalesce' is used when eigenvalues and eigenvectors become the same, and the term 'degenerate' is used when only the eigenvalues are identical. Exceptional points arise due to nonhermiticity of the system. Non-Hermiticity is introduced when the system has an external input or output so that the energy is not conserved. This can be an open boundary so that the system exhibits radiation loss or it can be made out of the material exhibiting loss or gain. Then, the eigenvectors do not form an orthogonal basis and the eigenvalues are complex with the imaginary part indicating growth or decay. Usually, non-Hermiticity of the system is simply associated with amplification or dissipation being present in the system. However, this is not a whole picture as the non-Hermitian physics differs drastically from Hermitian physics when degeneracies are present [61].

In real life configurations, the PhC is always of finite thickness. In this case, guided modes in the PhC slab are coupled to the continuum of radiation modes above the light line due to periodic modulation of the refractive index and become so-called guided resonances [108]. These states are no longer perfectly confined to the slab and exhibit radiation loss resulting in the system becoming non-Hermitian.

PhC slab is modelled as shown in Fig. 2.3(a). The open boundary is simulated by perfectly matched layer placed $2a$ away from the PhC slab. The results are obtained for the TE polarization enforced in the middle of the slab. However, the thicker the slab is, the larger the contribution from the transverse-magnetic (TM) polarization becomes. The field is said to be TE-like polarized as long as the slab thickness is lower than the wavelength [107]. Subsequently, we vary the radius of the air-holes for the configuration considered in Fig. 2.7, but this time the PhC slab is of finite thickness, $h = 250nm$. When two degenerate dipole-like modes become degenerate with a quadrupole-like mode at the centre of the BZ, the dispersion becomes much different than in Fig. 2.7, see Fig. 2.9. Particularly, it is found that the real (imaginary) part

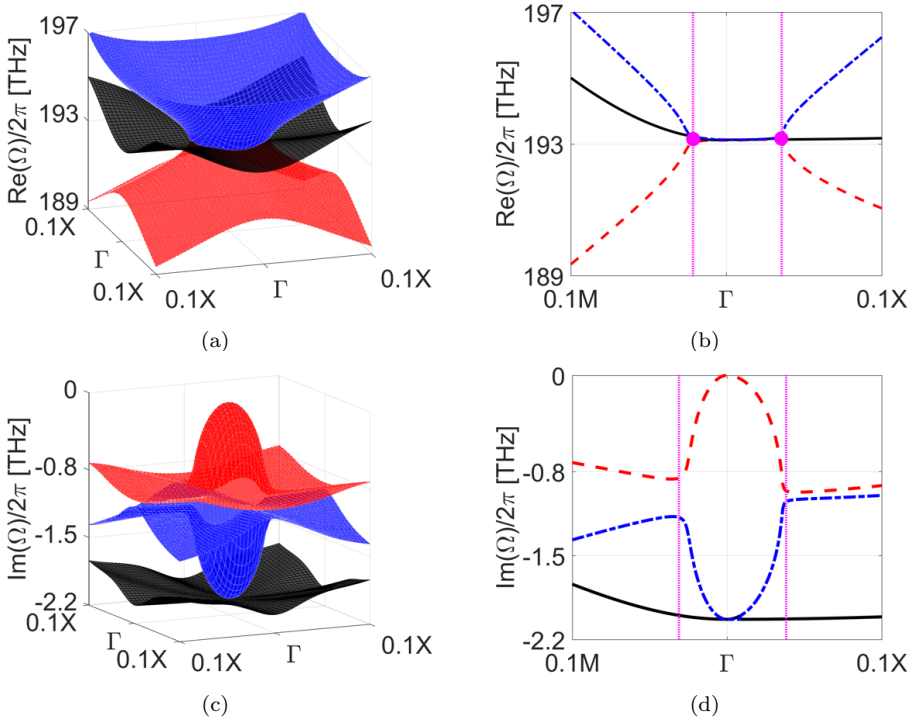


*Figure 2.9: (a), (b) Real and (c), (d) imaginary parts of the eigenvalues versus $k_{||}$ for a PhC slab ($\epsilon_r = 10.05$) with finite thickness $h = 250nm$, a square lattice ($a = 780nm$) of circular air-holes $r = 0.304a$ under the TE-like polarization. (b), (d) show the cuts of the 3D dispersion diagrams along the high symmetry directions, Γ-$M$ and Γ-$X$. The dispersion is plotted over 10% of each direction. Pink dots in (b) mark the exceptional points while pink dotted-lines indicate the extent of the ring of exceptional points.*

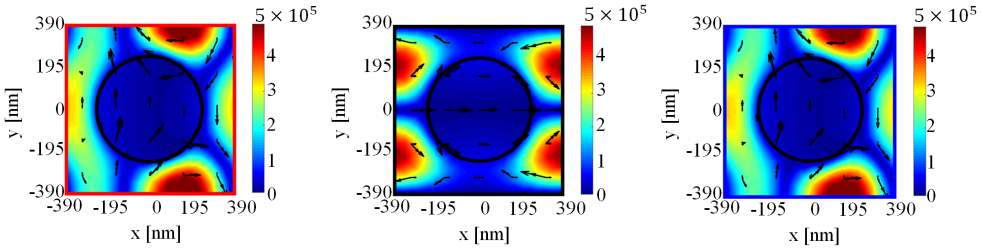


*Figure 2.10: Magnitudes of the magnetic field of the three modes at the exceptional-point. Obtained for the configuration in Fig. 2.9(b), (d). Frames colors correspond to colors of the bands in Fig. 2.9. The arrows show $(E_x, E_y)$.*

of the eigenvalue is degenerate and non-dispersive with respect to $k_{||}$ inside (outside) the ring of exceptional points. The exceptional points are marked with pink dots in Fig. 2.9(b). At these points the real and imaginary parts of the eigenvalues are identical as well as the corresponding field profiles of the coalescing modes. These field profiles are shown in Fig. 2.10.

Moreover, strong dispersion of losses is observed close to the Γ-point in Fig. 2.9(c), (d). The two dipole-like modes exhibit the same considerable radiation losses, whereas the loss of the quadrupole-like mode is zero at the Γ-point as this is a symmetry-protected BIC discussed in section 2.2. When we approach the exceptional point in Fig. 2.9(d), the imaginary parts of the eigenvalues rapidly approach the same value while following square-root dispersion, which is a birthmark of exceptional point.

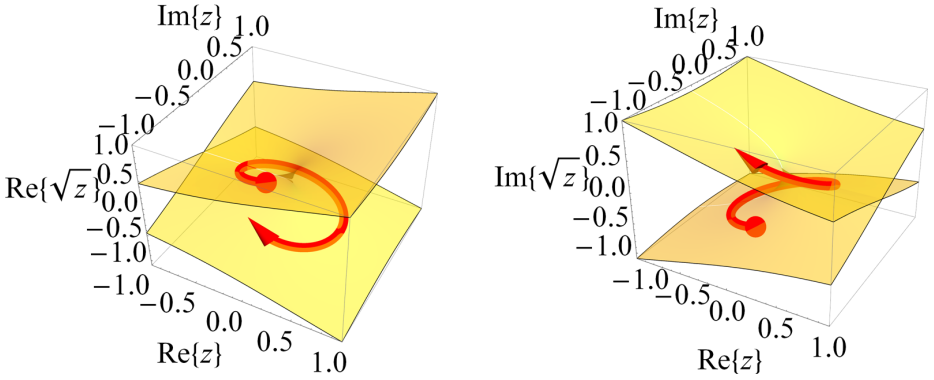


(a) (b)

*Figure 2.11: (a) Real and (b) imaginary parts of complex square root function* $\sqrt{z}$ *plotted versus* $\mathrm{Re}(z)$ *and* $\mathrm{Im}(z)$*. The red trajectory indicates how the initial state, marked with red dot, changes when* $\mathrm{Re}(z)$ *and* $\mathrm{Im}(z)$ *make a loop around the exceptional point, which is at* $\mathrm{Re}(z) = 0$ *and* $\mathrm{Im}(z) = 0$*.*

Outside the ring of exceptional points, it is the real part of the eigenvalues which follows square-root dispersion. The square root dispersion can be understood by considering a simple effective Hamiltonian which describes the evolution of the system. The effective Hamiltonian near the Γ-point has been derived in [57] for a square lattice PhC. The flat band is decoupled from the other two bands forming a Dirac-like cone dispersion [60], that is why the considered Hamiltonian is only a 2x2 matrix:

$$\mathbf{H}_{eff} = \begin{bmatrix} \omega_0 & v_g|\vec{k}| \\ v_g|\vec{k}| & \omega_0 - i\gamma_d \end{bmatrix}. \tag{2.2}$$

The eigenvalues of $\mathbf{H}_{eff}$ are $\omega_\pm = \omega_0 - i\frac{\gamma_d}{2} \pm v_g\sqrt{|\vec{k}|^2 - \gamma_d^2/(4v_g^2)}$, where $\omega_0$ is the frequency at the degeneracy, $|\vec{k}|$ is the magnitude of $\vec{k}_{||}$, $v_g$ is the group velocity when $\gamma_d = 0$ (Dirac-like dispersion). In Eq. (2.2), only a dipole-like mode exhibits radiation loss, $\gamma_d$, since the quadrupole-like mode is a symmetry-protected BIC at the Γ-point, $\gamma_q = 0$. The equations show that the eigenvalues coalesce when the square-root is zero. In this approximate scenario, extent of the ring of exceptional point depends on $\gamma_d/(2v_g)$. When dispersion of loss of the quadrupole-like mode is taken into account, extent of the ring is dependent on $(\gamma_d - \gamma_q)/(2v_g)$ [60].

Moreover, the square-root behaviour in the vicinity of exceptional points is associated with some very unique topological properties, particularly an exceptional point is encircled [70–72, 88, 130–132]. When the loop in the parameter space is made around the exceptional point in a quasistatic manner, then due to square root behavior only half of the loop is spanned by real and imaginary parts of the eigenvalues. It is simply because of $\sqrt{z} = \sqrt{r}e^{i\phi/2}$, where $r$ and $\phi$ are magnitude and phase of $z$. Then, the two eigenvalues connected by the square root behaviour are exchanged after the full loop in parameter space [61, 130, 132, 133]. This phenomenon can be understood by studying Fig. 2.11 which shows a complex square-root function, $\sqrt{z}$, plotted versus real and imaginary parts of the variable $z$. Additionally, the corresponding eigenvectors are also exchanged upon a loop in parameter space around the exceptional point, however, they acquire an additional phase change of $\pm i$ [62, 134–138]. Therefore, while only two loops are needed for the eigenvalues to go back to the initial state, four loops are required for the eigenvectors [130–133].

Phenomenon of encircling an exceptional point has been used in [60] to prove that a ring of exceptional points has been spawned out of the Dirac-like dispersion and not a single exceptional point along only one direction. Particularly, it has been shown that

by choosing a parameter space composed of $k_{||}$ along any direction and radius of the air-hole, and then by following a loop enclosing an exceptional point, the eigenvalues switch along any direction [60]. This proves that an exceptional point exists along all directions. This is important because Fig. 2.9 shows that even though the exceptional point is along Γ-X direction, it is not fully present along Γ-M direction. The radius of the air-holes has to be adjusted by $0.25nm$ so that an exceptional point is found. Change of $0.25nm$ is too small to be distinguished in reality. Therefore, if the slab was to be fabricated, fabrication errors would lead to the slab that is very close to exceptional point along all directions, but it would not be an exact exceptional point along any of them. Additionally, when radius of the air-holes is decreased (increased) by 1%, all bands shift down (up) in wavelength by $8nm$, the double-degenerate bands are no longer degenerate with the third band at the Γ-point resulting in splitting between the bands of around $4nm$. Therefore, special care has to be taken of the PhC slab fabrication when it exhibits a ring of exceptional points.

## 2.4 Control of the rings of exceptional points

### 2.4.1 Photonic crystals with circular air-holes

This section elaborates results presented in [P1], [P3] which can be found in appendix C.1 and C.4. Particularly, we demonstrate that by varying thickness of the PhC slab, we can control the extent of the ring of exceptional points. We show that for a specific thickness, the extent of the ring can be reduced almost to a point. This is accompanied by large Q-factor values over the broad region of the BZ.

In the previous section, it has been shown that the extent of the ring of exceptional points depends on the ratio of dipole-like mode radiation loss and the group velocity. Thus, if one is able to control one of them, it would allow not only to control the position of the exceptional point in the $k$-space, but also the strong dispersion of loss that is strongly connected to it. On one hand, this control over the strong dispersion of loss could be exploited in improving the characteristics of large-area single-mode PCSELs as the loss contrast between the modes is enhanced [60]. On the other hand, if the radiation loss is reduced, the lasing threshold of the PCSEL could be significantly decreased leading to a potential design of very small foot print, large Q-factor PhC-based resonators that could be used as lasing cavities [P2].

Initially, one may expect that by introduction of gain in the PhC slab, e.g. several layers of quantum wells or quantum dots in the membrane, one could compensate for radiation loss present in the PhC slab of finite thickness. However, it is found that realistic gain values have negligible impact on the extent of the ring, see Fig. 2.12 which shows the real and imaginary part of the eigenvalues in the case of gain/loss in the slab. The presence of material absorption or gain can be modelled with the refractive index imaginary part $n_c = n - i\kappa$. Negative $\kappa$ stands for gain whereas positive $\kappa$ accounts for absorption. $\kappa$ can be directly related to the required material gain $g_0$ through equation $g_0 = -2\kappa\omega/c$ [139]. Thus, in our case, when $\kappa = -0.1$ and $\lambda = 1550nm$ the material gain is $g_0 = 808.4cm^{-1}$. In Fig. 2.12, it is found that these values of $\kappa$ introduce very small variation of the real part of the eigenvalues, and only the imaginary part of the eigenvalues is shifted. In order to significantly affect the real part of the eigenvalues and extent of the ring of exceptional points, the imaginary part of the refractive index has to be comparable to its real part. The required amount of gain would introduce a variation in the real part of the refractive index due to Kramers-Kroning relation. This would require corresponding adjustment of the PhC parameters, e.g. air-hole radius, to preserve the ring of exceptional points when large amount of gain is introduced. Anyway, this large $\kappa$ values require extremely high

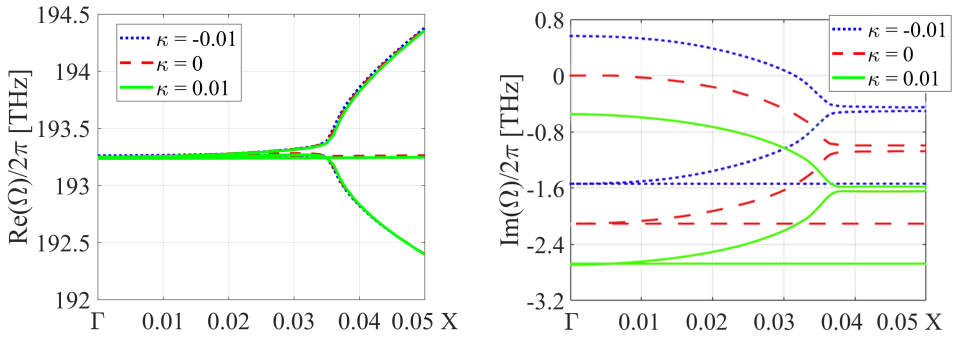


*Figure 2.12: (a) Real and (b) imaginary parts of the eigenvalues versus $k_{||}$ in the direction of $\Gamma$-$X$ for different values of $\kappa$. Data obtained for the same parameters as in Fig. 2.9*

*Table 2.1: Data presenting the influence of the PhC slab thickness, h, on the extent of the ring of exceptional points. Results obtained for a PhC slab with a square lattice ($a = 780nm$) of circular air-holes introduced in a dielectric material ($\epsilon_r = 10.05$) of a varying thickness h.*

| Frequency [THz] | Thickness [nm] | Part of the Γ-X | Radius of the air-hole |
|---|---|---|---|
| 340 | 25 | 0.018 | $0.2965a$ |
| 293 | 50 | 0.038 | $0.2985a$ |
| 263 | 75 | 0.046 | $0.3a$ |
| 242 | 100 | 0.046 | $0.3a$ |
| 203 | 200 | 0.038 | $0.303a$ |
| 193 | 250 | 0.036 | $0.303\,85a$ |
| 175 | 450 | 0.032 | $0.309a$ |
| 173 | 625 | 0.014 | $0.3185a$ |
| 171.1 | 650 | 0.0055 | $0.3173a$ |
| 170 | 675 | 0.0015 | $0.3156a$ |
| 168.5 | 700 | 0.000 26 | $0.3142a$ |
| 168 | 711.3 | ∼0 | $0.3136a$ |
| 167.5 | 725 | 0.000 15 | $0.313a$ |
| 164.3 | 850 | 0.0026 | $0.311a$ |
| 161.3 | 1000 | 0.0037 | $0.3076a$ |
| 165.3 | 1125 | 0.004 | $0.319\,45a$ |
| 164 | 1250 | 0.0054 | $0.3176a$ |
| 162.6 | 1375 | 0.000 54 | $0.317a$ |
| 162.1 | 1420 | ∼0 | $0.3163a$ |
| 161 | 1500 | 0.0004 | $0.316a$ |

material gain which is not achievable experimentally, thus this idea to control the ring of exceptional points has been abandoned.

On the other hand, one may observe that when the PhC slab is infinitely thick, then no radiation losses are exhibited and the ring of exceptional points is non-existent. The system is Hermitian and the eigenvectors and the eigenvalues are purely real. Upon parameter variation of the PhC only an accidental degeneracy of the eigenvalues can be present at the Γ-point in terms of a Dirac-like cone dispersion. Therefore, one may expect that when the thickness of the non-Hermitian system, which a PhC slab is, is increased, then we could at least approach a 2D case. This would result in reduced radiation losses, and thus the ring of smaller extent.

Therefore, in the following, we consider PhC slabs of various thicknesses. For each thickness of the slab, radius of the air-hole is adjusted in order to ensure an accidental degeneracy in the vicinity of the Γ-point. It is noted that we consider a first-order Dirac-like dispersion at the Γ-point, meaning that first-order mode in the $z$ direction is considered. Higher order Dirac-cone like dispersions can be obtained for higher frequencies or thicker PhC slabs, however here they will not be considered. In Figs. 2.14 and 2.15, we plot the band structure along the Γ-X direction and examine influence of the slab thickness on the extent of the ring of exceptional points; the results are shown for the following thicknesses: Fig. 2.14(a),(b) $h = 100nm$, Fig. 2.14(c),(d) $h = 250nm$, Fig. 2.14(e),(f) $h = 625nm$, Fig. 2.14(g),(h) $h = 675nm$, Fig. 2.15(a),(b) $h = 711.3nm$, Fig. 2.15(c),(d) $h = 850nm$, Fig. 2.15(e),(f) $h = 1250nm$, Fig. 2.15(g),(h) $h = 1420nm$. The results for all the thickness are summarized in Table 2.1, which presents frequency at which the ring of exceptional points has

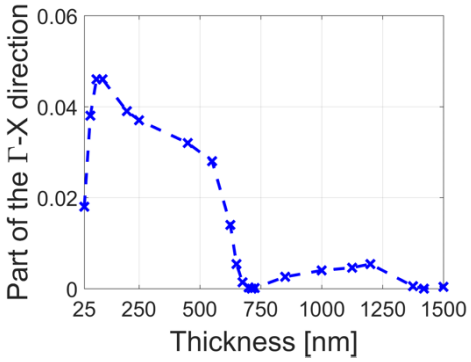


*Figure 2.13: Extent of the ring of exceptional points as a part of the Γ-X direction plotted versus thickness of the PhC slab. Based on the data from Table 2.1.*

appeared, considered thickness of the PhC slab, extent of the ring in terms of the fraction of the Γ-X direction and required radius of the air-hole in order to ensure an accidental degeneracy in the vicinity of Γ-point. The way extent of the ring changes with thickness of the PhC slab is summarized in Fig. 2.13.

The extent of the ring is the largest when thickness of the slab is $h = 100nm$, see Figs. 2.14(a),(b) and 2.13. It is found that as thickness of the slab increases, not only the extent of the ring of exceptional points decreases, but also the difference in losses between the modes at the Γ-point. This behaviour can be explained by two related effects. Firstly, as the slab thickness increases, the mode confinement in the slab improves resulting in lower radiation losses. Secondly, as the mode is more and more confined to the slab, the group velocity decreases as the field propagates mostly in the high index membrane, not in air. Thus, as the extent of the ring approximately depends on the ratio of the dipole-like mode radiation losses and the group velocity, larger thickness of the slab leads to a ring of exceptional points being closer to the Γ-point and a smaller difference of losses between the quadrupole-like and the dipole-like modes at the Γ-point.

Furthermore, it is found in Fig. 2.13 that as thickness of the slab increases, there are two distinct minima in the extent of the ring of exceptional points at $710nm$ and around $1420nm$. This is also seen in Figs. 2.15(a),(b) and (g),(h) showing that in both cases the real parts of the eigenvalues create Dirac-like cone dispersion close to the Γ-point, while the imaginary parts become very small, almost negligible compared to other cases in Fig. 2.13. However, it is emphasized that the system is still non-Hermitian. Losses have been greatly reduced and the system approximately behaves like a Hermitian system with Dirac-like cone dispersion at the Γ-point, but the ring of exceptional points has not disappeared. It has been significantly reduced and can be found in a very close vicinity of the Γ-point.

On the other hand, when thickness of the slab becomes lower than $h = 100nm$, the mode confinement is worsened, and large part of the field propagates in air. This results in strong increase of the group velocity counteracting further increase of the extent of the ring. As thickness of the slab is decreased, the frequency, at which the ring is present, increases rapidly. Eventually, the free space case is approached when no radiation loss is present.

It is found in Fig. 2.13 that the minima in the extent of the ring appear at equidistant points from each other and the curve varies in a periodic-like manner. Subsequently, we calculate an effective wavelength in the slab to gain an additional insight. The approximate formula for the effective refractive index is $n_{eff} = (1 - FF)n_r + FF$ [24], where $n_r = 3.17$ is the refractive index of the membrane, $FF$ is a

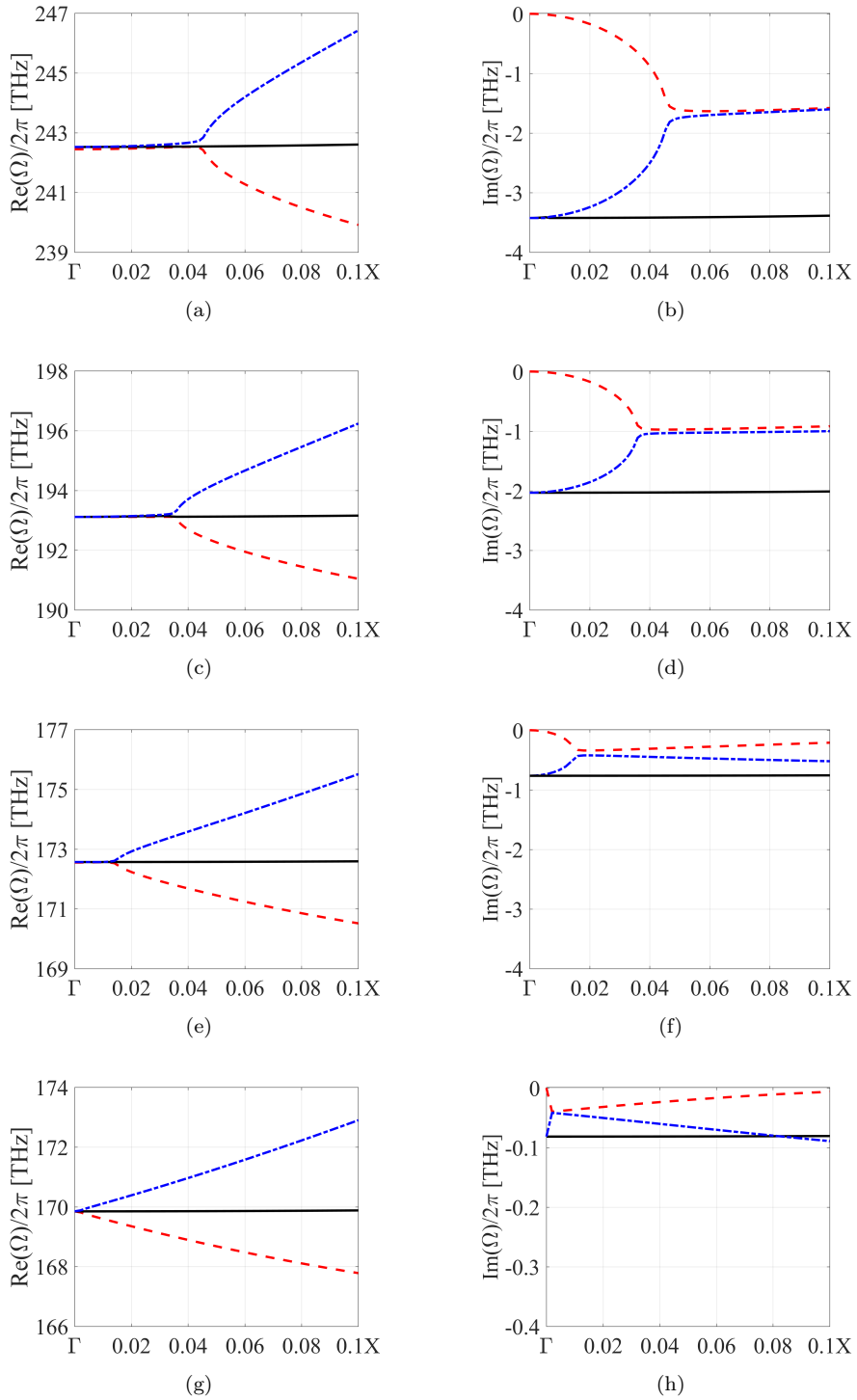


*Figure 2.14: (a),(c),(e),(g) Real and (b),(d),(f),(h) imaginary parts of the eigenvalues versus $k_{||}$ along the Γ-X direction. Results obtained for a PhC slab with a square lattice ($a = 780nm$) of circular air-holes introduced in a dielectric material ($\epsilon_r = 10.05$) of a varying thickness $h$. Thickness of the slab is (a),(b) $h = 100nm$, (c),(d) $h = 250nm$, (e),(f) $h = 625nm$, (g),(h) $675nm$. Radius of the air-holes is adjusted accordingly in each case in order to ensure accidental degeneracy at the Γ-point. Note that the scale in (h) is different than in (b), (d), (f).*

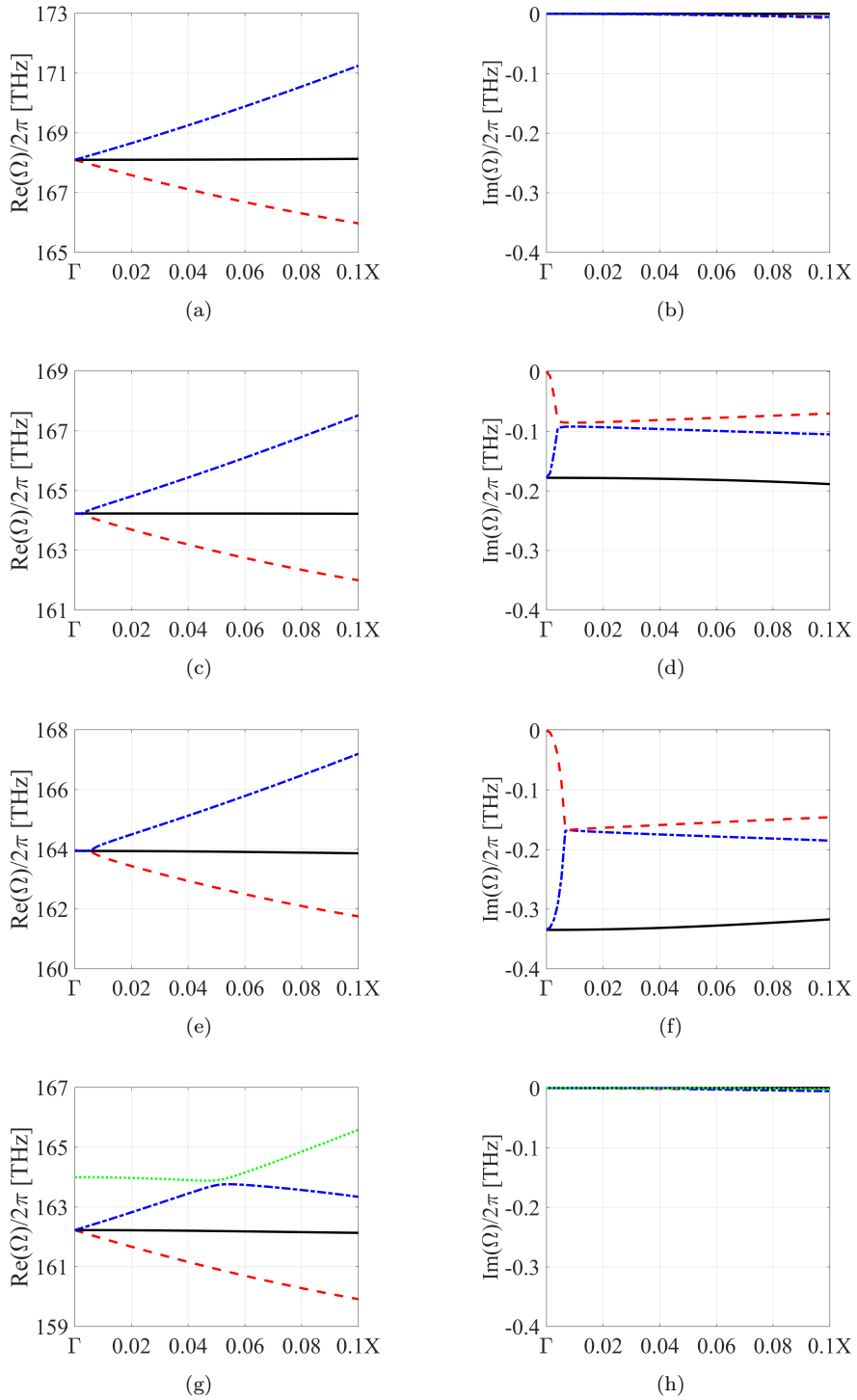


*Figure 2.15: (a), (c), (e), (g) Real and (b), (d), (f), (h) imaginary parts of the eigenvalues versus $k_{||}$ along the $\Gamma$-$X$ direction. Results obtained for a PhC slab with a square lattice ($a = 780nm$) of circular air-holes introduced in a dielectric material ($\epsilon_r = 10.05$) of a varying thickness $h$. Thickness of the slab is (a),(b) $h = 711nm$, (c),(d) $h = 850nm$, (e),(f) $h = 1250nm$, (g),(h) $1420nm$. Radius of the air-holes is adjusted accordingly in each case in order to ensure accidental degeneracy at the $\Gamma$-point.*

filling fraction $FF = 30.9\%$ at the first minimum seen in Fig. 2.13, when $h = 711.3nm$. In the case considered, $n_{eff} = 2.5$ which corresponds to an effective wavelength $\lambda_{eff} = 713nm$. It is found to be very close to the slab thickness at the first minimum. Thus, the recovery of the Dirac-like cone dispersion in the vicinity of the Γ-point appears to be strongly related to dielectric slab phenomena. Here, we recall that the TE-like polarization is enforced by a perfect magnetic conductor boundary condition in the middle of the PhC slab, Fig. 2.3. Thus, when the slab thickness becomes very small, it can be understood that the perfect magnetic conductor short-circuits $(H_x, H_y)$ and $E_z$, which are inevitably present in the membrane of finite thickness, thereby reducing the radiation loss. Moreover, due to the enforced TE-like polarization, all antisymmetric modes in the $z$ direction with respect to the in-plane electric field intensity components are excluded. This results in the minima in Fig. 2.13 occurring at even multiples of $\lambda_{eff}/2$.

Similar variation of radiation loss has been observed in [30] in the PhC slab under the TE-like polarization. This has been explained in terms of destructive interference of the waves diffracted vertically within the slab. When the slab has been $\lambda_{eff}/2$ thick, only the waves diffracted at the bottom and the top of the air-hole satisfy perfect destructive interference, the rest contributes to the radiation loss. Once the slab thickness is increased to $\lambda_{eff}$, then for each diffracted wave there is another one interfering destructively with the former one leading to the reduced radiation loss and the extent of the ring of exceptional points. This observation has been used to reduce the destructive interference and extract more radiation by introduction of the air-holes with vertically asymmetric profiles [21, 30, 31]. This would increase an extent of the ring beyond what is achievable with thickness variation and would result with an even stronger dispersion of loss close to the Γ-point finding application in large area, single mode PCSELs due to the increased loss margin between the modes. However, in the following we focus on the opposite, i.e. minimizing the radiation loss minima, and thus reducing the extent of the ring as found in Fig. 2.13. This knowledge will be used in the design of small footprint, large Q-factor PhC resonators in section 2.5.

In addition to Fig. 2.15(a),(b), Figure 2.16 shows the band structure along all directions for the first minimum in Fig. 2.13 when the slab thickness is $h = 711.3nm$, the inset shows a closer look on the imaginary parts of the eigenvalues. It is found in Fig. 2.16(a), (b) that the real parts of the eigenvalues resemble very closely the eigenvalues of the 2D PhC shown in Fig. 2.7. The main differences is in the frequency at which Dirac-like cone dispersion appears: (2D: 158THz, 3D: 168THz), and the flatness of the third quadratic band which is flatter in the 3D case. The imaginary parts of the eigenvalues are found to be very close to zero in the 3D optimized case. Therefore, when the thickness of the membrane is optimized, the 3D PhC (non-Hermitian system) behaves approximately as a 2D PhC (Hermitian system). Notably, the radius of the air-holes required to ensure an accidental degeneracy at Γ-point is the same in both cases, $r = 0.3136a$. However, the insets of Fig. 2.16(c),(d) reveal that the imaginary parts of the eigenvalues are not exactly zero in the optimized thickness case, and the losses increase away from the Γ-point.

It is found in Fig. 2.16(c),(d) that the quadratic band (black) exhibits the most stable behaviour, i.e. its imaginary part is the closest to zero and stays very close to zero over the broad area of the BZ. The low imaginary part of the eigenvalue signifies very large out-of-plane Q-factors which are shown in Fig. 2.17. Originally, when the slab thickness is $h = 250nm$, only one of the bands exhibits a symmetry-protected BIC present at the center of the BZ and its Q-factor drops rapidly away from the center, Fig. 2.17(a). The other two bands exhibit out-of-plane Q-factors on the order of $10^2$. On the other hand, in the optimized thickness case, all three bands exhibit very large out-of-plane Q-factors in the vicinity of the Γ-point, Fig. 2.17(b). Particularly, both,

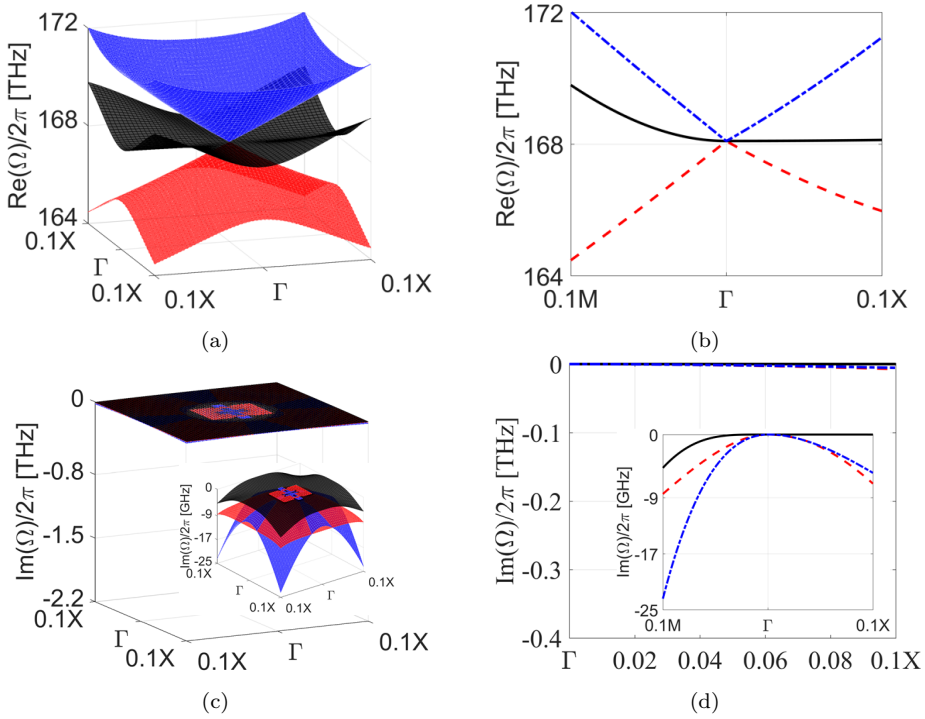


*Figure 2.16: (a), (b) Real and (c), (d) imaginary parts of the eigenvalues versus $k_{||}$ for a PhC slab ($\epsilon_r = 10.05$) with $h = 711.3nm$ and a square lattice ($a = 780nm$) of circular air-holes $r = 0.3136a$ under the TE-like polarization. (b),(d) show the cuts of the 3D dispersion diagrams along the high symmetry directions, Γ-M and Γ-X. The dispersion is plotted over 10% of each direction.*

quadrupole-like and dipole-like, modes are characterized by two peaks in the Q-factor at the Γ-point. Difference in losses between these two modes becomes almost negligible in the close vicinity of the Γ-point resulting in the extent of the ring being reduced almost to zero $k_{||} \approx 0$. Therefore, the increase in thickness allowed to bring a Q-factor of the dipole-like mode up to a comparable value with the symmetry protected BIC resulting in the ring compressed almost to a point.

Particularly, the out-of-plane Q-factor of the quadratic band (black) is shown to be larger than $10^6/10^8$ over 20%/8% of the Γ-X direction, respectively, and is more than 400 times larger than in the case of the other two bands, Fig. 2.17(b). In the

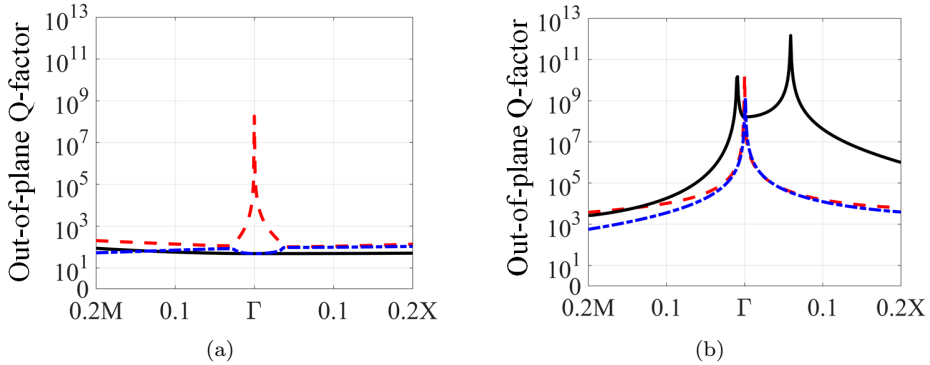


*Figure 2.17: Out-of-plane Q-factors for the PhC slab of finite thickness (a) $h = 250nm$, (b) $h = 711.3nm$ plotted versus $k_{||}$ along 20% of the Γ-M and the Γ-X directions. The PhC is composed of a square lattice ($a = 780nm$) of circular air-holes introduced in a dielectric material ($\epsilon_r = 10.05$), radius of the air-holes has been adjusted in order to ensure an accidental degeneracy at the Γ-point.*

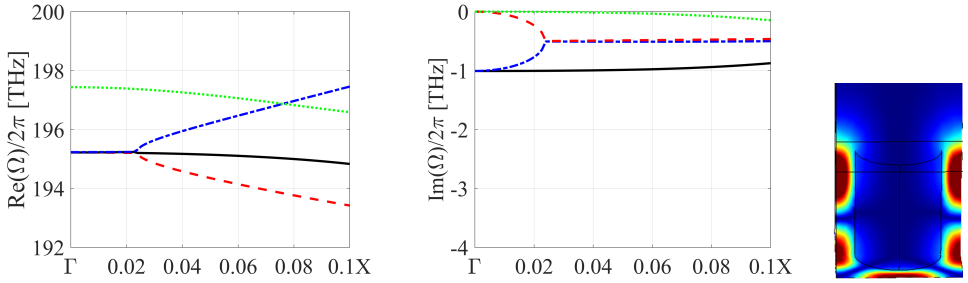


*Figure 2.18: (a) Real and (b) imaginary parts of the eigenvalues versus $k_{||}$ along the Γ-X direction. Results obtained for the same configuration as in Fig. 2.16. (c) shows distribution of $|H_z|$ calculated at the Γ-point for the quadrupole-like mode having second order distribution along the z direction.*

case of 250$nm$-thick slab, these values of the Q-factor have been achievable only at the BIC and have been dropping rapidly away from it. This Q-factor enhancement in the optimized PhC slab thickness have been achieved due to trapped BICs being present along both, Γ-M and Γ-X, directions of the black band close to the Γ-point. Thickness optimization have allowed to move these BICs from the edges of the light cone towards the centre of the BZ. This has resulted in a broad area of the BZ being covered with large Q-factor values due to flatness of the black band, which is referred to as the flat band in the following. This is particularly important in the design of small area PhC-based lasers since the finite-size structure always sample a dispersion relation in a finite neighborhood of the desired point in $k$-space. The Q-factor of the flat band drops faster along the Γ-M than the Γ-X direction because of a decreased flatness of the band along this direction. It becomes comparable to the other two bands at around 10% of the Γ-M direction. The Q-factor value along this direction could be improved by moving the trapped BICs slightly away from the Γ-point so that large Q-factor values would be available over a broader region of $k$-space.

When the slab thickness is increased beyond 711.3$nm$, the extent of the ring of exceptional points increases again. However, even in the most pronounced case the extent of the ring does not reach the same value as in the case of the thinner slabs. At this point, we recall that the rings in Table 2.1 and Fig. 2.13 are obtained for the first order modes in the $z$ direction. When the slab thickness increases beyond 711.3$nm$, not only higher-order modes come into play, but also the field polarization cannot be said to be TE-like anymore. As the slab thickness increases beyond $\lambda_{eff}$, the contribution from the TM-like polarization becomes comparable [107]. Thus, the configuration becomes increasingly difficult to analyze. When the first-order mode is considered for $h > \lambda_{eff}$, radiation losses are reduced compared to the slabs thinner than $\lambda_{eff} = 711nm$ as the case approaches a 2D PhC, similar trend is observed in [30]. When the second order mode in the $z$ direction is considered for thicknesses $\lambda_{eff} < h < 2\lambda_{eff}$, extent of the ring can reach similar values as in the case of the first order mode for thinner structures. For instance, Fig. 2.18(a),(b) shows the band structure when the slab is $h = 1375nm$ thick and the ring is obtained for a second order mode in the $z$ direction, see Fig. 2.18(c), then the extent of the ring constitutes 0.023 of the Γ-X direction.

Therefore, we have shown that by increasing thickness of the PhC slab, we can move trapped BICs close to the Γ-point, and thus decrease difference in losses between a symmetry-protected BIC and the coupled dipole-like mode at the Γ-point. This decreases extent of the ring of exceptional points almost to the point and ensures large Q-factor values over the broad region of the BZ. This is used in section 2.5 to design small-area, large Q-factor PhC slabs.

### 2.4.2 Photonic crystals with elliptical air-holes

In the following, we study a PhC configuration with a square lattice ($a = 730nm$) of elliptical air-holes. The 2D and 3D unit cell models are shown in Fig. 2.19. We consider an elliptical air-hole of constant ellipticity with semi-major axis $a_0 = 1.25r_0$ and semi-minor axis $b_0 = 0.8r_0$, where $r_0$ is the parameter we vary. As before, we vary the size of the air-holes to achieve an accidental degeneracy at the Γ-point.

#### 2D PhC Hermitian system - elliptical air-holes

Firstly, we consider a 2D PhC Hermitian system. Figure 2.20 shows the corresponding band structure. It is found that an ellipticity of the air-holes breaks the degeneracy between the two dipole-like modes at the Γ-point and separates them in frequency. Therefore, in this case an accidental degeneracy is obtained only between the quadrupole-like and dipole-like modes at the Γ-point. It results in a pure Dirac cone while the quadratic band (black) is shifted upwards in frequency. This shift in frequency can be controlled by the ellipticity of the air-hole. Due to the air-hole ellipticity, we also observe different dispersion relations along the semi-major and semi-minor axis and we distinguish between the Γ-X and the Γ-X′ directions as indicated in Fig. 2.19(a). It is observed that dispersion curvatures along the Γ-X and the Γ-X′ directions differ radically. Particularly, in the case of the Dirac cone, the dispersion curvature is very small along the Γ-X′ direction and very large along the Γ-X direction. Similar, but not as pronounced observation can be made in the case of the quadratic black band. However, here the relation between the direction and curvature is reversed.

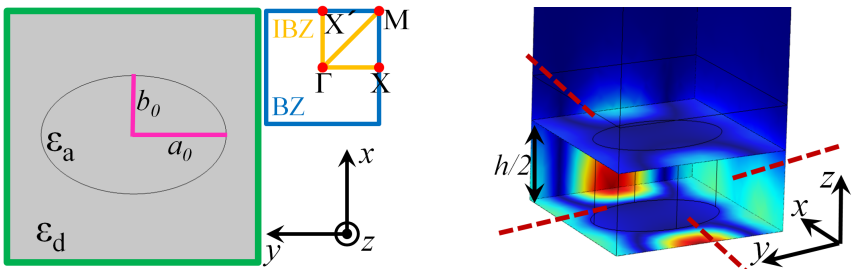


(a) (b)

*Figure 2.19: (a) 2D unit cell of a PhC together with the BZ and IBZ. (b) 3D unit cell of a PhC.*

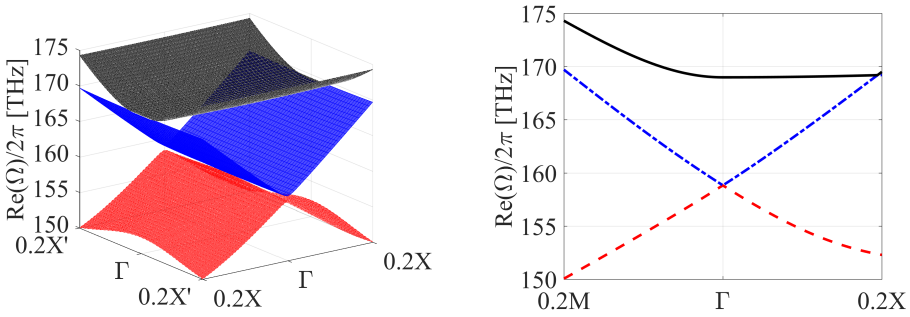


(a) (b)

*Figure 2.20: (a) The eigenvalues versus $k_{||}$ of a 2D PhC ($\epsilon_r = 10.05$) of a square lattice ($a = 730nm$) of elliptical air-holes with semi-major axis $a_0 = 1.25r_0$ and semi-minor axis $b_0 = 0.8r_0$, where $r_0 = 0.295a$. (b) shows a cut of the 3D dispersion diagram along the high symmetry directions, Γ-$M$ and Γ-$X$ plotted over 20% of each direction. The results obtained for the TE polarization.*

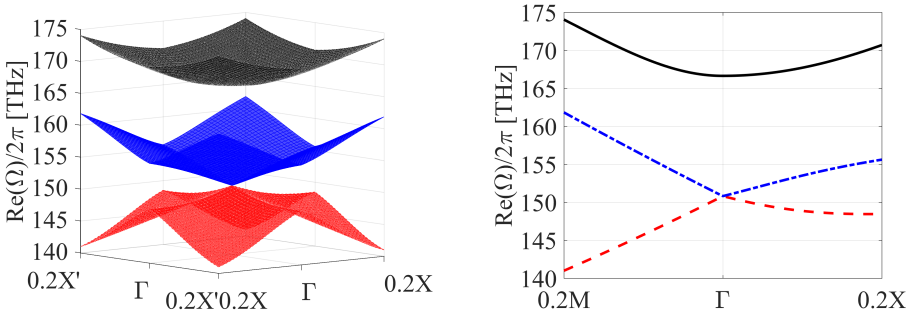


*Figure 2.21: (a) The eigenvalues versus $k_{||}$ for a 2D PhC ($\epsilon_r = 10.05$) of a square lattice ($a = 730nm$) of elliptical air-holes with $a_0 = 1.25r_0$ and $b_0 = 0.8r_0$, where $r_0 = 0.295a$. The air-holes are rotated by $45^\circ$ compared to the case in Fig. 2.20 with major axis along the diagonal of the unit cell. (b) shows the cut of the 3D dispersion diagram along the Γ-M and Γ-X directions plotted over 20% of each direction. The results obtained for the TE polarization.*

When the finite size structure is considered, the dispersion relation is sampled in a finite neighbourhood of $k$-space [140]. Then, small (large) curvature of the dispersion leads to small (large) spacing between the modes [141]. Thus, the modes along the Γ-X′ would be grouped with very small spacing in wavelength, while being strongly separated from the modes along the Γ-X direction. This results in a phenomenon of mode grouping which could potentially be used to boost the speed of surface-emitting lasers [141–143]. Additionally, at the Dirac cone, all the modes have the same in-plane losses due to the constant group velocity. Thus, all of the grouped modes could lase as long as the out-of-plane Q-factors are on the similar high level [141].

Therefore, mode spacing can be controlled by manipulating the shape of the air-hole, which alters the photonic band structure. The possibility to engineer dispersion of PhCs also allows to design exotic photonic well structures used to confine the modes [141, 144]. For an elliptical air-hole structure, manipulation of the dispersion structure is particularly easy as a sheer rotation of an ellipse can completely alter photonic band structure. It is found in Fig. 2.21 that when semi-major axis of an elliptical air-hole are aligned with a diagonal of the unit cell, there is no distinction between the Γ-X and the Γ-X′ directions. Then, the Dirac cone dispersion structure resembles the one of the PhC with circular air-holes shown in Fig. 2.7 with an exception of the black band which is still separated in frequency from the Dirac cone. The third band is no longer flat along any of the directions, and is characterized by quadratic dispersion.

### PhC slab non-Hermitian system - elliptical air-holes

We next consider a PhC slab of finite thickness $h$ which is a non-Hermitian system due to an open boundary resulting in radiation losses. We focus on the band structures along the Γ-X and the Γ-X′ directions as the permittivity of the unit cell experiences the largest variation along these directions. In Figure 2.22 a photonic band structure is shown for the PhC slab of a standard slab thickness $h = 250nm$, the size of the air-hole has been adjusted to ensure an accidental degeneracy at Γ-point. In this case, no ring of exceptional points is spawned, but two roughly parallel contours of exceptional points are present. It is found in Fig. 2.22(b) that radiation losses are almost unchanged along the Γ-X′ direction for the two bands coalescing at the contour of exceptional points, while in the case of the third band (black) the radiation loss does not vary along the Γ-X direction. Furthermore, it is found that due to broken degeneracy of the dipole-like modes at the Γ-point, radiation losses are no longer the same at the Γ-point. They are considerably larger for the black band, which is

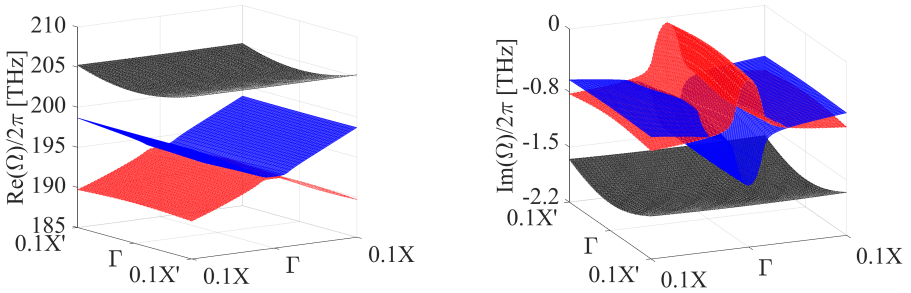


*Figure 2.22: (a) Real and (b) imaginary parts of the eigenvalues versus $k_{||}$ for a PhC slab ($\epsilon_r = 10.05$) with finite thickness $h = 250nm$ and a square lattice ($a = 730nm$) of elliptical air-holes with $a_0 = 1.25r_0$ and $b_0 = 0.8r_0$, where $r_0 = 0.2839a$. The results obtained for the TE-like polarization.*

separated not only in the real, but also the imaginary part of the eigenvalues from the other two bands.

As in the previous section, also in this case spacing between two contours of exceptional points can be controlled by varying thickness of the PhC slab. However, in the present case, the slab thickness can be optimized either 1) to reduce distance between contours of exceptional points or 2) to reduce radiation loss of the flat band. In Fig. 2.23, the structure is optimized to exhibit reduced radiation losses for the flat band. Even in this case, the distance between the contours of exceptional points is significantly reduced, Fig. 2.23(a). Furthermore, once the structure is optimized, small curvature of the flat band results in imaginary part of the eigenvalue varying very slowly and being very close to zero over broad region of the BZ as shown in Fig. 2.23(b).

The out-of-plane Q-factor dispersion is shown in Fig. 2.24 in three cases (a) standard thickness case $h = 250nm$, (b) thickness optimized to reduce radiation loss for the flat band and (c) thickness optimized to reduce distance between contours of exceptional points. In all cases, the quadrupole-like mode is a symmetry-protected BIC at the Γ-point. In both optimized thickness cases, Figs. 2.24(b),(c), it is found that the blue band exhibits a trapped BIC along the Γ-X direction. The difference between both cases is that in (c) the trapped BIC is closer to the Γ-point than in (b). Ideally, the trapped BIC in (c) should be at the Γ-point to reduce difference in losses to zero between the red and blue bands. Furthermore, the flat black band exhibits very large out-of-plane Q-factors over a broad region of the BZ in Fig. 2.24(b).

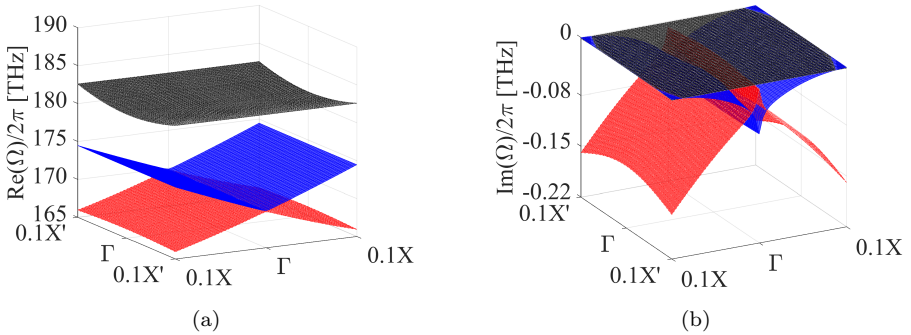


*Figure 2.23: (a) Real and (b) imaginary parts of eigenvalues versus $k_{||}$ for a PhC slab ($\epsilon_r = 10.05$) with finite thickness $h = 658.8nm$ and a square lattice ($a = 730nm$) of elliptical air-holes with $a_0 = 1.25r_0$ and $b_0 = 0.8r_0$, where $r_0 = 0.296a$. The results are obtained for the TE-like polarization. Note that the scale in (b) is 10 times smaller than in Fig. 2.22(b).*

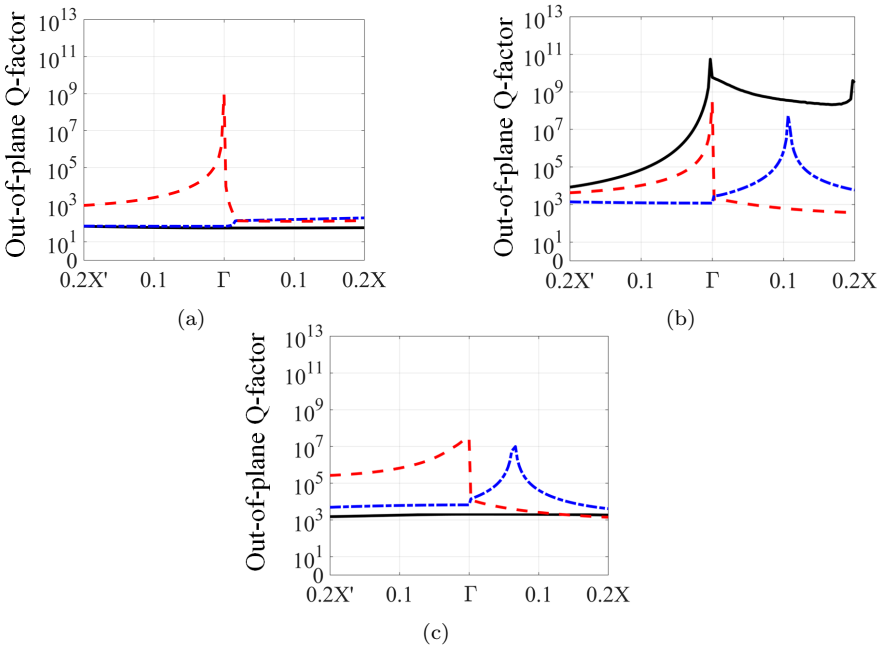


*Figure 2.24: Out-of-plane Q-factors for the PhC slab ($\epsilon_r = 10.05$) of finite thickness (a) $h = 250nm$, (b) $h = 658.8nm$ and (c) $h = 711.3nm$ plotted versus $k_{||}$ along 20% of the Γ-$X'$ and Γ-$X$ directions. The PhC is composed of a square lattice ($a = 730nm$) of elliptical air-holes with $a_0 = 1.25r_0$ and $b_0 = 0.8r_0$, where (a) $r_0 = 0.2839a$, (b) $r_0 = 0.296a$, (c) $r_0 = 0.292a$. The size of the air-holes was adjusted to ensure an accidental degeneracy at the Γ-point.*

Trapped BIC is found just next to the Γ-point along the Γ-X′ direction, the Q-factor drops as we move away from the Γ-point. However, it is still larger than $10^4$ over more than 20% of the Γ-X′ direction. On the other hand, along the Γ-X direction, a trapped BIC is found at the edge of the figure and the Q-factor value is extremely large ($Q > 10^8$) over the whole interval. This feature can be exploited in the design of small area, large Q-factor resonators as the small curvature of the band implies small in-plane losses while small imaginary part of the eigenvalue signifies small out-of-plane losses. Once known, out-of-plane and in-plane Q-factors can be used to estimate total Q-factor of the structure [144]. In Fig. 2.24(c), the flat black band is found to exhibit Q-factor slightly larger than 1000 over the considered region. On the other hand, the red band with the quadrupole-like mode at the Γ-point exhibits stable Q-factor along the Γ-X′ direction. It drops slowly and is significantly larger than $10^5$.

Therefore, we have shown that by optimizing the slab thickness we can vary the distance of exceptional points from the Γ-point. Moreover, ellipticity of the air-holes breaks degeneracy of the two dipole-like modes at Γ-point and separates them in frequency as well as in losses. Thus, it allows to separately optimize the structure for the flat band or the Dirac cone and avoid mode-mixing at the Dirac point in finite size configurations. Furthermore, the dispersion of the PhC with elliptical air-holes is found to be radically different along the Γ-X and Γ-X′ directions and can be significantly altered by a sheer rotation of the air-hole. This may allow to easily control band curvature along specific directions and thus control mode spacing in finite size structures. This results in an interesting phenomenon of mode grouping which could be used to boost the speed of PCSELs [141–143].

Finally, we note that even though exceptional points have been spawned at wavelengths longer than desired $1550nm$, all the parameters can be made dependable on the lattice constant and the structure can be made operational at the desired wavelength simply by adjusting the lattice constant.

## 2.5 Compact photonic crystal-based resonators and lasers

This section elaborates and extends the results presented in [P2, P3]. Results presented in the previous sections have shown that by optimizing the PhC slab thickness, the distance of exceptional points from the Γ-point can be controlled. Particularly, for a specific thickness the configurations have been shown to approximately behave as 2D configurations with an exceptional points being in very close vicinity of the Γ-point. In these configurations, the radiation losses were negligible and their band structures were resembling the ones of the 2D structures. These findings have allowed to identify PhC slab configurations exhibiting the out-of-plane Q-factors on the order of $10^8$ over a broad region of the BZ. These large Q-factors are obtained despite being above the light line and thus being inherently coupled to the continuum of radiation modes. Currently, these results are used to design small footprint PhC slabs with total Q-factor values rapidly increasing with an in-plane size of the structure.

The total Q-factor value is decided by two factors: 1) small in-plane losses ensured by a very small group velocity because of the small curvature, almost flat bands and 2) a proper matching of the $k$-space mode profile of the finite structure with the out-of-plane Q-factor dispersion calculated for the periodic structure [80]. Combination of these two factors allows to design large Q-factor, small footprint resonating cavities as demonstrated in this section. In the following, we consider a 3D model of the PhC slab which is finite along all directions. The slab is immersed in air and the computational domain is terminated with perfectly matched layers to simulate an open boundary condition. In Table 2.2 we compare how the total Q-factor changes with an in-plane size of the slab for the optimized configurations. In the table, only the largest Q-factors close to the exceptional points with respect to frequency are included. The Q-factor is found to rapidly increase with the size of the structure and reaches values larger than 1000 already when the structure dimensions are $8a \times 8a$. In comparison, the standard $250nm$ thick PhC slab would require tens or hundreds of lattice constants to reach this Q-factor value [145].

Figure 2.26 shows $|H_z|$ for the largest Q-factor modes in the 3D PhC slabs. For comparison, Fig. 2.27 shows $|H_z|$ for a unit cell of finite thickness with the elliptical air-holes, similar figure for the circular air-holes has been shown in Fig. 2.4.

In the case of the circular air-holes, Fig. 2.26(a) reveals that the field distributions do not resemble any of the modes found in Fig. 2.4 which was computed for a periodic structure. This is due to the finiteness of the structure. The finite configuration samples the dispersion relation in a finite neighbourhood in $k$-space. In the case of the PhC with circular air-holes, two large Q-factor bands become degenerate at

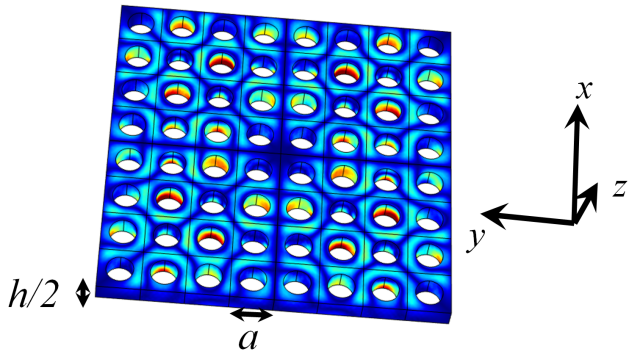


*Figure 2.25: 3D model of a PhC slab of finite thickness h with circular air-holes with dimensions $8a \times 8a$. The slab is terminated in the middle of thickness with perfect magnetic conductor to enforce the TE-like polarization.*

*Table 2.2: Largest Q-factor close to the exceptional point with respect to frequency for the PhC slabs of various in-plane sizes and thickness in cases of elliptical and circular air-holes.*

| Thickness / In-plane size | Circular | | Elliptical | | |
|---|---|---|---|---|---|
| | $250nm$ | $711.3nm$ | $250nm$ | $711.3nm$ | $658.8nm$ |
| $4a \times 4a$ | 60 | 260 | 120 | 160 | 110 |
| $6a \times 6a$ | 90 | 420 | 220 | 350 | 450 |
| $8a \times 8a$ | 110 | 1100 | 280 | 1100 | 1500 |
| $10a \times 10a$ | 130 | 1100 | 420 | 2600 | 1500 |
| $12a \times 12a$ | 150 | 2700 | 560 | 3900 | 3100 |

the Γ-point, these bands are the flat black and red bands, Fig. 2.16. Because of the frequency proximity and comparable losses of these bands, the modes of the 3D structure are cross-coupled through the radiation continuum resulting in the mixed mode, Fig. 2.26(a). This mode is found at the frequency of 175.6THz, as the in-plane size of the PhC slab increases, the mode frequency approaches the exceptional point. Moreover, already for the PhC slab with dimensions $10a \times 10a$, the two bands result in the modes that begin to be distinguishable and compete between each other in terms of the largest Q-factor. Already these modes of the 3D structure could be compared with and resemble the mode profiles in the case of the single unit cell. When the slab dimensions are $12a \times 12a$, the two corresponding modes are observed at 170.17THz and 170.2THz. They have very close Q-factors, which are on the level of 2750, and the frequency spacing is only of 0.03THz. Therefore, these two modes will compete as the in-plane size of the slab increases further. It is expected that eventually the mode originating from the flat band should dominate as it has larger out-of-plane Q-factor over a broader region of the BZ than the other mode. However, for small in-plane size structures such as $12a \times 12a$, the competition between these modes is fierce and might lead to multi-mode lasing if the PhC is used as the lasing cavity.

In the case of elliptical air-holes, the large Q-factor bands are well separated in frequency, these bands are the flat black and red bands, Fig. 2.23. This limits the cross-coupling between the two bands resulting in the 3D modes which are much more easily associated with the modes in the periodic structure. Figures 2.26(b),(c) show the largest Q-factor field profiles (b) when the slab is optimized for the two bands coalescing at the exceptional point and (c) when the slab is optimized for the flat band. As discussed in Section 2.3, the quadratic dispersion of the flat band implies small group velocity, large in-plane Q-factor, and also large in-plane feedback, which leads to strong field localization. The linear dispersion of the Dirac-like cone dispersion implies large and frequency invariant group velocity. This allows to avoid field localization. Both of these mechanisms are found in Fig. 2.26.

Fig. 2.26(b) shows that due to linear dispersion in the Γ-X direction, we have almost perfectly uniform mode distribution along the $x$ direction and the mode is localized in the centre of the PhC slab with respect to the $y$ direction due to the quadratic dispersion. Moreover, the mode clearly resembles the mode originating from the lower band of the periodic structure with the symmetry-protected BIC at the Γ-point. The mode in Fig. 2.26(b) is found at 171.92THz and its frequency is increasing as the in-plane size of the slab increases, further confirming that this mode corresponds to the lower band in Fig. 2.23.

On the contrary, in Fig. 2.26(c) the field distribution is fount to be confined to the specific parts of the slab. This is because of the very small group velocity and the quadratic dispersion of the flat black band. The field distribution in the vicinity of

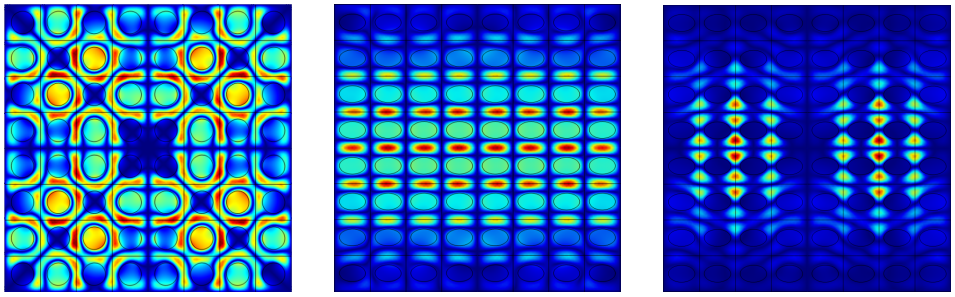

(a) (b) (c)

*Figure 2.26: Field profiles of the modes with the largest Q-factor in the vicinity of the exceptional point for the three optimized 3D PhC slabs of in-plane dimensions $8a \times 8a$. Magnitudes of $H_z$, respectively, for (a) the optimized thickness PhC slab with circular air-holes ($a = 780nm, h = 711.3nm, r = 0.3136a$), (b) the PhC slab with elliptical air-holes optimized to reduce distance between contours of exceptional points ($a = 730nm, h = 711.3nm, r_0 = 0.292a$), (c) the PhC slab with elliptical air-holes optimized to reduce radiation losses for the third, flat band ($a = 730nm, h = 658.8nm, r_0 = 0.296a$). The field profiles are obtained over the surface placed in the middle of the PhC slab thickness.*

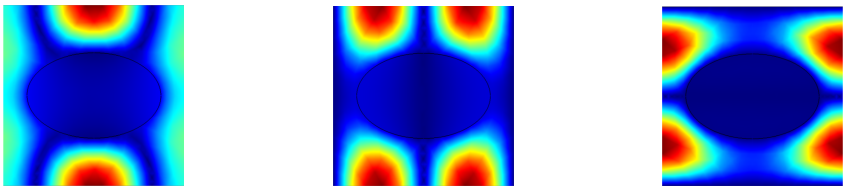

(a) (b) (c)

*Figure 2.27: Field profiles of the three modes at the Γ-point for the configuration with elliptical air-holes. Magnitudes of $H_z$, respectively, for (a) the lower band and (b) the upper band of the recovered Dirac-like cone dispersion, (c) the upper flat band. Note that the ellipticity of the air-hole breaks degeneracy of the modes shown in (b) and (c).*

the single air-hole resembles the field distribution around the single unit cell for the periodic structure as shown in Fig. 2.27(c). The effect of field localization becomes even more pronounced as the size of the PhC slab is increased further, then the field becomes concentrated around a few unit cells of the PhC slab. The mode in Fig. 2.26(c) is found at 182.6THz and its frequency is very slowly decreasing towards the frequency of the flat band at the Γ-point as the in-plane size of the slab increases. It confirms that this mode originates from the flat band separated in frequency from the other two bands in Fig. 2.23.

In the following, we explain differences in the total Q-factor values in Table 2.2. It is found that the PhC slab with elliptical air-holes optimized for the flat band has the largest Q-factor value when an in-plane dimension is $8a \times 8a$. This is explained by large out-of-plane Q-factor along the Γ-X direction, Fig. 2.24(b), and very small in-plane losses due to very small group velocity. However, these effect does not persist as the in-plane size of the slab is increased. In both cases of the configurations optimized for the flat band, the largest Q-factor has not increased with size of the slab when the in-plane dimension is $10a \times 10a$. The largest Q-factor modes in these cases originated from the flat band, they owed their Q-factor mostly to small in-plane losses due to small group-velocity, but an overlap of the $k$-space mode profile with the corresponding out-of-plane Q-factors could be improved.

The effective out-of-plane Q-factor is determined as an overlap integral of a Q-factor dispersion and a $k$-space distribution of the mode. Figure 2.28 shows examples of $k$-space matching demonstrating its importance. Figure 2.28(a) shows that the first order mode (orange) would have a larger effective out-of-plane Q-factor since the second order mode (red) is zero at the $k_{||}$ at which the Q-factor dispersion has

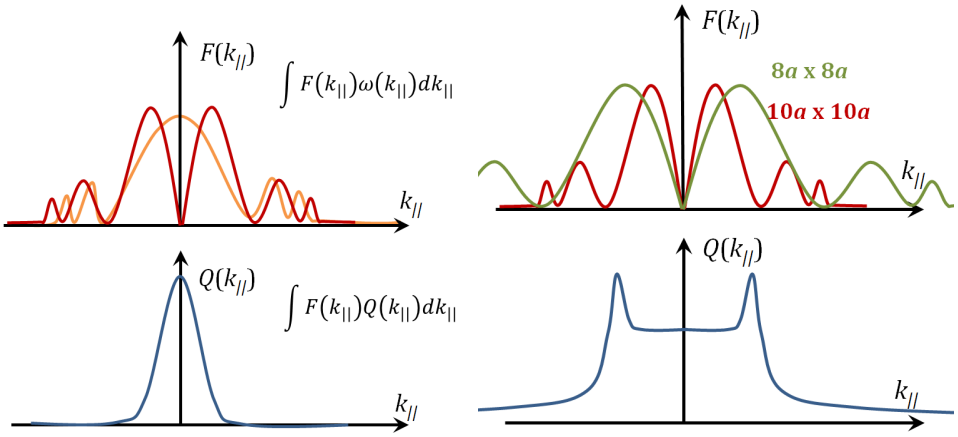


*Figure 2.28: Schematic illustrating the mechanism of k-space matching of the mode profile of the finite size structure with the Q-factor dispersion of the periodic PhC slab. (a) The effective out-of-plane Q-factor is determined as an overlap integral of Q-factor dispersion (bottom, blue) and a example of a k-space distribution of first (orange) and second order (red) modes in k-space (top). (b) Changes in k-space mode profile distribution with in-plane size of finite PhC slab.*

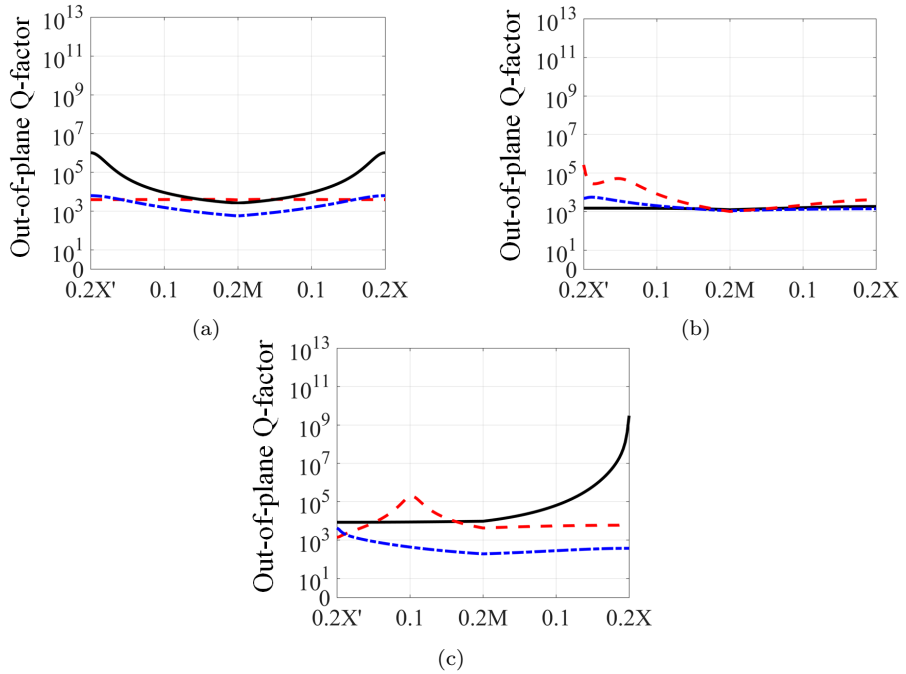


*Figure 2.29: Out-of-plane Q-factors for the PhC slab ($\epsilon_r = 10.05$) of a square lattice of (a) circular air-holes of radius $r = 0.3136a$, $a = 780nm$ and (b), (c) elliptical air-holes with $a_0 = 1.25r_0$ and $b_0 = 0.8r_0$, where (a) $r_0 = 0.292a$, (b) $r_0 = 0.296a$, $a = 730nm$. Slab thicknesses are (a) $711.3nm$ (b) $h = 711.3nm$ and (c) $h = 658.8nm$, respectively, plotted versus $k_{||}$ from the point at 20% of the $\Gamma$-$M$ towards the $\Gamma$-$X'$ and $\Gamma$-$X$ directions.*

its maximum. Figure 2.28(b) shows that the PhC slab with dimensions $8a \times 8a$ would have a larger effective out-of-plane Q-factor than the PhC slab with dimensions $10a \times 10a$. It is due to a favorable matching of the $k$-space mode profile of the $8a \times 8a$ PhC slab with the maxima of the Q-factor dispersion. This could lead to a $8a \times 8a$ PhC slab with the total Q-factor larger than $10a \times 10a$ PhC slab despite its larger in-plane size and thus smaller in-plane losses. Therefore, it is seen that it is crucial to have a properly $k$-space matched mode profile with the Q-factor dispersion as a sole optimization of the Q-factor might not lead to the largest total Q-factor.

Thus, in our case, when the size of the structure is increased from $8a \times 8a$ to $10a \times 10a$, in-plane losses are slightly reduced as the third flat band exhibits a quadratic dispersion and becomes flatter close to the Γ-point. However, matching of the $k$-space mode profile has not improved. It is because in both cases of the configurations optimized for the flat band, the Q-factor drops rather quickly along the directions other than the Γ-X direction as shown in Figs. 2.17 and 2.24. The structure size has to increase further in order to benefit from the large out-of-plane Q-factors exhibited by the flat bands close to Γ-point.

Figure 2.29 shows the Q-factor dispersion away from the Γ-point, along the $M$-X and $M$-X$'$ directions inside the IBZ. It shows that away from the Γ-point, the Q-factor of all three bands in all cases becomes significantly smaller than the Q-factor exhibited along the high-symmetry directions, Γ-X, Γ-M and Γ-X$'$. In the case of the elliptical air-holes optimized for the flat band, it is found in Fig. 2.29(b) that even though the structure is optimized for the black flat band, the lower conical band (red) exhibits very comparable values. There is even part of $k$-space where the red band Q-factor is the largest. Therefore, it is not certain that the 3D PhC optimized for the flat band will exhibit mode with the largest Q-factor which originates from the flat band as it is strongly dependent on the $k$-space profile of the mode. In fact, in the case of the elliptical air-holes and the slab thickness optimized for the flat black band, when its in-plane size is $10a \times 10a$, there are two modes exhibiting total Q-factor of 3100 at 174.44THz and at 184.73THz corresponding to the red and black bands, respectively. Due to ellipticity of the air-holes, the modes are well separated in frequency. On the other hand, in the case of the elliptical air-holes and the slab thickness optimized for the exceptional point, the mode originating from the red band, 172.8THz, has the largest Q-factor, 3900, as expected. The second largest is the mode originating from the black flat band, 178THz, with the Q-factor of 3200.

To conclude, it has been shown that the distance of exceptional points from the Γ-point can be controlled by the thickness of the PhC slab as it allows to reduce radiation losses by moving trapped BICs close to the centre of the BZ. This has allowed to identify configurations with Q-factors rapidly increasing with an in-plane size of the slab compared to the standard $h = 250$nm thickness structures. Moreover, utilization of elliptical air-holes has allowed to introduce frequency separation between the two dipole-like modes at the Γ-point. Thus, it allows to separately optimize the structure for the flat band or the Dirac cone and avoid mode-mixing at the Dirac point in finite size configurations. It led to a large Q-factor mode with uniform field profile without field localization effects. The Q-factors of the proposed PhC slabs can be further improved by tapering outer rows of PhCs. Alternatively, BICs may be understood as they arise from tight-binding model of individual resonance of each unit cell and thus by optimizing a Q-factor a single unit cell we could obtain a small foot print PhC slab resonators. These approaches are briefly discussed in Appendix A.

## 2.6 Fano laser - double cavity configuration

While the next chapter focuses on the laser dynamics of the PhC-based Fano laser, this section introduces the configuration of the Fano laser and investigates the possibility of enhancement of the lasing cavity Q-factor. Particularly, we demonstrate that introduction of the second side-coupled nanocavity can significantly increase accessible Q-factor values of the 3D PhC Fano structure. Configuration of the PhC-based Fano laser is illustrated in Fig. 2.30(a). The lasing cavity is formed by a PhC line defect waveguide terminated with a broad-band and a narrow-band mirror. The broad-band mirror is formed by a termination of the waveguide with a PhC exhibiting a photonic band gap. The narrow-band mirror is formed at a resonance frequency of the side-coupled nanocavity. At this frequency the transmission through the waveguide is reduced to zero because of the destructive interference of the wave travelling through the waveguide and the leaked radiation from the nanocavity [81]. At the resonance frequency of the nanocavity, the phase of the field in the nanocavity changes by $\pi$ with respect to frequency, while the phase of the field in the waveguide varies slowly. Because of this rapid phase transition, an asymmetric lineshape arises. It is described by a Fano formula which is shown in Fig. 2.30(b) [146, 147]. Fano formula is a function of the Fano parameter, $q$, which controls the asymmetry of the lineshape. In reality, the Fano parameter is controlled by a partially transmitting element (PTE), e.g. an air-hole of varying size, placed in the waveguide just below the side-coupled nanocavity [148, 149]. Due to low distance between minimum and maximum of the Fano lineshape, Fano resonances have also been utilized in optical switches [82, 150] and non-reciprocal transmission [151].

When the structure in Fig. 2.30(a) is 2D, i.e. it is infinite in the $z$ direction, the nanocavity coupled to the waveguide results in the formation of a Fabry-Perot BIC, which is described in section 2.2. Then, the lasing cavity is characterized by an infinite Q-factor and no radiation escapes from the cavity at the resonance frequency of the nanocavity. This configuration has been described and realized using a semi-infinite lattice of waveguides with a side-coupled waveguide introduced to provide a Fano resonance [152, 153]. However, the Fano laser is based on a PhC slab, which is usually 250nm thick. This breaks the Fabry-Perot BIC and leads to out-of-plane losses deceasing the Q-factor of the nanocavity. It sets a lower bound on a spectral width of the Fano lineshape.

In the following, we investigate the influence of a second nanocavity side-coupled to the waveguide. The double-cavity configuration provides an access to many fascinating phenomena that could enable new functionality in the Fano laser structure,

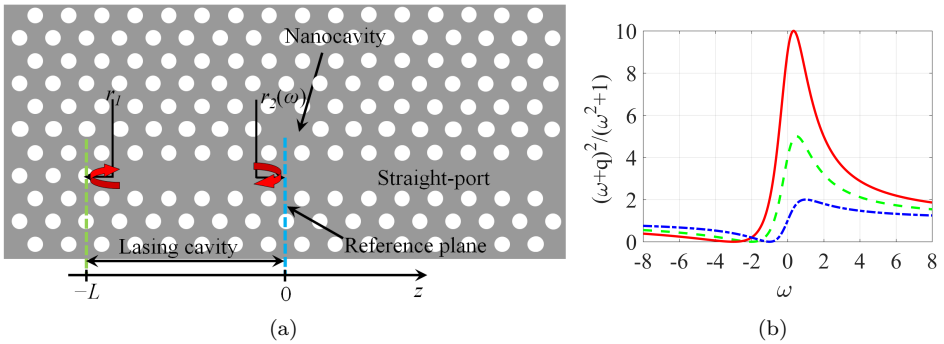


*Figure 2.30: (a) Schematics illustrating a PhC-based Fano laser. The lasing cavity is composed of a PhC waveguide terminated with a broad-band mirror (left) and a narrow-band mirror (right). (b) Visualisation of the Fano formula [146, 147] for several values of Fano parameter, q, $q = 3$ (red), $q = 2$ (green), $q = 1$ (blue).*

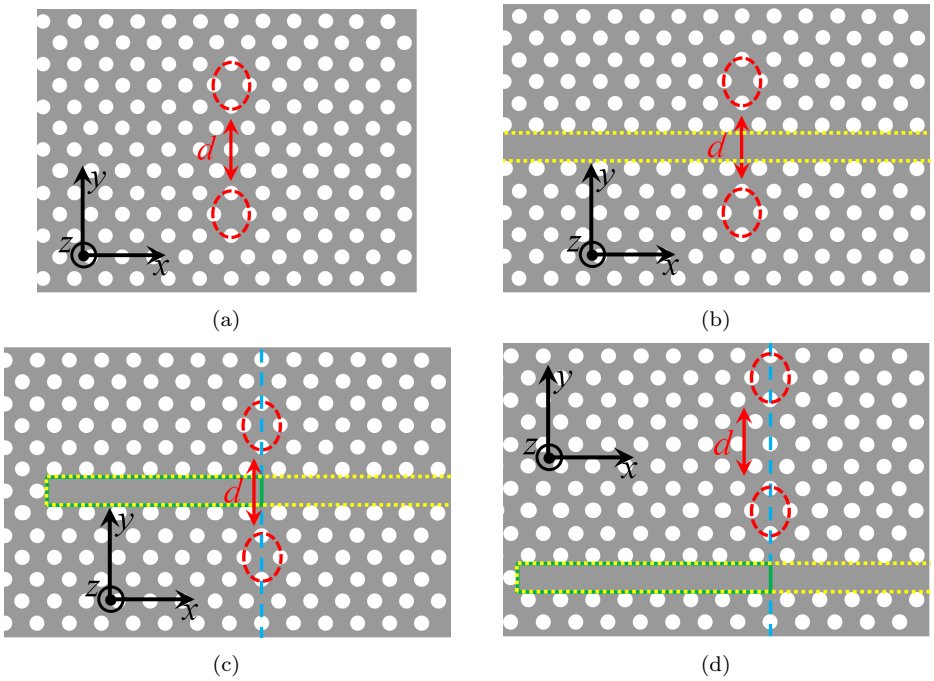


*Figure 2.31: Top view of the studied configurations. The 250nm-thick PhC slab consists of triangular lattice ($a = 455nm$) of circular air-holes ($r = 109nm$) introduced in an InP slab having the dielectric constant of $\epsilon_r = 10.05$. The configuration is immersed in air. (a) Two coupled PhC nanocavities (red) separated by a distance d. (b) Two nanocavities coupled through an open waveguide (yellow) and placed on the opposite sides of the waveguide. (c) Fano structure with two side-coupled nanocavities on the opposite sides of the semi-infinite waveguide. The lasing cavity (green) is formed by a PhC line defect waveguide terminated with a broad-band and a narrow-band (blue) mirrors. (d) Fano structure with two side-coupled nanocavities on the same side of the semi-infinite waveguide.*

e.g. electromagnetically induced transparency (EIT) [149, 154–156], Autler-Townes splitting (ATS) [156, 157], spontaneous symmetry-breaking [158, 159] and transfer of light via a continuum [160, 161]. Here, we focus on the enhancement of the Q-factor of the configuration. Figure 2.31 overviews configurations studied in the current section.

We begin an investigation with two coupled nanocavities in a PhC slab under the TE-like polarization shown in Fig. 2.31(a). Calculations are performed numerically using finite-difference time domain (FDTD) method in Lumerical software [162]. We employ a 3D model, finite in all directions, and terminated with perfectly matched layers to simulate an open boundary condition. The cavities are separated by a distance $d$ along the $y$ axis. The nanocavities are identical and their isolated resonance wavelength is 1541nm. The nanocavities are of H0 type which is formed by moving air-holes to the sides, without removing any of them; they are characterized by very small volume [163]. The resonance frequency of the nanocavity is designed to lie within the in-plane photonic band gap of guided modes. The confinement of light in the in-plane direction is determined by the number of periods of the lattice surrounding the cavity [145]. The more periods surrounding the nanocavity, the larger the in-plane Q-factor is. The rule of thumb is that there should be no less than five periods of the PhC so that the in-plane field starts to experience the photonic band gap.

The vertical confinement of the light in the nanocavity relies on the waveguiding by total internal reflection, i.e. the state lies below the light line. However, the abrupt change in the electric field distribution at the cavity edges generates unwanted in-plane components of the $k$-space mode profile within the light cone which are responsible for coupling of the field to the radiation continuum[163–167]. It leads to considerable

out-of-plane losses and reduction of the total Q-factor. These in-plane components of the $k$-space mode profile can be pushed outside the light cone by careful tuning of air-holes position which leads to smoother field distribution in the cavity. The nanocavities have been optimized in order to avoid the abrupt interface and ensure the lowest possible losses. The the total Q-factor of the isolated nanocavity is $10^6$.

Subsequently, we vary the distance between the two nanocavities and investigate its influence on the Q-factor of the system. The results in this case are shown in Fig. 2.32. Due to the nature of the triangular lattice we vary the distance between the nanocavities in odd multiples of rows separating the two nanocavities. That is why data points in Fig. 2.32 are so sparse. We emphasize that each of them has been carefully verified with numerous simulations. The nanocavities are strongly coupled when the coupling between them is much stronger than their losses [149]. In the strong coupling regime, the eigenfrequency of the nanocavities splits into two distinct eigenfrequencies. This behaviour is called ATS or vacuum Rabi splitting as the cavities exchange their energy faster than it decays away [149]. The stronger the coupling is, the larger the splitting becomes. This can be observed in Fig. 2.32 as the distance between the cavities decreases.

The two eigenfrequencies have corresponding eigenmodes, symmetric and antisymmetric with respect to the $xz$-plane and $H_z$. The field profiles of these modes are shown in Fig. 2.33 in the case when distance between the nanocavities is $d = 3$. It is found in Fig. 2.32 that strong coupling not only leads to the eigenfrequency splitting, but also the Q-factors of the modes differ. As the separation between the nanocavities increases, the Q-factor of the antisymmetric mode approaches the Q-factor of the isolated cavity. On the other hand, the Q-factor of the symmetric mode is very close to the isolated cavity Q-factor when the cavities are separated by a single row, $d = 1$. When the distance is increased to $d = 3$, the Q-factor is considerably enhanced compared to a single cavity case and is found to be $1.36 \cdot 10^6$. When the separation between the nanocavities increases further, $d = 5$, the splitting is hardly noticeable. The corresponding Q-factors exhibit negligible differences.

It is found in Fig. 2.33(b),(e) that $E_x$ is odd with respect to the $x$ and $y$ axes when the cavity is isolated. This results in field cancellation in the forward vertical direction and negligible contribution to the radiation loss [168, 169]. On the other hand, $E_y$ is odd with respect to the $y$-axis, but not with respect to the $x$-axis, and thus contributes to the radiation loss. The fine tuning of the air-holes aims at reducing this loss mechanism. However, a similar optimization for the double-cavity geometry

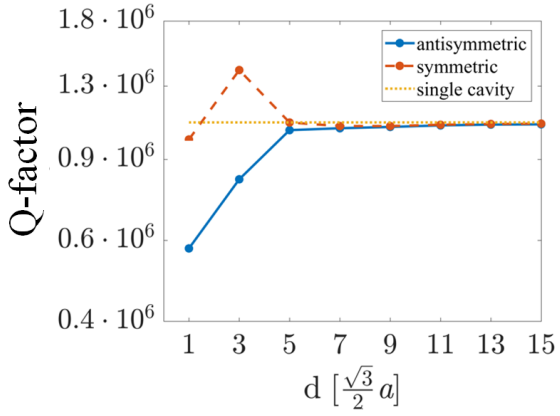


(a)

*Figure 2.32: Q-factor of the system plotted versus distance between the two nanocavities expressed in terms of number of rows separating the two cavities.*

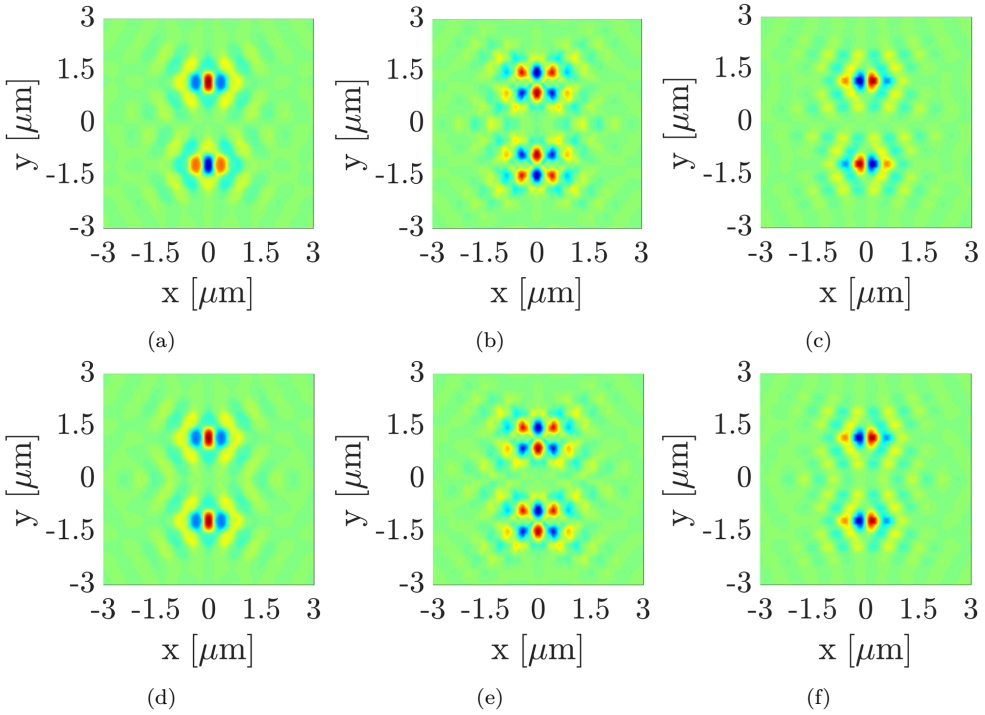


*Figure 2.33: Field profiles of the antisymmetric mode (a)-(c) and the symmetric mode (d)-(f) in the double-cavity geometry ($d = 3$). (a), (d) imaginary parts of $H_z$, (b), (e) real parts of $E_x$, and (c), (f) real parts of $E_y$. Color scales run from blue (negative) to red (positive); the scale is symmetric. The configuration is considered under the TE-like polarization.*

becomes complicated and not straightforward to resolve. Initially, one may expect the antisymmetric field distribution, Fig. 2.33(a), (c), to have larger Q-factor than the symmetric one. However, this is not true as seen in Fig. 2.32.

In the following, we employ $k$-space analysis to resolve this issue. We employ the 2D Fourier transform, $FT_2(\cdot)$, of $H_x$, $H_y$, $E_x$ and $E_y$ in the plane just above the surface of the PhC slab. The total radiated power can be estimated using [170]:

$$P_{rad} = \frac{\eta_0}{8\lambda^2 k^2} \iint\limits_{|\overrightarrow{k_{||}}| \leq k} I \cdot dk_x \cdot dk_y, \tag{2.3}$$

where $\eta_0 = \sqrt{\mu_0/\epsilon_0}$, $k = 2\pi/\lambda$, and

$$I = \left| FT_2(H_y) + \frac{FT_2(E_x)}{\eta_0} \right|^2 + \left| FT_2(H_x) - \frac{FT_2(E_y)}{\eta_0} \right|^2. \tag{2.4}$$

The distribution of $I$ is shown in Fig. 2.34(a)-(c) for the double-cavity geometry when $d = 3$. The larger the fraction of the in-plane components of the $k$-space mode profile lies inside the light cone, the smaller the Q-factor is. Analysis of Fig. 2.34(c) indicates that indeed larger fraction of the in-plane components is within the light cone for the antisymmetric mode than the symmetric one. Since the configuration is investigated under the TE-like polarization and the thickness of the slab is only $250nm$, the contribution from $FT_2(H_x)$ and $FT_2(H_y)$ to the total intensity $I$ is negligible, and thus are not included in Fig. 2.34.

In the double-cavity case, it is found in Fig. 2.34(g),(h) that the contribution from $FT_2(E_y)$ inside the light cone is significantly reduced compared to the $FT_2(E_x)$,

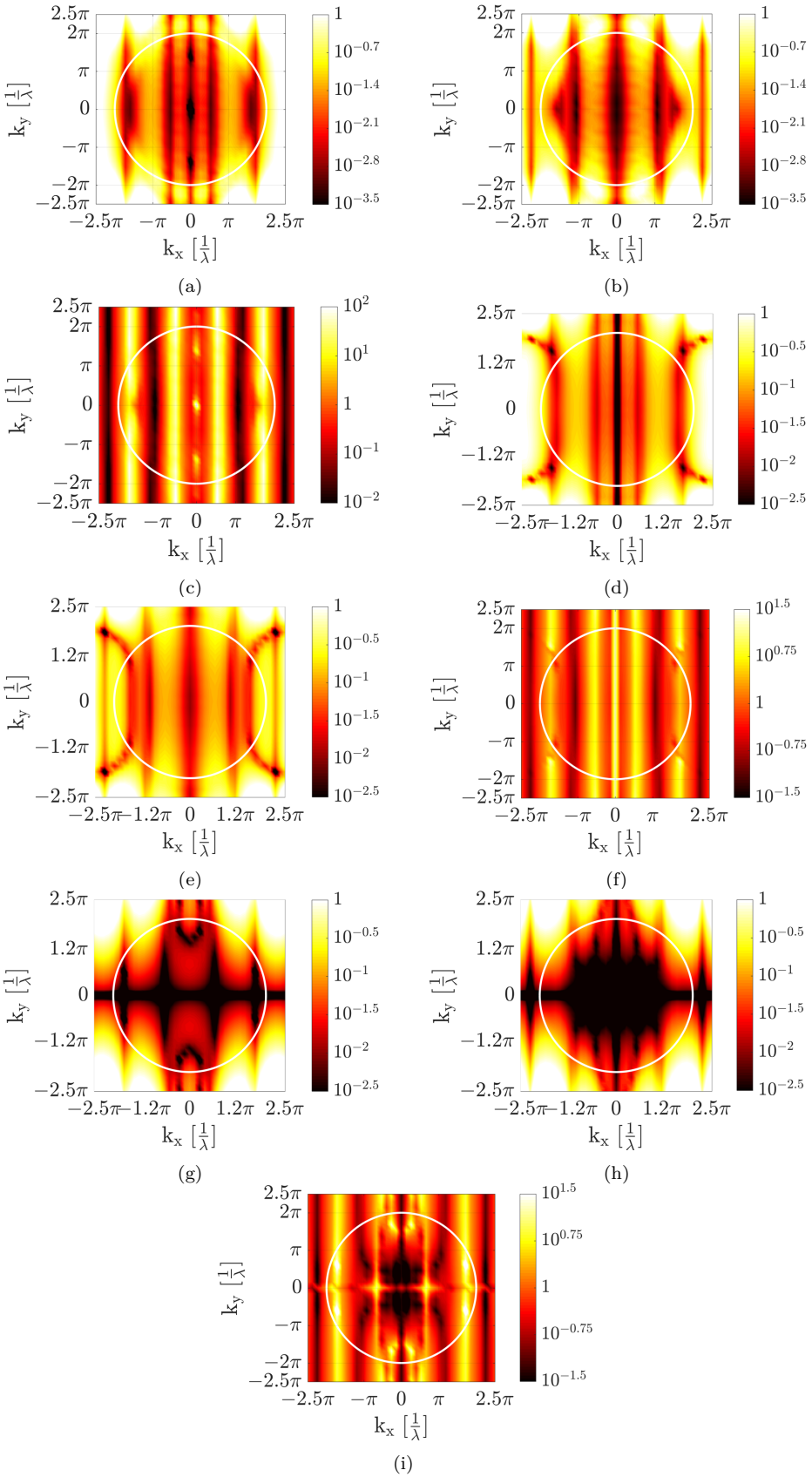


*Figure 2.34: (a), (b) The k-space intensity profiles, I, of (a) the symmetric and (b) the antisymmetric modes in the double-cavity geometry (d = 3). (c) the ratio between (b) and (a). (d), (e) $|FT_2(E_x)|$ for (d) the symmetric and (e) the antisymmetric modes. (f) shows the ratio between (e) and (d). (g), (h) $\left|FT_2(E_y)\right|$ for (g) the symmetric and (h) the antisymmetric modes. (i) shows the ratio between (h) and (g). The region inside the white circle (the light line) is the leaky region.*

which is shown in Fig. 2.34(d),(e). It is because of the fine tuning of the air-holes which was aimed to reduce the contribution from $FT_2(E_y)$ in an isolated cavity. Thus, $E_y$ is not a component that decides which mode has the largest Q-factor. When both cases are compared for $|FT_2(E_y)|$ in Fig. 2.34(h), it is also not straightforward to say in which case the contribution from $FT_2(E_y)$ is larger.

In Fig. 2.34(d)-(f) it is found that $E_x$ is the main component behind the radiation loss of the antisymmetric and symmetric modes. In the case of the antisymmetric mode, $E_x$ is even with respect to the $x$ axis as shown in Fig. 2.33(b). Thus, the contribution from $|FT_2(E_x)|$ of each cavity adds up inside the light cone, see Fig. 2.34(e). On the other hand, in the case of the symmetric mode, $E_x$ is odd with respect to the $x$ axis, see Fig. 2.33(e). It results in the strong suppression of the in-plane components inside the light cone along the $k_y$-axis as the cavities are placed along the y-axis, see Fig. 2.34(d). When both cases are compared in Fig. 2.34(f), it is found that the antisymmetric mode has a significantly larger contribution from the $|FT_2(E_x)|$ inside the light cone. Thus, the even-parity of the $E_x$ is the main reason why the Q-factor of the antisymmetric mode decreases as the coupling between the cavities increases. The reduction in the Q-factor for both modes at $d = 1$ is because of the strong perturbation of the optimized fields in the individual nanocavities caused by the strong coupling.

Subsequently, we consider a geometry with two side-coupled nanocavities to an open waveguide, Fig. 2.31(b). The nanocavities are separated by the optimal distance, $d = 3$. Initially, we consider a 2D FDTD model which is infinite in the $z$ direction. The nanocavities are in the strong coupling regime and the mode profiles of the two supermodes, symmetric and antisymmetric, are shown in Fig. 2.35. The cavities are coupled through an open waveguide. This can significantly reduce the Q-factor. The waveguide supports symmetric modes with respect to the $y$-axis. The symmetric supermode can couple to the continuum of modes in the waveguide. Thus, its Q-factor is limited due to the field decay to the waveguide, Fig. 2.35(a). Similar behaviour is observed in the single side-coupled nanocavity geometry. On the other hand, the antisymmetric mode is completely decoupled from the waveguide, Fig. 2.35(b), since it does not support asymmetric modes. The field distribution is zero in the middle of the waveguide. Thus, the antisymmetric mode, despite having a resonance frequency among the frequencies supported by the waveguide, is completely confined to the nanocavities in the 2D geometry. This is a symmetry-protected BIC which was analysed and verified experimentally using side-coupled waveguides in [25, 152, 153].

When the same geometry is considered with a 3D FDTD model in which the PhC membrane is 250$nm$ thick, the BIC is broken due to finite thickness of the slab.

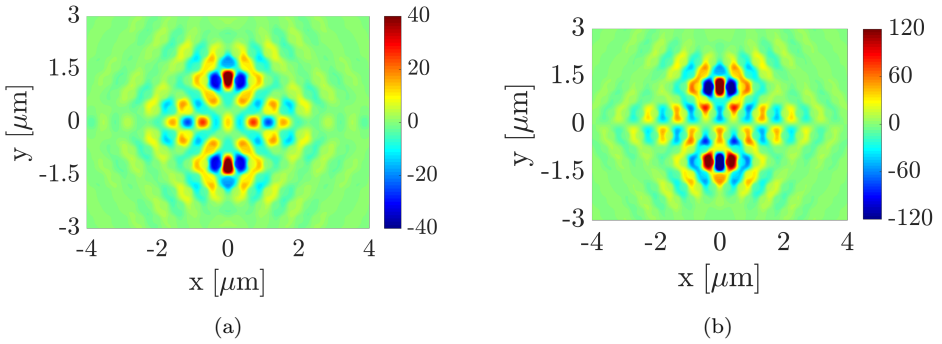


*Figure 2.35: Field profiles of (a) the symmetric and (b) antisymmetric modes in an open waveguide geometry ($d = 3$). Imaginary parts of $H_z$ are shown. Color scales run from blue (negative) to red (positive); the scale is symmetric. The configuration is under the TE-like polarization.*

Finite thickness breaks purity of the TE polarization and introduces field components which couple to the waveguide. Then the Q-factor of the antisymmetric mode is reduced from infinity to 10200, while the Q-factors of the symmetric mode and the single nanocavity configuration are 8300 and 7600, respectively. The coupling of the antisymmetric mode is relatively limited due to the symmetry and thus the Q-factor is larger for the antisymmetric mode, but still significantly reduced as the coupling to the waveguide is the main loss mechanism. The difference between the Q-factors of the symmetric mode and the single cavity case follows from the explanation presented above and is due to an odd symmetry of $E_x$.

Subsequently, the waveguide is blocked from one side to create the laser cavity, Fig. 2.31(c), the PhC is of finite thickness ($h = 250$nm); 3D FDTD model is used. The laser cavity has been optimized by shifting the first air-hole of the broad-band mirror and the waveguide confinement has been improved by shifting the neighbouring rows of the waveguide. The Q-factor of the nanocavity limits the Q-factor of the laser cavity and thus the spectral width of the Fano lineshape. In the case of a single side-coupled nanocavity, the Q-factor of the laser cavity is 135000. When the two nanocavities are considered, the lasing cavity in the case of the antisymmetric mode has the same Q-factor, 10200, as in the case of an open waveguide. This is because the antisymmetric mode is decoupled from the waveguide and its interaction with the waveguide termination is limited. The symmetric mode couples to the waveguide, interacts with the waveguide termination and exhibits enhanced Q-factor of 171000.

When the cavities are on the opposite sides of the waveguide, their coupling strength is limited by the decay of the field to the waveguide. Subsequently, we place the cavities on the same side of the waveguide and consider the configuration in Fig. 2.31(d). Then, one of the cavities is coupled to the waveguide only through the original side-coupled cavity, the cavities are coupled directly and exhibit stronger coupling and larger Q-factor than in the previous case. When the distance between the cavities is $d = 1$, the Q-factor of the lasing cavity for the symmetric mode is 492000, while for $d = 3$, the Q-factor reaches 750000.

Notably, at the transition between weakly coupled cavities and the strong coupling regime, an exceptional point can be found. Recently, a family of lineshapes has been observed in the vicinity of the exceptional point. These lineshapes have the origin strictly related to the Fano lineshape and thus have been named as generalized Fano lineshapes [157]. We have also observed them in a double-cavity configuration coupled to the waveguide and present them here as a final remark. By considering a configuration in Fig. 2.31(c) with asymmetrically placed nanocavities with respect to the reference plane, a two lasing cavities of different Q-factors are formed in the waveguide and are coupled to each other and the waveguide. By controlling the coupling between the cavities and the waveguide, the generalized Fano lineshapes indicating proximity of the exceptional point can be obtained [155, 157]. In our case, this can be done by controlling the position of the nanocavities on the opposite sides of the waveguide. In most of the cases, standard Fano lineshape is present as one of the cavities dominates over the other. However, for some particular positions of the lower side-coupled nanocavity, the generalized Fano lineshapes are obtained. These cases are shown in Fig. 2.36.

Therefore, a double-cavity configuration provides a lot of freedom in the design of the structure. It can lead to enhanced Q-factors of the lasing cavity in the Fano configuration. It also provides to new fascinating physics and applications such as generalized Fano lineshapes [155, 157] and broadband optical signal processing [171].

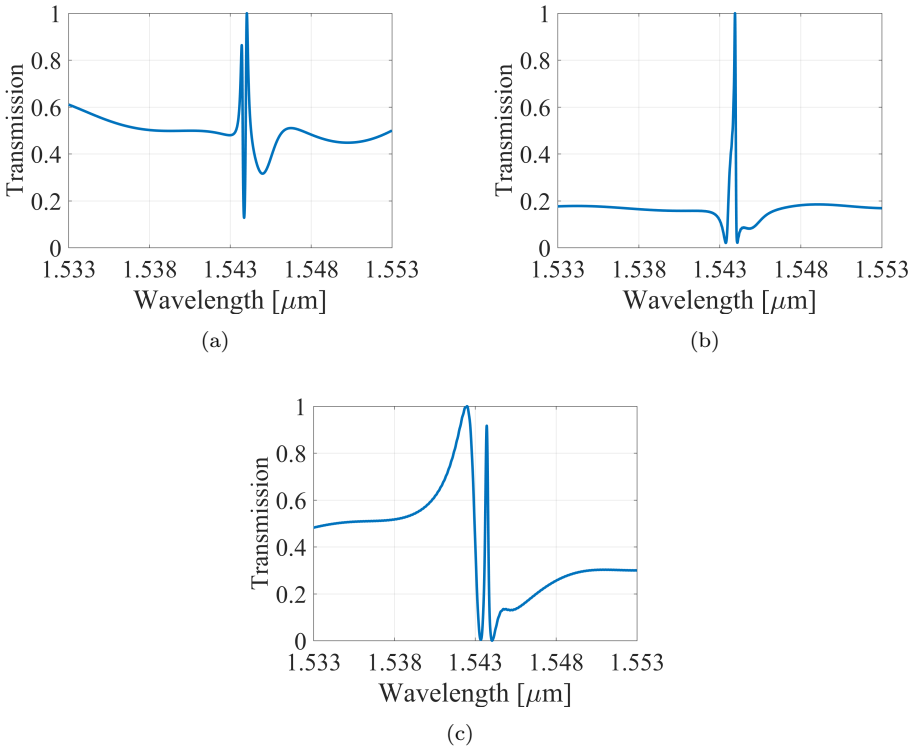


*Figure 2.36: Normalized transmission through a semi-infinite PhC waveguide with two side-coupled nanocavities. The cavities are asymmetrically positioned with respect to the reference plane on the opposite sides of the waveguide. The lower cavity is shifted by (a) 7 columns to right with respect to the top cavity, (b), (c) 8 and 9 columns to the left from the top cavity, respectively. The 250nm-thick PhC slab ($\epsilon_r = 10.05$) consists of triangular lattice ($a = 455nm$) of circular air-holes ($r = 109nm$).*

## 2.7 Summary

The first three sections 2.1, 2.2 and 2.3 have introduced subjects such as BICs, Dirac cones, exceptional points and Fano resonances in the context of PhC-based lasers.

Subsequently, section 2.4 has shown that by varying thickness of the slab, we can move trapped BICs towards the centre of the BZ and thus reduce difference in losses between the modes at the Γ-point. This reduces extent of the ring of exceptional points almost to a point and results in large values of the out-of-plane Q-factor over the broad region of the BZ.

These studies allowed to identify configurations with the total Q-factors increasing rapidly with an in-plane size of the PhC slab compared to the standard 250nm-thick structures, see section 2.5. Elliptical air-holes PhCs have been shown to introduce frequency separation between the two large Q-factor bands and reduce cross coupling between them. It led to a large Q-factor mode with an uniform field profile. The dispersion of the PhC with elliptical air-holes is found to be radically different along the high symmetry directions and can be significantly altered by a sheer rotation of the air-hole. Q-factors of the proposed configurations could be further improved by tapering outer rows of the PhCs or constructing larger PhC-like structures from single large Q-factor unit cells. These approaches are briefly discussed in Appendix A.

Finally, the introduction of the second side-coupled nanocavity has been shown to increase accessible Q-factor values of the 3D PhC Fano structure in section 2.6.

# Chapter 3

# Two-dimensional phase-space picture of the Fano laser

This chapter investigates dynamic model of the PhC Fano laser. Section 3.1 introduces the subject, motivation and tackled challenges in the following sections. Section 3.2 discusses the dynamic model of the Fano laser, which is known from the literature [172]. In section 3.3.1, we review the current knowledge on the stability of the laser.

In the following sections, we present our own results which would not be possible without the foundation established in sections 3.2 and 3.3.1. In section 3.3.2, we found that the laser dynamics are confined to the curved surface after the initial transition stage, which lasts only a few picoseconds. In section 3.3.3, we analyze the instantaneous eigenvalues of the Jacobian matrix of the dynamic model. We demonstrate that there are at most two eigenvalues with positive real parts. In section 3.3.4, we prove that the two eigenvectors corresponding to the two dominating eigenvalues can span the whole phase space after the initial transition stage as the contribution from the remaining eigenvectors decays rapidly. Here, we also prove that after the initial transition stage, the original 5D model can be reduced to only 1D in the limited region of the parameter space when the steady-state eigenvalues are purely real and that the system evolves into 2D beyond the exceptional point when the eigenvalues form a complex conjugate pair. In section 3.4, we used the simplified 2D model to associate the unknown origin of instability with a new unstable periodic orbit separating the stable steady-state from the stable periodic orbit. We have classified the bifurcation standing behind the two orbits and the steady-state as a Bautin bifurcation. Finally, in section 3.5, the simplified model is used to investigate non-Hermitian dynamics at the periodic orbit. Here, the intervals of the solution following the adiabatic prediction are found to be interrupted by abrupt nonadiabatic transitions.

## 3.1 Photonic crystal Fano laser - introduction

In the last two decades, the internet traffic has risen thousands times and currently an energy consumption needed to sustain these networks constitutes 10% of the world's electricity consumption [173]. As the demand for higher data rates is increasing with each year, it is crucial to provide solutions sustaining this growth, but also do it at a reasonable energy costs. Nowadays, it is widely accepted that a next step in the development of the telecommunication networks is to integrate photonic circuits on a

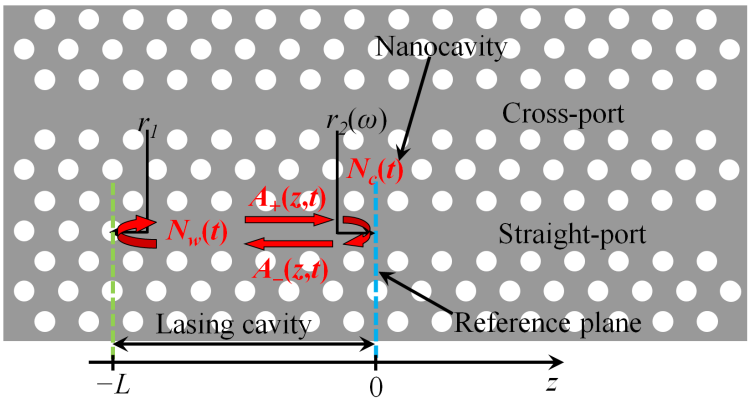


*Figure 3.1: Schematic illustrating a PhC-based Fano laser. The dynamic variables are marked in red. The lasing cavity is between the broad-band mirror (green) and the reference plane (blue).*

chip [174]. This would significantly reduce not only the cost and power consumption, but would also allow for much faster data processing. An ideal platform for integration of photonic circuits are PhC-based membranes, mainly due to their flexibility in design, ease in fabrication and precise control over the structure properties. Indispensable part of such photonic circuits are light sources which can be conveniently realised with PhCs [175–179]. As discussed in the previous chapter, PhCs allow for realisation of very compact, large quality factor resonators with gain material being directly implemented in a PhC membrane.

Recently, a new type of a PhC-based laser has been proposed [112]. It relies on a Fano resonance and it has been predicted that the laser can be modulated at THz frequencies and not be limited by relaxation oscillations [112]. Moreover, the laser has been demonstrated to be able to operate in a self-pulsing regime [83]. This was the first demonstration of the nanolaser generating self-sustained pulses without any external modulation. These properties make the Fano laser an unique light source which is well suited for future on-chip processing of information in the optical domain.

The schematic of the Fano laser configuration is shown in Fig. 3.1. The lasing cavity is formed by a PhC line defect waveguide terminated with a broad-band and a narrow-band mirrors. The broad-band mirror is formed by a termination of the waveguide with a PhC exhibiting photonic band gap. The narrow-band mirror is formed at a resonance frequency of the side-coupled nanocavity due to Fano interference which arises as a consequence of the interference of a discrete mode in the nanocavity with the continuum of modes in the waveguide. The active material is introduced in an InP PhC membrane as several layers of InAs quantum dots or quantum wells. The side-coupled nanocavity is coupled to a cross-port which is used to improve out-coupling of the laser power at the cost of lasing threshold [112]. The cross-port can be used for an in-plane control of the resonance frequency of the nanocavity [172].

The dynamic behaviour of the laser is modelled by combining temporal coupled mode theory [81, 180] with traditional rate equations governing carrier dynamics [174]. The model is based on four coupled differential equations describing the complex envelopes of the fields propagating away $A_-(t)$ and towards $A_+(t)$ the mirror plane evaluated at the reference plane (blue dashed curve in Fig. 3.1), and carrier densities in the waveguide $N_w(t)$ and in the nanocavity $N_c(t)$. It has been shown that the Fano laser can operate in two regimes, continuous wave operation and self-pulsing operation [83, 172]. By linearizing the model and computing its eigenvalues at the equilibrium point (steady-state), it has been shown that a pair of complex conjugate eigenvalues may cross the imaginary axis and their real parts may become positive. When it happens, it means that as the laser is slightly perturbed from the steady-state point,

relaxation oscillations grow exponentially within the linear approximation. Then, the steady-state becomes unstable and repels the state towards the stable periodic orbit. This is a Hopf bifurcation which has been observed before [172]. It stands behind the unstable operation of the laser and leads to the self-pulsing operation. On the other hand, when the real part of the eigenvalues is negative, then upon a slight perturbation of the laser from its steady-state point, it will quickly approach the steady-state operation again. However, it has been found that there is a region in a parameter space in which the real parts of all eigenvalues can be negative and despite this, the laser can become unstable if perturbed strongly enough. Thus far, it has not been explained. It will be tackled in section 3.4 in which the origin of the instability is associated with Bautin bifurcation, which is characterized by a bifurcation of two periodic orbits and an equilibrium point [181, 182].

Furthermore, exceptional points have been linked to a single mode self-pulsing in distributed feedback lasers [84–87] and, as in our case, this self-pulsing mechanism was attributed to dispersive quality factor self-switching [83]. Moreover, exceptional points have been shown to be related to Fano resonances [157, 183–185] and have been linked to the phenomenon of stability loss delay in dynamical bifurcations [88]. Therefore, it is of importance to further investigate the dynamics of the laser and the potential role of exceptional points in the unstable behavior of the laser as well as alternative sources of instability [186]. This study is conduced in sections 3.3 and 3.5 in which the instantaneous exceptional points have been found in the vicinity of the pulse and their relation to the self-pulsing operation has been unveiled.

Particularly, when the laser is in the self-pulsing regime under constant pump power, the carrier densities $N_w(t)$, $N_c(t)$ and the field envelopes $A_-(t)$, $A_+(t)$ are varying periodically in its phase space without any need for external modulation. In dynamical field theory, phase space is defined as the space which represents all possible states of the system [187]. In this case, behind the periodic variation of the state of the system stands nonlinear interaction between the carrier densities and the fields in the waveguide and the cavity. Therefore, it is tempting to utilize this self-adopting interaction to dynamically sweep across or encircle an exceptional point of instantaneous eigenvalues. This idea of dynamic self-encircling of an exceptional point in the eigenspace of the laser has been the original motivation standing behind the investigations discussed in the current chapter. Interestingly, in section 3.3.3, the laser trajectory has been found to cross four exceptional points within a single period.

Moreover, dynamic encircling of an exceptional is quite different from the parametric/quasistatic encircling described in section 2.3. Quasistatic encirclement means that for each change in the structure parameters, new structure is fabricated and the eigenvalues and eigenvectors are measured. By concatenating a series of measurements for the parameter loop around an exceptional point, it is found that the eigenvalues and eigenvectors swap. This process is due to the gradual transition between the intersecting complex surfaces of the square root function [132, 188, 189], as was also shown in Fig. 2.11. However, the exceptional point can also be encircled dynamically. It means that a single configuration is fabricated and its parameters are designed to change in time/space and the instantaneous eigenvectors and eigenvalues of the time/space-dependent matrix are traced. In this case, even when the exceptional point is encircled slowly, the adiabatic theorem breaks down, and the non-adiabatic transition leads to a chiral behaviour, i.e. the final state depends solely on the direction of encircling [78, 98, 100, 190–196]. By a system satisfying an adiabatic theorem, we understand a system that upon gradually varying conditions follows its instantaneous eigenvalues [197]. The chiral behaviour has been used in the design of mode and polarization converters [70–72]. In section 3.5, pulsing behaviour has been found to be related to nonadiabatic transitions occurring in the vicinity of the exceptional points.

## 3.2 Dynamic model of the Fano laser

In the current section, we introduce a dynamic model of the Fano laser which is known from the literature [172]. Only the most important steps in its derivation are presented here; for a more detailed description see [83, 172]. In order to set up a dynamic model of the Fano laser, we decompose the complex field at the reference plane (blue dashed line in Fig. 3.1) into the components propagating towards $E_+(\omega)$ and away $E_-(\omega)$ from the reference plane. At the reference plane, they can be related through the following conditions:

$$E_+(\omega) = r_L(\omega, N)E_-(\omega), \tag{3.1a}$$

$$E_-(\omega) = r_R(\omega, \omega_c)E_+(\omega), \tag{3.1b}$$

where $r_R$, $r_L$ are the narrow-band (right) and the broad-band (left) reflection coefficients with respect to the reference plane, respectively. Here, we have neglected the contribution from spontaneous emission. The reflection coefficients are defined as:

$$r_L(\omega, N) = r_1(\omega)e^{i2k(\omega,N)L}, \tag{3.2a}$$

$$r_R(\omega, \omega_c) = \frac{s_1^-(\omega, \omega_c)}{s_1^+(\omega, \omega_c)}. \tag{3.2b}$$

The narrow-band reflection coefficient $r_R$ corresponds to the reflection coefficient due to the Fano mirror determined under a continuous incoming wave at frequency $\omega$. $r_R$ is strictly dependent on the resonance frequency of the nanocavity $\omega_c$ and can be found using the coupled mode theory [172]. Here, it is defined in terms of the $s$-parameters of the incoming $s_1^+$ and outgoing $s_1^-$ waves in the lasing cavity with respect to the reference plane [81, 180]. These are normalized so that $|s_1^{-/+}|^2$ represents propagating power and can be directly related to $A_-(t)$, $A_+(t)$ via $|s_1^{-/+}(t)|^2 = 2\epsilon_0 nc|A_{-/+}(t)|^2$, where $n$ is the refractive index in the waveguide, $c$ is speed of light and $\epsilon_0$ is vacuum permittivity. On the other hand, the broad-band reflection coefficient $r_L$ arises due to photonic band gap. The reflection coefficient at the waveguide termination $r_1$ is assumed to be equal to unity and has to be transformed towards the reference plane using the standard transmission line theory. However, Eq. (3.2a) is only valid under the assumptions that the carrier densities are uniformly distributed in the waveguide/cavity and that the lasing cavity functions as a Fabry-Perot cavity [198]. In Eq. (3.2a), $L$ is the length of the lasing cavity, $k(\omega, N)$ is the complex wavenumber which depends on the carrier density in the waveguide $N$ and frequency $\omega$, and it is expressed as [198]:

$$k(\omega, N) = \frac{\omega}{c}n(\omega, N) - \frac{i}{2}\Gamma(g(\omega, N) - \alpha_i). \tag{3.3}$$

where $\Gamma$ is the confinement factor in the waveguide, $\alpha_i$ is the internal waveguide loss factor, $g(\omega, N)$ is the gain. By neglecting the gain dispersion $g(\omega, N)$ can be approximated as $g(N) = g_N(N - N_0)$, where $N_0$ is the transparency carrier density and $g_N$ is the differential gain. The refractive index can approximated by the first-order Taylor expansion in the vicinity of the reference carrier density $N_r$ and the reference frequency $\omega_r$ [172, 198]. The reference wavelength coincides with the isolated nanocavity resonance frequency. By combining both boundary conditions in Eq. (3.1), we can arrive at the oscillation condition for the steady-state laser modes:

$$r_R(\omega_s, \omega_c)r_1(\omega_s)e^{i2k(\omega_s,N_s)L} = 1, \tag{3.4}$$

The oscillation condition is solved for $(\omega_s, N_s)$, which are the lasing frequency and the steady-state carrier density. In order to solve Eq. (3.4), one can substitute Eq. (3.3) into Eq. (3.4) and split the equation into the conditions for the amplitude and phase. Both conditions have to be satisfied simultaneously. There are multiple solutions of Eq. (3.4); these are the modes of the laser and the one with the lowest required threshold gain is chosen as the lasing mode.

Subsequently, following the procedure in [172, 198], one can derive a dynamic equation in time domain for the complex field envelopes $A_-(t)$, $A_+(t)$. These are related to the complex fields $E_+(\omega)$ and $E_-(\omega)$ evaluated at the reference plane by:

$$A_{-/+}(t)e^{-i\omega_s t} = \frac{1}{2\pi}\int_0^\infty E_{-/+}(\omega)e^{-i\omega t}d\omega. \tag{3.5}$$

Note that the steady-state lasing frequency $\omega_s$ derived from the oscillation condition serves as the carrier frequency. Assuming that $r_L(\omega, N)$ varies slowly in the vicinity of $(\omega_s, N_s)$, Eq. (3.1a) is multiplied by $1/r_L(\omega, N)$ which is subsequently Taylor expanded up to the first order around $(\omega_s, N_s)$. Then, the result can be inverse Fourier transformed knowing that the time derivative corresponds to $-i(\omega - \omega_s)$ in the frequency domain and assuming that $r_1(\omega)$ is not frequency dependent, we can arrive at:

$$\frac{dA_+(t)}{dt} = -\gamma_L A_+(t) + \frac{1}{2}(1 - i\alpha)\Gamma v_g g_N(N_w(t) - N_s)A_+(t) + \frac{\gamma_L A_-(t)}{r_R(\omega_s, \omega_c)}, \tag{3.6}$$

where $\gamma_L = v_g/2L$ is the inverse of the round trip time in the lasing cavity, $\alpha$ is the linewidth enhancement factor [199], and $N_w(t)$ is the carrier density in the waveguide. On the other hand, $A_-(t)$ is strictly related to the field in the nanocavity $a(t)$. Thus, since in the case considered the waveguide is open to the right, i.e. the right mirror is merely due to the Fano resonance, the coupled-mode equation for the field in the nanocavity, $a(t)$, can be reformulated using $A_-(t) = -P\sqrt{\gamma_C/(2\epsilon_0 nc)}a(t)$ [112], where $P$ is the parity of the mode in the nanocavity and $\gamma_C$ is the coupling constant between the nanocavity and the waveguide. It leads to the dynamic equation for $A_-(t)$ as:

$$\frac{dA_-(t)}{dt} = (-i\Delta\omega - \gamma_T)A_-(t) + \frac{1}{2}(1 - i\alpha)\Gamma_C v_g g_N(N_c(t) - N_0)A_-(t) - P\gamma_C A_+(t), \tag{3.7}$$

where $\Delta\omega = \omega_c - \omega_s$, $\gamma_T$ is the total decay rate of the field in the nanocavity, $\Gamma_C$ is the confinement factor in the nanocavity, and $N_c(t)$ is the carrier density in the nanocavity. $\gamma_T$ takes into account coupling to the waveguide, $\gamma_C$, out-of-plane losses and coupling to the cross-port. It is noted that the absorption term in Eq. (3.7) has been added phenomenologically in the case of an active material present in the nanocavity. Subsequently, the two dynamic equations for $A_-(t)$, $A_+(t)$ are combined with the traditional rate equations for the carrier densities in the waveguide $N_w(t)$ and in the nanocavity $N_c(t)$ as [174]:

$$\frac{dN_w(t)}{dt} = \frac{J_c}{eV_{LC}} - \frac{N_w(t)}{\tau_w} - \Gamma v_g g_N(N_w(t) - N_0)\frac{I(t)}{V_{LC}}, \tag{3.8}$$

$$\frac{dN_c(t)}{dt} = -\frac{N_c(t)}{\tau_c} - \Gamma_C v_g g_N(N_c(t) - N_0)\rho\frac{|A_-(t)|^2}{V_{NC}}, \tag{3.9}$$

where $\tau_w$ and $\tau_c$ are the carrier lifetimes in the waveguide and in the cavity, respectively,

$V_{LC}$ and $V_{NC}$ are the volumes of the laser cavity and the nanocavity, respectively, $e$ is the elementary charge, $J_c$ is the effective pump current, $I(t) = \sigma_s(\omega_s, N_s)|A_+(t)|^2$ is the photon number, where $\sigma_s(\omega_s, N_s)$ and $\rho$ relate the photon number to the field strength in the waveguide and the nanocavity, respectively. $\rho$ is simply a normalization factor resulting from the reformulation of the coupled-mode theory equation for the field in the nanocavity $a(t)$ to Eq. (3.7), $\rho = 2\epsilon_0 nc/(\gamma_C \hbar\omega_r)$, while $\sigma_s(\omega_s, N_s)$ follows a more complicated equation which was derived in [198] and can also be found in [83, 172]. Note that since we pump the waveguide, the pumping current is included in Eq. (3.8) describing the dynamics of $N_w(t)$.

In the following, we include some minor modifications in Eqs. (3.6), (3.7), (3.8) and (3.9). These modifications are:

1. the differential equations for $A_-(t)$ and $A_+(t)$ are separated into equations for the corresponding amplitudes and phase evolutions,

2. the system of differential equations is considered in a dimensionless form.

These modifications do not influence the final result. When detuning from the expansion point frequency, $\omega_s$, is not zero, the laser has to compensate for it by adjusting the mode frequency, $\omega_s$, away from the cavity resonance in order to fulfil the oscillation condition. This results in an additional small phase being imparted to the complex fields envelopes, i.e. $A_{-/+}(t)e^{-i\delta\omega t}$ [172]. This results in time-varying real and imaginary parts of the complex fields envelopes at the steady-state due to an oscillatory part introduced by $\delta\omega$. It is thus helpful to separate Eqs. (3.6) and (3.7) into the corresponding amplitudes and the phase difference of both. This is done by substituting $A_{-/+}(t) = |A_{-/+}(t)|e^{i\Phi_{-/+}(t)}$ into both Eqs. (3.6), (3.7) and by splitting the equations into the corresponding real and imaginary parts. Moreover, the system depends only on the phase difference $\Phi(t) = \Phi_-(t) - \Phi_+(t)$; thus the equations describing the dynamics of $\Phi_-(t)$, $\Phi_+(t)$ can be combined by subtracting them and exploiting linearity of the differentiation. These modifications lead us to a system of five differential equations. Furthermore, we normalize the system of five differential equations and consider a dimensionless system of equations. This is to ensure numerical stability of the model since there are huge differences in orders of magnitude between some of the variables, e.g. the carrier densities $N_w(t)$, $N_c(t)$ are always on the order of the transparency carrier density $N_0$, which is $10^{24}$, while the amplitudes of the complex field envelopes $|A_{-/+}(t)|$ can even reach zero between the pulses. The normalization constants are introduced as:

$$|A_+(t)| = p_1|a_+(t)|, \quad |A_-(t)| = p_2|a_-(t)|, \quad N_w(t) = p_3 n_w(t), \quad N_c(t) = p_4 n_c(t),$$
$$J_c = p_5 j_c, \quad \Delta\omega = p_6\delta\omega, \quad N_s = p_7 n_s, \quad t = p_8\tau. \tag{3.10}$$

By substituting the normalization constants Eq. (3.10) into Eqs. (3.6), (3.7), (3.8), (3.9), the normalization constants are found to be:

$$p_1 = \sqrt{\frac{V_{LC}}{\tau_s G_N \sigma_s}}, \qquad p_2 = \sqrt{\frac{V_{NC}}{\tau_c G_{NC}\rho}}, \qquad p_5 = \frac{V_{LC} e N_0}{\tau_s} \qquad p_3 = p_4 = p_7 = N_0,$$
$$p_6 = G_{NC}N_0, \qquad p_8 = \frac{1}{G_{NC}N_0}, \tag{3.11}$$

where $G_{NC} = \Gamma_C v_g g_N$ and $G_N = \Gamma v_g g_N$. Following the procedure outlined above, finally one can arrive at the system of five coupled nonlinear differential equations describing the laser dynamics:

$$\frac{d|a_+|(\tau)}{d\tau} = -\frac{\gamma_L|a_+|(\tau)}{G_{NC}N_0} + \frac{\Gamma|a_+|(\tau)(n_w(\tau)-n_s)}{2\Gamma_C} + \frac{\gamma_L|a_+|(\tau)}{G_{NC}N_0}\mathrm{Re}\left(\frac{A_-(\tau)}{r_R A_+(\tau)}\right), \tag{3.12a}$$

$$\frac{d|a_-|(\tau)}{d\tau} = -\frac{P\gamma_C}{G_{NC}N_0}|a_-|(\tau)\mathrm{Re}\left(\frac{A_+(\tau)}{A_-(\tau)}\right) - \frac{\gamma_T|a_-|(\tau)}{G_{NC}N_0} + \frac{|a_-|(\tau)(n_c(\tau)-1)}{2}, \tag{3.12b}$$

$$\begin{aligned}\frac{d\Delta\phi(\tau)}{d\tau} = -\frac{\alpha}{2}(n_c(\tau)-1) + \frac{\Gamma\alpha(n_w(\tau)-n_s)}{2\Gamma_C} - \frac{\Delta\omega}{G_{NC}N_0} \\ - \mathrm{Im}\left(\frac{r_R P\gamma_C A_+^2(\tau) + \gamma_L A_-^2(\tau)}{r_R G_{NC}N_0 A_-(\tau)A_+(\tau)}\right),\end{aligned} \tag{3.12c}$$

$$\frac{dn_w(\tau)}{d\tau} = \frac{-|a_+(\tau)|^2(n_w(\tau)-1) - n_w(\tau) + j_c}{G_{NC}N_0\tau_s}, \tag{3.12d}$$

$$\frac{dn_c(\tau)}{d\tau} = \frac{-|a_-(\tau)|^2(n_c(\tau)-1) - n_c(\tau)}{G_{NC}N_0\tau_c}. \tag{3.12e}$$

The system of equations shown in Eq. (3.12) can be compactly expressed as a function $V(\cdot)$ of the state vector $\vec{\psi}(\tau)$:

$$\vec{\psi}(\tau) = \{|a_+(\tau)|, |a_-(\tau)|, \Delta\phi(\tau), n_w(\tau), n_c(\tau)\} \tag{3.13a}$$

$$\frac{d\vec{\psi}(\tau)}{d\tau} = V(\vec{\psi}(\tau)) \tag{3.13b}$$

The components of $\vec{\psi}(\tau)$ are the time-dependent variables describing the laser dynamics. For a given $\tau$, all the possible state vectors form the phase space of the laser. The system of equations is then linearized by taking the total derivative with respect to $\tau$. It can be interpreted as a directional derivative along the curve, which is traversed by the state, parameterized by $\tau$. Then the system takes the following form:

$$\frac{d^2\vec{\psi}(\tau)}{d\tau^2} = \nabla_{\vec{\psi}} V(\vec{\psi}(\tau))\frac{d\vec{\psi}(\tau)}{d\tau} = \boldsymbol{A}(\vec{\psi}(\tau))\frac{d\vec{\psi}(\tau)}{d\tau}, \tag{3.14}$$

$d\vec{\psi}(\tau)/d\tau$ is treated as the velocity of the state vector and is a function of the state vector as expressed in Eq. (3.13b). $d^2\vec{\psi}(\tau)/d\tau^2$ is interpreted as the acceleration of the state vector. Matrix $\boldsymbol{A}$ is known under several names, e.g., stability matrix or Jacobian matrix. When the matrix $\boldsymbol{A}$ is evaluated at the steady state, then its eigenvalues indicate whether the system is stable or unstable. The system is stable when all the eigenvalues have negative real parts, while the system is unstable when at least one of the eigenvalues has positive real part.

Note that the stability matrix $\boldsymbol{A}$ is purely real, but not symmetric because the variables were separated into the amplitudes $|a_{-/+}|(\tau)$ and the phase difference $\Delta\Phi(\tau)$ of the complex field envelopes. Therefore, the matrix $\boldsymbol{A}$ is non-Hermitian as it is not equal to its own conjugate transpose. Thus, the eigenvalues of the matrix $\boldsymbol{A}$ can be purely real or form complex conjugate pairs. Furthermore, one should note an uncanny resemblance of Eq. (3.14) to the Schrödinger type equations. The only difference being the fact that in the Schrödinger type equations, the matrix governing an evolution of the system, which is a time-dependent Hamiltonian, is multiplied by

$-i$. Thus, in order to relate eigenvalues and eigenvectors and apply similar analysis as in [68–72, 88, 200, 201] to our system, the eigenvalues and eigenvectors in these works should be scaled by $-i$, or in our case by $i$. The Jacobian matrix $\boldsymbol{A}$ performs a similar role as a time-dependent Hamiltonian in the Schrödinger type equation and describes the dynamic evolution of the system.

Furthermore, when the stability matrix $\boldsymbol{A}$ is evaluated at the steady-state, the matrix $\boldsymbol{A}$ is constant, and the system of equations, Eqs. (3.12), (3.14), can be interpreted as a small-signal analysis in the vicinity of steady-state solution. Then, the system is an autonomous system [202], and the small-signal solution can be expressed as:

$$\vec{x}(\tau) = e^{\boldsymbol{A}t}\vec{x}_0, \qquad \vec{x}(\tau) = \overrightarrow{d\psi}(\tau), \qquad \vec{x}(0) = \vec{x}_0 \tag{3.15}$$

We can use eigenvectors and eigenvalues of the $\boldsymbol{A}$ matrix to diagonalize and simplify Eq. (3.15) as:

$$\vec{x}(\tau) = e^{\boldsymbol{A}t}\vec{x}_0 = \boldsymbol{T}e^{\Lambda t}\boldsymbol{T}^{-1}x(0) = \sum_{i=1}^{n} e^{\lambda_i t}(\vec{w}_i^{\,T}\vec{x}(0))\,\vec{v}_i \tag{3.16}$$

where $\boldsymbol{T}$ is a matrix whose columns are the eigenvectors of $\boldsymbol{A}$ and $\boldsymbol{\Lambda}$ is a diagonal matrix of the eigenvalues of $\boldsymbol{A}$. Since the matrix $\boldsymbol{A}$ is non-Hermitian, we have to distinguish between right $\vec{v}$ and left $\vec{w}$ eigenvectors which we normalize so that $\vec{w}_i^{\,T}\vec{v}_j = \delta_{ij}$. In this case, the right $\vec{v}$ and the left $\vec{w}$ eigenvectors are the columns/rows of $\boldsymbol{T}/\boldsymbol{T}^{-1}$ satisfying $\boldsymbol{A}\boldsymbol{T} = \boldsymbol{T}\boldsymbol{\Lambda}$ and $\boldsymbol{T}^{-1}\boldsymbol{A} = \boldsymbol{\Lambda}\boldsymbol{T}^{-1}$, respectively. The definition of left and right eigenvectors will be essential in section 3.5. Eq. (3.16) shows that for a positive real part of an eigenvalue, the perturbation grows exponentially and thus the system becomes unstable. On the other hand, when the real part of the eigenvalue is negative, the contribution from the corresponding eigenvector decays quickly and becomes negligible. This is a key observation to understand section 3.3. Moreover, Eq. (3.16) allows for a neat physical interpretation of the dynamic trajectory. As discussed in Chapter 2.3, the right eigenvectors may be interpreted as modes of the system. Thus, from Eq. (3.16) it is seen that the left eigenvectors decompose the initial state $x_0$ into the modal components $\vec{w}_i^{\,T}\vec{x}(0)$. These components are then propagated in time by $e^{\lambda_i t}$ and finally the state is reconstructed in terms of the linearly combined right eigenvectors.

We note that in the previous works considering exceptional points and symmetry-breaking, i.e. two real eigenvalues transitioning into a complex conjugate pair at the exceptional point, the pump current $J_c$ and phenomenologically introduced gain terms $|a(\tau)|(n(\tau)-1)$, which are coupled to the carrier densities in the waveguide and the nanocavity, were included in a fixed negative imaginary part of the refractive index [68, 69]. Here, we consider a more complex case as we account for the dynamic and nonlinear behaviour of the carrier densities $n_w(t)$, $n_c(t)$ as well as the complex field envelopes $a_-(t)$, $a_+(t)$ evaluated at the reference plane. Thus, the considered case is significantly more complex and requires additional steps, however it also provides an access to richer physics.

Finally, we also note the matrix $\boldsymbol{A}$ can be evaluated at each time instant along the trajectory parameterized by $\tau$. We can the determine the eigenvalues and the eigenvectors at each time instant, i.e. for each state vector, these eigenvalues and eigenvectors are said to be instantaneous. The model described in Eqs. (3.12) and (3.13) is used in all subsequent sections, and the steady-state eigenvalues as well as the instantaneous eigenvalues constitute the core of the following study.

## 3.3 Two dimensional phase-space picture

### 3.3.1 Steady-state eigenvalues

When the Fano laser is above threshold, it has been found to operate in two regimes, continuous wave regime and self-pulsing regime [83, 172]. In these studies, the steady-state eigenvalues have been used solely to assess the stability of the system. In this section, we review the current state of the knowledge on the stability of the laser. Additionally, we also observe that the steady-state eigenvalues exhibit an exceptional point at $\Delta\omega_c = -1.72\gamma_T$. It is found that as $\Delta\omega_c$ decreases and the exceptional point is crossed, a pair of complex conjugate steady-state eigenvalues transitions into two purely real eigenvalues. This observation influences the conclusions of section 3.3.4 and has not been found before.

In order to compute the steady-state eigenvalues, we solve the oscillation condition Eq. (3.4) for each combination of $(\Delta\omega_c, J_c)$. Then we calculate the steady-state of the set of differential equations, Eqs. (3.12), which approximate the dynamics of the laser, for each $(\omega_s, N_s)$. Subsequently, these steady-state values are fed to the stability matrix $\boldsymbol{A}$, Eq. (3.14), and its eigenvalues and eigenvectors are determined.

Figure 3.2 shows the real and imaginary parts of all five steady-state eigenvalues of the stability matrix $\boldsymbol{A}$. The eigenvalues in Fig. 3.2 are plotted versus $\Delta\omega_c = \omega_c - \omega_r$, which is detuning of the resonance frequency of the nanocavity, $\omega_c$, from the resonance frequency of the isolated cavity, $\omega_r$, normalized with respect to $\gamma_T$. Importantly, it is emphasized that $\Delta\omega_c = \omega_c - \omega_r$ differs from $\Delta\omega = \omega_c - \omega_s$ in Eq. (3.12). In fact, $\Delta\omega_c$ defines $\Delta\omega$ through the oscillation condition, Eq. (3.4), and can be controlled

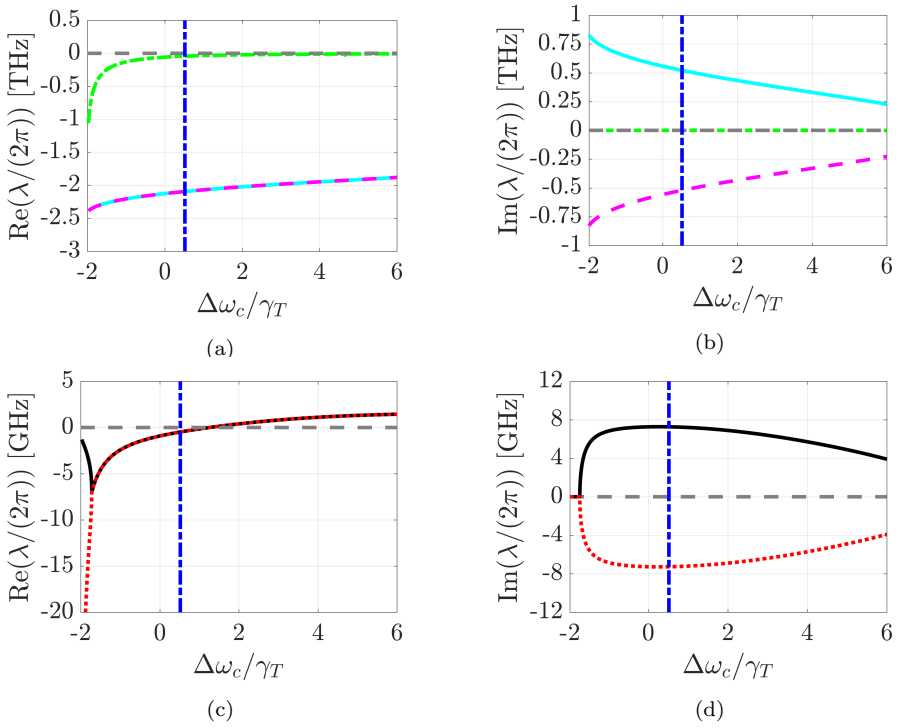


*Figure 3.2: (a), (c) Real and (b), (d) imaginary parts of the steady-state eigenvalues of the stability matrix $\boldsymbol{A}$. The system is composed of five coupled differential equations, (a), (b) show the three eigenvalues with the lowest real parts while (c), (d) show the two eigenvalues with the largest real parts. The horizontal dashed gray line marks zero. The vertical dashed blue line marks $\Delta\omega_c$ for which Fig. 3.3 is obtained. The pump current is $J_c = 1.2J_thr$.*

*Table 3.1: Laser parameters used in all numerical simulations.*

| Parameter name | Symbol | Value |
|---|---|---|
| Reference refractive index | $n_{ref}$ | 3.5 |
| Linewidth enhancement factor | $\alpha$ | 1 |
| Parity of the cavity mode | $P$ | 1 |
| Lasing cavity volume | $V_{LC}$ | $1.05\mu\text{m}^3$ |
| Nanocavity volume | $V_{NC}$ | $0.243\mu\text{m}^3$ |
| Nanocavity resonance | $\lambda_r$ | 1554nm |
| Lasing cavity length | $L$ | $5\mu$m |
| Carrier lifetimes | $\tau_s$, $\tau_c$ | 0.5ns |
| Group refractive index | $n_{grp}$ | 3.5 |
| Differential gain | $g_N$ | $5 \cdot 10^{-20}\text{m}^2$ |
| Left mirror reflectivity | $R_1$ | 1 |
| Transparency carrier density | $N_0$ | $1 \cdot 10^{24}\text{m}^{-3}$ |
| Nanocavity-waveguide coupling | $\gamma_C$ | $1.14\text{ps}^{-1}$ |
| Nanocavity total passive decay rate | $\gamma_T$ | $1.21\text{ps}^{-1}$ |
| Internal loss factor | $\alpha_i$ | $1000\text{m}^{-1}$ |
| Nanocavity confinement factor | $\Gamma_C$ | 0.3 |
| Waveguide confinement factor | $\Gamma$ | 0.5 |

externally by an external optical pump or in-plane pulses in the cross-port. Figures 3.2 and 3.3 as well as all the other figures in the following section are obtained for the parameters listed in Table 3.1 unless stated otherwise. Furthermore, the pump current is chosen to $J_c = 1.2J_{thr}$, where $J_{thr}$ is the minimum threshold current. It is found by solving the oscillation condition for the varying $\Delta\omega_c$. Then for each $\omega_s$, $r_R(\omega_s, \omega_c)$ is found and substituted to an equation for the modal threshold gain $g_{thr}$ [174], which is related to the current through: $N_{thr} = g_{thr}/(\Gamma g_N) + N_0$ and $J_{thr} = N_{thr}/\tau_s e V_{LC}$. Subsequently, the lowest $J_{thr}$ is used for the normalization of the pump current $J_c$.

Figure 3.2(a), (b) show the three eigenvalues with real parts significantly lower than in the case of the two eigenvalues in (c), (d). It is found that none of the three eigenvalues have positive real parts. One of the eigenvalues (green), which is purely real, approaches zero as $\Delta\omega_c$ is increased. However, it is not crossing zero. Thus, a complex conjugate pair of the eigenvalues in Fig. 3.2(c), (d) governs the stability of the laser. The remaining pair of the complex conjugate eigenvalues in Fig. 3.2(a), (b) has a very small real part of the eigenvalue and an extremely large imaginary part. Note that the scale in (a), (b) is in THz, while it is in GHz in (c), (d). Thus, these eigenvalues decay very quickly with time and their contribution to the laser dynamics becomes negligible very quickly. Similarly, the purely real eigenvalue becomes less and less significant with time as it never becomes positive.

Interestingly, it has been observed in [172] that there is a parameter region $(\Delta\omega_c, J_c)$ in which the laser can operate in the self-pulsing regime and thus become unstable despite all the stead-state eigenvalues having negative real parts. However, it can also converge towards the steady-state and exhibit continuous wave operation. The final regime of operation depends on the initial conditions. These region occurs in the vicinity of $\Delta\omega_c = 0.52\gamma_T$, which is marked with a dashed blue line in Fig. 3.2. Origin of this laser instability has been unknown thus far and will be explained in the upcoming sections. Therefore, $\Delta\omega_c$ is set to $\Delta\omega_c = 0.52\gamma_T$, unless stated otherwise.

Figure 3.2(c),(d) show the two eigenvalues with the largest real parts. It is found

that when $\Delta\omega_c$ is increased beyond $1.26\gamma_T$, the real parts of the two eigenvalues become positive. $\Delta\omega_c = 1.26\gamma_T$ is the critical point at which the complex conjugate pair of eigenvalues becomes purely imaginary. As $\Delta\omega_c$ is increased beyond this point, the steady-state point becomes unstable and a periodic solution appears. When the laser is slightly perturbed from the steady-state, the relaxation oscillation frequency, i.e. the imaginary part of the eigenvalues, becomes undamped due to positive real part of the eigenvalue. Then, the state-vector spirals out towards a stable periodic orbit for any initial conditions. This is Hopf bifurcation which has been observed in [172]. This change in stability of the steady-state point is local and the state sufficiently far away from the steady will still flow in and approach the stable periodic orbit where the repelling force of the steady state finds balance with the contracting force of the system. In our case, it is interpreted as the energy dissipated over one cycle is balanced by the energy that is provided by a constant pump power. Notably, due to the requirement of the pair of complex conjugate eigenvalues, the Hopf bifurcation can occur in at least a 2D system.

Furthermore, it is found in Fig. 3.2(c),(d) that when $\Delta\omega_c$ is decreased below $-1.72\gamma_T$, the imaginary parts of the eigenvalues become zero, both eigenvalues are purely real and their real parts split into two separate branches. The transition takes place at the exceptional point which is found at $\Delta\omega_c = -1.72\gamma_T$. As discussed in section 2.3 in more details, at the exceptional point, not only the eigenvalues are identical, but also the eigenvectors [61, 67, 130–132]. This phenomenon is known as the coalescence of eigenvalues and eigenvectors. Furthermore, exceptional points are known as symmetry breaking points [63, 65, 68, 69, 95, 200, 201, 203–205]. When the matrix $\boldsymbol{A}$ satisfies certain symmetries, then its eigenvalues can be purely real despite the system being non-Hermitian [69, 95, 206]. However, above a specific gain-loss contrast, the symmetry usually breaks down and the eigenvalues become complex [63, 69, 207]. The point at which the transition occurs is the exceptional point. Then, the eigenvalues/eigenvectors are said to be in the symmetric phase when they are purely real. When they are complex conjugate, they are said to be in the broken phase. In our case, the exceptional points arise because of the different decay rates $\gamma_L$, $\gamma_C$ and the gain terms $|a|(\tau)(n(\tau) - 1)$.

### 3.3.2 Two-dimensional phase space

In this section, we found that the laser dynamics are confined to the curved surface after the short initial transition stage. Therefore, we conclude that two degrees of freedom are sufficient to describe the state after the initial transition stage. This and the following sections form the basis of the journal paper [P4].

Figure 3.3(a), (b), (c) show three trajectories of the laser for three different initial conditions versus the normalized carrier density in the waveguide $n_w$ and the normalized amplitude of the complex field envelope propagating away from the reference plane $|a_-|$. The trajectories are parameterized with a dimensionless time $\tau = tG_{NC}N_0$ and the data has been obtained for $J_c = 1.2J_{thr}$ and $\Delta\omega_c = 0.52\gamma_T$ which is indicated by the blue line in Fig. 3.2. As it has been observed in [172], depending on the initial conditions, the state either approaches a periodic solution at the edge of the yellow surface or it converges towards the steady state point (black dot). Surprisingly, the laser might reach the periodic orbit despite all steady-state eigenvalues having negative real parts which suggests that the state always approaches the steady-state point.

Moreover, it is found that the trajectories display three different stages of laser operations: 1) the initial transition stage, 2) the later transition stage and 3) the self-pulsing/continuous wave stage. In the past works, only two stages have been

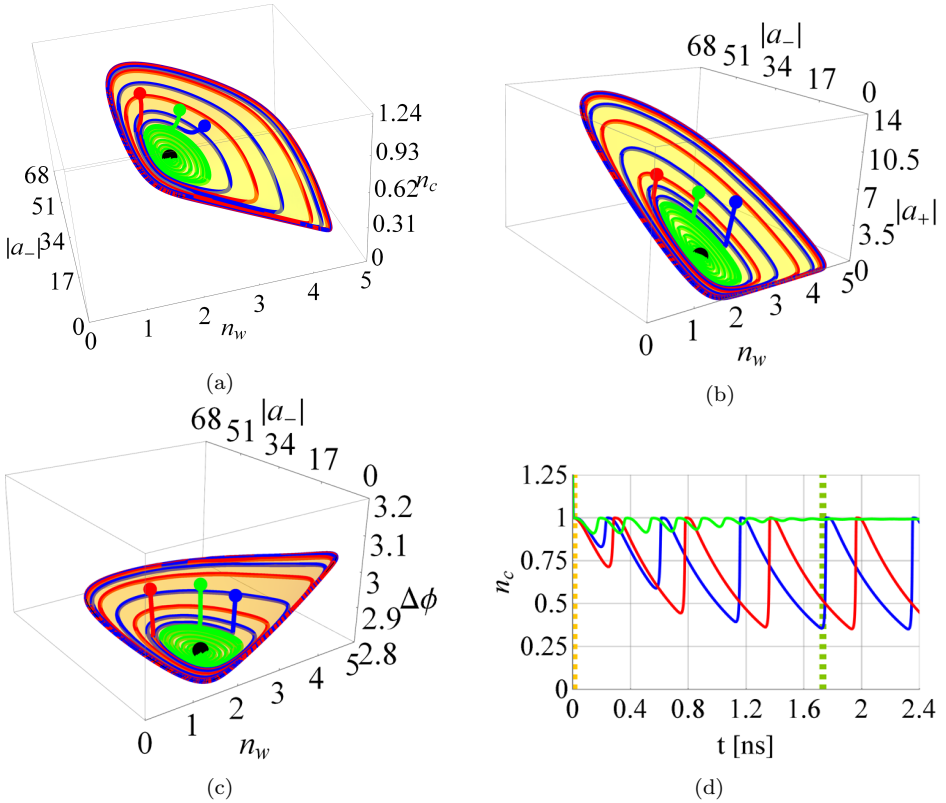


*Figure 3.3: a) Trajectories of $n_c$ against $n_w$, $|a_-|$. The black dot is the steady state. The red, green and blue dots are three different initial conditions which are above the surface. During an initial transition stage, the state approaches the surface. Then the state continues its evolution on the surface. Similar results can be obtained for the other two variables $|a_+|$ and $\Delta\phi$. (b), (c) the trajectories and the surface for the remaining two variables (c) $|a_+|$, (d) $\Delta\phi$ d) The trajectories plotted in time-domain show the initial transition stage on the order of a few picoseconds, the later transition stage lasting around 1.7ns and the self-pulsing stage. The dashed orange/green line marks the end of the initial/later transition stage.*

reported: 1) the later transition stage and 2) the self-pulsing/continuous wave stage. In Fig. 3.3(d) we show the blue trajectory from Fig. 3.3(a) in the time domain. It is found that the initial transition stage lasts only a few picoseconds and during this stage, the state decays towards the yellow surface on which all the consecutive dynamics take place. The end of the initial transition stage is marked by the orange dashed line in Fig. 3.3(d). Afterwards, the state is in the later transition stage during which all the dynamics are confined to the yellow surface and the state heads either to the periodic orbit or to the steady-state point. This stage is found to last approximately 1.7ns and is marked by the green dashed line in Fig. 3.3(d). Once the periodic solution or steady-state are reached, the state will remain there indefinitely unless strongly perturbed; this is the last stage. It is critical to emphasize that during the initial transition stage, the state decays towards the surface and is confined to it afterwards. This means that the state is confined to a 2D space and its movement can be entirely described by two degrees of freedom after the initial transition stage.

In Fig. 3.3, the carrier density in the waveguide $n_w$ and the magnitude of the left-propagating complex field envelope $|a_-|$ have been chosen as the two degrees of freedom. Numerical experiments in Mathematica [208] have shown that the data collapses as: $|a_-/a_+|$ can be expressed as a function of $n_w$ and $n_c$ while $n_c$ can be expressed as a function of $n_w$ and $|a_-|$. Taking into account that $n_c$ is bounded from both sides (it is real positive and does not exceed the transparency carrier density

$N_0$), we conclude that after the initial transition stage, the state could be described by the combination of $n_w$ with one of the complex field amplitudes, which in our case is $|a_-|$. This leads to the most stable numerically description of the laser dynamics. The same phenomenon of data collapse happens for the other two variable $|a_+|$ and $\Delta\phi$ as shown in Fig. 3.3(b), (c).

The remaining three degrees of freedom can be reconstructed once $n_w$ and $|a_-|$ are known. Then the state vector can be expressed as:

$$\vec{\psi} = \{|a_+|(n_w, |a_-|), |a_-|, \Delta\phi(n_w, |a_-|), n_w, n_c(n_w, |a_-|)\}. \tag{3.17}$$

In the same way, we can express each component of the velocity vector $d\vec{\psi}/d\tau$ as functions $V_i(\cdot)$ of $|a_-|$ and $n_w$:

$$\frac{d\vec{\psi}}{d\tau} = \{V_1(n_w, |a_-|), V_2(n_w, |a_-|), V_3(n_w, |a_-|), V_4(n_w, |a_-|), V_5(n_w, |a_-|)\}. \tag{3.18}$$

Furthermore, we can take a total derivative of $d\vec{\psi}/d\tau$ to linearize the problem, then each component of the acceleration vector $d^2\vec{\psi}/d\tau^2$ is expressed as:

$$\left(\frac{d^2\psi(\tau)}{d\tau^2}\right)_i = \left\{\frac{\partial V_i}{\partial |a_-|}\frac{d|a_-|}{d\tau} + \frac{\partial V_i}{\partial n_w}\frac{dn_w}{d\tau}\right\}. \tag{3.19}$$

Importantly, when Eq. (3.19) is compared with Eq. (3.14), it is observed that once the state vector is expressed as functions of $|a_-|$ and $n_w$, then the Jacobian matrix, which approximates the laser dynamics locally, becomes in fact a $2 \times 2$ matrix. Furthermore, functions $|a_+|(n_w, |a_-|)$, $\Delta\phi(n_w, |a_-|)$ and $n_c(n_w, |a_-|)$ describe the yellow surfaces shown in Fig. 3.3(a), (b), (c). These surfaces are approximated by polynomials. In order to do that we solve the system of differential equations, Eq. (3.12), several times for different initial conditions. Then, each solution results in a different trajectory, which can be plotted versus $|a_-|$ and $n_w$. These trajectories are found to lie on the yellow surfaces after the initial transition stage as in the case of the trajectories in Fig. 3.3. Subsequently, we exclude the part of the trajectory during the initial transition stage and fit a polynomial with the remaining part of all the trajectories for each function, $|a_+|(n_w, |a_-|)$, $\Delta\phi(n_w, |a_-|)$ and $n_c(n_w, |a_-|)$. More details on the polynomial approximation and validity of the 2D phase space picture can be found in the appendix B.

Therefore, once the surfaces are described by the polynomials, we are able to recover the whole state at any point in the phase space within the periodic orbit for the given $n_w$ and $|a_-|$ without solving the system of differential equations. Thus, we possess the information of the whole laser dynamics within the periodic orbit for any initial conditions after the initial transition stage, which last only a few picoseconds. This picture is justified in the following sections.

Note that the 2D phase space picture, Fig. 3.3, also allows to clearly analyse the behaviour of the state while it is in the self-pulsing stage. Particularly, when the self-pulsing behavior is analysed in the time-domain, most of the period is seen to be between the pulses, i.e. when $n_c$ decreases and $|a_-|$ is zero, see Fig. 3.3(d). This time interval is found on the surface along the line $|a_-| = 0$, which is parallel to the $n_w$ axis, see Fig. 3.3(a). However, the most important part of the pulse i.e. growth and decay of $|a_-|$ as well as growth and steady behaviour of $n_c$ are found to take place over a very short amount of time. On the other hand, the yellow surfaces in Fig. 3.3 are created by and emphasize the evolution of the state within the pulse.

### 3.3.3 Instantaneous eigenvalues

In this section, we further analyse the phenomenon of data collapse to the curved surface after the initial transition stage. We study instantaneous eigenvalues of the Jacobian matrix $\boldsymbol{A}$ over the whole surface determined in the pervious section. We demonstrate that there are at most two eigenvalues with positive real parts. We found that, as the pulse power increases, the dominating pair of the eigenvalues transitions from being purely real to a complex conjugate pair beyond the exceptional point. The pulse is bounded by two exceptional points with positive/negative real parts before/after the pulse, respectively. In total, four exceptional points are found to be crossed within a single loop in the phase space.

Figure 3.4 shows the instantaneous eigenvalues of the Jacobian matrix $\boldsymbol{A}$ computed along the trajectories parameterized with $\tau$ as well as over the whole surfaces. Notably, the polynomial approximation of the surfaces allows us to establish an effective band structure of the matrix $\boldsymbol{A}$. This is done by observing that after the initial transition stage, all the dynamics are confined to the curved surface. Thus, we can feed each point on the surface to the stability matrix $\boldsymbol{A}$ and determine the instantaneous eigenvalues.

In Fig. 3.4(a),(b) it is found that the two eigenvalues marked in pink form a complex conjugate pair over the whole surface. Moreover, the real parts of these two eigenvalues are significantly smaller than the real parts of the remaining three eigenvalues (orange, yellow, purple), while their imaginary parts are the largest. Furthermore, the 3$^{\text{rd}}$ eigenvalue (purple), which is purely real, is also considerably smaller than the dominating pair of the eigenvalues (orange, yellow) over the major part of the surface. The difference is most pronounced for large amplitudes of $a_-$, i.e. during the pulse. The purple eigenvalue is only comparable with the dominating pair (orange, yellow) along the line $|a_-| = 0$. However, even in this case the eigenvalue is only approaching zero, but is never becoming positive. Because of the very small real parts of these eigenvalues, the contribution from the corresponding eigenvectors decays very quickly and becomes negligible in reconstruction of the state vector. This decay is observed in Fig. 3.3 during the initial transition stage. During this stage, the three eigenvalues decay very quickly and approach the surface. Once the surface is reached by the state vector, the state is confined to the surface, and it can be entirely described using two degrees of freedom, as found in Fig. 3.3. As a consequence, we show the eigenvalues in the vicinity of the top two eigenvalues in the rest of Fig. 3.4.

In Fig. 3.4(e),(f),(g),(h),(i), we show the instantaneous eigenvalues along the green trajectory during (e), (f) the latter transition stage and (g), (h) in the vicinity of the pulse. In both cases, we show the pulse power in the straight port (dashed green line) with the corresponding scale on the right axis. The pulse power is expressed as [172]:

$$P_+(t) = 2\epsilon_0 nc(|s_2^-(t)|^2 = 2\epsilon_0 nc\,|A_+(t) + PA_-(t)|^2\,. \tag{3.20}$$

Figure 3.4(e), (f) shows the instantaneous eigenvalues in the later transition during, i.e. when the periodic orbit is approached. Particularly, the 3$^{\text{rd}}$ eigenvalue reaches an increasingly larger value with each period and eventually interacts with the 2$^{\text{nd}}$ largest eigenvalue (yellow), but still stays negative. Furthermore, Fig. 3.4(g),(h),(i) shows the eigenvalues in a close vicinity of the pulse. It is found that for low pulse power when $|a_-| \approx 0$, the top three eigenvalues (orange, yellow, purple) are purely real while one of the eigenvalues (orange) is slowly increasing. Once the limiting value of $n_w$ is reached, the pulse power increases and the real parts of the top two eigenvalues increase rapidly, collapse at the exceptional point and undergo a transition from being purely real to a pair of complex conjugate eigenvalues. Beyond the exceptional point, the real part of these two eigenvalues decreases and reaches its minimum when the pulse has reached its maximum power. As the power of the pulse decreases, the eigenvalues

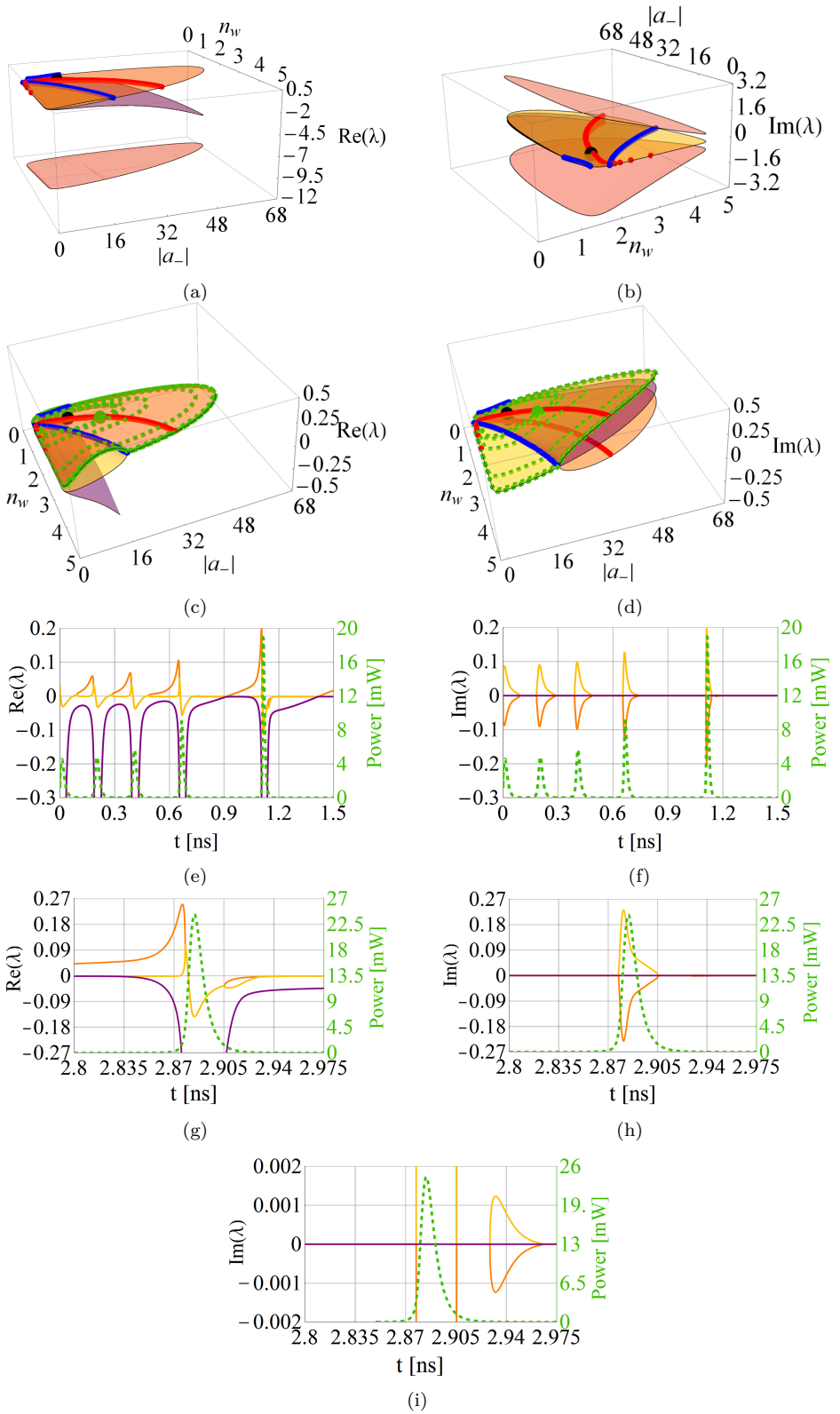


*Figure 3.4: (a), (c), (e), (g) Real and (b), (d), (f), (h), (i) imaginary parts of the instantaneous eigenvalues of the matrix* $\boldsymbol{A}$*. (a), (b), (c), (d) Bandstructure obtained for the surfaces obtained in sec. 3.3. (b), (d) closer look on the eigenvalues with the largest real parts. (e), (g), (f), (h), (i) the eigenvalues along the green dashed trajectory in Fig. 3.4(c), (d). (e), (f) show the eigenvalues during the later transition stage. (g), (h), (i) show the eigenvalues in the vicinity of the single pulse. The pulse power in the straight-port (dashed green line) is shown on the right axes, while the left axes scale concerns all the other curves. (a), (b), (c), (d) The blue line indicates the contour of exceptional points. The red line indicates the line when* $Re(\lambda) = 0$*, the black dot is the steady-state eigenvalues. Since the system of equations is dimensionless, the eigenvalues are also dimensionless.*

cross another exceptional point and transition from a complex conjugate pair into two purely real eigenvalues. Therefore, it is found that most of the pulse is bounded by two exceptional points with positive/negative real parts at the beginning/end of the pulse, respectively, and that the eigenvalues are in the broken phase within the pulse, i.e. form a complex conjugate pair.

Interestingly, the eigenvalues undergo two more transitions at the exceptional points as the real parts of the eigenvalues grow and approach zero, which is crossed only in the middle of the cycle. Therefore, within a single loop at the periodic orbit, the state crosses four exceptional points. This is particularly important observation for sections 3.4 and 3.5. In [195], it has been shown that a loop crossing an exceptional point can be treated as a limiting case of an exceptional point being encircled. Furthermore, in [192] it has been noted that when a periodic loop is made around an exceptional point, then the eigenvectors are not periodic with the same period. It has been shown that when an exceptional point is approached and the state evolves along a trajectory in the diminishing vicinity of an exceptional point, the eigenvectors acquire a phase shift of $\pm i$ [62, 136–138, 209]. Moreover, it has been demonstrated that while a two-fold loop is enough for the eigenvalues to go back to the original state, it is a four-fold that is required for the eigenvectors to recover the original case [130–132, 134, 135]. Therefore, in our case, the presence of four exceptional points along a single loop is enforced by the periodicity of the system. Since the state is at the periodic orbit in the self-pulsing regime, it has to cross four exceptional points or none within a single cycle in order to remain periodic, i.e. after crossing all four exceptional points within a loop, the state is back to the initial position and the cycle can commence again.

### 3.3.4 Reconstruction of the solution

In this section, we prove that the two eigenvectors corresponding to the two dominating eigenvalues can span the whole phase space after the initial transition stage as the contribution from the remaining eigenvectors decays rapidly. Here, we also prove and present that after the initial transition stage, the original 5D model can be reduced to only 1D in the limited region of the parameter space when the steady-state eigenvalues are purely real and that the system evolves into 2D beyond the exceptional point when the eigenvalues form a complex conjugate pair.

In Fig. 3.4, it has been found that there are at most two instantaneous eigenvalues with positive real parts. Therefore, after the initial transition stage, the solutions of Eqs. (3.14), (3.13b), (3.12) can be reconstructed solely in terms of the two eigenvectors corresponding to the two dominating instantaneous eigenvalues; in the general form the solutions are expressed as:

$$\frac{d\vec{\psi}}{d\tau} = c_1(\tau)\vec{v_1}(\tau) + c_2(\tau)\vec{v_2}(\tau) \tag{3.21a}$$

$$\frac{d^2\vec{\psi}}{d\tau^2} = c_1(\tau)\lambda_1(\tau)\vec{v_1}(\tau) + c_2(\tau)\lambda_2(\tau)\vec{v_2}(\tau) \tag{3.21b}$$

where $\vec{v}_{1,2}(\tau)$, $\lambda_{1,2}(\tau)$ are the instantaneous right eigenvectors and the instantaneous eigenvalues of the stability matrix $\boldsymbol{A}$, respectively, $c_{1,2}(\tau)$ are the amplitudes of the corresponding eigenvectors. The amplitudes $c_{1,2}(\tau)$ can be retrieved from the solution $d\vec{\psi}(\tau)/d\tau$ using the left eigenvectors as: $c_{1,2} = \vec{w}^T_{1,2}(\tau)d\vec{\psi}(\tau)/d\tau$. The left and right eigenvectors follow the normalization $\vec{w}_i^T\vec{v_j} = \delta_{ij}$. Therefore, based on Eqs. (3.21) it is seen that only two instantaneous eigenvectors are needed to span the whole phase space, which is confined to the curved surface after the initial transition stage.

From Eq. (3.21) it follows that the instantaneous eigenvectors can be interpreted

on the velocity level. Similarly, the instantaneous eigenvalues can be interpreted on the acceleration level of the model. For instance, it is found in Fig. 3.4(g) that within the pulse, when the top two eigenvalues form a complex conjugate pair and $\mathrm{Re}(\lambda) = 0$, the acceleration of the state is zero, the velocity of the state $d\vec{\psi}(\tau)/d\tau$ is the largest and the pulse power is increasing linearly. Furthermore, the imaginary part of the instantaneous eigenvalue can be related to the width of the pulse. Just before the peak of the pulse, the imaginary part reaches its maximum, see Fig. 3.4(h). When one takes the inverse of the maximum imaginary part to calculate the time period, it is found to correlate with the pulse width. The maximum $\mathrm{Im}(\lambda)$ corresponds to approximately twice the width of the pulse at half of the pulse power.

Subsequently, we prove that the two eigenvectors can be used to span the whole phase space of the laser after the initial transition stage. This is done by demonstrating that the two eigenvectors can be used to approximate the two tangential vectors to the surface pointing along the coordinate lines, $n_w$ and $|a_-|$. We start by considering tangential vectors to a surface $z = f(x, y)$ along the parametric curve parameterized with $t$. The parametric curve on this surface has a vector equation $r(t) = \{x(t), y(t), z(t)\}$. The tangent vector to the surface along this curve is known to be $r'(t) = \{x'(t), y'(t), z'(t)\}$, where $z'(t) = \nabla f \cdot \vec{u}$, $\vec{u} = \{x'(t), y'(t)\}$.

Similarly, in our case, we can determine the tangential vectors to the surfaces approximated by the polynomials, Eq. (3.17). The tangential vectors to these surfaces along the dynamic trajectory are expressed as:

$$\vec{r}'_i(\tau) = \left\{ \frac{d|a_-|}{d\tau}, \frac{dn_w}{d\tau}, \left\{ \frac{d\vec{\psi}}{d\tau} \right\}_i \right\}, \tag{3.22}$$

where $i$ indicates each surface of the state vector $\vec{\psi}(\tau)$. The velocity vector in Eq. (3.22) can be expressed as:

$$\frac{d\vec{\psi}}{d\tau} = \frac{\partial\vec{\psi}}{\partial|a_-|}\frac{d|a_-|}{d\tau} + \frac{\partial\vec{\psi}}{\partial n_w}\frac{dn_w}{d\tau}. \tag{3.23}$$

We can decompose the tangential vector to the surface along the parameterized trajectory into a linear combination of the two tangential vectors pointing in the direction of the coordinate lines, $n_w$ and $|a_-|$ as:

$$\vec{r}'_1 = \left\{ 1, 0, \frac{\partial\vec{\psi}}{\partial|a_-|} \right\}, \qquad \vec{r}'_2 = \left\{ 0, 1, \frac{\partial\vec{\psi}}{\partial n_w} \right\}, \tag{3.24}$$

Therefore, we observe in Eq. (3.22) that the tangential vectors along the dynamic trajectory are expressed in terms of the components of the velocity vector which can be expanded in terms of the eigenvectors, Eq. (3.21). Thus, the two eigenvectors can be used for the reconstruction of the solution as long as the two tangential vectors, Eq. (3.24), are approximated by them. As found in Fig. 3.4, the eigenvalues, and thus the corresponding eigenvectors, are either real or form complex conjugate pairs. In order to be able to compare these eigenvectors with the tangential vectors in Eq. (3.24), we linear combine the eigenvectors to point along the coordinate lines as:

$$\begin{bmatrix} \vec{v}'_1 \\ \vec{v}'_2 \end{bmatrix} = \begin{bmatrix} v_{12} & v_{14} \\ v_{22} & v_{24} \end{bmatrix}^{-1} \begin{bmatrix} v_{12} & v_{14} & v_{11} & v_{12} & v_{13} & v_{14} & v_{15} \\ v_{22} & v_{24} & v_{21} & v_{22} & v_{23} & v_{24} & v_{25} \end{bmatrix} \tag{3.25}$$

where $\vec{v}_1$ and $\vec{v}_2$ are the original eigenvectors and the second number in the subscript indicates the corresponding components. The resultant vectors $\vec{v}'_1$ and $\vec{v}'_2$ are purely real and point along the $n_w$ and $|a_-|$ coordinate lines. These vectors are plotted over the whole surfaces in Fig. 3.5. Note that the vectors $\vec{v}'_1$ and $\vec{v}'_2$ have seven

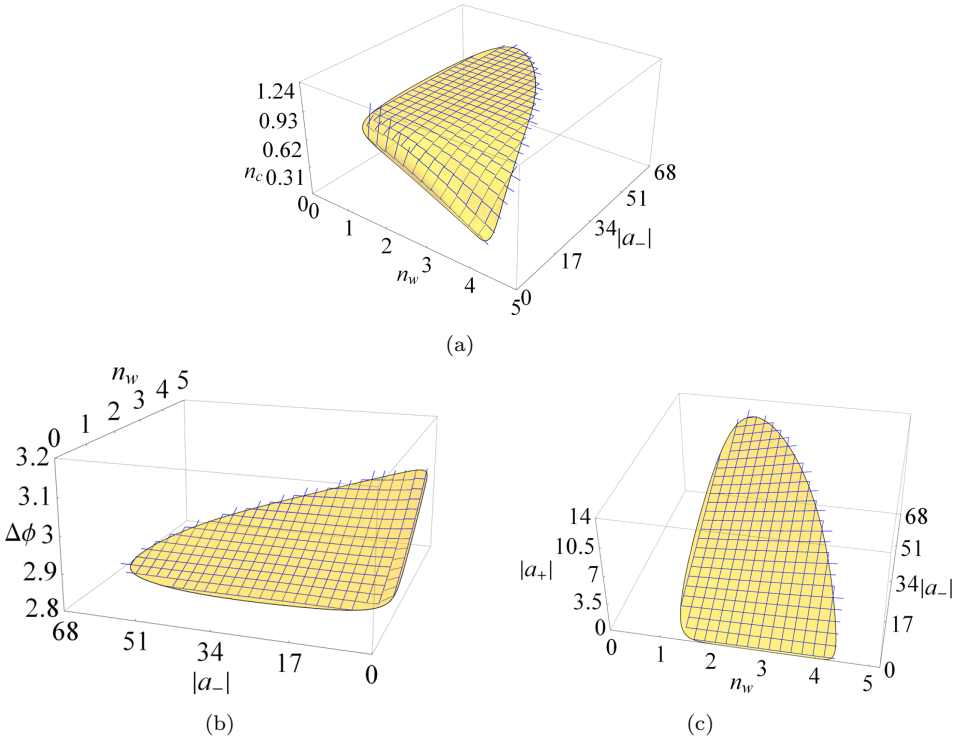


*Figure 3.5: The vectors $\vec{v}'_{1,2}$ plotted on the three surfaces, (a) $n_c$, (b) $\Delta\phi$, (c) $|a_+|$.*

components, first two correspond to the coordinates $n_w$ and $|a_-|$, while one out of five consecutive components has to be picked for each surface. We scale these vectors by the spacing between each position for which they are computed. This is done in order to avoid an overlap of them and create a square grid pattern. If these vectors create a perfect grid, it means that they perfectly approximate the tangential vectors, Eq. (3.24). It is found that the vectors $\vec{v}'_1$ and $\vec{v}'_2$ very well approximate the tangential vectors to the surfaces. Small discrepancy is only visible along the line $|a_-| \approx 0$. This is explained by the third (purple) eigenvalues becoming comparable with the two dominating eigenvalues along this line. However, it does not influence the approximation over the rest of these surfaces. Therefore, we conclude the solution can be successfully reconstructed in terms of the two eigenvectors and the two degrees of freedom picture is justified. Additional consistency checks/verifications of the two-dimensional picture are discussed in Appendix B. Therefore, the system of five differential equations can be reduced to only two differential equations describing the dynamics of $n_w$ and $|a_-|$. Once $n_w$ and $|a_-|$ are known, we can determine the remaining three dimensions from the established surfaces. Therefore, the simplified 2D model is expressed as:

$$\frac{d|a_-(\tau)|}{d\tau} = V_2(|a_-(\tau)|, n_w(\tau)), \tag{3.26a}$$

$$\frac{dn_w(\tau)}{d\tau} = V_4(|a_-(\tau)|, n_w(\tau)), \tag{3.26b}$$

The simplified system in Eq. (3.26) can be obtained in two ways either by 1) taking the two differential equations for $|a_-|$ and $n_w$ from the set of equations in Eq. (3.18) and approximating the remaining degrees of freedom by polynomials or 2) by approximating the velocity surfaces $d|a_-|/d\tau$ and $dn_w/d\tau$ by polynomials and solving the set of differential equations. Both methods give similar results depending on the

accuracy of the polynomial approximation.

Finally, we note that there exists a region in the parameter space $(\Delta\omega_c, J_c)$ in which even a 1D model is sufficient, after the initial transition stage, to describe the laser dynamics which were originally modeled by a 5D system. Figure 3.2 shows that when $\Delta\omega_c$ is largely negative, the two dominating steady-state eigenvalues undergo a phase transition from a complex conjugate pair (the broken phase) to the two purely real eigenvalues (the symmetric phase). Then, the relaxation oscillations of the laser ceases to exist, and the laser immediately adjusts its trajectory when it experiences any perturbations, e.g. modulation of $\Delta\omega_c$. Furthermore, it is observed that one of the steady-state eigenvalues (red) rapidly decreases, while the other one increases and approaches zero. Once it is very close to zero, the lasing mode $(\omega_s, N_s)$ ceases to exist due to collision of the stable mode with an unstable one [112]. However, within this small region of $(\Delta\omega_c, J_c)$ values, i.e. for $-2.05\gamma_T < \Delta\omega_c < -1.72\gamma_T$, the single eigenvalue dominates. Based on the analysis above, it is clear that in this case the velocity vector $d\vec{\psi}(\tau)/d\tau$ could be expanded solely into a single instantaneous eigenvector corresponding to the dominating eigenvalue after the transition stage. Then, a single differential equation could be used to describe the laser dynamics after the transition stage. Therefore, the system evolves from the 1D to the 2D system as $\Delta\omega_c$ increases and crosses the exceptional point for steady-state eigenvalues.

## 3.4 Origin of the Fano laser instability

This section elaborates the subject included in the journal paper [P4]. We use the simplified model, Eq. (3.26), to explain the origin of the laser instability in a region of the parameter space $(\Delta\omega_c, J_c)$ when all steady-state eigenvalues have negative real parts and thus suggest the stable operation of the laser. This instability has been observed in [172], but has not been explained. Here, we associate the unknown origin of instability with a new unstable periodic orbit separating the stable steady-state from the stable periodic orbit. Moreover, we have classified the bifurcation standing behind the two orbits and the steady-state as a generalized Hopf (Bautin) bifurcation. In the studied case, we set $\Delta\omega_c = 0.52\gamma_T$ and $J_c = 1.2J_{\text{thr}}$, unless stated otherwise.

### 3.4.1 Detection of periodic orbits

We start the analysis searching for periodic orbits in the phase space of the Fano laser. This is done by solving a simplified model of the two differential equations for varying initial conditions and observing a change in the position of the state vector after a single period. We chose the initial condition as follows: 1) $|a_-|$ is constant and equal to the value at steady-state point and 2) we only vary $n_w$ over the whole phase space. The initial conditions are varied along the purple line in Fig. 3.6(a). For each initial condition along the purple line, we compute the trajectory by solving Eq. 3.26 up to the point when $|a_-|(\mathcal{T}) = |a_-|(0)$, where $\mathcal{T}$ is the time required for it to happen. Afterwards, we evaluate the change in $n_w$ as $\Delta x = n_w(0) - n_w(\mathcal{T})$ and show it in Fig. 3.6(b). When the change $\Delta x$ is zero it means that after the time $\mathcal{T}$ the state is at the same position and thus the laser has been initialized at a steady-state point or a periodic orbit. On the other hand, if the change $\Delta x$ is nonzero, then it means that the state is approaching or leaving either a periodic orbit or a steady-state.

Figure 3.6(b) shows that the curve has five crossings with zero, these crossings are marked with two pairs of blue, red dots and a single black dot, which represents a steady-state. The pairs of blue and red dots mark two periodic orbits. The outer periodic orbit (blue) is known to become stable when the pair of complex conjugate eigenvalues crosses the imaginary axis and their real parts become positive [172]. It arises as a consequence of Hopf bifurcation. However, it does not explain bifurcation of two periodic orbits and an equilibrium point when all steady-state eigenvalues have negative real parts. Moreover, Fig. 3.6(a) shows that the outer periodic orbit can be reached despite the steady-state being stable and attracting the state. Therefore, we

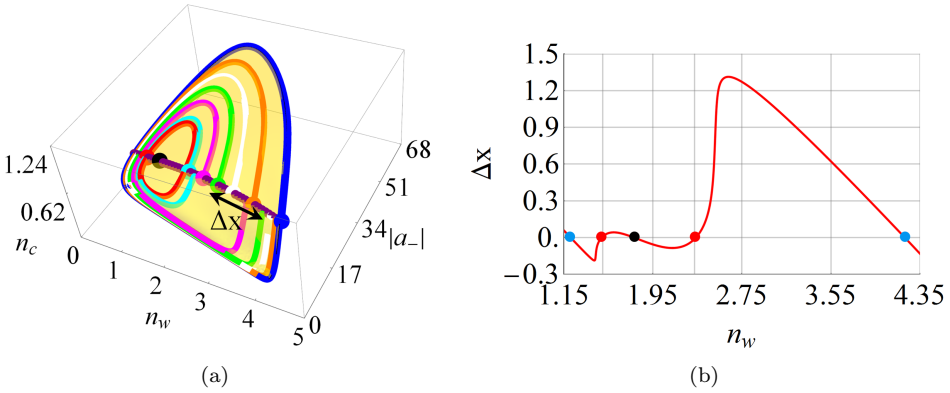


*Figure 3.6: (a) Figure showing a single cycle of several trajectories (various colours) initialized along the purple line. The initial states are indicated with dots. (b) $\Delta x = n_w(0) - n_w(\mathcal{T})$ over one cycle, where $\mathcal{T}$ is the time of a single cycle. The pairs of red and blue dots indicate the periodic orbits, the black dot indicates the steady state; the initial states are along the purple line in (a).*

have found an additional periodic orbit in the phase space. This orbit separates the known outer periodic orbit from the stable steady-state.

### 3.4.2 Stability of the orbits

In the following, we use the simplified model, Eq. (3.26), to determine the stability of the newly found periodic orbit as well as the outer periodic orbit. Stability of the periodic solutions can be evaluated using Floquet multipliers [202, 210]. Floquet multipliers are defined as eigenvalues of the fundamental solution matrix $\boldsymbol{\Phi}(\tau)$ evaluated at $\tau$ equal to $\mathcal{T}$ which is the period of the orbit. $\boldsymbol{\Phi}(\tau)$ is a matrix whose columns are the linearly independent solutions of Eq. (3.14) [202, 210]. Eq. (3.14) can be written as $d\vec{v}(\tau)/d\tau = \boldsymbol{A}(\tau)\vec{v}(\tau)$, and solved for $\vec{v}$ with $\vec{v}(\tau) = d\vec{\psi}(\tau)/d\tau$. Matrix $\boldsymbol{\Phi}(\tau)$ is a fundamental solution matrix of $d\vec{v}(\tau)/d\tau = \boldsymbol{A}(\tau)\vec{v}(\tau)$ only if it satisfies [202, 210]:

$$\frac{d\boldsymbol{\Phi}(\tau)}{d\tau} = \boldsymbol{A}(\tau)\boldsymbol{\Phi}(\tau). \tag{3.27}$$

Additionally, if $\boldsymbol{\Phi}(\tau)$ satisfies $\boldsymbol{\Phi}(0) = \boldsymbol{I}$, then the solution to the system $d\vec{v}(\tau)/d\tau = \boldsymbol{A}(\tau)\vec{v}(\tau)$ can be propagated directly from the initial condition as:

$$\vec{v}(\tau) = \boldsymbol{\Phi}(\tau)\vec{v}(0), \tag{3.28}$$

where $\vec{v}(0) = d\vec{\psi}/d\tau\big|_{\tau=0}$. It is seen in Eq. (3.28), that if the model is initialized at $\vec{v}(0)$ which corresponds to the periodic orbit or the steady-state point, and the fundamental solution matrix $\boldsymbol{\Phi}(\mathcal{T})$ is evaluated at $\mathcal{T}$, then $\vec{v}(\mathcal{T}) = \boldsymbol{\Phi}(\mathcal{T})\vec{v}(0)$ and $\vec{v}(\mathcal{T}) = \vec{v}(0)$. Fundamental solution matrix $\boldsymbol{\Phi}(\tau)$ evaluated at $\tau = \mathcal{T}$, $\boldsymbol{\Phi}(\mathcal{T})$, is called a monodromy matrix and its eigenvalues determine whether the state will approach or be repelled from the periodic orbit upon a small perturbation of the initial conditions from the ones at the orbit. This conclusion is directly related to the origin of the monodromy matrix. One may consider how much the trajectory will be displaced after one period $\mathcal{T}$ when its initial condition is slightly perturbed from the periodic orbit. Mathematically speaking $\delta\vec{\psi}(\mathcal{T}) = \vec{\phi}(\mathcal{T}; \vec{\psi}_0 + \delta\vec{\psi}_0) - \vec{\phi}(\mathcal{T}; \vec{\psi}_0)$, where $\vec{\phi}(\tau; \vec{\psi}_0)$ is the state vector after time $\tau$ when the system was initialized at $\vec{\psi}_0$ [202]. Then up to a first order approximation, the displacement $\delta\vec{\psi}(\mathcal{T})$ is given by:

$$\delta\vec{\psi}(\mathcal{T}) = \frac{\partial\vec{\phi}(\mathcal{T}; \vec{\psi}_0)}{\partial\vec{\psi}_0}\delta\vec{\psi}_0. \tag{3.29}$$

Equation (3.29) describes the variation of the solution with respect to the initial conditions. In fact, $\partial\vec{\phi}(\mathcal{T}; \vec{\psi}_0)/\partial\vec{\psi}_0$ is a definition of a monodromy matrix and it can be shown to be the same as $\boldsymbol{\Phi}(\mathcal{T})$. This is done by differentiating Eq. (3.13b) with respect to $\vec{\psi}_0$ and using linearity of a differentiation operator, then we obtain:

$$\frac{d}{dt}\left(\frac{\partial\vec{\phi}}{\partial\vec{\psi}_0}\right) = \frac{\partial}{\partial\vec{\phi}}\left(V(\vec{\phi})\right)\frac{\partial\vec{\phi}}{\partial\vec{\psi}_0}. \tag{3.30}$$

By setting $\partial\vec{\phi}/\partial\vec{\psi}_0|_{\tau=0} = \boldsymbol{I}$ and comparing with Eq. (3.27), we conclude that $\partial\vec{\phi}(\mathcal{T}; \vec{\psi}_0)/\partial\vec{\psi_0} = \boldsymbol{\Phi}(\mathcal{T})$ is the monodromy matrix. Eigenvalues of the monodromy matrix $\lambda_f$ (Floquet multipliers) have the following properties [210]:

$$\boldsymbol{\Phi}(n\mathcal{T})\vec{\Psi} = \lambda_f(n\mathcal{T})\vec{\Psi}, \qquad \boldsymbol{\Phi}^n(\mathcal{T})\vec{\Psi} = \lambda_f^n(\mathcal{T})\vec{\Psi}, \tag{3.31a}$$

$$\boldsymbol{\Phi}(n\mathcal{T}) = \boldsymbol{\Phi}^n(\mathcal{T}), \qquad \lambda_f(n\mathcal{T}) = \lambda_f^n(\mathcal{T}), \tag{3.31b}$$

where $\vec{\Psi}$ is an eigenvector of the monodromy matrix $\mathbf{\Phi}(\mathcal{T})$. Therefore, similarly as in the stability analysis in the vicinity of the steady-state solution, we can expand the displacement $\delta\vec{\psi}_0$ into the eigenvectors of the monodromy matrix $\vec{\Psi}$. Then from Eq. (3.29) it is seen that if the eigenvalues $\lambda_f$ lie within the unit circle, then $\delta\vec{\psi}(\mathcal{T})$ tends to zero and the orbit is stable as the state will be attracted to it. On the other hand, when the eigenvalues $\lambda_f$ are outside the unit circle, then the displacement will grow with each cycle, i.e. the state will be repelled from the orbit as the orbit is unstable.

Therefore, the essential step in the assessment of the stability of the orbit is the computation of the monodromy matrix $\mathbf{\Phi}(\mathcal{T})$. This is done using Eq. (3.27) and solving it for the fundamental solution matrix $\mathbf{\Phi}(\tau)$. We solve the simplified 2D model, Eq. (3.26), for the initial conditions at each orbit. Then we feed these trajectories into the 2-by2 $\boldsymbol{A}(\tau)$ matrix and solve four differential equations for each entry of the fundamental solution matrix $\mathbf{\Phi}(\tau)$ simultaneously requiring that $\mathbf{\Phi}(0) = \boldsymbol{I}$. Once $\mathbf{\Phi}(\tau)$ is known, we evaluate it at the corresponding $\mathcal{T}$ of the periodic orbit, which is known from the data required to obtain Fig. 3.6(b), and compute the eigenvalues of the monodromy matrix. These eigenvalues are shown in Fig. 3.7.

Floquet multipliers of the outer periodic orbit (blue) in Fig. 3.6(b) are found to lie at the unit circle and within it, very close to the centre of the coordinate system. We note that one of the Floquet multipliers is always equal to +1, and the corresponding eigenvector is tangential to the orbit [202]. This is a neutral stability of the orbit allowing for a drift along the periodic orbit. Therefore, we conclude that the outer orbit is stable even in the case when all steady-state eigenvalues have negative real parts and the two orbits are present within the phase space. On the other hand, Fig.

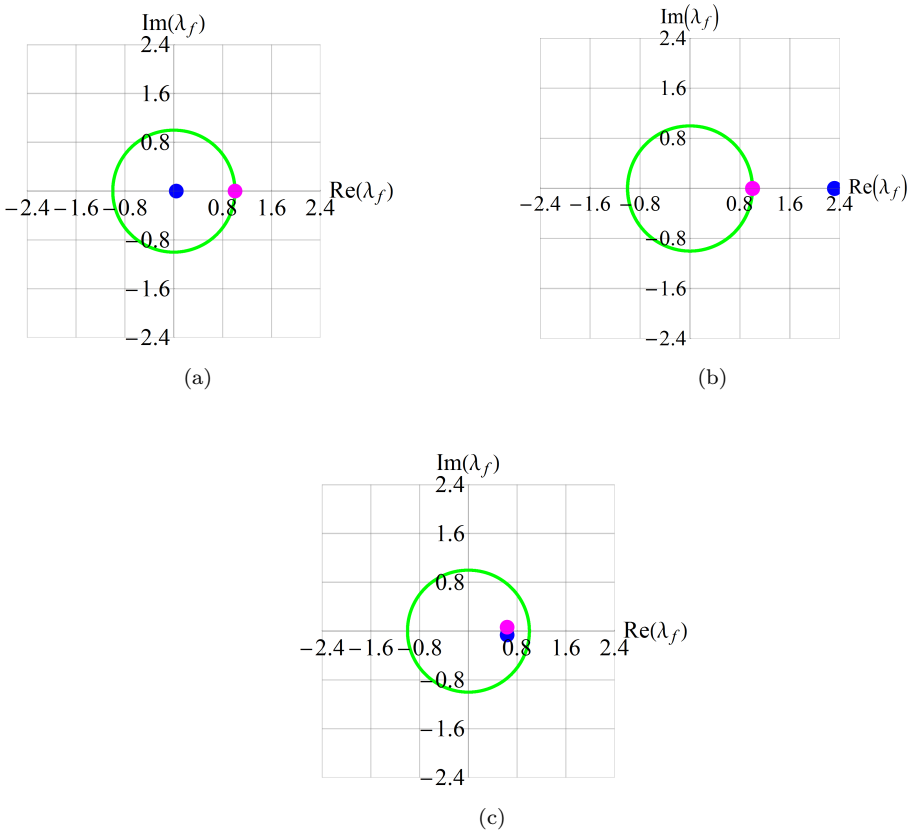


*Figure 3.7: Floquet multipliers obtained for (a) the outer orbit (blue in Fig. 3.6), (b) the inner orbit (red in Fig. 3.6), (c) the steady-state (black in Fig. 3.6). Obtained for* $\Delta\omega_c = 0.52\gamma_T$, $J_c = 1.2J_{\mathrm{thr}}$.

3.7(b) shows that the inner periodic orbit (red) in Fig. 3.6(b) is unstable, as one of the multipliers has crossed the unit cycle along the positive axis and is found at $\lambda_f = 2.31$. The other one, similarly as in the previous case, is exactly at $+1$ indicating the possibility of the drift along the orbit. The steady-state is known to be stable, however, it is interesting to observe that the Floquet multipliers are within the unit circle, but are approaching its border and none of them is at $+1$ as it is not an orbit.

Furthermore, Floquet multipliers provide an additional information about the nature of the instability, e.g. 1) when real eigenvalues cross the unit circle at $-1$, it represents period-doubling bifurcation, 2) when real eigenvalues cross the unit circle at $+1$, it represents exchange of instability [211]. In fact, it is found that as $\Delta\omega_c$ decreases, the new unstable periodic orbit increases in size. Eventually, it collides with a stable periodic orbit and annihilates it; then only the stable steady-state is left in the phase-space. It is confirmed in Fig. 3.8(a),(b) which shows the numerically evaluated change $\Delta x$ in $n_w$ as well as the Floquet multipliers for the steady-state when $\Delta\omega_c = 0$, just after annihilation of the orbits. Only a single crossing with zero is found in Fig. 3.8(a) proving that there are no orbits in the phase space. If $\Delta\omega_c$ increases, the unstable periodic orbit decreases in size. Eventually, it collides with the stable steady-state and the stability of the steady-state is changed as it becomes unstable. It is confirmed in Fig. 3.8(c),(d),(e) which shows $\Delta x(n_w)$ as well as the Floquet multipliers for the periodic orbit and the steady-state when $\Delta\omega_c = 1.52\gamma_T$, just after the stability of the steady-state has been changed. Three crossings with zero are found in Fig. 3.8(c) proving that there is a single orbit in the phase space and an equilibrium point. Interestingly, Fig. 3.8(d) shows a complex conjugate pair of eigenvalues crossing the unit circle. This might indicate the existence of a more complicated source of instability, i.e. Neimark-Sacker bifurcation [211], which might require investigation of Floquet multipliers of the original 5D system of equations.

We note that the behaviour of the stability exchange of the equilibrium point (steady state) and annihilation of the orbits upon an external parameter variation, $\Delta\omega_c$, is a signature of Bautin bifurcation, which is also known as generalized Hopf bifurcation [181, 182]. Bautin bifurcation is characterized by a bifurcation of two periodic orbits of opposite stability and an equilibrium point [181, 182].

Finally, we note that the stability of the orbits can also be assessed based on Fig. 3.6. Consider the red dots in Fig. 3.6(b); they correspond to the unstable periodic orbit occurring at the initial position $\vec{\psi}_0$. If the initial displacement is negative $-\delta\vec{\psi}_0$, the displacement after one cycle is found in Fig. 3.6(b) to be also negative $-\delta\vec{\psi}(\mathcal{T})$. If the initial displacement is positive $\delta\vec{\psi}_0$, the displacement after one cycle is found in Fig. 3.6(b) to be also positive $\delta\vec{\psi}(\mathcal{T})$. Thus, we can never return to the initial position at the orbit upon a small initial perturbation $\delta\vec{\psi}(\mathcal{T})$. Therefore, the new orbit is unstable. On the other hand, if the blue dots in Fig. 3.6(b) are considered. It is found that upon a positive/negative initial displacement, we observe negative/positive displacement after one period, respectively. Thus, the state is always attracted back to the stable periodic orbit upon a small initial perturbation.

Therefore, using the simplified 2D model, we have detected the orbit which has not be found before. We have assessed stability of the orbits using Floquet multipliers. We have classified the bifurcation standing behind the two orbits and the steady-state point as Bautin bifurcation. We have found that upon an external parameter variation, $\Delta\omega_c$, the two orbits may annihilate or the stability of the steady-state may exchange; it is a signature of Bautin bifurcation. We explained the unknown origin of the laser instability when all steady-state eigenvalues have negative real parts. The new unstable orbit separates the stable steady-state from the stable orbit. If the model is initiated outside/inside the inner unstable orbit, the state is repelled from the unstable orbit and is attracted towards the stable orbit or the stable steady-state, respectively.

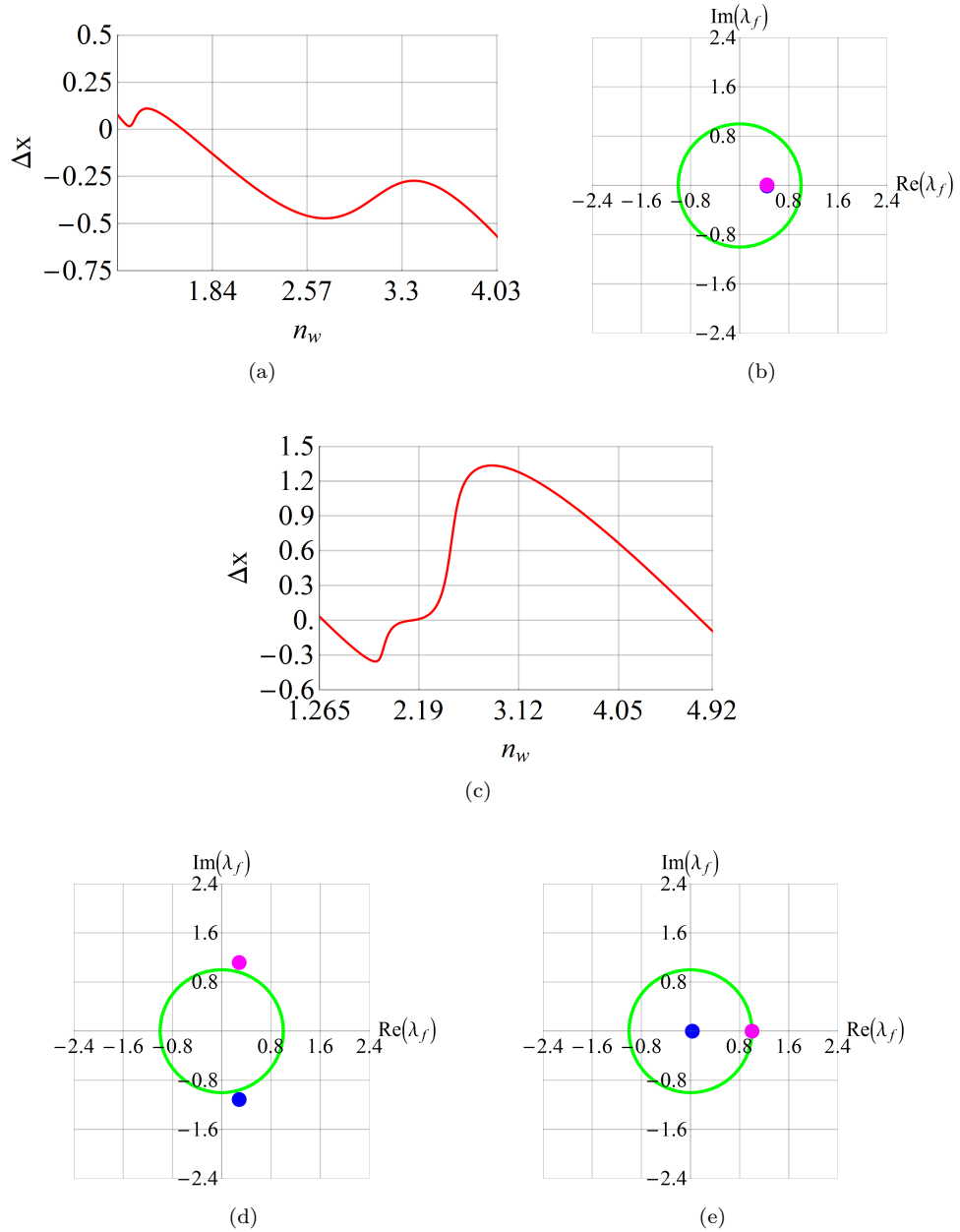


*Figure 3.8: Stability analysis. (a), (b) $\Delta\omega_c = 0\gamma_T$, $J_c = 1.2J_{\text{thr}}$ and (c), (d), (e) $\Delta\omega_c = 1.52\gamma_T$, $J_c = 1.2J_{\text{thr}}$. (a), (c) Numerically evaluated $\Delta x = n_w(0) - n_w(\mathcal{T})$ over one cycle of the trajectory. (b), (d), (e) Floquet multipliers obtained for (b), (d) the steady-state and (e) the periodic orbit.*

## 3.5 Non-Hermitian Dynamics

In this section, using the simplified model we investigate non-Hermitian dynamics of the model. Particularly, using the general framework of [88], we identified that the intervals of the solution following the adiabatic prediction are abruptly interrupted by nonadiabatic transitions due to presence of the instantaneous exceptional points.

### 3.5.1 Quasiadiabaticity

When the laser is in the self-pulsing stage, all variables described by the dynamical model, Eq. (3.12), vary in the self-modifying manner and are described by a dynamic trajectory making consistent loops in the phase space, Fig. 3.4. Behind the periodic behaviour stands the nonlinear interaction between the carrier densities and the fields in the waveguide and the cavity. We emphasize that the periodic motion does not require any external variation of the laser parameters such as pump power or cavity detuning. In the previous sections, we have observed four phase transitions (symmetric $\leftrightarrow$ broken phase) at each of the four exceptional points crossed within one cycle in the phase space. In [195], it has been shown that the loop in the parameter space crossing an exceptional point is the limiting case of a dynamic encircling of an exceptional point. Furthermore, the presence of non-Hermiticity in the system prevents application of the adiabatic theorem and leads to non-adiabatic transitions [88]. This results in a chiral behaviour of the system as the final state depends solely on the direction of encircling [78, 98, 100, 190–196]. These observations have led to many fascinating phenomena. However, the complexity of the problem calls for a delicate and comprehensive analysis. Here, we employ a generalized framework for the analysis of the dynamical phenomena associated with crossing of exceptional points [88].

As proved in sections 3.3.3, 3.3.4, the velocity vector $d\vec{\psi}/d\tau$ can be expanded in the instantaneous eigenvectors corresponding to the two dominating eigenvalues with the largest real parts, Eq. (3.21). The corresponding amplitudes of the eigenvectors can be reconstructed from the velocity vector using the left instantaneous eigenvectors as $c_{1,2} = \vec{w}^T_{1,2}(\tau)d\vec{\psi}(\tau)/d\tau$. Due to the system being non-Hermitian, the left $\vec{w}$ and the right $\vec{v}$ instantaneous eigenvectors form a biorthogonal eigenbasis, i.e. $\vec{w}_i^T\vec{v}_j = \delta_{ij}$. Additionally, in order to ensure that the biorthogonal eigenbasis is uniquely defined for the given initial condition, an additional condition for the parallel transported eigenbasis is enforced, i.e. $\vec{w}^T_{1,2}(\tau)\vec{v}'_{1,2}(\tau) = 0$, where the prime denotes the derivative with respect to $\tau$ [212, 213]. Parallel transported eigenbasis allows to avoid evaluation of the geometric phase in the evolution of the amplitudes $c_{1,2}$ under the adiabatic prediction which can be expressed as [88, 213]:

$$c^{\mathrm{ad}}_{1,2}(\tau) = c_{1,2}(0)e^{\int_0^\tau \lambda_{1,2}(\tau')d\tau'} \tag{3.32}$$

In Fig. 3.9(a), (b) we compare the eigenvector populations $|c_{1,2}|^2$ with the adiabatic prediction $|c^{\mathrm{ad}}_{1,2}|^2$ in the case of the non-Hermitian dynamics in the self-pulsing stage. The model is initiated at the periodic orbit, just after the pulse has been released and the initial eigenvector populations are equal. Figure 3.9(a), (b) shows $|c_{1,2}|^2$ along the dynamic trajectory over the whole period and in the vicinity of the pulse, respectively.

In a non-Hermitian system, the adiabatic condition ensures adiabaticity only for the least dissipative eigenvector i.e. the one with the greatest $\mathrm{Re}\{\int_0^\tau \lambda_{1,2}(\tau')d\tau'\}$ [88]. The adiabatic condition is expressed as:

$$\epsilon_{1,2}(t) = \left| \frac{\mathcal{T}^{-1}\vec{w}^T_{1,2}(\tau)\vec{v}'_{2,1}(\tau)}{\lambda_{2,1}(\tau) - \lambda_{1,2}(\tau)} \right| << 1. \tag{3.33}$$

We note that normally this condition can always be satisfied for an appropriate time $\mathcal{T}$ which is the time taken to perform the loop in the parameter space. However, our case is different from the usual cases, as we do not have a control over $\mathcal{T}$. It is a fixed parameter determined by the periodic orbit. In the present case, the condition in Eq. (3.33) is found to be satisfied everywhere except of exactly at the exceptional points and in the middle of the cycle, i.e. between the pulses when $t \approx 0.22$ns in Fig. 3.9(a). Therefore, since we initiated the model when $|c_1|^2 = |c_2|^2$, the population $|c_{1,2}|^2$ will follow the corresponding adiabatically predicted $|c_{1,2}^{\mathrm{ad}}|^2$ when it is largest.

It is confirmed in Fig. 3.9(a),(b) that as long as $|c_2^{\mathrm{ad}}(\tau)|^2$ (dashed magenta) is largest, $|c_2(\tau)|^2$ (solid purple) follows the adiabatic prediction. It is $|c_1(\tau)|^2$ that exhibits a nonadiabatic jump ($\vec{v}_1 \rightarrow \vec{v}_2$) and $\vec{v}_1$ coalesces with $\vec{v}_2$ at the first exceptional point, $t \approx 0.22$ns. Then, the eigenvectors undergo a phase transition and form a complex conjugate pair. At the second exceptional point, the eigenvectors transition back to the two purely real eigenvectors again. Then, the populations $|c_{1,2}(\tau)|^2$ are no longer identical, and $|c_1(\tau)|^2$ transitions back to the populations following the adiabatic prediction. We note that in the simplified 2D model the pair of the exceptional points in the middle of the cycle is very closely spaced and only a dip in $|c_1(\tau)|^2$ is observed. The adiabatic condition is not satisfied at the exceptional points and hardly satisfied inbetween them. Therefore, in order to draw more conclusions regarding the first pair of exceptional points, one should investigate the full 5D system.

On the other hand, the adiabatic condition is satisfied beyond the pair of exceptional points at $t \approx 0.22$ns. In Fig. 3.9(a) it is found that when $|c_1^{ad}(\tau)|^2$ becomes the greatest, adiabaticity for $|c_2(\tau)|^2$ is no longer guaranteed, $t \approx 0.42$ns. It is found that $|c_2(\tau)|^2$ follows the adiabatic prediction $|c_2^{ad}(\tau)|^2$ up until 0.48ns. However, beyond 0.48ns, the discrepancy between $|c_2(\tau)|^2$ and the adiabatic prediction rapidly increases, and a sudden nonadiabatic transition ($\vec{v}_2 \rightarrow \vec{v}_1$) is observed. It is emphasized that the nonadiabatic transition has occurred just before the pulse has been released. Interestingly, in the second half of the period, before the pulse is released, the eigenvectors $\vec{v} = (\partial_\tau |a_-(\tau)|, \partial_\tau n_w(\tau))$ can be approximately expressed as $\vec{v}_1 \approx (1, 0)$ $\vec{v}_2 \approx (0, 1)$. Thus, it is not surprising that ($\vec{v}_2 \rightarrow \vec{v}_1$) before the pulse is released as $|a_-(\tau)|$ changes the most rapidly as the pulse is released. Then, the eigenvectors coalesce at the third exceptional point and form a complex conjugate (broken phase) pair beyond it. The populations $|c_{1,2}(\tau)|^2$ are identical within the broken phase and are found to approximately match the adiabatic prediction in the vicinity of the pulse. At $t \approx 0.52$ns, the eigenvectors coalesce at the $4^{\mathrm{th}}$ exceptional point and transition back to the two purely real eigenvectors beyond it. The populations $|c_{1,2}(\tau)|^2$ are no longer identical as the eigenvectors transition to the original scenario from the beginning of the cycle. The nonadiabatic transition observed here is a signature mark of the non-Hermitian dynamics. As also found here, the adiabatic theorem generally does not hold in non-Hermitian systems since even negligible nonadiabatic couplings between the eigenvectors can be amplified [88].

### 3.5.2 Relative nonadiabatic transition amplitudes

Here, we investigate the nonadiabaticity of the solution by considering the fundamental solution matrix $\mathbf{\Phi}(\tau)$, which contains the full dynamics of the system, Eq. (3.28). When the dynamics perfectly follow an adiabatic prediction, the instantaneous eigenvectors are completely decoupled ($\vec{w}_{1,2}^T(\tau)\vec{v}'_{2,1}(\tau) = 0$) [88]. In this case, $\mathbf{\Phi}(\tau)$ is a diagonal matrix [88]. However, even small coupling between the eigenvectors ($\vec{w}_{1,2}^T(\tau)\vec{v}'_{2,1}(\tau) \neq 0$) leads to significant off-diagonal entries in $\mathbf{\Phi}(\tau)$ through Eq. (3.27) and thus singularly perturbs the system [88]. Then, as we have shown above, the solution cannot be obtained from the adiabatic prediction [88].

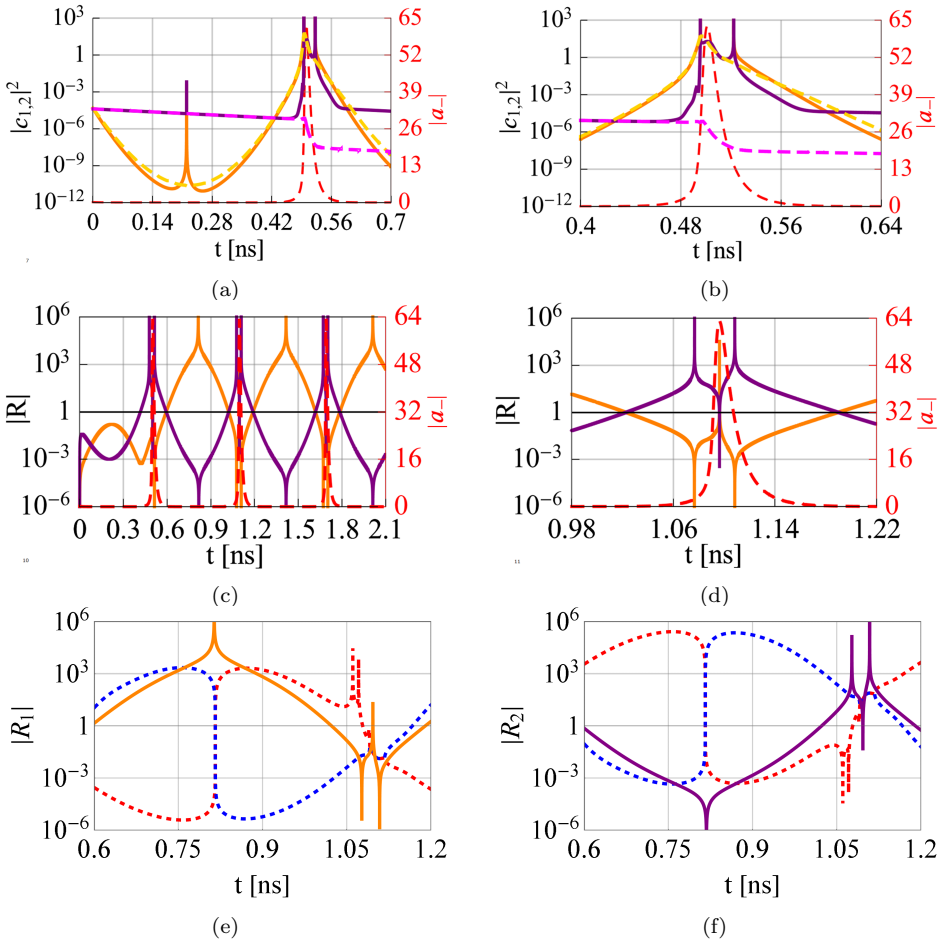


*Figure 3.9: The eigenvector populations $|c_1(\tau)|^2$ (orange, solid line) and $|c_2(\tau)|^2$ (purple, solid line) together with the corresponding adiabatic predictions, $|c_1^{ad}(\tau)|^2$ (yellow, dashed line) and $|c_2^{ad}(\tau)|^2$ (magenta, dashed line) over (a) the whole period and (b) close to the pulse. (c), (d) $|R_1(\tau)|$ (orange) and $|R_2(\tau)|$ (purple) over (c) the whole period and (d) close to the pulse. $|a_-(\tau)|$ (red, dashed line) marks the position of the pulse (scale on the right y-axis). In (e), (f) $|R_{1,2}(\tau)|$ are compared with the instantaneous fixed points of Eq. (3.35), stable and unstable fixed points are blue/red, respectively.*

In order to investigate the nonadiabatic character of the fundamental solution matrix $\mathbf{\Phi}(\tau)$, we compute the relative nonadiabatic transition amplitudes [88, 192]:

$$R_1(\tau) = \frac{\Phi_{21}(\tau)}{\Phi_{11}(\tau)}, \qquad R_2(\tau) = \frac{\Phi_{12}(\tau)}{\Phi_{22}(\tau)}, \tag{3.34}$$

which are shown in Fig. 3.9(b), (c), (d), (e). The transition amplitudes $R_{1,2}$ characterize the amount of nonadiabaticity in the solution and can be used to investigate dynamical phenomena associated with exceptional points [88]. For instance, the transition amplitude $R_1(\tau)$ measures the magnitude of the net nonadiabatic transition from $\vec{v_1}(\tau)$ to $\vec{v_2}(\tau)$, while $R_2(\tau)$ measures the transition from $\vec{v_2}(\tau)$ to $\vec{v_1}(\tau)$. If $R_{1,2}(\tau) << 1$ then it indicates that the corresponding amplitude of the eigenvector $c_{1,2}$ follows an adiabatic prediction. On the other hand, when $R_{1,2}(\tau) >> 1$ then the nonadiabatic transition took place. It can be shown that the transition amplitudes $R_{1,2}$ are the solutions of the Riccati equation [88]. In [88], the Riccati equation is presented for the simplified hypothetical case, here we have derived a general formula which is used in the following investigations:

$$R_1' = -A_{12}R_1^2 + (A_{22} - A_{11})R_1 + A_{21}, \tag{3.35a}$$

$$R_2' = -A_{21}R_2^2 + (A_{11} - A_{22})R_2 + A_{12}. \tag{3.35b}$$

The initial condition is $R_{1,2}(0) = 0$ and follows from the initial conditions for Eq. (3.27). The Riccati equations, Eq. (3.35), are first order differential equations which are quadratic in its unknown function. Therefore, it has two steady-state solutions (fixed points) ($R_{1,2}' = 0$) which can be found by searching for roots of Eqs. (3.35). These fixed points are shown in Fig. 3.9(e), (f) with dashed lines. The fixed point close to the origin of the complex plane ($R \approx 0$) corresponds to the adiabatic prediction, $R_{\mathrm{ad}}$, then nonadiabatic transition are not present. The fixed point away from the origin ($R >> 0$) corresponds to the nonadiabatic transition, $R^{\mathrm{nad}}$. Subsequently, we perform the stability analysis of the two equations in the vicinity of the fixed points. This is done by linearization of the quadratic equations by differentiating both equations and evaluating them at a fixed point. If the resulting value is negative, any perturbation from the fixed point decays exponentially towards the fixed point, the fixed point is stable. If the resulting value is positive, the solution will diverge away from the fixed point, which is, thus, unstable. The stability is found to be governed by the difference of the real parts of the instantaneous eigenvalues ($\lambda_1 - \lambda_2$), if positive, then $R_2^{\mathrm{ad}}$, $R_1^{\mathrm{nad}}$ are unstable, if negative, $R_2^{\mathrm{ad}}$, $R_1^{\mathrm{nad}}$ are stable. The stability of the fixed points is marked in Fig. 3.9(e),(f) with blue (stable) and red (unstable) colours.

We note that the stability of the two fixed points is neutral at each of the exceptional points as well as in the broken phase, i.e. when the eigenvalues form a complex conjugate pair. Furthermore, the stability of the fixed points swaps after each pair of the exceptional points. For instance, $R_2^{\mathrm{ad}}, R_1^{\mathrm{nad}}$ become unstable and $R_2^{\mathrm{nad}}, R_1^{\mathrm{ad}}$ become stable after the first pair of exceptional points ($t \approx 0.81$ns), see Fig. 3.9(e),(f). The fixed points $R_{1,2}^{\mathrm{ad}}$ and $R_{1,2}^{\mathrm{nad}}$ coalesce at the exceptional points. Interestingly, in the broken phase $R_1^{\mathrm{ad}}$, $R_1^{\mathrm{nad}}$ and $R_2^{\mathrm{ad}}$, $R_2^{\mathrm{nad}}$ form neutrally stable complex conjugate pairs amplitudes of which are smaller/larger (0.1/10) than 1, respectively.

It is found in Fig. 3.9(e),(f) that the solution $R_1$, $R_2$ (orange and purple, respectively) still follows $R_1^{\mathrm{nad}}$, $R_1^{\mathrm{ad}}$ after $t \approx 0.8$ns and does not immediately transition to $R_1^{\mathrm{ad}}$, $R_2^{\mathrm{nad}}$ when $R_1^{\mathrm{nad}}$, $R_2^{\mathrm{ad}}$ become unstable. Therefore, there is a certain delay time, between loss of stability and nonadiabatic transition, which is seen to be approximately equal to half of the period. Very similar behaviour has been observed in the simple, hypothetical model in [88], and here we observe it in the dynamic model of the self-pulsing Fano laser. After the certain delay time of the stability loss, the nonadiabatic transition occurs, and the stability of the fixed points become neutral. Then, we have $|R_1| << 1$ and $|R_2| >> 1$ which indicates that the nonadiabatic transition for ($\vec{v}_2$ has occurred ($\vec{v}_2 \to \vec{v}_1$). The solution passes through a degenerate bifurcation while the state is in the broken phase and the pulse is released. In this case, the fixed points are the center and are neither unstable, nor stable. After the last exceptional point in the cycle, $R_1$, $R_2$ follow stable $R_1^{\mathrm{nad}}$, $R_2^{\mathrm{ad}}$, which increase/decrease, respectively. It indicates that another transition has occurred ($\vec{v}_1 \to \vec{v}_2$) and the system has recovered its original state from the beginning of the cycle. The delay in the stability is known as the phenomenon of stability loss delay and arises due to degenerate Hopf bifurcation [88]. We note that there is some discrepancy between the solution $R_1$, $R_2$ and the instantaneous fixed points being followed (marked with the dashed lines), but it is still clearly seen when the nonadiabatic transition occurs.

It is noted that $R_1$, $R_2$ in the first cycle differ considerably from the transition amplitudes observed later on. This is because of the high sensitivity to the initial condition $R_{1,2}(0) = 0$, which is far from $R^{\mathrm{ad}}(0)$ [88]. However, after a single cycle, the system approaches the unique relaxation oscillation found in Fig. 3.9(c).

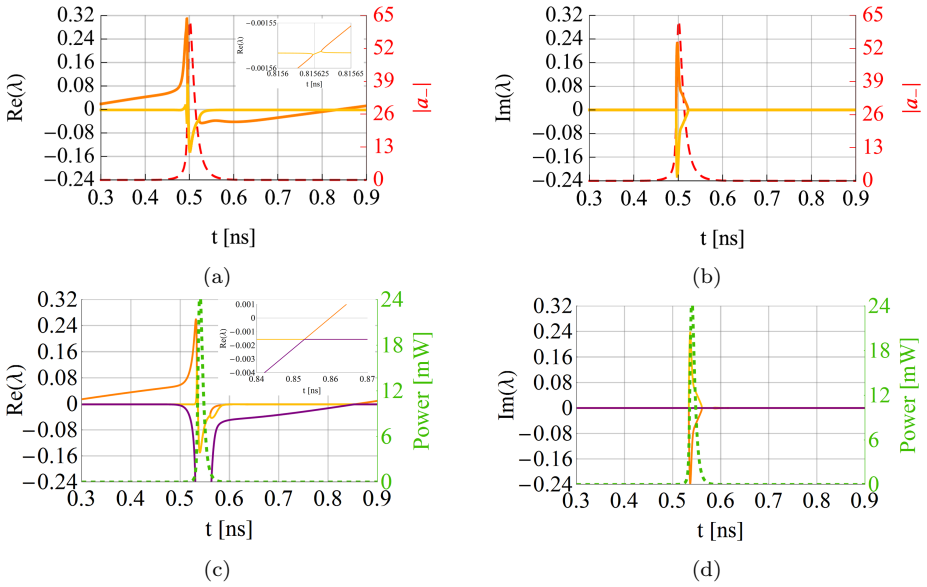


*Figure 3.10: (a), (c) Real and (b), (d) imaginary parts of the eigenvalues of the 2D and 5D systems over one period, respectively. (a),(b)$|a_-(\tau)|$ (red, dashed line) and (c),(d) power in the straight-port (green, dashed line) mark the position of the pulse (scale on the right y-axis). Insets in (a),(c) show real parts of the eigenvalues close to the crossing in the middle of the cycle.*

We finish this section with a comment on the nonadiabatic behaviour in the vicinity of the pair of the exceptional points inbetween the pulses. In Fig. 3.10, we show the instantaneous eigenvalues of (a), (b) the simplified 2D system and (c), (d) the full 5D system. Generally, it is found that the pair of the dominating eigenvalues with the largest real part is recovered in the 2D system. However, away from the pulse, the second eigenvalue differs from the second largest eigenvalue of the full system. It is found to inherit some of the features of the eigenvalue with the third largest real part (purple) of the full system. Particularly, in Fig. 3.10(a) the difference between the real parts of the top two eigenvalues is much larger after the broken phase than in Fig. 3.10(c). Furthermore, in Fig. 3.10(a), (b) the second pair of the exceptional points does not appear shortly after the first one, but it is found in the middle of the cycle where the first and the third largest eigenvalues interact in the full system, see Fig. 3.10(c). Finally, the time-spacing between the second pair of the exceptional points is extremely small, see inset in Fig. 3.10(a). The adiabatic condition is not satisfied in the vicinity of this crossing. Thus, the analysis presented above cannot be used to explain the nonadiabatic character of $\vec{v}_1$ in the middle of the cycle, i.e. inbetween the pulses. The analysis of the 5D system is needed to explain this behaviour. However, the analysis presented above is applicable over the remaining part of the cycle.

Therefore, we have demonstrated that the intervals of the solution following the adiabatic prediction are interrupted by abrupt nonadiabatic transitions at the periodic orbit. These transitions have been observed just before/after the pulse is released. We have described the nonadiabatic character of the non-Hermitian dynamics in terms of the relative nonadiabatic transition amplitudes. We have derived a general Riccati equations governing the dynamics of the transition amplitudes. Furthermore, we analysed the stability of the Riccati equations and found that it is governed by the difference of the instantaneous eigenvalues. We have also shown that the stability loss of the transition amplitudes is delayed. To the best of author's knowledge, this is the first time when the nonadiabatic phenomena are observed in the complex Fano laser system in which the exceptional points are crossed due to the self-modifying behaviour, without any need for an external parameter variation.

## 3.6 Summary

The first section 3.1 of the current chapter has introduced the subject as well as unveiled our intentions and investigations that are going to be conducted. Subsequently, section 3.2 has introduced the dynamic model of the Fano laser, described its derivation and presented it in the dimensionless form with the complex field envelopes $A_{-/+}(t)$ being separated into its magnitudes $|A_{-/+}(t)|$ and phase difference $\Delta\Phi(t) = \Phi_-(t) - \Phi_-(t)$.

Afterwards, section 3.3 have investigated the steady-state and the instantaneous eigenvalues of the linearized dynamic model. It has been demonstrated and proved that the laser dynamics are confined to a 2D phase space picture after the initial transition stage which lasts only a few picoseconds. The pulse has been found to be bounded by two exceptional points with positive/negative real parts before/after the pulse, respectively. Four exceptional points are crossed within a single loop in the phase space ensuring that eigenvectors and eigenvalues are periodic. Furthermore, we have shown that after the initial transition stage the original 5D model can be reduced to only 1D in the region of the parameter space (in our case, $J = 1.2J_{\text{thr}}$, $-2.05\gamma_T < \Delta\omega_c < -1.72\gamma_T$). The system evolves into 2D at the exceptional point (in our case, $J = 1.2J_{\text{thr}}$, $\Delta\omega_c = -1.72\gamma_T$).

In section 3.4, we have used the reduced 2D model to associate the unknown source of laser stability with the new unstable periodic orbit, which separates stable steady-state point from the stable periodic orbit. We have classified the bifurcation standing behind the two orbits and an equilibrium point (steady-state) as a Bautin bifurcation. We have found that upon an external parameter variation, $\Delta\omega_c$, the two orbits may annihilate or the stability of the steady-state may exchange; it is a signature of Bautin bifurcation.

Finally, in section 3.5, using the general framework of [88], we have identified that the intervals of the solution following the adiabatic prediction are interrupted by abrupt nonadiabatic transitions at the periodic orbit. We have derived a general Riccati equations governing the dynamics of the nonadiabatic transition amplitudes and analysed their stability. We have also shown that the stability loss of the transition amplitudes is delayed and happens just before the pulse is released. To the best of author's knowledge, this is the first time when the nonadiabatic phenomena are observed in the complex Fano laser system in which the exceptional points are crossed due to the self-modifying behaviour without any need for external parameter variation.

# Chapter 4

# Conclusion

In this study, we investigate novel phenomena such as BICs, Dirac cones and exceptional points in PhC-based lasers. The work consists of two parts: 1) examination of the relation between BICs and exceptional points in PhC slabs which led to the design of small, high Q-factor PhC resonators; 2) reduction of the 5D dynamic model of the PhC Fano laser and eigenanalysis of its stability and non-Hermitian dynamics.

Chapter 2 investigates phenomena such as bound states in the continuum, Dirac cones and exceptional points with the aim of further improvement of PhC-based lasers. The first three sections 2.1, 2.2 and 2.3 introduced these phenomena based on the recent literature and in the context of PhCs. We began with a brief introduction of the basics concepts in PhCs and discuss the models of the PhC slab used in the study. Furthermore, we discussed the concept of BICs which offer a perfect confinement of light despite being inside the continuous spectrum of radiating modes. Subsequently, we reviewed the literature on Dirac-like cone dispersion in PhCs using our own examples and explained some of the advantages of the Dirac-like dispersion, e.g. slowly decreasing mode spacing with an in-plane size of the PhC compared to the quadratic dispersion and lack of field localization effects due to large and constant in-plane group velocity. We have also discussed recently demonstrated phenomenon of rings of exceptional points being spawned out of a Dirac-like dispersion. This phenomenon arises due to presence of losses in the structure and provides very strong dispersion in the vicinity of the center of the BZ.

In section 2.4, we have exploited the knowledge from the previous sections and we examined the relation between BICs and extent of the ring of exceptional points in PhC slabs with circular as well as elliptical air-holes. Particularly, we demonstrated that by varying thickness of the PhC slab, we can move trapped BICs close to the $\Gamma$-point, and thus decrease difference in losses between a symmetry-protected BIC and the coupled dipole-like mode at the $\Gamma$-point. In this way, we were able to control the extent of the ring of exceptional points in the BZ. We have shown that for a specific thickness, the extent of the ring can be reduced almost to a point. Then, large Q-factor values are found over the broad region of the BZ. These results were used in section 2.5 in the design of large Q-factor, small footprint PhC slabs that potentially could serve as a resonating cavity for a PCSEL. The designed 3D configurations have exhibited the total Q-factors which have been rapidly increasing with an in-plane size of the PhC slab compared to the standard 250nm-thick structures. Particularly, the designed PhC

slabs with an in-plane dimensions as small as 12-by-12 lattice constants squared have been found to exhibit the total Q-factors of 3900. In appendix A, we have proposed possible improvements that can enhance the Q-factor further, e.g. tapering of the outer rows of the PhCs or constructing larger PhC-like structures from single large Q-factor unit cells. Moreover, we have shown that utilization of elliptical air-holes breaks degeneracy of the two dipole-like modes at Γ-point. It introduces frequency separation between the two large Q-factor bands in the optimized configurations and reduces cross coupling between them in the finite 3D structures. It allows to separately optimize the structure for the flat quadratic band or the Dirac cone and results in the configuration with a large Q-factor mode having an uniform field profile without field localization effects. Furthermore, the dispersion of the PhC with elliptical air-holes is found to be radically different along the Γ-X (very large curvature) and Γ-X′ (very small curvature) directions and is shown to be significantly altered by a sheer rotation of the air-hole. This may allow to easily control band curvature along specific directions and thus control mode spacing in finite size structures. Finally, section 2.6 introduced configuration of the Fano laser. It has demonstrated that by introduction of the second side-coupled nanocavity, we can significantly increase accessible Q-factor values of the 3D PhC Fano structure and thus reduce the spectral linewidth of the Fano resonance.

Chapter 3 investigates dynamic model of the PhC Fano laser. We began with a brief introduction of the subject as we unveiled our intentions, challenges and ideas motivating the investigation. In section 3.2, we introduced the dynamic model of the Fano laser which is known from the literature [172]. We described its derivation and presented it in the dimensionless form with the complex field envelopes separated into its magnitudes and the phase difference in order to ensure numerical stability. Subsequently, in section 3.3.1 we review the current knowledge on the stability of the laser. It has been shown to operate in two regimes, the continuous wave operation (stable) and the self-pulsing operation (unstable) [83, 172]. The self-pulsing operation has been demonstrated to occur when the real part of the pair of complex conjugate eigenvalues evaluated at the steady-state becomes positive [172]. This is a Hopf bifurcation. However, it has been observed that there exists a region in a parameter space in which the laser may become unstable if perturbed strongly enough despite all steady-state eigenvalues having negative real parts and thus suggesting stable operation. This has not been explained thus far.

In order to tackle this, we analyze the steady-state and instantaneous eigenvalues of the Jacobian matrix of the dynamic model. We found that the laser operation can be characterized by three stages: initial transition stage, later transition stage and the self pulsing or continuous wave stage. This is in contrast to the previously reported picture of the two stages: later transition stage and the self pulsing or continuous wave stage. We observed that the laser dynamics are confined to the curved surface after the initial transition stage, which lasts only a few picoseconds. During this short transient, the contribution from the three instantaneous eigenvectors corresponding to the three eigenvalues with the smallest negative real parts is found to decay rapidly. Therefore, we concluded that after the initial transient, the state vector can be expressed solely by two degrees of freedom and is confined to the 2D phase space in the latter transition stage as well as in the self-pulsing or continuous wave stage.

Subsequently, we demonstrated that after the initial transition stage, the original 5D model can be reduced to only 1D in the limited region of the parameter space (in our case, $J = 1.2J_{\mathrm{thr}}$, $-2.05\gamma_T < \Delta\omega_c < -1.72\gamma_T$), when the steady-state eigenvalues are purely real and that the system evolves into 2D beyond the exceptional point (in our case, $J = 1.2J_{\mathrm{thr}}$, $\Delta\omega_c = -1.72\gamma_T$), when the eigenvalues form a complex conjugate pair. Using the simplified 2D model, we have detected the orbit which

has not be found before. We have assessed stability of the orbits using Floquet multipliers. We have classified the bifurcation standing behind the two orbits and an equilibrium point (steady-state) as a Bautin bifurcation. We have found that upon an external parameter variation, $\Delta\omega_c$, the two orbits may annihilate or the stability of the steady-state may exchange; it is a signature of Bautin bifurcation. The new unstable orbit separates the stable steady-state from the stable orbit. If the model is initiated outside/inside the inner unstable orbit, the state is repelled from the unstable orbit and is attracted towards the stable orbit or the stable steady-state. Therefore, we explained the unknown origin of the laser instability when all steady-state eigenvalues have negative real parts. Furthermore, it has been found that, as the pulse power increases, the dominating pair of instantaneous eigenvalues transitions from two purely real eigenvalues to a complex conjugate pair beyond the exceptional point. The pulse is bounded by two exceptional points with positive/negative real parts before/after the pulse, respectively. In total, four exceptional points are found to be crossed within a single loop in the phase space. The number of exceptional points is enforced by the periodicity of the system ensuring that eigenvectors and eigenvalues are recovering their original state after the full cycle.

Finally, the simplified model has been used to investigate the non-Hermitian dynamics. Using the general framework of [88], we have demonstrated that the intervals of the solution following the adiabatic prediction are interrupted by abrupt nonadiabatic transitions when the state is at the periodic orbit. These transitions have been observed in close vicinity of the pulse. We have described the nonadiabatic character of the non-Hermitian dynamics in terms of the relative nonadiabatic transition amplitudes. We have derived a general Riccati equations governing the dynamics of the transition amplitudes. Furthermore, we analysed the stability of the Riccati equations and found that it is governed by the difference of the instantaneous eigenvalues of the simplified model. We have also shown that the stability loss of the transition amplitudes is delayed. To the best of author's knowledge, this is the first time when the nonadiabatic phenomena are observed in the complex Fano laser system in which the exceptional points are crossed due to the self-modifying behaviour, without any need for an external parameter variation.

The work presented in this thesis can be extended in several ways which can be divided in two parts. The first part concerns the investigations in chapter 2. Here, the most important next step is to fabricate the structures designed in section 2.5 and investigate how small the PhC slab could become and still lase. Subsequently, a toy-model based on the coupled-mode theory could be developed to better understand origin of the generalized Fano lineshapes mentioned at the end of section 2.6. Furthermore, the Fano configuration with two side-coupled nanocavities could be modified to include two nanocavities with different Q-factors, but identical resonating frequencies. This could enable access to new phenomena such as EIT. The concept of parity-time symmetry could also be investigated by pumping only one of the two coupled active nanocavities and thus maintaining balance between gain and loss in the system. The second part concerns the investigations in chapter 3. Here, the most urging work is to introduce a time dependent modulation of the nanocavity detuning, $\Delta\omega_c$, and investigate how it influences the initial transition stage, whether the system dimension increases, whether the laser becomes chaotic and how the non-Hermitian dynamics behave in this case. This is a simple extension of an already developed procedure that could be very fruitful and experimentally verifiable. In the present model, the non-Hermitian dynamics and the Floquet multipliers should be also investigated with the full 5D system and compared with the current results. Finally, it might be possible to encircle the contour of exceptional points, which was observed in the band structure of the model, in the third dimension by proper modulation of the laser.

# Appendices

# Appendix A

# Photonic crystal slabs - quality factor optimization

In chapter 2, it has been shown that variation of the PhC slab thickness can move the trapped BICs towards the Γ-point. This can lead to reduced difference in losses between the dipole-like mode and the quadrupole-like mode, which is a symmetry-protected BIC, and thus significantly reduce the extent of the ring of exceptional points. This has led to the design of the large Q-factor, small footprint 3D PhC slabs in section 2.5. In this appendix, we discuss possible improvements that can be implemented in the PhC slabs to increase the Q-factor further. In section A.1, we modify the air-holes radius in outer rows of the PhC in order to improve confinement of light in the slab. In section A.2, we aim to design large Q-factor small footprint slabs by starting with single unit cells and then combining them in larger structures.

## A.1 Tapered PhC slabs

One way to improve the confinement of light in PhC-based cavities is to use photonic heterostructures [166, 167, 214–217]. They can be obtained by tuning parameters of the PhC slab in order to introduce spatial variation of the photonic dispersion. Even small variation of PhC parameters can result in significant enhancement of the light confinement. However, very often this small variation implies larger sizes required to accommodate for an additional heterostructures. Here, we aim to design large Q-factor PhC slabs of small footprint and thus are not willing to introduce large heterostructures confining the mode inside the original PhC-based resonator. Therefore, we will taper only one or at most two outer rows of the PhC slab. This is done by a small variation of the air-hole radius or the lattice constant.

In the following, we focus on the 3D structures with in-plane size $8a \times 8a$ as they can be simulated within a reasonable amount of time. Out of the three investigated structures, several competing modes with large Q-factor values have been exhibited only by the PhC slab with elliptical air-holes which was optimized to reduce distance between the contours of exceptional points. The field profiles of these competing modes are shown in Fig. A.1, while the largest Q-factor mode has been shown in Fig. 2.26(b). The field profile in Fig. A.1(a) originates from the isolated flat band (black), its Q-factor is 1000. The field profile in Fig. A.1(b) originates from the upper conical band(blue) and its Q-factor is 1075. It is strongly localized and thus occurs

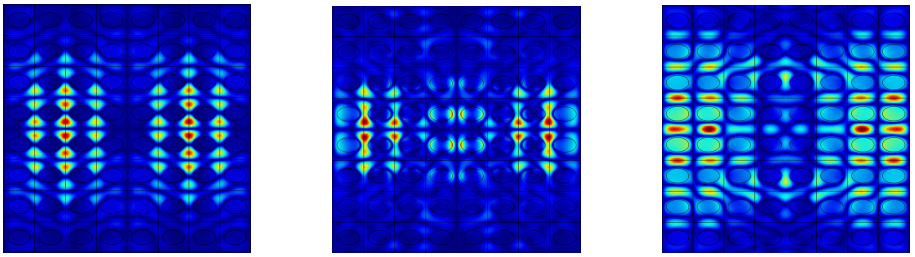

(a) (b) (c)

*Figure A.1: Field profiles of the competing modes with the largest Q-factor mode in the vicinity of the exceptional point for the 3D PhC slab of in-plane dimensions* $8a \times 8a$*. Magnitudes of* $H_z$ *are plotted for the PhC slab with elliptical air-holes optimized to reduce distance between contours of exceptional points* ($a = 730nm, h = 711.3nm, r_0 = 0.292a$).

thanks to a very low curvature of the band along the Γ-X′ direction. The field profile in Fig. A.1(c) resembles the largest Q-factor mode in Fig. 2.26(b) and its Q-factor is 930. Most likely, it has arisen due to mixture of modes along the Γ-X′ direction as the frequency spacing between these modes is very small along this direction.

We find that the largest total Q-factor can be enhanced from 1050 to slightly more than 2200 when the radius of the air-holes in the most outer row of the PhC slab is increased by 6%. Interestingly, it does not exhibit the same field profile as the largest Q-factor mode in the unmodified configuration, in that case the Q-factor has decreased from 1100 to 1000. We find that the largest Q-factor mode in the modified configuration is the one shown in Fig. A.1(b). Before the structure has been tapered this mode has exhibited low-in-plane losses due to low group velocity of the band along the Γ-X′ direction. Thus, its Q-factor enhancement is attributed to the improved matching of the $k$-space mode profile with the Q-factor dispersion. All the other competing modes are hardly affected by the modification of the radius and their Q-factors have dropped approximately by 100. Therefore, by a mere change of radius by 6%, the total Q-factor of the slab can be more than doubled.

Furthermore, in the case of the largest Q-factor mode in the unmodified configuration, the main loss is along the $x$ direction due to very uniform mode distribution along this direction. The uniform mode distribution arises as a result of relatively high and linear group velocity. Therefore, radius of the outer air-holes can be modified only along edges perpendicular to the major-axis of the elliptical air-holes, $a_0$, to increase the Q-factor. Particularly, when radius of the outer air-holes is increased by 5%, the Q-factor of the uniform mode, Fig. 2.26(b), is increased from 1100 to 1300. This is attributed to the low group velocity of the introduced heterostructure at the frequency of the uniform mode. On the other hand, if the radius of the outer air-holes is modified along all edges of the PhC, then in the best case scenario, the Q-factor is not enhanced. This is attributed to the worsened $k$-space matching along the Γ-X′ direction as the unmodified structure has already been optimized for it and any changes will deteriorate it.

We note that when radius of the outer air-holes is increased by 5% only along the edges perpendicular to $a_0$, then the Q-factor of the competing mode in Fig. A.1(b) is enhanced from 1050 to 1700. The large change in the Q-factor is attributed to the flat band being close to be $k$-space matched with the Q-factor dispersion and a small change leads to a substantial improvement of the total Q-factor. The Q-factor optimization of 3D structures is always tailored to a specific mode. Some of the modes may require more complex tapering of the slab than only a modification of the outer row. This becomes increasingly complex problem and difficult to simulate.

In section 2.4, we have shown that for the optimized thickness, the extent of the ring exceptional points can be reduced almost to zero. In this case, the photonic

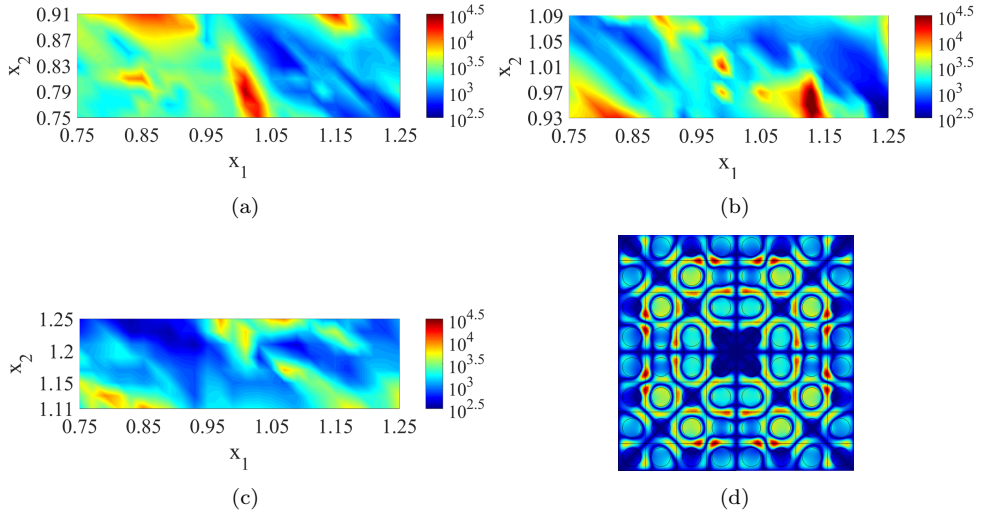


*Figure A.2: (a)-(c) The largest Q-factors in the vicinity of the Dirac-like dispersion plotted vs. scaling factors $x_1$, $x_2$. The in-plane dimensions of the PhC are $8a \times 8a$. The PhC ($\epsilon_r = 10.05$) is composed of a square lattice ($a = 780nm$) of circular air-holes, radius of which is adjusted in order to ensure an accidental degeneracy at the Γ-point. (d) The field profile of the mode in Fig. 2.26(a) after application of tapering according to the results in (a)-(c).*

band structure, Fig. 2.16, resembles the band structure of the 2D unit cell, Fig. 2.7. Moreover, the radius of the air-hole, which is required to ensure an accidental degeneracy at the Γ-point, is identical in both cases. Therefore, one may infer that an optimized PhC slab (non-Hermitian system) approximately behaves as a 2D PhC (Hermitian system) for a specific set of parameters. In the following, we aim to take an advantage of this fact. We consider the 2D PhCs with circular air-holes and modify lattice constants of the two outer rows as $a_1 = x_1 a$, $a_2 = x_2 a$, where $x_1$, $x_2$ are the scalings. Then these results are directly translated into 3D optimized PhC slab. In Fig. A.2, we show the largest Q-factors in the frequency range of the Dirac-like dispersion for a 2D PhC, which is finite in the $x$ and $y$ directions and infinite in the $z$ direction. In Fig. A.2, each large Q-factor region corresponds to a specific mode with an enhanced Q-factor.

Subsequently, we search in Fig. A.2 for the mode with an enhanced Q-factor, field profile of which resembles the largest Q-factor mode in the unmodified configuration, Fig. 2.26(a). Then, we apply the corresponding scalings $x_1$, $x_2$ to the lattice constants in the two outer rows of the PhC. The optimal scaling were found to be $x_2 = 1.1275, x_1 = 0.96$ and the field profile of the mode in the 2D PhC is shown in Fig. A.2(d). It is seen to closely resemble the field profile of the largest Q-factor mode in the unmodified configuration shown in Fig. 2.26(a). The Q-factor has increased from 1100 to 1400. It is a considerable improvement, however not as significant as 2D PhC simulations have indicated. Even though the PhC slab has been optimized to approximately behave as a 2D PhC, the additional manipulation of the lattice constants in the two outer rows disrupts this approximation as it changes the effective refractive index in these rows. Therefore, it would require an additional manipulation of the slab thickness in order to compensate for it. This would make fabrication of the structure nearly impossible. Despite this, a considerable improvement in the Q-factor has been observed when the two outer rows are modified, while almost no Q-factor enhancement, from 1100 to 1150, is observed when only a single row is modified in the 3D slab. Design of the configuration with the two outer rows modified would not be possible to optimize with the 3D model due to too many degrees of freedom.

## A.2 Individual unit cells

Thus far, the approach has been to optimize periodic PhC slabs for the largest out-of-plane Q-factors and lowest group velocities. Then, the finite structures sampled dispersion relation in a finite neighborhood of $k$-space, and the Fourier transformed mode profiles can be optimized to match the maxima of the Q-factor dispersion. In short, the procedure was to from optimization of infinite structures to large Q-factor small-size 3D configurations. However, one may take another perspective on the problem. We can interpret large Q-factors of PhC slabs as arising from individual unit cell resonances. Consequently, large Q-factor 3D PhC slabs derive their properties from high Q-factor unit cell resonances. This approach has been used in [80] to design small size high Q-factor high-contrast gratings which are 1D PhC slabs of bars. In the following, we aim to extend it into 2D periodic PhC slabs with circular air-holes under the TE-like polarization.

The smaller the configuration becomes, the more critical the in-plane losses are. Thus, to design truly small configurations it is crucial to ensure flat dispersion. Typically, the Q-factor of a single unit cell ranges from 1 to 10 [218, 219]. When the higher order modes of a single unit cell are considered, the Q-factors can reach even few hundreds. It is caused by extremely flat dispersion curvature in the vicinity of the Γ-point for these modes [80, 219].

In the pervious sections, we have found that the corresponding modes have considerably larger Q-factors in the optimized thickness case, 711.3nm, than in the case of the standard thickness, 250nm. Moreover, it has been observed that the mode profiles of a single unit cell are identical to the mode profiles exhibited by a PhC composed of these unit cell. In the following, we consider a single unit cell of the PhC slab with finite thickness $h = 711.3$nm and a circular air-holes $r = 0.3136a$. We use an eigenfrequency solver to compute modes of the system up to 280THz. When the single unit cell slab is 250nm-thick, there are no modes with Q-factors larger than 20 and most of them are below 10. When the thickness is $h = 711.3$nm, several modes with Q-factor larger than 40 are found, and there is even a single mode with much larger Q-factor than the other modes, 200. This mode is shown in Fig. A.3(a). It is found that it is a higher order mode not only in the plane but also in the $z$ direction; it occurs at 260THz.

Subsequently, we combine two of the large Q-factor unit cells shown in Fig. A.3(a). The distance between the unit cells is varied to optimize the matching of the $k$-space mode profile. When the distance is $0.096a$, the largest Q-factor is found and is around 750, Fig. A.3(b). It occurs at 268.8THz. Afterwards, we expand the configuration to a $2a \times 2a$ structure which starts to resemble a PhC slab. Also in this case, the distance

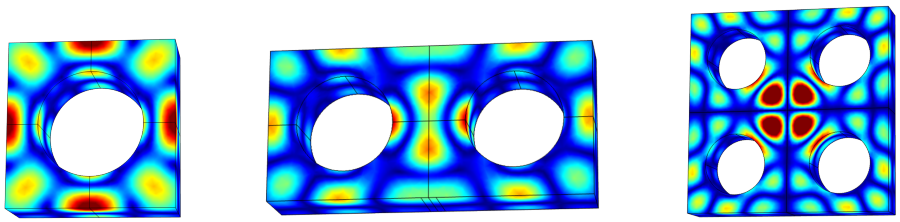

(a) (b) (c)

*Figure A.3: Field profiles of the large Q-factor high order modes for (a) a single unit cell, (b) two unit cells with an optimized distance, (c) two-by-two configuration of unit cells with an optimized spacing. Magnitudes of $H_z$ are plotted for the unit cells with circular air-holes ($a = 780nm, h = 711.3nm, r_0 = 0.3136a$). Half of unit cell thickness is seen since perfect magnetic conductor boundary condition is placed in the middle to enforce the TE-polarization, thus $H_z$ is the strongest in the middle of the unit cell thickness.*

between the unit cells is optimized. The largest Q-factor is found for an equal spacing along the $x$ and $y$ directions and equal to $0.096a$; the same as in the configuration with two unit cells. The Q-factor value is 1500 and the mode occurs at 295.5THz. This is an already large Q-factor value since in section 2.5 the structures with comparable Q-factors required dimensions of at least $8a \times 8a$. However, the frequency of the mode is significantly higher than the desired telecommunication frequency 193THz. This can be resolved by scaling dimensions of the structure resulting in a lattice constant $a = 1193.4nm$ and thickness $h = 1088.3nm$. Even then the total volume of the structure in Fig. A.3(c) is 4.5 times smaller than in the case of the $8a \times 8a$ PhC slab considered in section 2.4. Therefore, a considerable improvement in the overall Q-factor is found when the structure is designed starting from an individual unit cell and then combining them in a PhC-like structure. However, this process becomes increasingly difficult and computationally demanding as size of the configuration increases. Next step would be to optimize spacing in the structure with dimensions of $4a \times 4a$, however this process would have to be supported by an automatization scheme in order to become efficient. We could not reach Q-factors higher than 1100 in this case despite larger size of the structure than in Fig. A.3(c).

Moreover, the $2a \times 2a$ structure considered above is $h = 1088.3nm$ thick at the desired frequency. According to the author's knowledge, the thickness of $h = 711.3nm$ is already on the edge of being possible to be fabricated. As a slab becomes even thicker, there might be considerable difficulties in drilling air-holes through the slab. This might lead to asymmetric vertical profiles of the air-holes. It would break vertical symmetry of the slab and would not allow for presence of BICs significantly reducing out-of-plane Q-factors. Thus, it is discussable whether this design approach could be transferred from high-contrast gratings towards 2D PhC slabs due to considerable issues with fabrication. Therefore, it might appear necessary to stick to a design procedure introduced in Chapter 2.

# Appendix B

# Verification of the two-dimensional picture

## B.1 Required order of a polynomial

In section 3.3.2, we have shown that after the initial transition stage the laser dynamics are confined to the curved surface which can be approximated by polynomial function of the variables $n_w$ and $|a_-|$. In this section we briefly discuss the chosen order of the polynomial approximation.

The order of the polynomial approximating the surface is chosen empirically, high enough to closely approximate the surface, but not too high to avoid ripples on the surface. The orders of the polynomials used in the report are: $|a_+(|a_-|, n_w)|$ is approximated by a $6^{\text{th}}$ order polynomial, $\Delta\phi(|a_-|, n_w)$ is approximated by $5^{\text{th}}$ order polynomial, while $n_c(|a_-|, n_w)$ is approximated by a $12^{\text{th}}$ order polynomial. $n_c$ is the most difficult to approximate due to its large curvature.

Additionally, we apply some manipulations to the data coming from the solution of the full 5D system, Eq. (3.12), for varying initial conditions before fitting the polynomial in the case of $n_c$ surface. In order to make it easier for the polynomial to properly approximate the data, we flatten it by applying an ArcTanh function to the data. Subsequently, the $12^{\text{th}}$ order polynomial is fitted to approximate the flattened data and then $n_c(|a_-|, n_w)$ is transformed back by applying a Tanh function.

We note that even in the case of low polynomial orders such as $1^{\text{st}}$, $1^{\text{st}}$, $2^{\text{nd}}$ for the surfaces $|a_+(|a_-|, n_w)|$, $\Delta\phi(|a_-|, n_w)$, $n_c(|a_-|, n_w)$, respectively, the dynamics are well approximated as shown in Fig.B.1(a), (b), (c). The blue curve shows the solution of the original system of five differential equations, while the red curve shows the approximated variables $|a_+|$, $\Delta\phi$, $n_c$. The approximated variables are found to very closely follow the original solution and the fit becomes almost perfect when the orders are $2^{\text{nd}}$, $2^{\text{nd}}$, $4^{\text{th}}$, respectively, see Fig. B.1(d), (e), (f).

However, we emphasize that even small discrepancy between the approximated variables and the true solution is amplified once the polynomials 1) recover the full position vector $\vec{\psi}$, Eq. (3.17), which is subsequently fed to the stability matrix $\boldsymbol{A}$ to compute the approximated eigenvalues or 2) are fed to the 2D simplified model which is subsequently used to recover the laser dynamics. These discrepancies are discussed in the following section.

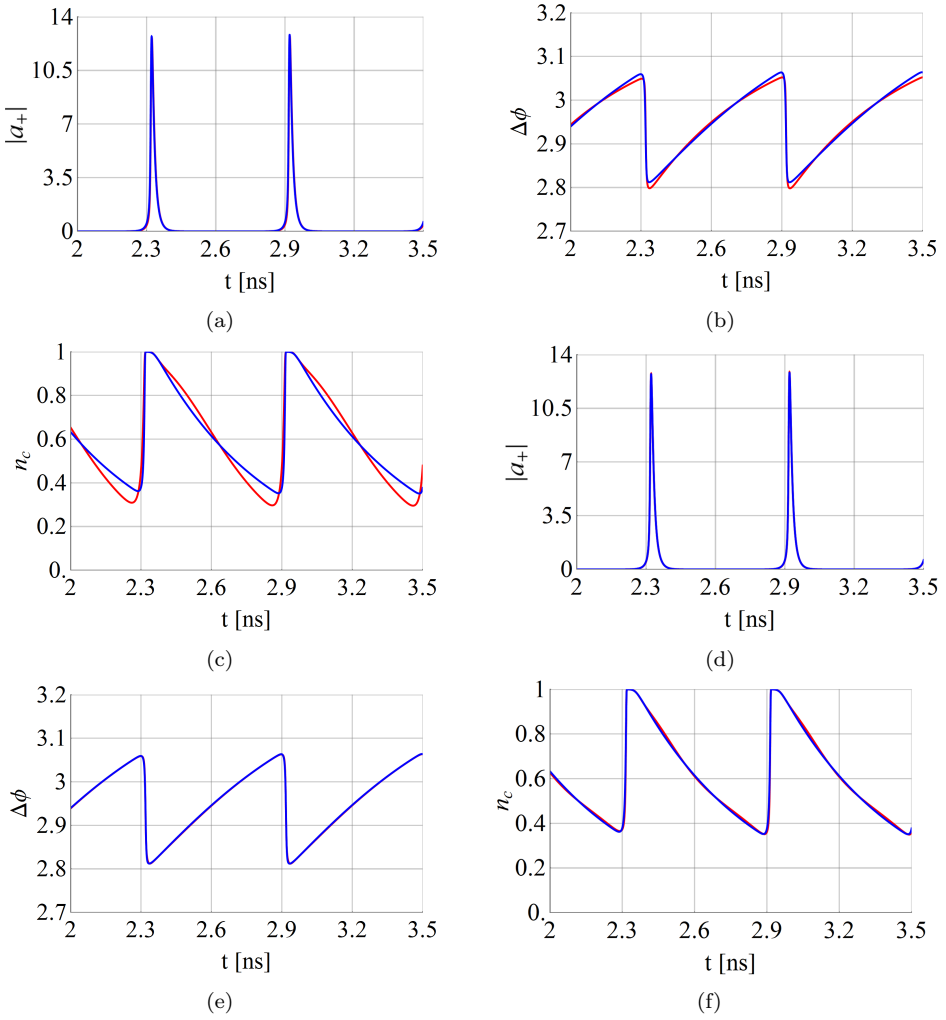


*Figure B.1: $n_c$, $|a_+|$ and $\Delta\phi$ in time-domain. Blue curve represents results coming directly from the 5D system, while red curve represents the approximated variables. (a), (b), (c) the polynomials orders are $1^{st}$, $1^{st}$, $2^{nd}$, while in (d), (e), (f) the polynomials orders are $2^{nd}$, $2^{nd}$, $4^{th}$ for the surfaces $|a_+(|a_-|, n_w)|$, $\Delta\phi(|a_-|, n_w)$, $n_c(|a_-|, n_w)$, respectively.*

We also note that in the similar way we can approximate the velocity surfaces, Eq. (3.18). Both methods give similar results depending on the accuracy of the polynomial approximation. This has been done during the investigation in section 3.3.4. Then, the eigenvectors approximating the tangential vectors to the velocity surfaces along the coordinate lines $n_w$ and $|a_-|$ can be obtained using:

$$\begin{bmatrix} \vec{v}'_1 \\ \vec{v}'_2 \end{bmatrix} = \begin{bmatrix} v_{12} & v_{14} \\ v_{22} & v_{24} \end{bmatrix}^{-1} \begin{bmatrix} v_{12} & v_{14} & \lambda_1 v_{11} & \lambda_1 v_{12} & \lambda_1 v_{13} & \lambda_1 v_{14} & \lambda_1 v_{15} \\ v_{22} & v_{24} & \lambda_2 v_{21} & \lambda_2 v_{22} & \lambda_2 v_{23} & \lambda_2 v_{24} & \lambda_2 v_{25} \end{bmatrix} \tag{B.1}$$

where ($\lambda_1$ and $\lambda_2$) are the two eigenvalues with largest real part and ($\vec{v_1}$ and $\vec{v_2}$) are the corresponding eigenvectors obtained for each position on the surface. The procedure is identical as in section 3.3.4 with the exception that the derivative of the velocity vector is in fact computed by taking a product of the $\boldsymbol{A}$ with the velocity vector $d\vec{\psi}/d\tau$ and can be expanded in the linear combination of the eigenvectors scaled by the corresponding eigenvalues, Eq. (3.21).

## B.2 Reconstruction of the surfaces - Line integral of the eigenvectors

In section 3.3.4, we have shown that the two eigenvectors corresponding to the two eigenvalues with the largest real parts approximate the tangential vectors to the surface along the coordinate lines, Fig. 3.5. Here, we consider different reconstruction schemes of the solution and compare it with the original 5D system of equations. We recall that we have considered a general surface $z = f(x, y)$ with the parametric curve on this surface having a vector equation $r(t) = \{x(t), y(t), z(t)\}$. The tangential vector to the surface along this curve is known to be:

$$r'(t) = \{x'(t), y'(t), z'(t)\}, \tag{B.2}$$

where

$$z'(t) = \nabla f \cdot \vec{u}, \qquad \vec{u} = \{x'(t), y'(t)\}. \tag{B.3}$$

The tangential vector in Eq. (B.2) along the parametric curve can be decomposed into the two tangential vectors along the coordinate lines, Eq. (3.24). These two tangential vectors are approximated by the eigenvectors $\vec{v}'_1$ and $\vec{v}'_2$ obtained with Eq. (3.25). Therefore, one may observe in Eqs. (B.3), (3.24) that if one performs a line integral along the coordinate lines $n_w$ and $|a_-|$ of the eigenvectors $\vec{v}'_1$ and $\vec{v}'_2$, then one can approximately recover the surfaces, $|a_+|(n_w, |a_-|)$, $\Delta\phi(n_w, |a_-|)$ and $n_c(n_w, |a_-|)$. This line integral in the case of the original tangential vectors along the coordinate lines is expressed as:

$$\int d\vec{\psi} = \int \nabla V(\vec{\psi}) \cdot d\vec{\psi} = \int \left\{ \frac{\partial \vec{\psi}}{\partial |a_-|}, \frac{\partial \vec{\psi}}{\partial n_w} \right\} \cdot \Big\{ d|a_-|, dn_w \Big\}. \tag{B.4}$$

Note that the eigenvectors $\vec{v}'_1$ and $\vec{v}'_2$ approximate the vectors $\partial\vec{\psi}/\partial|a_-|$ and $\partial\vec{\psi}/\partial n_w$. Therefore, in the following, we recover the surfaces integrating the eigenvectors. We always integrate along the path starting at the steady-state and integrate up to the given position of the state vector on the surface with infinitesimal steps, $\vec{\delta}$. However, there are two ways to do it:

1. we can compute the eigenvectors at each infinitesimal step from the full Jacobian matrix $\boldsymbol{A}(n_w, |a_-|)$, which is approximated by the polynomial expressions at each infinitesimal step of the state vector position,

2. we can compute the eigenvectors at each infinitesimal step from the original Jacobian matrix $\boldsymbol{A}(\vec{\psi})$, when the state vector at each infinitesimal step comes from the previous infinitesimal step state vector approximated by the integration of the eigenvectors.

The results for both cases are shown in Fig. B.2. Figures B.2(a), (c), (e) show the surfaces recovered following the procedure in 1, while Figures B.2(b), (d), (f) show the surface recovered following the procedure in 2. We emphasize that in the former case, at each infinitesimal step we approximate the state vector with the polynomials, while in the latter case, only knowledge about the initial state vector is required, which in our case is the steady-state, and the state vector is approximate by the integral at each infinitesimal step. Therefore, the procedure in 2 is equivalent to an adiabatic prediction calculated along the dynamic trajectory for the eigenvector amplitudes $c_{1,2}$ in section 3.5.

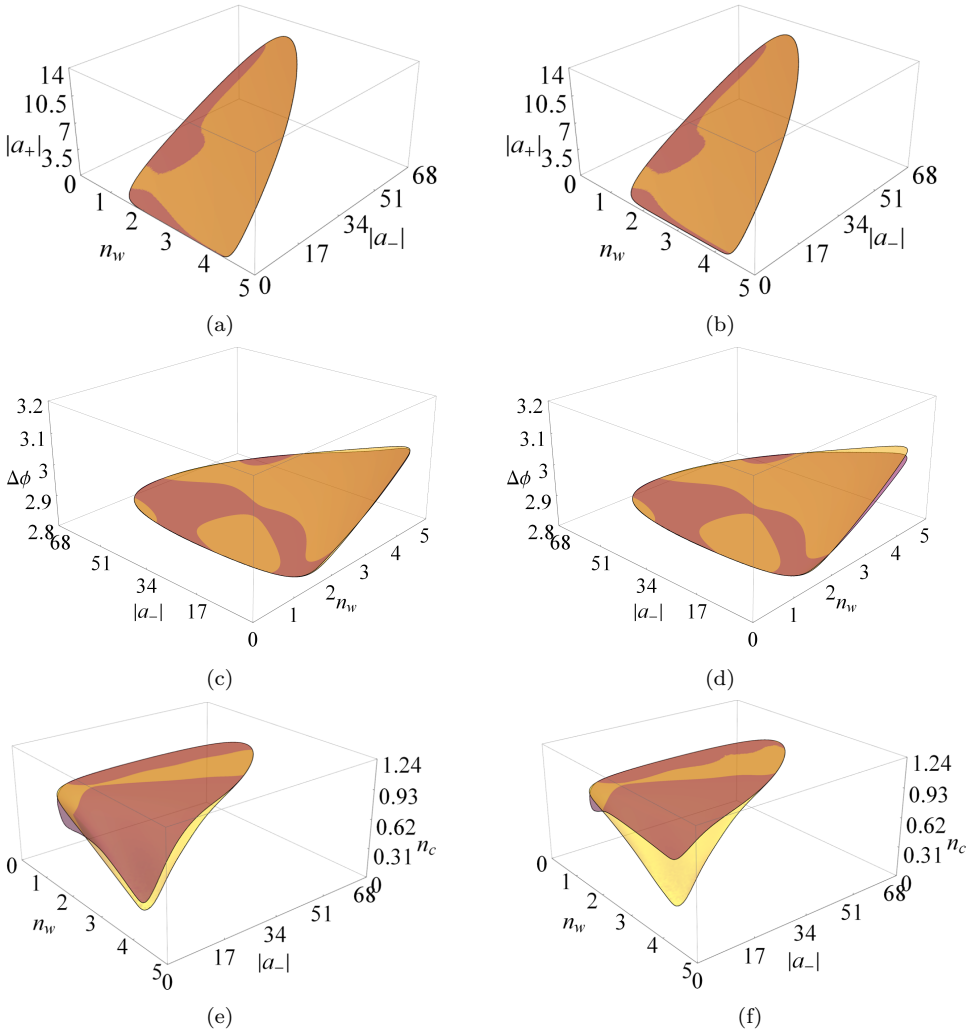


*Figure B.2: (a), (c), (e) The three surfaces $|a_+|$, $\Delta\phi$, $n_c$, respectively, recovered from the integration of the eigenvectors $\vec{v}'_{1,2}$ using the polynomial approximation at each infinitesimal step. (b), (d), (f) The three surfaces $|a_+|$, $\Delta\phi$, $n_c$, respectively, recovered from the integration of the eigenvectors $\vec{v}'_{1,2}$ without the polynomial approximation. Yellow surfaces are the original surfaces based on the polynomial approximation, purple surfaces are the recovered surfaces using the line integration.*

It is found in Figs. B.2(b), (d) that the surface $|a_+|$ is very well recovered, small discrepancy is observed only in the case of the $\Delta\phi$ surface for large values of $n_w$, but it is not significant. On the other hand, the $n_c$ surface in Fig. B.2(f) clearly does not follow the adiabatic approximation and the recovered surface does not reach a dip for large $n_w$ as the original surface (yellow) does. Thus, in addition to the discussion in section 3.5, it further confirms that the sole presence of non-Hermiticity in the system prevents a general application of the adiabatic theorem. The solution does not follow the adiabatic prediction, and thus the full understanding of the dynamics requires knowledge of nonadiabatic transition occurring in the system.

The surfaces in Figures B.2(a), (c), (e) are rather well recovered in all cases. We note that in the ideal scenario when the eigenvectors $\vec{v}'_1$ and $\vec{v}'_2$ perfectly approximate the tangential vectors along the coordinate lines $n_w$, $|a_-|$, then the surfaces should be perfectly recovered in these cases. Some discrepancy is only found for the $n_c$ surface in Fig. B.2(e) and is seen to be the most pronounced in the area when $|a_-|/n_w$ is small/large, respectively. In this region, the eigenvalue with the third largest real part

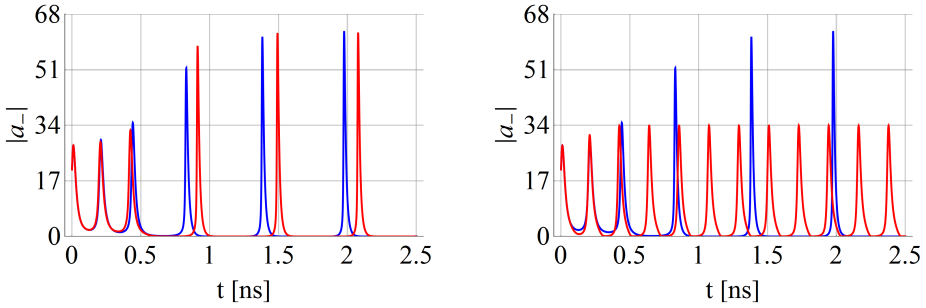


*Figure B.3: The dynamics of $|a_-|$ recovered using the 2D system. Blue curve shows the original solution, red curve shows the recovered solution. (a) the dynamics recovered using the polynomial approximation as in Eq. (3.26). (b) the dynamics recovered with the line integral and having knowledge solely about the steady-state and the $\boldsymbol{A}$ matrix.*

is comparable to the other two dominating eigenvalues, Fig. 3.4. This results in an increased discrepancy between the eigenvectors $\vec{v}'_1$ and $\vec{v}'_2$ and the original tangential vectors along the coordinate lines as found in Fig. 3.24, and thus discrepancy between the recovered (purple) and the original (yellow) surfaces, Fig. B.2(e).

In the following, we verify how well the dynamics are recovered by the simplified 2D system of equations. Similarly as above, this can be done in two ways:

1. we can approximate the variables $|a_+|$, $\Delta\phi$ and $n_c$ with polynomials and then solve a 2D system of equations describing the dynamics of the $n_w$ and $|a_-|$ as in Eq. (3.26); this is equivalent to the integration done in the point 1,

2. on the other hand, in the point 2, we have recovered the surfaces using solely the line integration and having knowledge only about the steady-state and the $\boldsymbol{A}$ matrix. Once the surfaces are known, we can recover the velocity vector over the whole surfaces, Eq. (3.13b). Then, for the given initial conditions, we solve a 2D system of equations describing the dynamics of the $n_w$ and $|a_-|$.

The recovered dynamics of $|a_-|$ are shown in Fig. B.3. In both cases, the initial condition is just outside the unstable periodic orbit, and a few cycles in the later transition stage can be observed. In Fig. B.3(a), we show the dynamics recovered using the polynomial approximation in the 2D system. It is found that the recovered dynamics (red) follow very closely the original solution (blue) in the first two cycles. Some discrepancy is found in the latter stage. However, once the periodic orbit is reached, the pulses in $|a_-|$ are found to have the same magnitude and period as the original solution. The shift in the solution comes from the discrepancy of the polynomial approximation in the middle of the surface, and can be fixed by improving the polynomial approximation. Generally, the solution is found to be very well recovered. On the other hand, Fig. B.3(b) shows the dynamics following the procedure in the point 2. Taking into account how significant the discrepancy in Fig. B.2(f) was, it has to be said that the fact that we can recover the pulsing behaviour is already a success. Moreover, the dynamics (red) are found to closely follow the original solution (blue) during the first few cycles. The pulses are found to be of much smaller magnitude than in the case of the original solution, but this is because the dip in Fig. B.2(f) is not recovered under the adiabatic approximation.

Finally, in Figs. B.4 and B.5 we show the instantaneous eigenvalues over the whole surface and along the periodic orbit trajectory at the edge of the surfaces, respectively. The eigenvalues are shown in the three cases considered above. Figs. B.4(a),(b) and B.5(a),(b) show the eigenvalues in the case of the original 5D model. It is found that

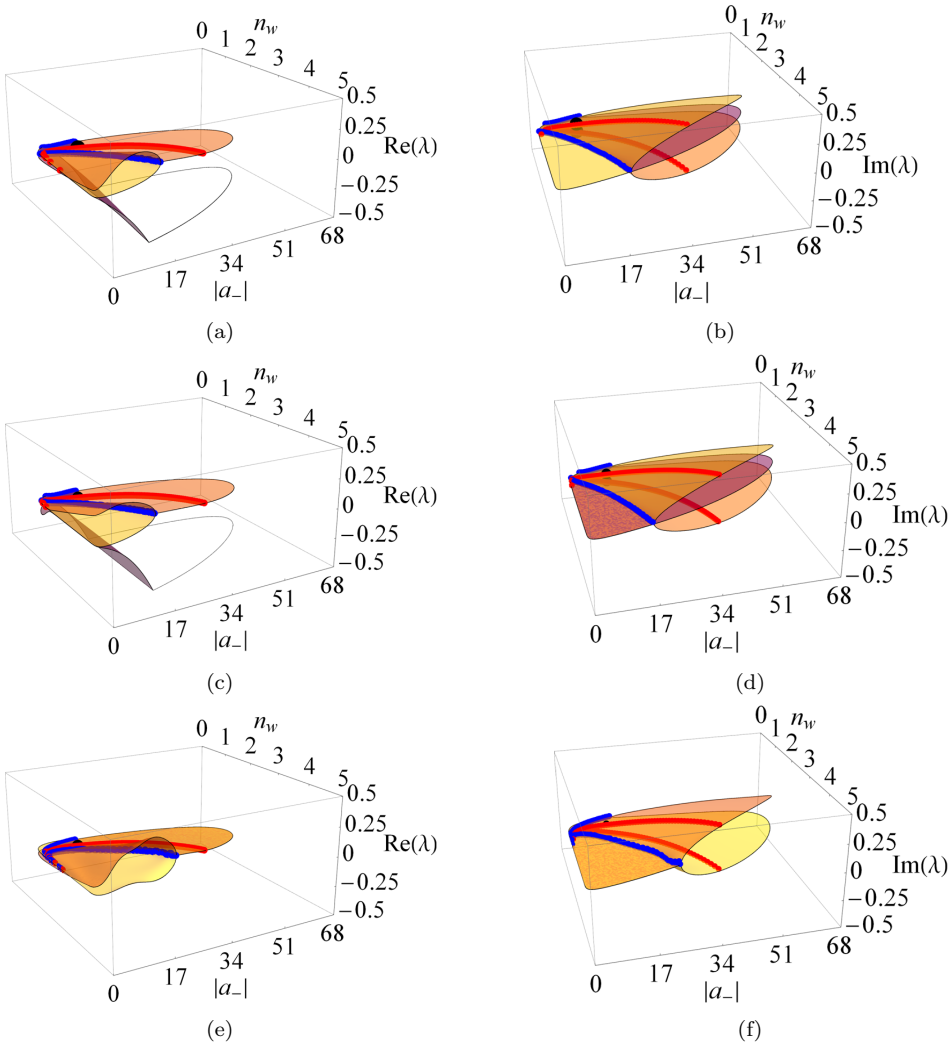


*Figure B.4: (a), (c), (e) Real and (b), (d), (f) imaginary parts of the instantaneous eigenvalues over the whole surface. (a), (b) show the original set of the eigenvalues of the 5D system in the vicinity of the two dominating eigenvalues. (c), (d) the eigenvalues based on the recovered surfaces using the line integral and following the procedure in the point 2. (e), (f) the eigenvalues of the 2D model.*

the imaginary parts, Figs. B.4(b),(d),(e) and B.5(b),(d),(e), of the complex conjugate pair of the eigenvalues is well recovered in all three cases. On the other hand, there are noticeable discrepancies observed in the real parts of the recovered eigenvalues.

Particularly, Fig. B.4(c),(d) and B.5(c),(d) show the eigenvalues for the surfaces recovered using the line integral and having knowledge solely about the steady-state point and the $\boldsymbol{A}$ matrix, i.e. following the procedure in the point 2. It is found that in the close vicinity of the pulse, $t = 1.7$ns, the three eigenvalues with the largest real parts recover the original eigenvalues in Fig. B.5(a). However, away from the pulse ($1.75\text{ns} < t < 2.15\text{ns}$), the third largest eigenvalue (purple) is very poorly recovered. This is because in this region the third largest eigenvalue is comparable with the pair of the dominating eigenvalues. The surfaces were recovered using the eigenvectors $\vec{v}'_1$ and $\vec{v}'_2$ corresponding to the two dominating eigenvalues. Thus, the third eigenvalue (purple) is poorly recovered in the region in which the corresponding eigenvector is significant for the reconstruction of the solution, but has not been included in it. Interestingly, the eigenvalue with the largest real part (orange) is rather well recovered

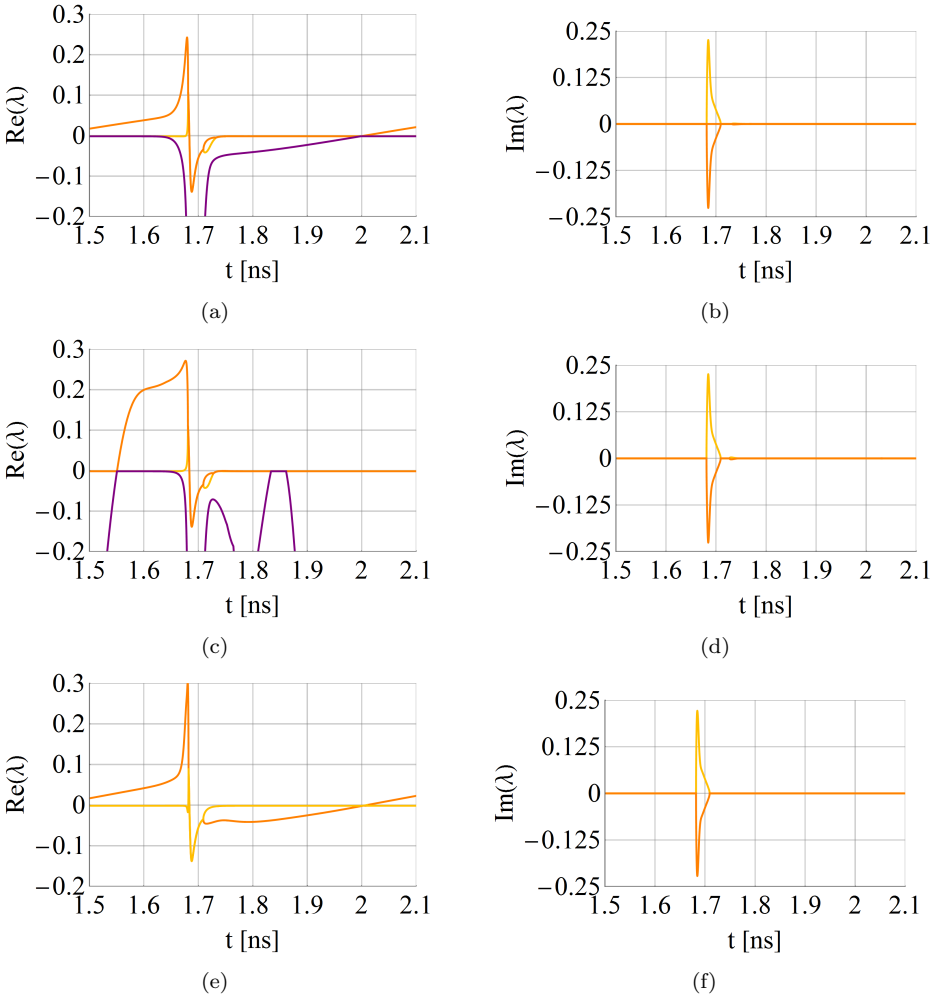


*Figure B.5: (a), (c), (e) Real and (b), (d), (f) imaginary parts of the instantaneous eigenvalues along the periodic orbit at the edge of the surfaces in Fig. B.4. (a), (b) show the original set of the eigenvalues of the 5D system in the vicinity of the two dominating eigenvalues. (c), (d) the eigenvalues based on the recovered surfaces using the line integral and following the procedure in the point 2. (e), (f) the eigenvalues of the 2D model. We note that the initial condition is different than in Fig. B.3.*

in the vicinity of the pulse and after the pulse, but it is far from the purple eigenvalue of the original system just before the pulse. This is related to the poor reconstruction of the third eigenvalue (purple), which in the original system interacts with the orange eigenvalue in the middle of the cycle (inbetween the pulses), see Fig. B.5(a) ($t = 2$ns).

Furthermore, Fig. B.4(e),(f) and B.5(e),(f) show the eigenvalues of the simplified 2D system. Generally, it is found that the pair of the dominating eigenvalues with the largest real part is recovered in the 2D system. However, away from the pulse, the second eigenvalue differs from the second largest eigenvalue of the full system. In Fig. B.5(e),(f), the orange eigenvalue is found to inherit some of the features of the eigenvalue with the third largest real part (purple) of the full system, B.5(a). Particularly, in Fig. B.5(e) the difference between the real parts of the top two eigenvalues is much larger after the broken phase than in Fig. B.5(a). Furthermore, in Fig. B.5(e), (f) the second pair of the exceptional points does not appear shortly after the first one, but it is found in the middle of the cycle where the first and the third largest eigenvalues interact in the full system, see Fig. B.5(a). Moreover, in Fig.

B.4(e) the real part of the eigenvalues is found to fluctuate close to the edge of the surface. These fluctuations are caused by the polynomial approximation and could be removed if the improved approximation scheme is used.

In this Appendix, we have introduced more details concerning the polynomial approximation. Moreover, we have considered different reconstruction schemes of the solution based on the polynomial approximation or the line integral of the eigenvectors. These schemes were compared with the results of the original 5D system. Particularly, we have shown that the 2D model recovers all the main features of the full 5D model after the initial transition stage. The discrepancy between them is most pronounced in the later transition stage. It might result in the shift of the pulsing behaviour in time, but preserves magnitude and period of the pulses.

## Appendix C

# Papers

## C.1 Conference Paper 1

# Control of the rings of exceptional points in photonic crystal slabs

Piotr M. Kamiński, Olav Breinbjerg, Jesper Mørk, and Samel Arslanagić

*Status: Presented June 2017.*

## Bibliography

[P1] P. M. Kamiński, O. Breinbjerg, J. Mørk, and S. Arslanagic. "Control of the rings of exceptional points in photonic crystal slabs". In: *2017 Conference on Lasers and Electro-Optics Europe European Quantum Electronics Conference (CLEO/Europe-EQEC)*. June 2017, pp. 1–1.

www.doi.org/10.1109/CLEOE-EQEC.2017.8087806

# Control of the rings of exceptional points in photonic crystal slabs

**Piotr M. Kamiński[1], Olav Breinbjerg[1], Jesper Mørk[2], Samel Arslanagić[1]**

1. *Department of Electrical Engineering, Technical University of Denmark*
*Ørsteds Plads, Building 348, DK-2800 Kongens Lyngby, Denmark*
*e-mail: pmarka@elektro.dtu.dk*

2. *Department of Photonics Engineering, Technical University of Denmark*
*Ørsteds Plads, Building 343, DK-2800 Kongens Lyngby, Denmark*

Accidental Dirac cones of linear dispersion can occur in photonic crystal (PhC) structures [1]. These configurations can be easily manufactured providing an accessible platform for studying topological properties of Dirac cones and their influence on light-matter interactions. Recently, it has been shown that when the system becomes non-Hermitian, e.g. it is an open system exhibiting radiation losses, Dirac cones can be deformed spawning rings of exceptional points [2]. Within the ring, the dispersion follows the two-dimensional flat band which provides a high density of states and therefore high Purcell factors. Moreover, strong dispersion of loss in the center of the Brillouin zone allows to significantly improve the performance of large-area single mode PhC lasers [3]. These lasers exploit bound states in the continuum [4], and we discuss their relation to Dirac cones.

In this paper, we investigate various ways to control the extent of a ring of exceptional points. Non-Hermitian system, a PhC crystal slab shown in Fig. 1(a), is considered. Particularly, it is observed that when the thickness of a PhC slab is varied, the extent of the flat part of the ring varies periodically, see Figs 1 (b) and (c). It is found that for a specific thickness of the slab, the Dirac cone exhibited by a 2D PhC can be recovered, see Fig. 1 (c). Thus, a PhC slab, which is a non-Hermitian system, starts to behave as a 2D PhC. The imaginary parts of the eigenvalues become negligibly small, see Fig. 1 (d) and (e), the system stops exhibiting any radiation losses and the PhC slab starts to behave approximately as a Hermitian system. As the imaginary parts of all eigenvalues become very small, it is found that the flat band going through the Dirac point exhibits very high quality factors over a broad area of the Brillouin zone. In this case, all three bands exhibit a bound state in the continuum in close proximity of the Γ point. The present results may lead to new designs of PhC based lasers possibly reaching larger area and higher power single mode operation than ever before.

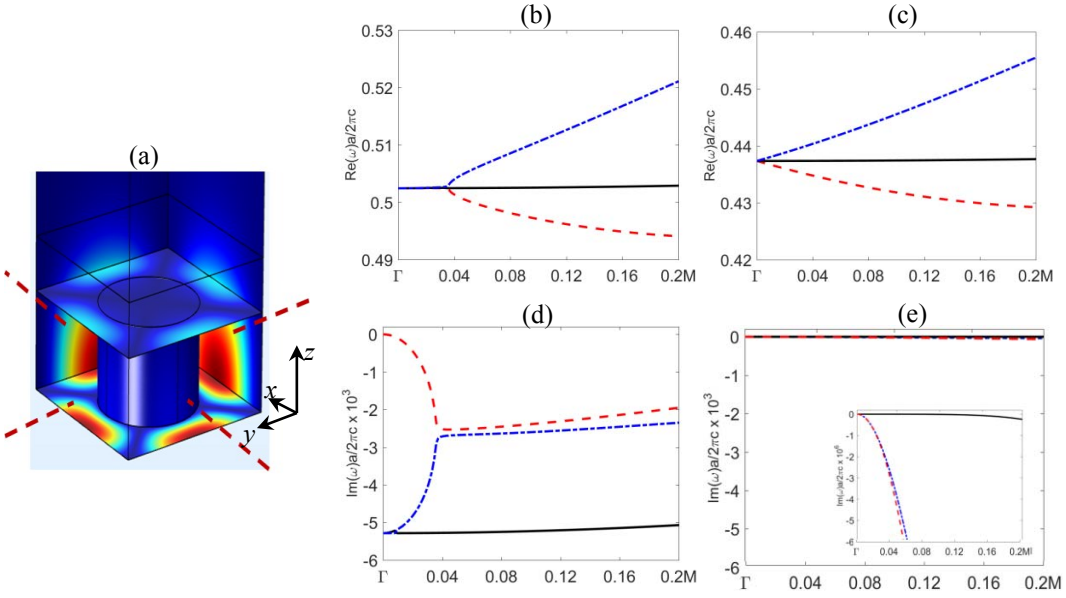


**Fig. 1** Unit cell of the PhC slab of finite thickness $h$ under investigation (a), dashed lines indicate PhC's periodicity. Real (b), (c) and imaginary (d), (e) parts of eigenvalues versus in-plane wavenumber $k$ in Γ-M direction of a PhC slab with finite thickness $h = 0.3205a$ and $h = 0.9115a$, respectively. Inset in (e), shows the data in Fig. 1 (e) multiplied by a factor of $10^3$.

## References

[1] X. Huang, Y. Lai, Z. H. Hang, H. Zheng, C. T. Chan, "Dirac cones induced by accidental degeneracy in photonic crystals and zero-refractive-index materials", Nature materials, **10**, 582-586, (2011).

[2] B. Zhen, C. W. Hsu, Y. Igarashi, L. Lu, I. Kaminer, A. Pick, S.-L. Chua, J. D. Joannopoulos, M. Soljačić, "Spawning rings of exceptional points out of Dirac cones", Nature, **525**, 354-358, (2015).

[3] S.-L. Chua, L. Lu, J. Bravo-Abad, J. D. Joannopoulos, M. Soljačić, 'Larger-area single-mode photonic crystal surface-emitting lasers enabled by an accidental Dirac point', Optics Letters, **39**, 2072-2075, (2014).

[4] C. W. Hsu, B. Zhen, A. D. Stone, J. D. Joannopoulos, M. Soljačić, 'Bound states in the continuum', Nature Reviews Materials, **1**, 16048, (2016).



978-1-5090-6736-7/17/$31.00 

## C.2 Conference Paper 2

# Quality factor enhancement in photonic crystal slabs by manipulation of the ring of exceptional points

Piotr M. Kamiński, Alireza Taghizadeh, Olav Breinbjerg, Jesper Mørk, and Samel Arslanagić

*Status: Presented July 2017.*

### Bibliography

[P2] P. M. Kamiński, A. Taghizadeh, O. Breinbjerg, J. Mørk, and S. Arslanagić. "Quality factor enhancement in photonic crystal slabs by manipulation of the ring of exceptional points". In: *2017 International Conference on Numerical Simulation of Optoelectronic Devices (NUSOD)*. July 2017, pp. 11–12.

www.doi.org/10.1109/NUSOD.2017.8009966

# Quality factor enhancement in photonic crystal slabs by manipulation of the ring of exceptional points

Piotr M. Kamiński, Alireza Taghizadeh, Olav Breinbjerg, Jesper Mørk, Samel Arslanagić
Technical University of Denmark
DK-2800 Kongens Lyngby, Denmark
pmarka@elektro.dtu.dk

***Abstract*—Presently, we investigate the influence of the extent of a ring of exceptional points on the Q-factor of three-dimensional photonic crystal slabs. By changing the thickness of the slab, the extent of the ring of exceptional points is varied, allowing us to recover the Dirac cones in open, non-Hermitian systems. In this case, three bound states in the continuum are exhibited close to the Γ-point. For an optimized thickness of the slab, the associated Q-factors are found to grow rapidly with the size of the slab. The present results may lead to novel, small area and high Q-factor photonic crystal surface-emitting lasers.**

***Keywords—exceptional point, Dirac point, small area high Q-factor PhC lasers,***

## I. Introduction

Photonic crystals (PhCs) can exhibit accidental Dirac cones of linear dispersion [1]. Considered PhCs are periodic arrangements of circularly shaped air-holes following square lattice, where $a$ is a lattice constant. These configurations provide a well-established platform for studying topological properties of Dirac cones. It has been shown that Dirac cones are deformed in non-Hermitian system, e.g. open systems which exhibit radiation losses, resulting in creation of rings of exceptional points [2]. The real and imaginary parts of the eigenvalues coalesce at an exceptional point (EP) [3]. The real parts of the eigenfunctions create a two-dimensional flat band within the ring. This band provides a high density of states. Moreover, strong dispersion of the imaginary part close to the Γ-point allows to considerably improve the performance of large-area single mode PhC lasers [4]. Furthermore, Dirac points have been shown to be related to bound states in the continuum (BICs) [5]. BICs are solutions of wave equation that are perfectly confined despite being inside the continuum of unbounded modes. They are characterized by an infinite Q-factor.

Presently, we investigate the influence of the extent of a ring of EPs on the Q-factor of a 3D PhC slab. It is found that the extent of the ring of EPs can be reduced and Dirac cone can be recovered in open, non-Hermitian system by changing thickness of the slab. This leads to considerable reduction in the radiation losses, and thus to the enhancement of the Q-factor. The Q-factor is found to rapidly increase with size of the slab when its thickness is optimized. This is the result of all three BICs being exhibited in vicinity of the Γ-point. These results may lead to new designs of low threshold lasers.

The authors gratefully acknowledge the support from Villum Fonden via the NATEC Centre of Excellence.

## II. Configurations

All computations in this work were performed numerically in COMSOL Multiphysics, version 5.2a. It uses finite element method and eigenfrequency solver was used in our calculations. In our investigations, two models have been employed; they are depicted in Fig. 1.

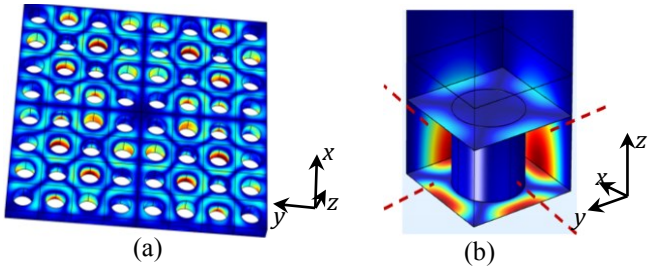


Fig. 1. (a) Unit cell of the PhC slab of finite thickness, $h$, with depicted amplitude of the $H_z$ for a non-degenrate mode at the Dirac point (b) 3D model of a PhC slab of finite thickness, $h$, with circular air-holes embedded in air with dimensions $8a$ x $8a$. Amplitude of the $H_z$ of the highest Q mode is depicted.

The configurations are investigated under the transverse-electric-like (TE-like) polarization; out-of-plane component of the magnetic field intensity (the H-field), $H_z$, and in-plane components of the electric field intensity (the E-field), $E_x$, $E_y$, are present. The models are terminated with perfect magnetic conductor boundary condition in the middle of the thickness to enforce TE-like polarization. Fig. 1(a) shows the 3D model of the PhC slab of finite thickness, $h$, consisting of a square lattice with dimensions $8a$ x $8a$ of circular air-holes introduced in a dielectric material, $\varepsilon_d = 10.05$. The slab is submerged in air and perfectly matched layer terminates the computational domain imitating infinite environment. The simplified model, which is considered at first, is shown in Fig. 1(b). It is a unit cell of the PhC slab of finite thickness, $h$. It is terminated with periodic boundary conditions in the $x$ and $y$ directions.

## III. Results

Firstly, a 2.5D model of the PhC slab, see Fig. 1(a), is considered. This is a non-Hermitian system because of an open boundary in the $z$ direction. We have varied the thickness of the slab and for each case the air-hole size has been adjusted to ensure the Dirac-like dispersion at the Γ-point. Particularly, we observed that for varying thickness of the slab, the extent of the ring of EPs varies periodically, see

Figs. 2 (a) and (b). Moreover, the Dirac cone exhibited by a 2D unit cell of a PhC (Hermitian system) is recovered for a specific thickness of the slab, see Fig. 2(b). As the thickness approaches an optimal value equal to the effective wavelength in the slab, the imaginary parts of the eigenvalues become negligibly small, as shown in Fig. 2 (c) and (d). It leads to significant reduction of radiation losses and the system begins to behave approximately as a Hermitian system.

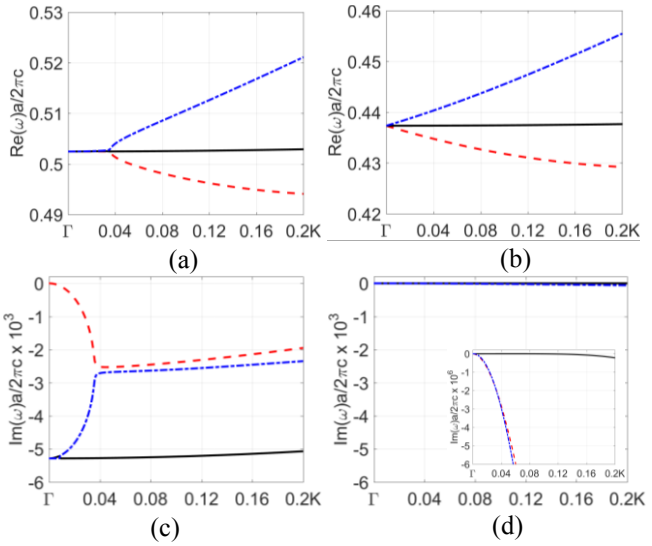


Fig. 2. Real (a), (b) and imaginary (c), (d) parts of eigenvalues plotted versus in-plane wavenumber, $k$, in Γ-K direction of the PhC slab with a finite thickness $h$ = 250nm (a), (c) and $h$ = 711.3nm (b), (d), respectively. Inset in (d), shows the data in Fig. 2 (d) multiplied by a factor of $10^3$.

Fig. 2 illustrates that the imaginary (real) part of the eigenvalue is dispersive and non-degenerate inside (outside) the ring of EPs. At one of the points the imaginary and the real parts are identical. This is an EP and a ring of EPs is formed around the Γ-point because the air-hole exhibits rotational symmetry. As the imaginary parts become negligibly small, the flat band crossing the Dirac point exhibits very high out-of-plane Q-factors over a broad range of in-plane wavenumbers, $k$, see Fig. 3 (a) and (b), where the Q-factors are plotted in dB, $10log_{10}(Q)$. In Fig. 3(a) it is seen that only one of the bands exhibits BIC at the Γ-point. This is a symmetry-protected BIC, which is always found at the Γ-point.

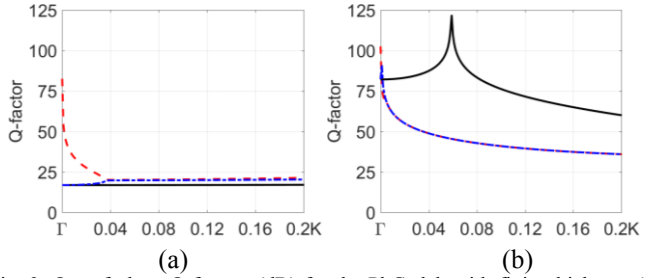


Fig. 3. Out-of-plane Q-factors (dB) for the PhC slab with finite thickness (a) $h$ = 250 nm, (b) $h$ = 711.3 nm plotted versus $k$ in the Γ-K direction. Quality factors are expressed in dB scale, 10 $\log_{10}$( Q ) and are plotted over 20% of the Γ-K direction.

However, in Fig. 3(b) one finds that all three bands exhibit BICs very close to the Γ-point. Furthermore, it is observed that the Q-factor is higher than 60 dB over 20% of the Γ-K direction for the flat band crossing Dirac point. This is an extraordinarily high value, especially bearing in mind that for the 250nm-thick slab, the Q-factor has reached 80dB only at the BIC. Moreover, the band is characterized by a very low group velocity as it is flat. This leads to small in-plane losses, and thus high in-plane Q-factors. These results are exploited in the design of small area, high Q-factor PhC slabs.

We next consider the 3D model of the PhC slab shown in Fig. 1(a). Table 1 presents the highest Q-factor values in the frequency range of the Dirac cones for the PhC slabs of various sizes and the two thicknesses considered above. It is found that the Q-factors rise rapidly with the size of the slab when its thickness is optimized and equals the effective wavelength. On the other hand, when the slab is 250nm-thick, hundreds of unit cells would be needed to satisfy the constructive interference condition very close to the Γ-point and exploit the symmetry-protected BIC [6].

TABLE I

THE HIGHEST Q-FACTOR IN THE FREQUENCY RANGE OF THE DIRAC CONES FOR THE PHC SLABS OF VARIOUS SIZES AND THICKNESSES.

| | 250nm | 711.3nm |
|---|---|---|
| 4$a$ x 4$a$ | 60 | 260 |
| 6$a$ x 6$a$ | 90 | 420 |
| 8$a$ x 8$a$ | 110 | 1100 |
| 10$a$ x 10$a$ | 130 | 1100 |
| 12$a$ x 12$a$ | 150 | 2600 |

We have found that the extent of the ring of EPs is connected to the presence of the BICs close to the Γ-point. The extent of the ring can be reduced and Dirac cone can be recovered in open, non-Hermitian system by varying thickness of the slab. This results in reduction of radiation losses and significant enhancements of the Q-factor. It is found to rapidly increase with size of the slab when the thickness is optimized. The present results may lead to interesting small area and high Q-factor photonic crystal surface-emitting lasers.

## REFERENCES


[1] X. Huang, Y. Lai, Z. H. Hang, H. Zheng, C. T. Chan, 'Dirac cones induced by accidental degeneracy in photonic crystals and zero-refractive-index materials', Nature materials, vol. 10, pp. 582-586, 2011.

[2] B. Zhen, C. W. Hsu, Y. Igarashi, L. Lu, I. Kaminer, A. Pick, S.-L. Chua, J. D. Joannopoulos, M. Soljačić, 'Spawning rings of exceptional points out of Dirac cones', Nature, vol. 525, pp. 354-358, 2015.

[3] I. Rotter, 'A non-Hermitian Hamilton operator and the physics of open quantum systems', J. Phys. A, vol. 42, 153001, 2009

[4] S.-L. Chua, L. Lu, J. Bravo-Abad, J. D. Joannopoulos, M. Soljačić, 'Larger-area single-mode photonic crystal surface-emitting lasers enabled by an accidental Dirac point', Optics Letters, vol. 39, pp. 2072-2075, 2014.

[5] B. Zhen, C. W. Hsu, L. Lu, A. D. Stone, M. Soljačić, 'Topological nature of optical bound states in the continuum', Phys. Rev. Lett., vol. 113, 257401, 2014.

[6] H.-Y. Ryu, M. Notomi, Y.-H. Lee, 'Finite-difference time-domain investigation of band-edge resonant modes in finite-size two-dimensional photonic crystal slab', Phys. Rev. Lett. B, vol. 68, 045209, 2003.

## C.3 Journal Paper 1

# Control of exceptional points in photonic crystal slabs

Piotr M. Kamiński, Alireza Taghizadeh, Olav Breinbjerg, Jesper Mørk, and Samel Arslanagić

*Status: Published August 2017.*

### Bibliography

[P3] P. M. Kamiński, A. Taghizadeh, O. Breinbjerg, J. Mørk, and S. Arslanagić. "Control of exceptional points in photonic crystal slabs". In: *Optics Letters* 42.15 (Aug. 1, 2017), pp. 2866–2869.

www.doi.org/10.1364/OL.42.002866

Optics Letters

# Control of exceptional points in photonic crystal slabs

Piotr M. Kamiński,[1,*] Alireza Taghizadeh,[2,3] Olav Breinbjerg,[1] Jesper Mørk,[3] and Samel Arslanagić[1]

[1]Department of Electrical Engineering, Technical University of Denmark, Ørsteds Plads, Building 348, DK-2800 Kongens Lyngby, Denmark
[2]Department of Physics and Nanotechnology, Aalborg University, Skjernvej 4A, DK-9220 Aalborg East, Denmark
[3]Department of Photonics Engineering, Technical University of Denmark, Ørsteds Plads, Building 343, DK-2800 Kongens Lyngby, Denmark
*Corresponding author: pmarka@elektro.dtu.dk

Received 29 May 2017; revised 24 June 2017; accepted 24 June 2017; posted 26 June 2017 (Doc. ID 296895); published 17 July 2017

**Various ways of controlling the extent of the ring of exceptional points in photonic crystal slabs are investigated. The extent of the ring in photonic crystal slabs is found to vary with the thickness of the slab. This enables recovery of Dirac cones in open, non-Hermitian systems, such as a photonic crystal slab. In this case, all three bands exhibit a bound state in the continuum in close proximity of the $\Gamma$ point. These results may lead to new designs of small photonic-crystal-based lasers exhibiting high-quality factors.**


***OCIS codes:*** (050.5298) Photonic crystals; (230.5298) Photonic crystals; (350.4238) Nanophotonics and photonic crystals; (140.3490) Lasers, distributed-feedback; (140.4780) Optical resonators.

https://doi.org/10.1364/OL.42.002866

Photonic crystal (PhC) membrane structures composed of a semiconductor with a periodic lattice of air-holes display a rich mode structure, which is tunable upon variation of the lattice parameters. It was shown that by tuning, e.g., the radius of the air-holes, a pair of doubly degenerate bands at the $\Gamma$ point can be made degenerate with a singly degenerate band. In that case, two of the three bands form a pair of Dirac cones, i.e., displaying linear bands and meeting in a single Dirac point, and the third band is flat [1]. At the Dirac point, the eigenvalues become degenerate resulting in identical real parts. These PhC configurations can be fabricated using standard nanofabrication techniques, providing an accessible platform for studying properties of Dirac cones and their influence on light–matter interactions. An example of a PhC slab is shown in Fig. 1; it consists of a membrane with finite thickness $h$, containing an array of circular air-holes, and has in the displayed example an overall size of $8a \times 8a$, where $a$ is the lattice constant. Recently, it has been shown that for non-Hermitian systems, open systems exhibiting radiation losses, e.g., Dirac cones, will in general be deformed spawning rings of exceptional points (EPs) [2]. At a second-order EP, both the real and the imaginary parts of the eigenvalues coalesce [3]. It means that two different eigenfunctions become one (have the same real and imaginary parts) at a given point in the $k$ space. This behavior results in two resonances having identical mode profiles and coinciding in their resonant frequencies and spectral widths. The EPs may lead to many fascinating phenomena, such as lasers with reversed pump dependence [4] or single-mode operation [5]. Depending on the symmetry of the structure, many EPs may be present in the $k$ space. They can create contours of EPs, for instance, a ring of these points is created around the $\Gamma$ point in case of a PhC slab with circular air-holes [2]. The extent of the ring approximately depends on the ratio of the radiation loss and a group velocity, as shown in Ref. [2]. The two-dimensional (2D) flat band is created within the ring of EPs, which provides a high density of states and, therefore, high Purcell factors. Moreover, strong dispersion of loss in the center of the Brillouin zone allows it to maintain single-mode operation of large-area, high output power PhC lasers, significantly improving their performance [6]. It has also been shown that Dirac points are connected to electromagnetic bound states in the continuum (BICs) [7]. These states are waves that are perfectly confined despite being inside the continuous spectrum of unbounded modes, which can freely radiate to infinity. BICs are characterized by an infinite quality factor ($Q$-factor), which corresponds to zero radiation losses. They arise due to either a symmetry mismatch of the PhC slab states and its surrounding states (a symmetry-protected BIC) or destructive interference of the waves constituting the resonance (a trapped BIC) [8]. Both are robust to small variations in parameters, but

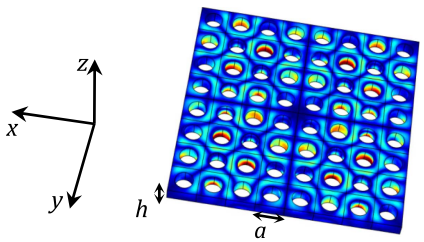


**Fig. 1.** 3D model of a PhC slab of finite thickness $h$ with circular air-holes with dimensions $8a \times 8a$.

the former one is very sensitive to symmetry perturbations and exhibits high $Q$ only in a very close proximity to the high symmetry points, such as the Γ point [8,9]. These phenomena find application in PhC surface-emitting lasers (PCSELs) [1,2,6,8–10]. As a consequence, further examination of the rings of EPs and BICs is crucial in the development of future PCSELs.

Inspired by these findings, it is presently of interest to investigate how to control the rings of EPs in PhC slabs and to exploit their benefits in the design of small PhC-based lasers. Specifically, the extent of the ring of EPs in PhC slabs is found to vary with the thickness of the slab. This enables recovery of Dirac cones in open, non-Hermitian systems, meaning that the system hardly exhibits any losses. This may be exploited for the development of high $Q$-factor, small PhC lasers. The present Letter is organized as follows: first, we introduce the configurations that are examined. Subsequently, fundamental observations and the way of controlling the extent of the ring of EPs are discussed. Finally, we demonstrate the application of the results to the design of small PhC lasers.

All calculations in this work are performed numerically with the finite element method [11]. Eigenvalues, $\Omega = \omega + j\delta$ with $\omega$ being the angular frequency and $\delta$ representing losses, are computed as a function of in-plane wavenumber $k$ in two directions Γ-$M$ and Γ-$X$. In our investigations, we exploit two three-dimensional (3D) models and one 2D model. One 3D model is finite in all directions, see Fig. 1, while the other is periodic in the $x$ and $y$ directions, but has a finite thickness, see Fig. 2(a). The 2D model is shown in Fig. 2(b).

The structures are investigated for transverse-electric (TE) polarization; thus, in-plane electric field components ($E_x$, $E_y$) and the out-of-plane magnetic field component ($H_z$) are the only non-zero field components. Figure 1 shows the 3D model of the PhC slab. It consists of a square lattice of circular air-holes introduced in a material with dielectric constant $\varepsilon_d$. The slab of finite thickness $h$ is immersed in air, and the computational domain is terminated with perfectly matched layers. The model is terminated with perfect magnetic conductor boundary condition in the middle in order to enforce the TE-like polarization. This model is closest to the real structures and the most complex. Thus, its usage is limited. Simplified models are investigated at first. They are shown in Figs. 2(a) and 2(b). In Fig. 2(a), a PhC slab of finite thickness is shown. The slab is periodic in the $x$ and $y$ directions; thus, the computational domain is terminated with periodic boundary conditions in these directions. Figure 2(b) shows the simplest model of a PhC, which is periodic in the $x$ and $y$ directions and infinitely long in the $z$ direction.

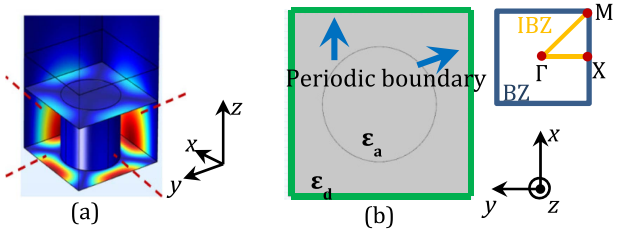


**Fig. 2.** (a) 3D unit cell of a PhC slab, (b) 2D unit cell of a PhC together with corresponding Brillouin zone (BZ) and irreducible Brillouin zone (IBZ).

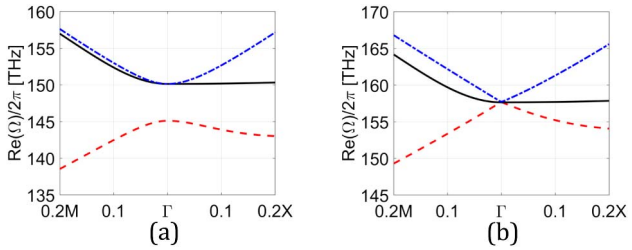


**Fig. 3.** Band diagrams in the Γ-$M$ and Γ-$X$ directions of a 2D PhC of square lattice ($a = 780$ nm) of circular air-holes (a) $r = 0.28a$ and (b) $r = 0.3136a$ introduced in a dielectric material ($\varepsilon_s = 10.05$). The blue, black and red curves correspond to bands exhibiting two dipole modes at the Γ-point, the upper-quadratic and the flat bands, and quadrupole mode at the Γ-point, the lower quadratic band, respectively.

We start by considering the dispersion diagrams for a 2D PhC of circular air-holes. There is neither material loss/gain nor open boundary, thus the system is Hermitian. In the dispersion diagrams, the frequency $\mathrm{Re}(\Omega)/2\pi$ is plotted versus in-plane wavenumber $k$ in the two directions Γ-$M$ and Γ-$X$. In Fig. 3(a), standard quadratic dispersion is presented. Two dipole modes are degenerate and are separated in frequency from the quadrupole mode at the Γ point. Subsequently, the size of the air-hole is adjusted so that Dirac-like dispersion is exhibited by the PhC, see Fig. 3(b). Since the air-hole is rotationally symmetric, the two linear bands create two cones meeting at a Dirac-like point; the flat band in the Γ-$X$ direction creates a plane crossing the Dirac-like point. A quadrupole and two degenerate dipole modes are accidentally degenerate at the Γ point. The modes in the flat band are quasi-longitudinal, such that the electric field is mostly parallel to the $k$-vector, and the linear bands resulting in the Dirac-like dispersion are always accompanied by a quadratic, very flat band when the triple accidental degeneracy occurs [12].

Subsequently, we consider a 3D unit cell of a PhC slab, see Fig. 2(a). Due to the open boundary in the $z$ direction, it is a non-Hermitian system, which allows for the creation of a ring of EPs [2]. We have tuned the air-hole size in order to ensure Dirac-like dispersion at the Γ point. Figures 4(a) and 4(c) show the complex eigenfrequencies versus in-plane wavenumber $k$ plotted over the part of the Brillouin zone, and Figs. 4(b) and 4(d) show cuts in the Γ-$M$ and Γ-$X$ directions of the PhC slab with the thickness $h = 250$ nm and circular air-holes ($r = 0.304a$, $a = 780$ nm) drilled in a dielectric material with $\varepsilon_d = 10.05$. From Fig. 4, we find that the real (imaginary) part of the eigenvalue is degenerate and non-dispersive with respect to $k$ inside (outside) the ring of EPs. It is also seen that the real and the imaginary parts are the same at one of the points. This is an EP, and a ring of these points is created around the Γ point [2]. Having both parts of the eigenvalues, the $Q$-factor can be determined as $Q = -\mathrm{Re}(\Omega)/2\,\mathrm{Im}(\Omega)$. In Fig. 4, the radius of the air-hole was optimized to create an EP along the Γ-$X$ direction. However, it is seen that the frequency becomes degenerate along the Γ-$M$ direction at a slightly different $k$ than along the Γ-$X$ direction; the losses and the group velocities are similar but not the same for the two cases for the given radius. If the radius is changed to $r = 0.303a$, the EP is found along the

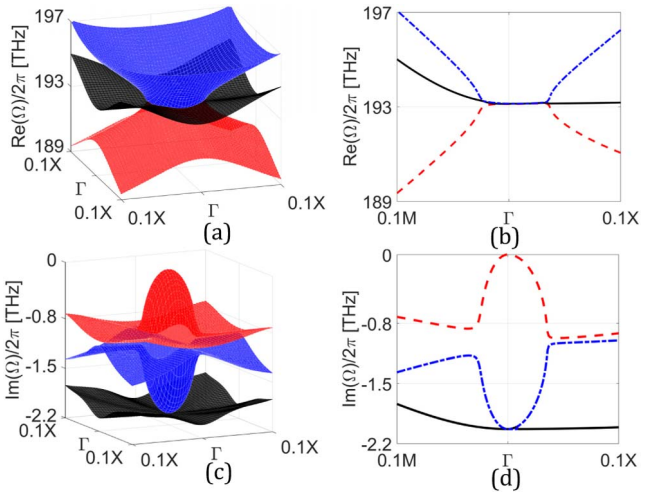


**Fig. 4.** (a), (b) Real and (c), (d) imaginary parts of eigenvalues versus in-plane wavenumber $k$ for a PhC slab with finite thickness $h =$ 250 nm and a square lattice ($a = 780$ nm) of circular air-holes $r = 0.304a$.

Γ-$M$ direction. Thus, there is always a combination of $r$ and $k$, which results in the EP [2]. The difference in radius is $0.001a$ between the Γ-$X$ and the Γ-$M$ directions. This difference cannot be distinguished in practice. When a PhC slab designed to exhibit EP along one direction is fabricated, it will also be close to EP along all the other directions, but most likely will not reach EP exactly for any of them [2].

One may expect that introduction of gain in the PhC slab, e.g., by the incorporation of quantum wells or layers of quantum dots in the membrane [10], would change the extent of the ring of EPs. However, with realistic gain values, this is not the case, because realistic gain mainly shifts the imaginary part of the eigenfrequency, while the influence on the real part, and thus the extent of the ring, is negligible.

For an infinitely thick slab (2D PhC), there are no radiation losses. Thus, the system is Hermitian and the eigenfrequnecies are real. Therefore, one may expect that by a variation of the PhC slab thickness, we could at least approach the 2D case, reduce the radiation losses, and, in this way, control the extent of the ring of EPs. We have varied the thickness of the PhC slab, and, for each thickness, the size of the air-hole was adjusted in order to ensure that Dirac-like dispersion was exhibited by the system. Afterwards, we examined how the extent of the ring of EPs changed along the Γ-$X$ direction. The results are shown in Fig. 5, where the extent of the ring is shown in terms of the part of the Γ-$X$ direction versus the thickness of the PhC slab. It is noted that the Dirac-like dispersion was obtained for a first-order mode in the $z$ direction. Figure 5 shows that the extent of the ring changes non-monotonously with increasing slab thickness, reaching minima at thicknesses of approximately 750 and 1500 nm. The ring collapses when we approach free space case, as the radiation loss is then zero. Subsequently, the extent of the ring increases, reaching maximum for a 100 nm thick PhC slab. As the thickness is increased further, the extent of the ring decreases. This variation is caused by the increasing confinement of the mode in the slab and can also be understood in terms of the destructive interference as in Ref. [13], where a similar plot for the radiation constant

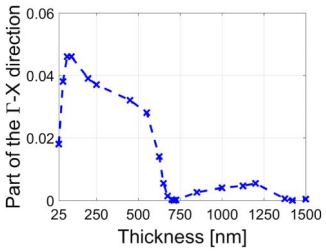


**Fig. 5.** Extent of the ring of EPs in the Γ-$X$ direction versus the thickness of the PhC slab.

was obtained. Eventually, a specific thickness is reached, for which the ring of EPs is reduced to a point, and a Dirac-like cone is recovered, see Figs. 6(a) and 6(b). For this thickness, the PhC slab behaves approximately as a 2D PhC (Hermitian system) and exhibits very small radiation loss. It is noted that for this specific thickness, the air-hole radius, which ensures Dirac-like dispersion, $r = 0.3135a$ is almost the same as in the 2D model designed to exhibit Dirac-like dispersion.

In Fig. 5, it is seen that the second minimum occurs at a thickness twice as large as that to achieve the first minimum. Thus, the minima in the extent of the ring appear in a periodic-like manner. The distance between the minima is very close to the effective wavelength $\lambda_{\text{eff}}$ of the fundamental, first-order mode in the PhC slab. The effective refractive index is $n_{\text{eff}} = (1 - \text{FF})n_r + \text{FF}$ with FF = 30.9% being the filling fraction of the air-hole, and $n_r = 3.17$ being the refractive index of the host material $n_{\text{eff}} = 2.5$, this corresponds to $\lambda_{\text{eff}} = 713$ nm. Thus, the specific thickness, at which nearly zero radiation loss occurs and the Dirac cone is recovered, equals the effective wavelength of the mode. Both parts of the eigenvalues for this case are shown in Fig. 6. Due to the enforced TE-like polarization, all antisymmetric modes in $z$ with respect to the in-plane electric field intensity are excluded. This is why the minima in Fig. 5 occur only at even multiples of $\lambda_{\text{eff}}/2$. Thus, this behavior is strictly related to the dielectric slab phenomena. Figure 6 shows that the imaginary part is very small over the broad extent of the Γ-$X$ direction, see Figs. 6(c) and 6(d). Interestingly,

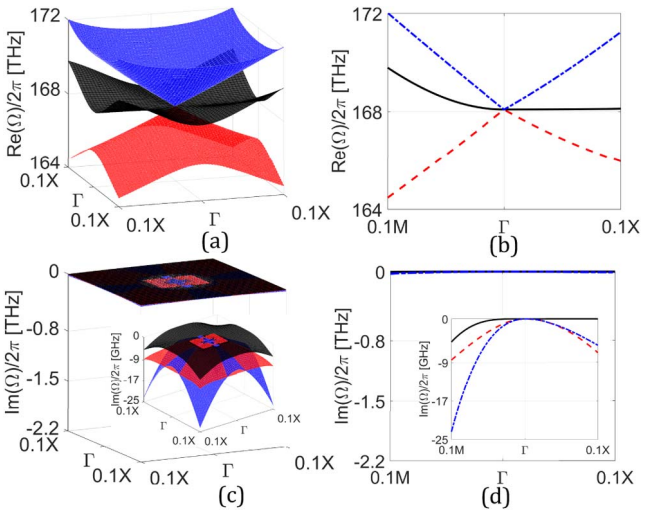


**Fig. 6.** (a), (b) Real and (c), (d) imaginary parts of the eigenvalues versus in-plane wavenumber $k$ for a PhC slab with finite thickness $h = 711.3$ nm and circular air-holes $r = 0.3135a$.

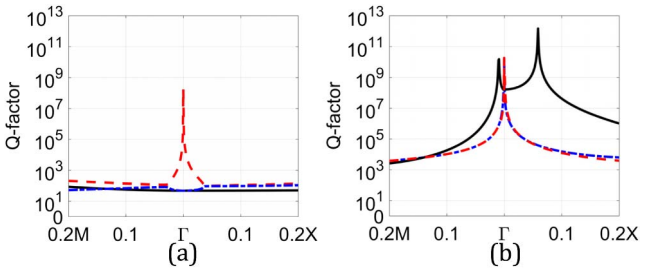


**Fig. 7.** Out-of-plane $Q$-factors for the PhC slab with finite thickness (a) $h = 250$ nm, (b) $h = 711.3$ nm versus in-plane wavenumber $k$ in the $\Gamma$-$M$ and $\Gamma$-$X$ directions. $Q$-factors are plotted over 20% of the considered directions.

when the thickness of the slab is increased beyond this specific thickness, $h = 711.3$ nm, the extent of the ring increases again since the radiation losses increase. This behavior can be explained based on the destructive interference [13]. In the inset of Figs. 6(c) and 6(d), which shows the zoom of the data shown in Figs. 6(c) and 6(d), it is seen that the imaginary part is not exactly zero, but its magnitude increases away from the $\Gamma$ point.

As the imaginary parts of all eigenvalues become very small, the flat band going through the Dirac point exhibits very high out-of-plane $Q$-factors over a broad area of the Brillouin zone. The $Q$-factors for the PhC slab with finite thickness (a) $h = 250$ nm and (b) $h = 711.3$ nm versus in-plane wavenumber $k$ in the $\Gamma$-$M$ and $\Gamma$-$X$ directions are shown in Fig. 7. One finds in Fig. 7(a) that only one of the bands exhibits a BIC, as the $Q$-factor diverges only at the $\Gamma$ point and only simulation precision limits its value. This is a symmetry-protected BIC, which is always present at the center of the Brillouin zone [8]. The $Q$-factor is on the level of $1 \times 10^2$ for the other two bands. On the other hand, Fig. 7(b) shows that all three bands exhibit BICs in a very close proximity of the $\Gamma$ point. Moreover, the $Q$-factor does not drop below $1 \times 10^6$ over 20% of the $\Gamma$-$X$ direction for the flat band and is around $1 \times 10^4$ for the other two bands, thus it is respectively $1 \times 10^4$ and $1 \times 10^2$ times higher than in the 250 nm PhC slab case. Finally, it is seen that the $Q$-factor is higher than $1 \times 10^8$ over 8% of the $\Gamma$-$X$ direction. This is an extremely high value, especially taking into account the fact that in the case of the 250 nm slab, the $Q$-factor has reached $1 \times 10^8$ only at the BIC. It is noted that the flat band along the $\Gamma$-$X$ direction is not completely flat along other directions, the $\Gamma$-$M$ direction being the most pronounced case. It results in growth in the amplitude of the imaginary part despite a BIC being present close to the $\Gamma$ point.

The above results have shown that by changing the thickness of the PhC slab, we can vary the extent of the ring of EPs. In this way, we could identify the configuration exhibiting a Dirac-like cone as a result of very high out-of-plane $Q$-factors. This has led to significant reduction in the radiation loss for PhC slabs that are $\lambda_{\text{eff}}$-thick. Furthermore, the flat band exhibits very low in-plane group velocity. This implies small in-plane losses, and, consequently, a high in-plane $Q$-factor. If we combine it with very high out-of-plane $Q$-factor values, it might enable the creation of a high $Q$ cavity laser based on the PhC slab with a small footprint.

That this indeed is possible is demonstrated in Table 1, which shows the highest $Q$-factor in the frequency range of the Dirac cones for the PhC slabs of various sizes and thicknesses considered above. Table 1 shows that when the slab thickness is optimized to be $\lambda_{\text{eff}}$-thick, the $Q$-factors grow rapidly with the slab size compared to the non-optimal thickness of 250 nm. The maximum value of the $Q$-factor is determined by the in-plane losses, which decrease with the slab size, and overlap of the $k$-space mode profile with the out-of-plane $Q$-factor shown in Fig. 7 [14].

**Table 1. Highest $Q$-Factor in the Frequency Range of the Dirac Cones for the PhC Slabs of Various Sizes and Thicknesses**

| | 250 nm | 711.3 nm |
|---|---|---|
| $4a \times 4a$ | 60 | 260 |
| $6a \times 6a$ | 90 | 420 |
| $8a \times 8a$ | 110 | 1100 |
| $10a \times 10a$ | 130 | 1100 |
| $12a \times 12a$ | 150 | 2600 |

In conclusion, we have shown that the extent of the ring of EPs in PhC slabs varies with the thickness of the slab. For a specific thickness, the Dirac cone can be recovered in an open, non-Hermitian system of the PhC slab. The minima in the extent of the ring are found to appear in a periodic-like manner. In these cases, all three bands exhibit BICs in close proximity of the $\Gamma$ point, resulting in nearly zero radiation loss. These results are exploited in the design of small-area, high $Q$-factor PhC slabs. $Q$-factors of these slabs are found to rapidly increase with the size of the slab when the thickness is optimized. This may result in new designs of small-area, high $Q$-factor PCSELs.

**Funding.** Villum Fonden (NATEC Center of Excellence, 8692).

## REFERENCES

1. X. Huang, Y. Lai, Z. H. Hang, H. Zheng, and C. T. Chan, Nat. Mater. **10**, 582 (2011).
2. B. Zhen, C. W. Hsu, Y. Igarashi, L. Lu, I. Kaminer, A. Pick, S.-L. Chua, J. D. Joannopoulos, and M. Soljačić, Nature **525**, 354 (2015).
3. I. Rotter, J. Phys. A **42**, 153001 (2009).
4. M. Liertzer, L. Ge, A. Cerjan, A. D. Stone, H. E. Tureci, and S. Rotter, Phys. Rev. Lett. **108**, 173901 (2012).
5. L. Feng, Z. J. Wong, R.-M. Ma, Y. Wang, and X. Zhang, Science **346**, 972 (2014).
6. S.-L. Chua, L. Lu, J. Bravo-Abad, J. D. Joannopoulos, and M. Soljačić, Opt. Lett. **39**, 2072 (2014).
7. B. Zhen, C. W. Hsu, L. Lu, A. D. Stone, and M. Soljačić, Phys. Rev. Lett. **113**, 257401 (2014).
8. C. W. Hsu, B. Zhen, A. D. Stone, J. D. Joannopoulos, and M. Soljačić, Nat. Rev. Mater. **1**, 16048 (2016).
9. A. Kodigala, T. Lepetit, Q. Gu, B. Bahari, Y. Fainman, and B. Kanté, Nature **541**, 196 (2017).
10. K. Hirose, Y. Liang, Y. Kurosaka, A. Watanabe, T. Sugiyama, and S. Noda, Nat. Photonics **8**, 406 (2014).
11. COMSOL Multiphysics 5.2a, 2017, https://www.comsol.com/.
12. C. T. Chan, Z. H. Hang, and X. Huang, Adv. OptoElectron. **12**, 313984 (2012).
13. S. Iwahashi, K. Sakai, Y. Kurosaka, and S. Noda, J. Opt. Soc. Am. B **27**, 1204 (2010).
14. A. Taghizadeh and I.-S. Chung, "Quasi bound states in the continuum with few unit cells of photonic crystal slab," 2017, https://arxiv:org/abs/1705.09842.

## C.4 Journal Paper 2

# Two-dimensional phase-space picture of the photonic crystal Fano laser

Piotr M. Kamiński, Samel Arslanagić, Jesper Mørk, and Jensen Li

*Status: In review.*

### Bibliography

[P4] P. M. Kamiński, J. Mørk, S. Arslanagić, O. Breinbjerg, and J. Li. "A two-dimensional phase-space picture of the photonic crystal Fano laser". In: *Physical Review A* ().

# A two-dimensional phase-space picture of the photonic crystal Fano laser

Piotr M. Kamiński,[1,*] Samel Arslanagić,[1,†] Jesper Mørk,[2] and Jensen Li[3,‡]

[1] *Department of Electrical Engineering, Technical University of Denmark, Ørsteds Plads, 2800 Kongens Lyngby, Denmark*
[2] *Department of Photonics Engineering, Technical University of Denmark, Ørsteds Plads, 2800 Kongens Lyngby, Denmark*
[3] *Department of Physics, Hong Kong University of Science and Technology, Clear Water Bay, Hong Kong, China*

(Dated: July 3, 2019)

The recently realized photonic crystal Fano laser constitutes the first demonstration of passive pulse generation in nanolasers [Nat. Photonics **11**, 81-84 (2017)]. We show that the laser operation is confined to only two degrees-of-freedom after the initial transition stage. We show that the original 5D dynamic model can be reduced to a 1D model in a narrow region of the parameter space and it evolves into a 2D model after the exceptional point, where the eigenvalues transition from being purely to a complex conjugate pair. The 2D reduced model allows us to establish an effective band structure for the eigenvalue problem of the stability matrix to explain the laser dynamics. The reduced model is used to associate a previously unknown origin of instability with a new unstable periodic orbit separating the stable steady-state from the stable periodic orbit.

## I. INTRODUCTION

Integrated photonic circuits require energy efficient, fast and compact light sources [1]. Particularly promising candidates to realize them are photonic crystal (PhC) lasers due to their flexibility in design and precise control of the cavity properties [2, 3]. PhC lasers can be electrically driven and allow for modulation in the GHz range [4, 5]. Moreover, they have been shown to exhibit very rich dynamics, e.g. spontaneous symmetry breaking [6]. Recently, a new type of PhC laser has been proposed [7] where one of the mirrors arises due to a Fano resonance [8, 9]. Furthermore, this laser has been demonstrated to be able to generate a self-sustained train of pulses at GHz frequencies, a property that has been observed only in macroscopic lasers thus far [10]. Generation of pulses by an ultracompact laser is of interest for applications in future on-chip optical signal processing.

The configuration of the Fano laser is shown in Fig. 1. The active material may be composed of several layers of InAs quantum dots or quantum wells and is incorporated inside the InP PhC membrane. The laser cavity is composed of a PhC line-defect waveguide blocked with a PhC mirror on the left side forming a broad-band mirror, whereas the right mirror is due to the Fano interference between the nanocavity and the waveguide. The Fano resonance arises due to the interference of a discrete mode of the nanocavity with the continuum of PhC waveguide modes. The spectral width of the resonance is determined by the quality factor of the nanocavity enabling the realization of a narrow-band mirror. The dynamic operation of the laser is modeled using a combination of coupled-mode theory and conventional laser rate equations [11]. The model has been used to demonstrate that there are two regimes of operation, the continuous-wave regime and a self-pulsing regime [11]. Particularly, it has been shown that as the real part of any of the eigenvalues of the underlying stability matrix, evaluated at the steady-state, becomes positive, the relaxation oscillation becomes undamped resulting in the laser becoming unstable and self-pulsing behaviour setting in [11, 12]. However, it does not fully explain the origin of instability in the whole parameter space of the laser as there exists a region in which the laser can become unstable even when all the steady-state eigenvalues are negative [11].

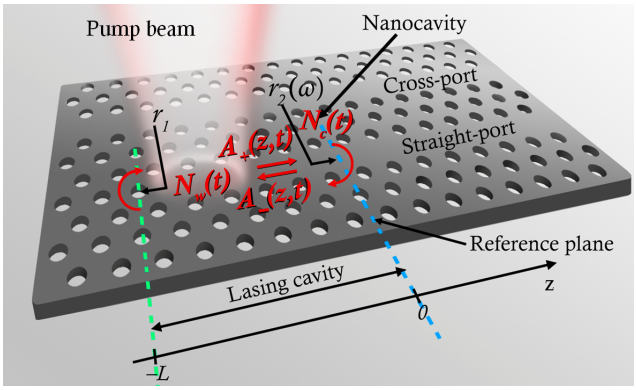


Figure 1. Schematic of a PhC Fano laser. The active material is uniformly incorporated in the PhC slab. The lasing cavity is composed of a PhC line-defect waveguide terminated with a broad-band mirror (green) and a narrow-band mirror due to the Fano interference between the nanocavity and the waveguide. The length of the lasing cavity is defined as the distance between the broad-band mirror and a reference plane (blue). The dynamic variables are marked in red and are: the carrier densities in the waveguide and the nanocavity, $N_w(t)$ and $N_c(t)$, respectively, and the right and left propagating complex field envelopes $A_+(0,t)$ and $A_-(0,t)$, respectively, evaluated at the reference plane.

The purpose of this work is to analyze not only the steady-state eigenvalues of the stability matrix of the dynamic model, but also the instantaneous eigenvalues during the laser operation. Moreover, we determine the

* pmarka@elektro.dtu.dk
† sar@elektro.dtu.dk
‡ jensenli@ust.hk

'minimal' model for the laser that is required to explain the dynamics in different regimes, thereby obtaining an alternative perspective on the dynamics of the Fano laser. We thus demonstrate that the laser operation can be effectively modeled by a one-dimensional (1D) system of differential equations in a limited region of the parameter space when the steady-state eigenvalues are purely real and that it evolves into an effective two-dimensional (2D) system beyond the steady-state exceptional point, when the eigenvalues form complex conjugate pairs. These findings are used to determine the origin of the instability that is observed when the steady-state eigenvalues are negative. We notice that the analysis of instabilities and chaos in injection-locked lasers, e.g., using bifurcation analysis has been very successful [13–16]. Here, we use it to analyse origin of laser instability when the steady-state is stable and set an important goal to identify reduced systems for getting further physical insight.

The manuscript is organized as follows. In Sec. II we introduce the model used to describe the laser dynamics. In Sec. III we show that the laser operation can be understood by means of a 2D phase-space picture and we analyze the steady-state and instantaneous eigenvalues of the stability matrix. In Sec. IV we exploit the simplified 2D model to associate a self-pulsing operation, when a steady-state is stable to a generalized Hopf (Bautin) bifurcation which is characterized by a bifurcation of two periodic orbits and an equilibrium point (steady-state) [17, 18].

## II. DYNAMIC MODEL OF THE FANO LASER

We next briefly describe the procedure required to establish the dynamic model of the Fano laser; for more details refer to [11]. The complex field is decomposed into the fields propagating to the right and left from the reference plane, see Fig. 1. By combining the boundary conditions for both fields, we can arrive at the oscillation condition [7]:

$$r_1(\omega_s) r_R(\omega_s, \omega_c) e^{i2k(\omega_s, N_s)L} = 1, \tag{1}$$

where $r_1$ and $r_R$ are the broad-band (left) and the narrow-band (right) reflection coefficients, respectively. $r_R$ is determined using the coupled-mode theory [19–21], while $r_1$ is the reflection coefficient due to the PhC band gap and has to be transformed towards the common reference plane using standard transmission line theory [22]. $k$ is the complex wavenumber of the waveguide, $L$ is the length of the lasing cavity, and $\omega_c$ is the resonance frequency of the nanocavity. The condition in Eq. (1), is solved for $(\omega_s, N_s)$, which are the steady-state lasing frequency and carrier density, respectively. They serve as expansion points of the dynamic model. There are multiple solutions of Eq. (1) [7, 12] among which the one with the lowest modal threshold gain is chosen. The wavenumber, $k$, accounts for dispersion of the refractive index of the PhC membrane and the gain of the active material.

Subsequently, the boundary condition is solved for the left propagating field and then the term $1/r_1(\omega)e^{i2k(\omega_s,N_s)L}$ is Taylor expanded around the steady-state operation point $(\omega_s, N_s)$ and a first-order differential equation for the right-propagating complex field envelope evaluated at the reference plane $A_+(t)$ is derived using the Fourier transform. In the special case of an open waveguide considered here, the coupled-mode equation for the field in the nanocavity can be directly reformulated as an equation for the left-propagating complex field envelope evaluated at the reference plane $A_-(t)$. The equations for $A_+(t)$ and $A_-(t)$ are complemented with the traditional rate equations for carrier densities in the waveguide and the nanocavity.

Since the variables introduced above differ by orders of magnitude, we introduce dimensionless near-unity variables in order to improve numerical stability. Moreover, detuning from the expansion point frequency $\omega_s$ results in time-varying real and imaginary parts of $A_+(t)$ and $A_-(t)$ at the steady-state. Because of that, the differential equations for $A_+(t)$ and $A_-(t)$ are separated into equations for amplitudes and phase evolutions by the following substitution: $A_+(t) = A_{0+}|a_+|(\tau/(G_{NC}N_0))e^{i\phi_+(\tau/(G_{NC}N_0)}$, $A_-(t) = A_{0-}|a_-|(\tau/(G_{NC}N_0))e^{i\phi_-(\tau/(G_{NC}N_0)}$, where $A_{0+}$ and $A_{0-}$ are the normalization constants, $a_-(\tau)$ and $a_+(\tau)$ are the normalized complex field envelopes, $\tau = tG_{NC}N_0$ is the normalized time, $G_{NC} = \Gamma_C v_g g_N$, and $v_g$ is the group velocity. The system depends solely on the phase difference $\Delta\phi(\tau) = \phi_-(\tau) - \phi_+(\tau)$; thus by subtracting the equations for phase evolutions $\phi_+(\tau)$, $\phi_-(\tau)$ and exploiting linearity of differentiation, these equations can be combined into one. This leads us to the following system of five differential equations describing the dynamics of the laser:

$$\frac{d|a_+|(\tau)}{d\tau} = -\frac{\gamma_L|a_+|(\tau)}{G_{NC}N_0} + \frac{\Gamma|a_+|(\tau)(n_w(\tau)-n_s)}{2\Gamma_C} + \frac{\gamma_L}{G_{NC}N_0}|a_+|(\tau)\mathrm{Re}\left(\frac{A_-(\tau)}{r_R A_+(\tau)}\right) \tag{2a}$$

$$\frac{d|a_-|(\tau)}{d\tau} = -\frac{P\gamma_C}{G_{NC}N_0}|a_-|(\tau)\mathrm{Re}\left(\frac{A_+(\tau)}{A_-(\tau)}\right) - \frac{\gamma_T|a_-|(\tau)}{G_{NC}N_0} + \frac{|a_-|(\tau)(n_c(\tau)-1)}{2} \tag{2b}$$

$$\frac{d\Delta\phi(\tau)}{d\tau} = -\frac{\alpha}{2}(n_c(\tau)-1) + \frac{\Gamma\alpha(n_w(\tau)-n_s)}{2\Gamma_C} - \frac{\Delta\omega}{G_{NC}N_0} - \mathrm{Im}\left(\frac{r_R P\gamma_C A_+^2(\tau) + \gamma_L A_-^2(\tau)}{r_R G_{NC}N_0 A_-(\tau)A_+(\tau)}\right) \tag{2c}$$

$$\frac{dn_w(\tau)}{d\tau} = \frac{-|a_+(\tau)|^2(n_w(\tau)-1) - n_w(\tau) + j_c}{G_{NC}N_0\tau_s} \tag{2d}$$

$$\frac{dn_c(\tau)}{d\tau} = \frac{-|a_-(\tau)|^2(n_c(\tau)-1) - n_c(\tau)}{G_{NC}N_0\tau_c} \tag{2e}$$

Here, $n_w(\tau)$ and $n_c(\tau)$ are the carrier densities in the waveguide and the nanocavity, respectively, normalized with respect to the transparency carrier density, $N_0$. $\gamma_L = v_g/(2L)$ is the inverse of the cavity roundtrip time, $n_s$ is the steady-state carrier density obtained from the oscillation condition normalized with respect to $N_0$, $\Delta\omega = \omega_c - \omega_s$ is the detuning of the steady-state lasing frequency, $\omega_s$, from the cavity resonance frequency, $\omega_c$, and $j_c$ is the normalized effective pumping current, which includes the injection efficiency.

Subsequently, we linearize the problem by calculating the total derivative of Eqs. (2) with respect to $\tau$. The system of equations describing the laser dynamics in Eqs. (2) can be expressed in the short form as a function $V(\cdot)$ of the state vector $\vec{\psi}(\tau)$:

$$\vec{\psi}(\tau) = \{|a_+(\tau)|, |a_-(\tau)|, \Delta\phi(\tau), n_w(\tau), n_c(\tau)\} \tag{3a}$$

$$\frac{d\vec{\psi}(\tau)}{d\tau} = V(\vec{\psi}(\tau)) \tag{3b}$$

By taking the total derivative of $V(\vec{\psi}(\tau))$, we obtain a directional derivative along the curve parameterized by $\tau$:

$$\frac{d^2\vec{\psi}(\tau)}{d\tau^2} = \nabla_{\vec{\psi}} V(\vec{\psi}(\tau))\frac{d\vec{\psi}(\tau)}{d\tau} = \boldsymbol{A}(\vec{\psi}(\tau))\frac{d\vec{\psi}(\tau)}{d\tau} \tag{4}$$

Consequently, $d\vec{\psi}(\tau)/d\tau$ in Eq. (3b) is interpreted as the velocity of the state vector and is expressed as a function of the current position of the state vector in Eq. (2). $d^2\vec{\psi}(\tau)/d\tau^2$ is interpreted as the acceleration of the state vector, see Eq. (4). Matrix $\boldsymbol{A}$ is the so-called Jacobian matrix; its eigenvalues $\lambda$ are used to determine the stability of the laser when evaluated at the steady-state. The system is stable if all eigenvalues have negative real parts. On the other hand, if any eigenvalue has a positive real part, the system is unstable. The matrix $\boldsymbol{A}$ is purely real, but not symmetric as we separated the complex field envelopes into the magnitudes $|a_+(\tau)|$, $|a_-(\tau)|$ and the phase difference $\Delta\phi$. Therefore, the matrix is non-Hermitian and we have to distinguish between right $\vec{v}$ and left $\vec{w}$ eigenvectors which are normalized so that $\boldsymbol{W}^T\boldsymbol{V} = \boldsymbol{I}$ is satisfied [23, 24]. The columns of $\boldsymbol{W}$ and $\boldsymbol{V}$ are the left and the right eigenvectors, and $\boldsymbol{I}$ is the identity matrix. Furthermore, eigenvalues of the matrix $\boldsymbol{A}$ can be purely real or form complex conjugate pairs [25]. In the following sections, we use Eqs. (2) and (5) to investigate the origin of instability in case of a stable steady-state and to show that the original laser model can be simplified to a system of two differential equations.

## III. TWO DIMENSIONAL PHASE-SPACE PICTURE

### A. Steady-state eigenvalues

Above the threshold, the laser can exhibit two types of operation, the continuous wave and the self-pulsing operation [10, 11]. Figure 2 shows the real and imaginary parts of the two steady-state eigenvalues of the Jacobian matrix, $\boldsymbol{A}$ with the largest real parts plotted versus $\Delta\omega_c$, which is the detuning of the cavity resonance frequency, $\omega_c$ from the resonance frequency of the isolated cavity, normalized with respect to $\gamma_T$. It is noted that $\Delta\omega_c$ defines $\Delta\omega$ in Eq. (2) through the oscillation condition, Eq. (1), and is controlled externally. As our case study, we choose $\Delta\omega_c$ marked with the blue line in Fig. 2.

Interestingly, it has been observed in [11] that in the vicinity of the $\Delta\omega_c$ marked by the blue dashed line in Fig. 2 the laser can exhibit the continuous wave or the self-pulsing operation depending on the initial condition despite its steady-state eigenvalues having negative real parts and thus suggesting stable operation of the laser. However, origin of this instability has not been explained and is examined in Sec. IV. On the other hand, when $\Delta\omega_c$ is increased beyond $1.26\gamma_T$, the real parts become positive, the relaxation oscillation becomes undamped, the laser becomes unstable, and the state approaches a stable periodic orbit for any initial condition. This is a Hopf bifurcation observed in [11]. All the following figures are obtained for the parameters listed in Table I, while the pumping current is set to $J = 1.2J_{thr}$, where $J_{thr}$ is the minimum threshold current.

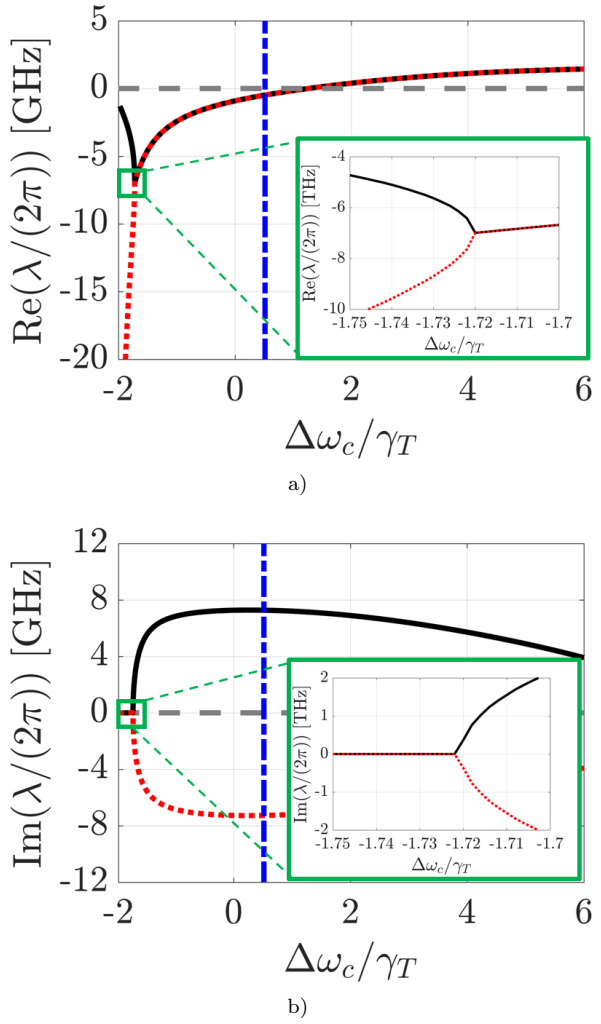


Figure 2. Real a) and imaginary b) parts of the two steady-state eigenvalues of the matrix, $\boldsymbol{A}$ with the largest real parts. The horizontal dashed gray line indicates zero. The vertical dot-dashed blue line indicates $\Delta\omega_c$ for which Fig. 3 is obtained. The pumping current is set to $J = 1.2J_{thr}$. The green frame marks the position of the exceptional point, while the insets show the eigenvalues in its vicinity.

Table I. Laser parameters used in all numerical simulations.

| Parameter name | Symbol | Value |
|---|---|---|
| Transparency carrier density | $N_0$ | $1 \cdot 10^{24}\text{m}^{-3}$ |
| Parity of the cavity mode | $P$ | 1 |
| Linewidth enhancement factor | $\alpha$ | 1 |
| Internal loss factor | $\alpha_i$ | $1000\text{m}^{-1}$ |
| Lasing cavity length | $L$ | $5\mu$m |
| Carrier lifetimes | $\tau_s$, $\tau_c$ | 0.5ns |
| Laser cavity volume | $V_{LC}$ | $1.05\mu\text{m}^3$ |
| Nanocavity volume | $V_{NC}$ | $0.243\mu\text{m}^3$ |
| Nanocavity resonance | $\lambda_r$ | 1554nm |
| Reference refractive index | $n_{ref}$ | 3.5 |
| Group refractive index | $n_{grp}$ | 3.5 |
| Differential gain | $g_N$ | $5 \cdot 10^{-20}\text{m}^2$ |
| Waveguide confinement factor | $\Gamma$ | 0.5 |
| Nanocavity confinement factor | $\Gamma_C$ | 0.3 |
| Left mirror reflectivity | $R_1$ | 1 |
| Nanocavity-waveguide coupling | $\gamma_C$ | $1.14\text{ps}^{-1}$ |
| Nanocavity total passive decay rate | $\gamma_T$ | $1.21\text{ps}^{-1}$ |

### B. Exceptional points

It is interesting to observe in Fig. 2 that for $\Delta\omega_c$ lower than $-1.72\gamma_T$, the real part of the two eigenvalues split and the eigenvalues become purely real, see Fig. 2b). At $\Delta\omega_c = -1.72\gamma_T$, the two eigenvalues coalesce and not only the eigenvalues are identical at this point, but so are the eigenvectors as well [26–30]. This constitutes an exceptional point which is also known as a symmetry breaking point for a non-Hermitian system [31–34]. However, exceptional points are a general phenomenon observed in optical waveguides [35], unstable laser resonators [36], coupled PhC nanolasers [37], quantum systems [38], electronic circuits [39] and mechanical resonators [40]. They only require non-Hermiticity of the system for their existence [27, 28, 41]. We emphasize that exceptional points may arise upon coalescence of eigenvectors/eigenvalues of any matrix, e.g. a Hamiltonian matrix [42], a S-parameter matrix [43] and an impedance/admittance matrices [44], to name a few. Exceptional points have also been linked to a self-pulsing mechanism in distributed feedback lasers [45, 46] in which case the self-pulsing mechanism was attributed to dispersive quality factor self-switching similarly as in the case of the Fano laser [10]. In the present case, exceptional points arise due to dissimilar decay rates, $\gamma_C$, $\gamma_L$ and phenomenologically introduced gain terms $|a(\tau)|(n(\tau) - 1)$, Eqs. (2a) and (2b). They play an analogous role to the loss and gain usually introduced as an imaginary part of the refractive index in parity-time symmetric systems [47, 48].

### C. Two-dimensional phase-space

In Fig. 3 we plot three trajectories of $n_c$, marked in red, green and blue versus $n_w$, $|a_-|$ and obtained for the three different initial conditions. The trajectories are parameterized by $\tau$. It is found that there are actually three different stages of the laser operation: the initial transition stage, the later transition stage and the self-pulsing stage. This is in contrast to the previously reported picture of two stages: the transition stage and the self-pulsing stage. The red, green and blue dots mark the initial conditions in Fig. 3. It is found that at first they lie above a yellow surface, this is the initial transition

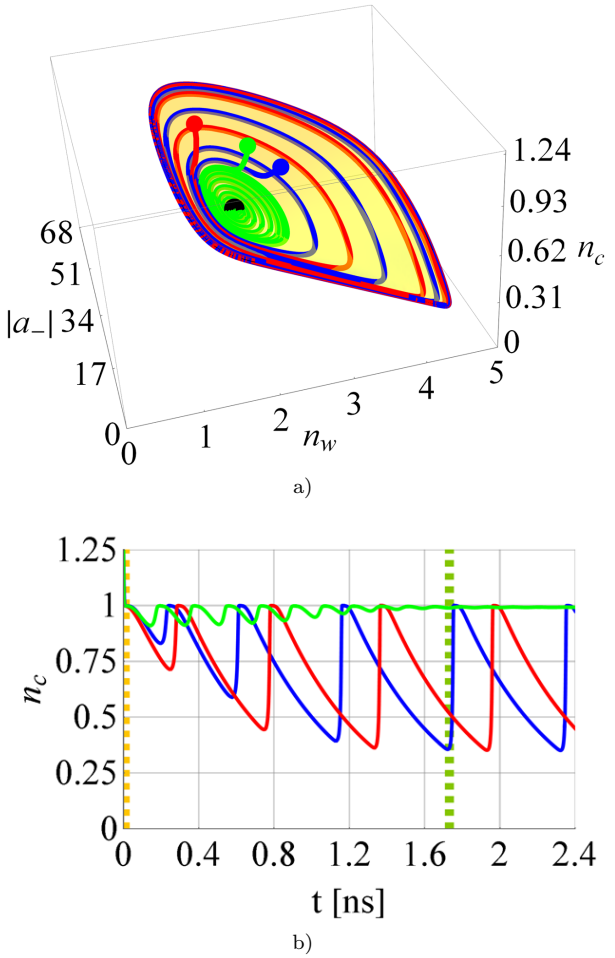


Figure 3. a) The trajectories of $n_c$ against $n_w$ and $|a_-|$. The black dot represents the steady state. The red, green and blue dots are the three different initial conditions lying above the yellow surface. During an initial transition stage, the state decays towards the surface. Then the state continues its evolution on the surface. b) The trajectories in time-domain show the initial transition stage lasting a few ps, the later transition stage lasting ∼1.2ns, and finally the self-pulsing stage at the edge of the surface. The vertical orange/green dashed lines mark the end of the initial/later transition stage.

stage which lasts only a few picoseconds. After a very short initial transition stage, the state reaches the surface at the time instant marked with the orange dashed line in Fig. 3b). The state stays on the surface within the later transition stage and the self-pulsing/continuous wave stage. The later transition stage is when the state approaches the stable steady-state or the stable periodic orbit. Eventually, the state reaches the stable periodic orbit at the time instant marked with the green dashed line in Fig. 3b). The state stays at the orbit unless perturbed; this stage is called the self-pulsing stage and takes place at the edge of the yellow surface.

Thus, it is found that once the state reaches the yellow surface, the state is confined to the surface. The phenomenon of data collapse to a surface happens also for the other two variables, $|a_+|$, $\Delta\phi$. Since the state always lies on the surface after a very short initial time, we conclude that two degrees of freedom are sufficient to specify the state after the initial transition stage and the propagation of the state is locally restricted to two directions. We note that this phenomenon is a general feature of a dynamical system close to a Hopf bifurcation and is called a reduction to the center manifold [18, 49, 58]. Dimension of the center manifold is strictly related to the number of steady-state eigenvalues, real parts of which cross zero [18, 49, 58]. In Fig 2a), we have seen that in the present case there are two eigenvalues with real parts crossing zero, while all the remaining eigenvalues have negative real parts giving rise to a stable manifold. Thus, the center manifold is two-dimensional as it is confirmed by the yellow curved surface in Fig. 3a). The dynamics in the remaining three directions quickly approach the surface during the initial transition stage.

In Fig. 3, $n_w$ and $|a_-|$ are the two degrees of freedom, while all the remaining degrees of freedom $\{|a_+|, \Delta\phi, n_c\}$ of the state vector $\vec{\psi}$ are expressed as functions of the variables $n_w$ and $|a_-|$ after the initial transition stage:

$$\vec{\psi} = \{|a_+|(|a_-|, n_w), |a_-|, \Delta\phi(|a_-|, n_w), n_w, n_c(|a_-|, n_w)\}, \tag{5a}$$

Similarly, equations for each component of the velocity vector $d\vec{\psi}/d\tau$ in Eqs. (2) and (3b) can be expressed as functions of $n_w$ and $|a_-|$:

$$\frac{d\vec{\psi}}{d\tau} = \{V_1(|a_-|, n_w), V_2(|a_-|, n_w), V_3(|a_-|, n_w), V_4(|a_-|, n_w), V_5(|a_-|, n_w)\}. \tag{5b}$$

By taking the total derivative of $d\vec{\psi}(\tau)/d\tau$, we obtain:

$$\left(\frac{d^2\vec{\psi}(\tau)}{d\tau^2}\right)_i = \left\{\frac{\partial V_i}{\partial |a_-|}\frac{d|a_-|}{d\tau} + \frac{\partial V_i}{\partial n_w}\frac{dn_w}{d\tau}\right\}, \tag{6}$$

which, when compared with Eq. (4), indicates that the laser dynamics can be locally approximated by a $2 \times 2$ Jacobian matrix $\boldsymbol{A}$.

The functions of $n_w$ and $|a_-|$ in Eq. (5a) and the yellow surface in Fig. 3 are approximated by polynomials. In order to do that, we solve the system of differential equations in Eqs. (2) for varying initial conditions. Each solution then corresponds to a different trajectory plotted versus $n_w$ and $|a_-|$. All of these trajectories are seen to lie on the surface after the initial transition stage similarly to Fig. 3. Next, we fit a polynomial with all the trajectories excluding the initial transition stage. Then the polynomial describes the surface $n_c$ in terms of $n_w$ and $|a_-|$. Similarly, we can approximate the surfaces for $|a_+|(|a_-|, n_w)$ and $\Delta\phi(|a_-|, n_w)$. We emphasize that in

order to keep the original coordinate system of the variables, we exclude the part of the trajectory in the initial transition stage and fit a polynomial with the remaining parts of all the trajectories. Thus, we fit the polynomials once the state has reached the center manifold. Having obtained these surfaces, we can determine any state in the phase space within the periodic orbit once $n_w$ and $|a_-|$ are known without any need of solving the five-dimensional system of equations in Eq. (2).

Moreover, in order to describe the dynamics on these surfaces, we need to solve a system of two differential equations describing the two degrees of freedom, $n_w$ and $|a_-|$. These equations are the components of the velocity vector in Eq. (5b):

$$\frac{d|a_-(\tau)|}{d\tau} = V_2(|a_-(\tau)|, n_w(\tau)), \tag{7a}$$

$$\frac{dn_w(\tau)}{d\tau} = V_4(|a_-(\tau)|, n_w(\tau)), \tag{7b}$$

Once Eq. (7) is solved, the remaining degrees of freedom $\{|a_+|, \Delta\phi, n_c\}$ can be determined using the polynomials.

### D. Instantaneous eigenvalues

We compute the instantaneous eigenvalues of the matrix $\boldsymbol{A}$ in Eq. (4) for the state vectors $\vec{\psi}$, Eq. (5a) over the whole surfaces. In Fig. 3, we have seen that we can define three surfaces for $|a_+|$, $\Delta\phi$, $n_c$ plotted versus $n_w$ and $|a_-|$. After the initial transition stage, the state always lies on these surfaces. Thus, all the dynamics are confined to these surfaces. Then, each point of these surfaces can be substituted into the matrix $\boldsymbol{A}$ and the instantaneous eigenvalues of the state at this position are obtained. Figure 4 shows the real and imaginary parts of the three instantaneous eigenvalues with the largest real parts over the whole surface as well as along the trajectory marked with the green dashed line. The two remaining eigenvalues have significantly smaller real parts, and thus are not included in Fig. 4 as the contribution from the corresponding eigenvectors decays rapidly.

Figure 4a) shows that the pair of eigenvalues marked with orange and yellow has considerably larger real parts than the third eigenvalue (purple) over the major part of the surface. The third eigenvalue is only comparable to the other two eigenvalues along the line $|a_-| = 0$, but it is still smaller and never becomes positive. The negative real parts of the purely real third eigenvalue (purple) and the remaining complex conjugate pair of eigenvalues (not shown) signifies that the contribution of the corresponding eigenvectors in a reconstruction of the solution decays very quickly. This is what is observed in Fig. 3 in the initial transition stage. Afterwards, once the state is on the surface, the contribution from the three corresponding eigenvectors is negligible and the state description is dominated by the eigenvectors corresponding to the two eigenvalues with the largest real part (orange and yellow).

The real parts of the pair of eigenvalues marked with orange and yellow are seen to dominate for large values of $|a_-|$; this is where the pulse is released. In Fig. 4c),d,e)) we show the instantaneous eigenvalues in the vicinity of the pulse along the green trajectory in a), b) when the state has already reached a limit cycle. On the right axis we plot the pulse power in the straight-port defined as:

$$P_+(t) = 2\epsilon_0 n_{ref} c_0 |A_+(t) + PA_-(t)|^2, \tag{8}$$

where $c_0$ is the speed of light and $\epsilon_0$ is vacuum permittivity.

Figure 4 shows that when the state moves along the $n_w$ axis (just after the previous pulse has been released and before a new one) the three eigenvalues with the largest real parts are purely real. As the limiting value of $n_w$ is reached, Fig. 4a), one of the eigenvalues (orange) starts to rapidly increase, Fig. 4c), while the third eigenvalue (purple) drops rapidly. Just as the pulse is released, the second eigenvalue (yellow) rapidly increases and collapses with the first one (yellow) at the exceptional point. Therefore, it is found that, as the pulse grows, the pair of eigenvalues transitions from being purely real to being complex conjugate when crossing the exceptional point. As the pulse power decreases, the complex conjugate pair of eigenvalues coalesce at the second exceptional point and transitions back to the pair of purely real eigenvalues. Thus, most of the pulse is observed to be bounded by the two instantaneous exceptional points with positive/negative real part of the eigenvalue at the beginning/end of the pulse, respectively. Interestingly, two more exceptional points are observed as the pulse is decaying, see Fig. 4e).

Within one period the state traverses a loop in the phase space of the model. We have seen that four exceptional points are crossed within a single loop when the laser state is a periodic orbit. When the exceptional point is approached, the eigenvectors exhibit a characteristic phase jump and are phase shifted relative to each other by $\pm i$ [41, 50]. Therefore, during an evolution along any trajectory in the diminishing vicinity of an exceptional point, eigenvectors will acquire a phase shift of $\pm i$ [42, 51, 52]. In [53], it has been shown that this effect is preserved as long as the exceptional point is inside the loop or crossed by it. Therefore, it is only a four-fold loop around an exceptional point or a single loop around four exceptional points that will restore an original scenario for the eigenvectors concerned [26, 27, 29, 54, 55]. Since the laser is operating in the periodic orbit in our case, in order to remain periodic it has to cross four exceptional points within one period in phase space.

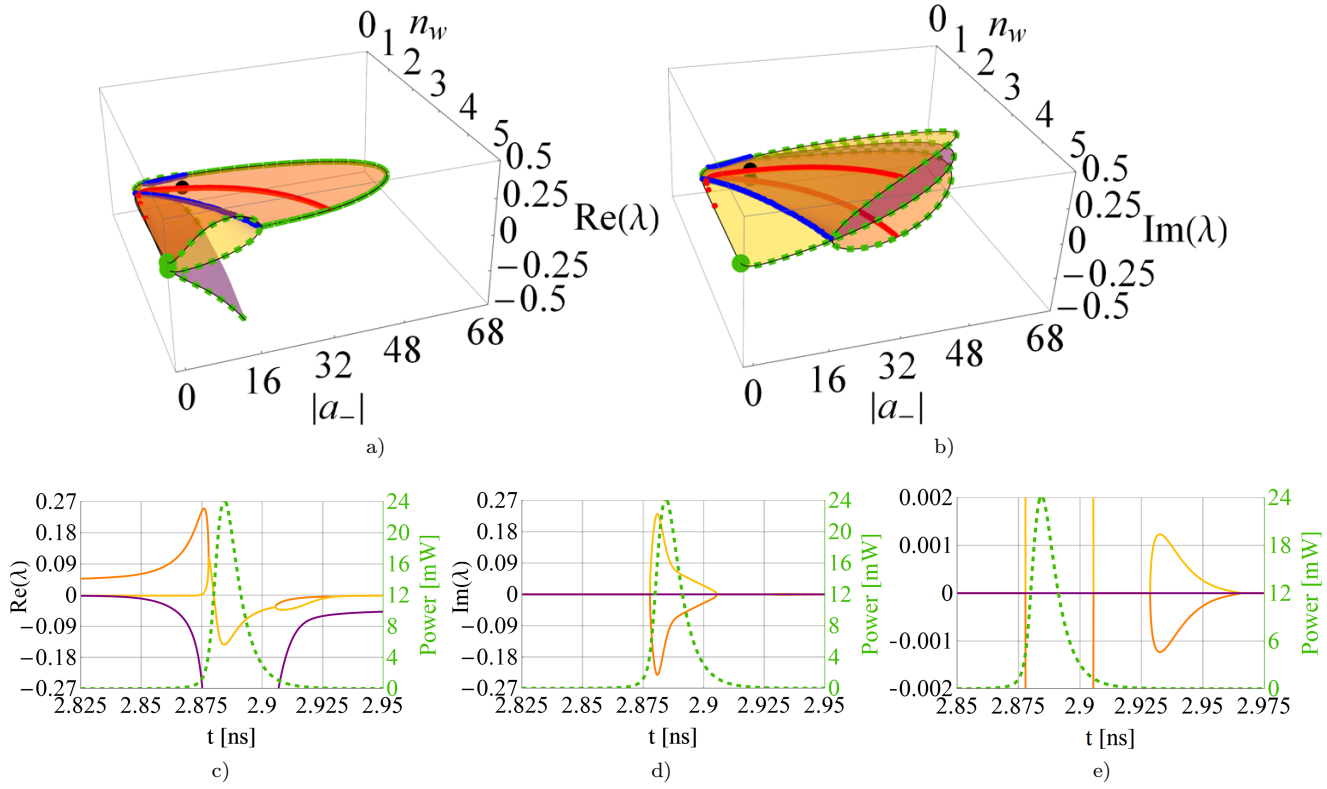


Figure 4. Real a) and imaginary b) parts of the three instantaneous eigenvalues, $\lambda$, of $\boldsymbol{A}$ with the largest real parts. The eigenvalues form a complex conjugate pair marked with orange and yellow, the remaining eigenvalue is purely real and marked with purple. The red line indicates the positions when $\mathrm{Re}(\lambda) = 0$. The blue line indicates the contours of exceptional points. The black dot indicates the eigenvalues at the steady-state. The green dot indicates initial eigenvalues of the trajectory, marked with the dashed green line, plotted in c), d). c), d) show real and imaginary parts of the instantaneous eigenvalues with the largest real parts along the green trajectory in a), b). The pulse-power in the straight-port is marked with dashed green line (on the right axes). e) shows the imaginary parts of the eigenvalues in the vicinity of the second pair of the exceptional points.

### E. Reconstruction of the solution

At most two out of five instantaneous eigenvalues have positive real parts. Thus, after the initial transition stage, the eigenvectors which correspond to the two dominating eigenvalues can be used to reconstruct the solution of Eq. (4) as follows:

$$\frac{d\vec{\psi}}{d\tau} = c_1(\tau)\vec{v_1}(\tau) + c_2(\tau)\vec{v_2}(\tau) \tag{9}$$

where $\vec{v}_{1,2}$ are the instantaneous right eigenvectors, and $c_{1,2}$ are the amplitudes of the corresponding eigenvectors. These amplitudes can be reconstructed from a solution $d\vec{\psi}(\tau)/d\tau$ using the left eigenvectors as $c_{1,2} = \vec{w}^T_{1,2}(\tau)d\vec{\psi}(\tau)/d\tau$. In the following we show that the two eigenvectors can be used to approximate the two tangential vectors to the surface pointing along the $|a_-|$, $n_w$ coordinate lines. This confirms that the solution can be approximately expanded in the two eigenvectors.

The tangential vector to the surface $z = f(x, y)$ along the parametric curve $\vec{r}(t) = \{x(t), y(t), z(t)\}$ on this surface is expressed as $\vec{r}'(t) = \{x'(t), y'(t), z'(t)\}$, where $z'(t) = \nabla f \cdot \vec{u}$, $\vec{u} = \{x'(t), y'(t)\}$. In our case, the tangential vectors to the surfaces, which approximate the components of the state vector $\vec{\psi}$, Eq. (5a), are expressed as:

$$\vec{r}'(\tau) = \left\{\frac{d|a_-|}{d\tau}, \frac{dn_w}{d\tau}, \frac{d\vec{\psi}}{d\tau}\right\}, \tag{10}$$

where

$$\frac{d\vec{\psi}}{d\tau} = \frac{\partial\vec{\psi}}{\partial|a_-|}\frac{d|a_-|}{d\tau} + \frac{\partial\vec{\psi}}{\partial n_w}\frac{dn_w}{d\tau}. \tag{11}$$

The tangential vectors $\vec{r}'(\tau)$ along the parameterized trajectory can be decomposed into a linear combination of the tangential vectors to the surface along its coordinates $|a_-|$, $n_w$:

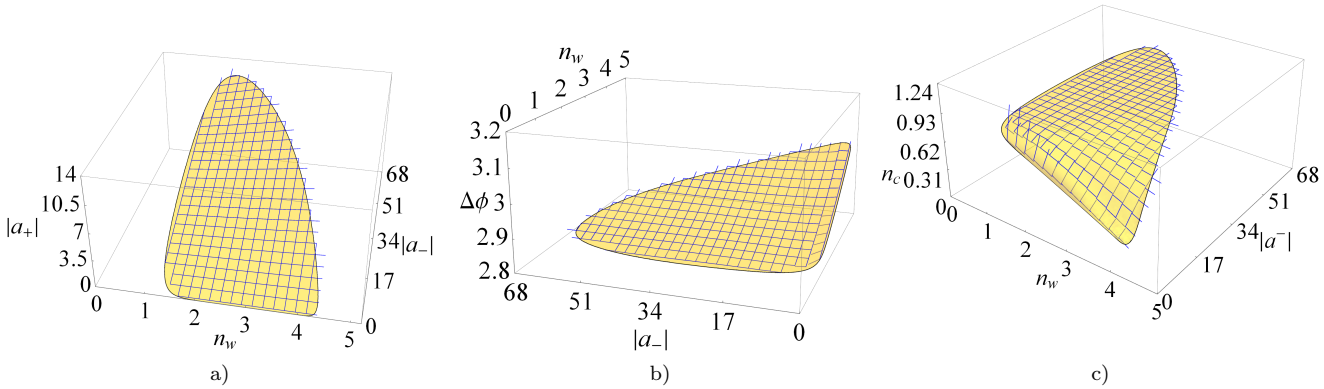


Figure 5. The vectors $\vec{v}'_{1,2}$ plotted on the three surfaces, a) $|a_+|$, b) $\Delta\phi$, c) $n_c$. The vectors $\vec{v}'_{1,2}$ result from the linear combination of the eigenvectors corresponding to the top two eigenvalues and enforcing them to point along the $n_w$, $|a_-|$ coordinate lines. These vectors are found to approximate the tangential vectors to the surface along the $n_w$, $|a_-|$ coordinate lines.

$$\vec{r}'_1 = \left\{1, 0, \frac{\partial\vec{\psi}}{\partial|a_-|}\right\}, \qquad \vec{r}'_2 = \left\{0, 1, \frac{\partial\vec{\psi}}{\partial n_w}\right\}, \tag{12}$$

It is observed that the tangential vectors to the surface are composed of the components of the velocity vector, Eq. (10), and the velocity vector can be expanded into the two eigenvectors, see Eq. (9). Since the five-dimensional (5D) matrix $\boldsymbol{A}$ is real, the top two eigenvalues ($\lambda_1$ and $\lambda_2$) and eigenvectors ($\vec{v_1}$ and $\vec{v_2}$) are either real or form a complex conjugate pair. Then, we change these eigenvectors to point along the original coordinate lines, $|a_-|$, $n_w$, as follows:

$$\begin{bmatrix}\vec{v}'_1\\ \vec{v}'_2\end{bmatrix} = \begin{bmatrix}v_{12} & v_{14}\\ v_{22} & v_{24}\end{bmatrix}^{-1}\begin{bmatrix}v_{12} & v_{14} & v_{11} & v_{12} & v_{13} & v_{14} & v_{15}\\ v_{22} & v_{24} & v_{21} & v_{22} & v_{23} & v_{24} & v_{25}\end{bmatrix} \tag{13}$$

Then, the two vectors $\vec{v}'_1$ and $\vec{v}'_2$ are determined at positions of the state vector approximated by the polynomials, see Eq. (5a), and separated by equidistant steps. The vectors are purely real and are plotted over the whole surfaces $|a_+|$, $\Delta\phi$, $n_c$, see Fig. 5. Subsequently, these vectors are scaled by the distance between the steps in the state vector along each direction in order to avoid an overlap and create a square grid pattern. If these vectors create an ideal square grid then they can perfectly reconstruct the tangential vectors in Eq. (12). A small discrepancy is only found in Fig. 5(c) for small values of $|a_-|$, which can be explained by the third eigenvalue becoming comparable to the dominating pair of eigenvalues at these points, see Fig. 4. However, the two vectors $\vec{v}'_1$ and $\vec{v}'_2$ are found to approximate the tangential vectors over the whole surface as observed in Figure 5. Thus, the two degree-of-freedom picture is justified over the whole surface and shown to precisely reconstruct $d\vec{\psi}(\tau)/d\tau$. Therefore, the system of five nonlinear differential equations can be reduced to only two differential equations after the initial transition stage. The other three dimensions are functions of $n_w$ and $|a_-|$ and are presently approximated by polynomials. We note that the instantaneous eigenvalues/eigenvectors are not needed to reduce dimensionality of the system, but they provide an additional insight into the solution. Furthermore, the fact that the two instantaneous eigenvectors approximate the tangential vectors to the surfaces prove that the system dimensionality can be reduced to two.

Moreover, we note that although a 2D model can be used to describe the laser dynamics after the initial transition stage, there exists a parameter region in which even a 1D model is sufficient to replace the original 5D model after the initial transition stage. One may observe in Fig. 2 that for a large negative detuning $\Delta\omega_c$, the steady-state eigenvalues undergo transition from a complex conjugate pair of eigenvalues to two purely real eigenvalues. Then, one of the eigenvalues decreases rapidly, and the other one approaches zero. Therefore, for detunings $-2.05\gamma_T < \Delta\omega_c < -1.72\gamma_T$, there is a single steady-state eigenvalue that dominates and thus, the velocity vector can be described by a single eigenvector, see Eq. (9). In this case, the laser dynamics can be described by a single differential equation after the transition stage in which the contribution from the other four eigenvalues rapidly decays. For detunings $\Delta\omega_c < -2.05\gamma_T$, the lasing mode ceases to exist [7, 11, 13]. Thus, as the detuning $\Delta\omega_c$ increases, the steady-state eigenvalues transition from being purely real to a complex conjugate pair and the system evolves from a 1D to a 2D system.

## IV. ORIGIN OF THE LASER INSTABILITY

### A. Detection of periodic orbits

In what follows, we use the simplified 2D model, Eq. 7, to explain the origin of the laser instability that may

be observed even when all real parts of the steady-state eigenvalues are negative.

At first, the phase space of the Fano laser is scanned in search for periodic orbits. We choose our initial conditions as follows: 1) $|a_-|^{\text{initial}}$ is set to the steady-state value and 2) $n_w^{\text{initial}}$ is varied over the whole phase space along the purple line as shown in Fig. 6b). For each initial condition, we then compute the trajectory by solving Eq. (7) up to the point when $|a_-|(T) = |a_-|^{\text{initial}}$, where $T$ is the time corresponding to one cycle. Some of these trajectories are shown in Fig. 6(b) in different colours. Subsequently, we evaluate the shift $\Delta x = n_w^{\text{initial}} - n_w^{\text{cycle}}$ in the state vector after the time $T$. If the shift between the initial state and the state after one cycle is zero then we are at a periodic orbit or steady-state. On the other hand if it is non-zero it means that the state is approaching or departing from the steady-state/periodic orbit.

In the present case, when a pair of complex conjugate steady-state eigenvalues crosses the imaginary axis and their real parts become positive, the steady-state becomes unstable and the state is spiralling out towards the stable periodic orbit [56, 57]. Since the stable limit cycle exists after the critical bifurcation parameter, $\Delta\omega_c = 1.26\gamma_T$, the bifurcation is a supercritical Hopf bifurcation and has been observed in the Fano laser before [11]. However, when the bifurcation parameter is before the critical value in the supercritical Hopf bifurcation, i.e. the real parts of the eigenvalues are negative, only the stable fixed point is present in the phase space. Thus, it does not explain the self-pulsing of the laser when all of the real parts are negative. Figure 6a) shows the numerically evaluated shift $\Delta x$ in $n_w$ after one cycle of the trajectory. It is seen that there are five crossings with zero. These crossings are marked with blue, red and black dots. The single black dot indicates the steady-state, while the pairs of blue and red dots indicate periodic orbits. The outer periodic orbit, marked with a pair of blue dots, has been observed before and is known to be stable for a pair of complex conjugate steady-state eigenvalues with a positive real part [11]. Here, it is seen that for a strong enough perturbation of the initial conditions from the steady-state value, the state can still reach the outer periodic orbit despite all the steady-state eigenvalues having a negative real part and thus the steady-state being stable and attracting the state. Furthermore, we find an additional periodic orbit marked with a pair of red dots in Fig. 6a). The newly found periodic orbit separates the steady-state and the outer periodic orbit.

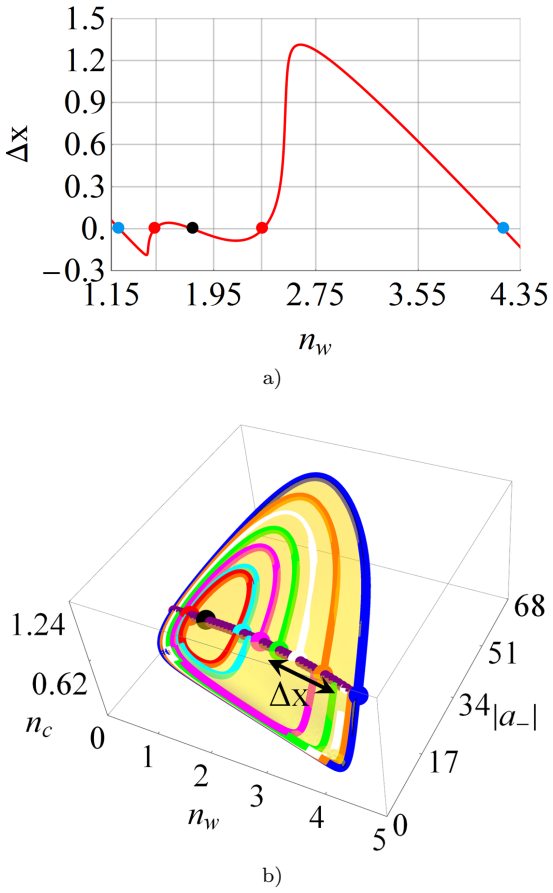


Figure 6. a) Numerically evaluated shift $\Delta x = n_w^{\text{initial}} - n_w^{\text{cycle}}$ in phase space after one cycle of the trajectory. The single black dot indicates the steady state, the pairs of red and blue dots indicate two periodic orbits. The initial value for $|a_-|$ is fixed and equal to the steady-state value, while the initial value for $n_w$ is varied. The initial states are marked on the surface along the purple line in b). b) Figure showing a single cycle of several trajectories (marked with different colours) initiated at different initial states along the purple line on the curved surface $n_c(|a_-|, n_w)$. The initial states are marked with dots. The definition of $\Delta x$ is also indicated.

### B. Stability of the orbits

We now prove the stability of the newly found orbit using the simplified 2D model. This is done by calculating the Floquet multipliers, $\lambda_f$, which tell us how the solution behaves in the vicinity of the periodic orbit, i.e., whether it diverges/converges from/towards the orbit [56, 57]. In order to compute the Floquet multipliers, we first obtain the fundamental solution matrix, $\mathbf{\Phi}(\tau)$, which can be determined using $d\mathbf{\Phi}(\tau)/d\tau = \boldsymbol{A}(\tau)\mathbf{\Phi}(\tau)$ and satisfies $d\vec{\psi}/d\tau = \mathbf{\Phi}(\tau)d\vec{\psi}/d\tau\big|_{\tau=0}$ with $\mathbf{\Phi}(0) = \boldsymbol{I}$. The Floquet multipliers are the eigenvalues of $\mathbf{\Phi}(\tau)$ evaluated at $\tau = T$, where $T$ is the period of the orbit.

If the Floquet multipliers are within the unit circle in the complex plane, the orbit is stable, otherwise it is unstable. The Floquet multipliers for the outer periodic orbit are $\lambda_{f1} = 0.04$ and $\lambda_{f2} = 1$ confirming its stability. On the other hand, the Floquet multipliers of the newly found orbit are $\lambda_{f1} = 2.31$ and $\lambda_{f2} = 1$, proving that this orbit is unstable. We note that for a periodic orbit there is always one of the Floquet multipliers for which $\lambda_f = 1$ and the corresponding eigenvector is tangential

to the periodic orbit. This neutral stability accounts for the possibility of drift along the periodic orbit [56].

Furthermore, we study the stability of the newly found orbit with variation of the detuning $\Delta\omega_c$. It is observed that the Floquet multiplier cross the unit circle along the real axis in the complex plane. This indicates an exchange of instability [58]. Indeed, as $\Delta\omega_c$ decreases, see Fig. 2, the newly found unstable periodic orbit increases in size. Eventually, it collapses with the stable periodic orbit. Both obits are annihilated and only the stable steady-state remains present in the phase space. On the other hand, when $\Delta\omega_c$ increases, the new orbit decreases in size. Eventually it collapses with the stable steady-state resulting in the steady-state becoming unstable. This behaviour is a signature of a Bautin bifurcation, also known as generalized Hopf bifurcation [17, 18]. A Bautin bifurcation is characterized by a presence of two orbits and an equilibrium point (steady-state) in phase space. We note that a Bautin bifurcation cannot be detected by merely monitoring the eigenvalues [17, 18]. Upon the external parameter variation, $\Delta\omega_c$, an inner orbit may collide with an outer orbit and annihilate or exchange stability with an equilibrium point. We note that since each $\Delta\omega_c$ results in different solutions $(\omega_s, N_s)$ of the oscillation condition in Eq. (1), we adjust the polynomial approximation of the surface in each case.

The stability of the orbits can also be assessed based on Fig. 6a). It is seen that if the model is initialized outside the orbit marked with the red dots, $n_w^{\text{cycle}}$ will increase after one cycle compared to the initial value. Thus, the state is repelled away from the orbit. If the model is initialized inside the orbit, $n_w^{\text{cycle}}$ will keep increasing with each cycle confirming that the newly found orbit is unstable.

## V. CONCLUSION

We demonstrate that after a fast initial transient the dynamics of the recently realized Fano laser [10] are confined to a 2D center manifold. Dimension of the center manifold follows the number of steady-state eigenvalues, real parts of which cross zero. We show that there are two steady-state eigenvalues with real parts crossing zero, while the remaining three eigenvalues have negative real parts forming a stable manifold. The dynamics is attracting along the corresponding three directions and quickly tends to the curved surface, i.e. the center manifold, during the initial transition stage. Afterwards, the state vector is confined to the curved surface and can be solely described by two degrees of freedom. The surface geometry of the phase space can be approximated by the two eigenvectors of the linear stability matrix corresponding to the eigenvalues with the largest real parts. As the pulse develops, the instantaneous eigenvalues transition from a pair of purely real eigenvalues to a complex conjugate pair at the first exceptional point. The main part of the repeating pulse is bounded by two exceptional points with positive/negative real part of the eigenvalue at the beginning/end of the pulse, respectively. Moreover, the trajectory encounters four exceptional points during one period, ensuring that both, the eigenvalues and the eigenvectors, are periodic in $\tau$. Furthermore, we show that the 5D model used to describe the laser dynamics, after the initial transition stage, can be reduced to only 1D in part of the parameter space and evolves into a 2D model beyond the exceptional point of steady-state eigenvalues as the detuning $\Delta\omega_c$ increases. Moreover, we have used the simplified 2D model to associate the unknown source of laser instability with the newly found unstable periodic orbit, which arises due to a generalized Hopf (Bautin) bifurcation. These findings allow to better understand the laser dynamics and may lead to the design of new functionalities in nanolasers used for on-chip communications and sampling.

## ACKNOWLEDGMENTS

The authors would like to thank T. S. Rasmussen for helpful discussions on the implementation of the dynamic model. This work was supported by Villum Fonden via the Centre of Excellence NATEC (grant 8692) and Research Grants Council of Hong Kong through project C6013-18GF.

[1] D. A. B. Miller. Device Requirements for Optical Interconnects to Silicon Chips. *Proceedings of the IEEE*, 97(7):1166–1185, July 2009.

[2] Yoshihiro Akahane, Takashi Asano, Bong-Shik Song, and Susumu Noda. High-$Q$ photonic nanocavity in a two-dimensional photonic crystal. *Nature*, 425(6961):944–947, October 2003.

[3] Nguyen-Vi-Quynh Tran, Sylvain Combrié, and Alfredo De Rossi. Directive emission from high-$q$ photonic crystal cavities through band folding. *Phys. Rev. B*, 79:041101, Jan 2009.

[4] S. Matsuo, T. Sato, K. Takeda, A. Shinya, K. Nozaki, H. Taniyama, M. Notomi, K. Hasebe, and T. Kakitsuka. Ultralow Operating Energy Electrically Driven Photonic Crystal Lasers. *IEEE J. Sel. Top. Quant.*, 19(4):4900311–4900311, July 2013.

[5] Hoon Jang, Indra Karnadi, Putu Pramudita, Jung-Hwan Song, Ki Soo Kim, and Yong-Hee Lee. Sub-microWatt threshold nanoisland lasers. *Nat. Commun.*, 6(1), December 2015.

[6] Philippe Hamel, Samir Haddadi, Fabrice Raineri, Paul Monnier, Gregoire Beaudoin, Isabelle Sagnes, Ariel Lev-

enson, and Alejandro M. Yacomotti. Spontaneous mirror-symmetry breaking in coupled photonic-crystal nanolasers. *Nat. Photonics*, 9(5):311–315, May 2015.

[7] J. Mork, Y. Chen, and M. Heuck. Photonic crystal fano laser: Terahertz modulation and ultrashort pulse generation. *Phys. Rev. Lett.*, 113:163901, Oct 2014.

[8] U. Fano. Effects of Configuration Interaction on Intensities and Phase Shifts. *Physical Review*, 124(6):1866–1878, December 1961.

[9] Mikhail F. Limonov, Mikhail V. Rybin, Alexander N. Poddubny, and Yuri S. Kivshar. Fano resonances in photonics. *Nat. Photonics*, 11(9):543–554, September 2017.

[10] Yi Yu, Weiqi Xue, Elizaveta Semenova, Kresten Yvind, and Jesper Mørk. Demonstration of a self-pulsing photonic crystal Fano laser. *Nat. Photonics*, 11(2):81–84, February 2017.

[11] Thorsten S. Rasmussen, Yi Yu, and Jesper Mørk. Theory of Self-pulsing in Photonic Crystal Fano Lasers: Theory of Self-pulsing. *Laser Photonics Rev.*, 11(5):1700089, September 2017.

[12] Thorsten S. Rasmussen, Yi Yu, and Jesper Mørk. Modes, stability, and small-signal response of photonic crystal Fano lasers. *Opt. Express*, 26(13):16365, June 2018.

[13] J. Mørk, B. Tromborg, and J. Mark. Chaos in semiconductor lasers with optical feedback: theory and experiment. *IEEE Journal of Quantum Electronics*, 28(1):93–108, January 1992.

[14] Bernd Krauskopf. Bifurcation analysis of laser systems. In *AIP Conference Proceedings*, volume 548, pages 1–30, Texel, (The Netherlands), 2000. AIP.

[15] S. Wieczorek, B. Krauskopf, T.B. Simpson, and D. Lenstra. The dynamical complexity of optically injected semiconductor lasers. *Physics Reports*, 416(1-2):1–128, September 2005.

[16] Hartmut Erzgräber, Bernd Krauskopf, and Daan Lenstra. Bifurcation Analysis of a Semiconductor Laser with Filtered Optical Feedback. *SIAM Journal on Applied Dynamical Systems*, 6(1):1–28, January 2007.

[17] W. Govaerts, Yu. A. Kuznetsov, and B. Sijnave. Numerical Methods for the Generalized Hopf Bifurcation. *SIAM Journal on Numerical Analysis*, 38(1):329–346, January 2000.

[18] Yuri Kuznetsov. *Elements of Applied Bifurcation Theory*. Springer, New York, 3rd edition edition, June 2004.

[19] Shanhui Fan, Wonjoo Suh, and J. D. Joannopoulos. Temporal coupled-mode theory for the Fano resonance in optical resonators. *J. Opt. Soc. Am. A, JOSAA*, 20(3):569–572, March 2003.

[20] Wonjoo Suh, Zheng Wang, and Shanhui Fan. Temporal coupled-mode theory and the presence of non-orthogonal modes in lossless multimode cavities. *IEEE Journal of Quantum Electronics*, 40(10):1511–1518, October 2004.

[21] Philip Trost Kristensen, Jakob Rosenkrantz de Lasson, Mikkel Heuck, Niels Gregersen, and Jesper Mørk. On the Theory of Coupled Modes in Optical Cavity-Waveguide Structures. *Journal of Lightwave Technology*, 35(19):4247–4259, October 2017.

[22] B. Tromborg, H. Olesen, Xing Pan, and S. Saito. Transmission line description of optical feedback and injection locking for Fabry-Perot and DFB lasers. *IEEE Journal of Quantum Electronics*, 23(11):1875–1889, November 1987.

[23] Philip McCord Morse, Herman Feshbach, and G. P. Harnwell. *Methods of Theoretical Physics, Part I*. McGraw-Hill Book Company, Boston, Mass, June 1953.

[24] S. Ibáñez and J. G. Muga. Adiabaticity condition for non-hermitian hamiltonians. *Phys. Rev. A*, 89:033403, Mar 2014.

[25] George B. Arfken and Hans J. Weber. *Mathematical Methods for Physicists, 6th Edition*. Academic Press, Boston, 6th edition edition, July 2005.

[26] C. Dembowski, H.-D. Gräf, H. L. Harney, A. Heine, W. D. Heiss, H. Rehfeld, and A. Richter. Experimental Observation of the Topological Structure of Exceptional Points. *Phys. Rev. Lett.*, 86(5):787–790, January 2001.

[27] W.D. Heiss. Exceptional Points – Their Universal Occurrence and Their Physical Significance. *Czechoslovak Journal of Physics*, 54(10):1091–1099, October 2004.

[28] M.V. Berry. Physics of Nonhermitian Degeneracies. *Czechoslovak Journal of Physics*, 54(10):1039–1047, October 2004.

[29] W D Heiss. The physics of exceptional points. *Journal of Physics A: Mathematical and Theoretical*, 45(44):444016, November 2012.

[30] M. Liertzer, Li Ge, A. Cerjan, A. D. Stone, H. E. Türeci, and S. Rotter. Pump-induced exceptional points in lasers. *Phys. Rev. Lett.*, 108:173901, Apr 2012.

[31] Carl M Bender, M V Berry, and Aikaterini Mandilara. Generalized PT symmetry and real spectra. *Journal of Physics A: Mathematical and General*, 35(31):L467–L471, August 2002.

[32] Christian E. Rüter, Konstantinos G. Makris, Ramy El-Ganainy, Demetrios N. Christodoulides, Mordechai Segev, and Detlef Kip. Observation of parity–time symmetry in optics. *Nat. Phys.*, 6(3):192–195, March 2010.

[33] Liang Feng, Ramy El-Ganainy, and Li Ge. Non-Hermitian photonics based on parity–time symmetry. *Nat. Photonics*, 11(12):752–762, December 2017.

[34] Ramy El-Ganainy, Konstantinos G. Makris, Mercedeh Khajavikhan, Ziad H. Musslimani, Stefan Rotter, and Demetrios N. Christodoulides. Non-Hermitian physics and PT symmetry. *Nat. Phys.*, 14(1):11–19, January 2018.

[35] Shachar Klaiman, Uwe Günther, and Nimrod Moiseyev. Visualization of branch points in $\mathcal{PT}$-symmetric waveguides. *Phys. Rev. Lett.*, 101:080402, Aug 2008.

[36] M V Berry. Mode degeneracies and the Petermann excess-noise factor for unstable lasers. *J. Mod. Opt.*, 50(1):63–81, 2003.

[37] Kyoung-Ho Kim, Min-Soo Hwang, Ha-Reem Kim, Jae-Hyuck Choi, You-Shin No, and Hong-Gyu Park. Direct observation of exceptional points in coupled photonic-crystal lasers with asymmetric optical gains. *Nat. Commun.*, 7:13893, December 2016.

[38] R. Lefebvre, O. Atabek, M. Šindelka, and N. Moiseyev. Resonance coalescence in molecular photodissociation. *Phys. Rev. Lett.*, 103:123003, Sep 2009.

[39] T Stehmann, W D Heiss, and F G Scholtz. Observation of exceptional points in electronic circuits. *Journal of Physics A: Mathematical and General*, 37(31):7813–7819, August 2004.

[40] H. Xu, D. Mason, Luyao Jiang, and J. G. E. Harris. Topological energy transfer in an optomechanical system with exceptional points. *Nature*, 537(7618):80–83, September 2016.

[41] W. D. Heiss. Repulsion of resonance states and exceptional points. *Phys. Rev. E*, 61(1):929–932, January 2000.

[42] Ingrid Rotter. A non-Hermitian Hamilton operator and the physics of open quantum systems. *Journal of Physics*

*A: Mathematical and Theoretical*, 42(15):153001, April 2009.

[43] Chong, Y. D. and Ge, Li and Stone, A. Douglas. $\mathcal{PT}$-Symmetry Breaking and Laser-Absorber Modes in Optical Scattering Systems. *Phys. Rev. Lett.*, 108(26):269902, June 2012.

[44] G. W. Hanson, A. B. Yakovlev, M. A. K. Othman and F. Capolino. Exceptional Points of Degeneracy and Branch Points for Coupled Transmission Lines—Linear-Algebra and Bifurcation Theory Perspectives. *IEEE Transactions on Antennas and Propagation*, 67(2):1025–1034, February 2019.

[45] U. Bandelow, H.J. Wunsche, and H. Wenzel. Theory of selfpulsations in two-section DFB lasers. *IEEE Photonics Technology Letters*, 5(10):1176–1179, October 1993.

[46] H. Wenzel, U. Bandelow, H.-J. Wunsche, and J. Rehberg. Mechanisms of fast self pulsations in two-section DFB lasers. *IEEE Journal of Quantum Electronics*, 32(1):69–78, January 1996.

[47] L. Feng, Z. J. Wong, R.-M. Ma, Y. Wang, and X. Zhang. Single-mode laser by parity-time symmetry breaking. *Science*, 346(6212):972–975, November 2014.

[48] H. Hodaei, M.-A. Miri, M. Heinrich, D. N. Christodoulides, and M. Khajavikhan. Parity-time-symmetric microring lasers. *Science*, 346(6212):975–978, November 2014.

[49] John Guckenheimer and Philip Holmes. *Nonlinear oscillations, dynamical systems, and bifurcations of vector fields*. Springer-Verlag, New York, October 1983.

[50] Uwe Günther, Ingrid Rotter, and Boris F Samsonov. Projective Hilbert space structures at exceptional points. *Journal of Physics A: Mathematical and Theoretical*, 40(30):8815–8833, July 2007.

[51] F Keck, H J Korsch, and S Mossmann. Unfolding a diabolic point: a generalized crossing scenario. *Journal of Physics A: Mathematical and General*, 36(8):2125–2137, February 2003.

[52] Markus Müller and Ingrid Rotter. Exceptional points in open quantum systems. *Journal of Physics A: Mathematical and Theoretical*, 41(24):244018, June 2008.

[53] Henri Menke, Marcel Klett, Holger Cartarius, Jörg Main, and Günter Wunner. State flip at exceptional points in atomic spectra. *Phys. Rev. A*, 93:013401, Jan 2016.

[54] W. D. Heiss, M. Müller, and I. Rotter. Collectivity, phase transitions, and exceptional points in open quantum systems. *Physical Review E*, 58(3):2894–2901, September 1998.

[55] W.D. Heiss. Phases of wave functions and level repulsion. *The European Physical Journal D - Atomic, Molecular and Optical Physics*, 7(1):1–4, August 1999.

[56] Paul Glendinning. *Stability, Instability and Chaos: An Introduction to the Theory of Nonlinear Differential Equations*. Cambridge University Press, Cambridge England ; New York, 1 edition edition, November 1994.

[57] Gerard Iooss and Daniel D. Joseph. *Elementary Stability and Bifurcation Theory*. Springer, New York, 2nd edition edition, October 1997.

[58] R. Seydel. *Practical bifurcation and stability analysis*. Number 5 in Interdisciplinary applied mathematics. Springer, New York, 3rd ed edition, 2010. OCLC: ocn462919396.

# Bibliography

[1] A. Einstein. “Zur Quantentheorie der Strahlung”. In: *Physikalische Zeitschrift* 18 (1917).

[2] A. L. Schawlow and C. H. Townes. “Infrared and Optical Masers”. In: *Physical Review* 112.6 (Dec. 15, 1958), pp. 1940–1949.

[3] S. Mor Cases, K. Jianwattananukul, K. Saenyot, S. Lekchaum, and K. Locharoenrat. “Portable laser 1-D barcode scanner for material identification”. In: *Materials Today: Proceedings*. The 3rd International Conference on Applied Physics and Materials Applications (ICAPMA 2017), 31 May–2 June 2017 5.7 (Jan. 1, 2018), pp. 15143–15148.

[4] J. Soo Hong et al. “Long pulsed 1064 nm Nd:YAG laser treatment for wrinkle reduction and skin laxity: Evaluation of new parameters”. In: *International Journal of Dermatology* 54 (Dec. 1, 2014).

[5] C. Rüffler and K. Gürs. “Cutting and welding using a CO2 laser”. In: *Optics & Laser Technology* 4.6 (Dec. 1, 1972), pp. 265–269.

[6] H. Lee, C. Huat Joel Lim, M. J. Low, N. Tham, M. Vadakke Matham, and Y.-J. Kim. “Lasers in additive manufacturing: A review”. In: *International Journal of Precision Engineering and Manufacturing-Green Technology* 4 (July 1, 2017), pp. 307–322.

[7] J. C. Brock and S. J. Purkis. “The Emerging Role of Lidar Remote Sensing in Coastal Research and Resource Management”. In: *Journal of Coastal Research* (Nov. 1, 2009), pp. 1–5.

[8] A. E. Ortiz, R. R. Anderson, C. DiGiorgio, S. I. B. Jiang, F. Shafiq, and M. M. Avram. “An expanded study of long-pulsed 1064 nm Nd:YAG laser treatment of basal cell carcinoma”. In: *Lasers in Surgery and Medicine* 50.7 (Sept. 1, 2018), pp. 727–731.

[9] J. Zhang, M. Gecevičius, M. Beresna, and P. G. Kazansky. “5D Data Storage by Ultrafast Laser Nanostructuring in Glass”. In: *CLEO: 2013 Postdeadline*. San Jose, California: OSA, 2013, CTh5D.9.

[10] W.-C. Wang, H.-Y. Wang, and G.-R. Lin. “Ultrahigh-speed violet laser diode based free-space optical communication beyond 25 Gbit/s”. In: *Scientific Reports* 8.1 (Sept. 3, 2018), p. 13142.

[11] T. H. Maiman. “Stimulated Optical Radiation in Ruby”. In: *Nature* 187.4736 (Aug. 1960), pp. 493–494.

[12] A. Mereuta et al. “Increasing single mode power of 13-$\mu$m VCSELs by output coupling optimization”. In: *Optics Express* 23.9 (May 4, 2015), p. 10900.

[13] M. Grabherr et al. “High-power VCSELs: single devices and densely packed 2-D-arrays”. In: *IEEE Journal of Selected Topics in Quantum Electronics* 5.3 (May 1999), pp. 495–502.

[14] H. Moench et al. “High-power VCSEL systems and applications”. In: ed. by M. S. Zediker. San Francisco, California, United States, Mar. 13, 2015, 93480W..

[15] J.-F. Seurin et al. “High-power high-efficiency 2D VCSEL arrays”. In: ed. by C. Lei and J. K. Guenter. San Jose, CA, Feb. 7, 2008, p. 690808.

[16] A. Onomura, M. Arai, T. Kondo, A. Matsutani, T. Miyamoto, and F. Koyama. “Densely Integrated Multiple-Wavelength Vertical-Cavity Surface-Emitting Laser Array”. In: *Japanese Journal of Applied Physics* 42 (Part 2, No. 5B May 15, 2003), pp. L529–L531.

[17] F. Koyama. “VCSEL Integration for Silicon Photonics”. In: *3rd IEEE International Conference on Group IV Photonics, 2006.* Sept. 2006, pp. 194–196.

[18] J. Jewell, J. Harbison, A. Scherer, Y. Lee, and L. Florez. “Vertical-cavity surface-emitting lasers: Design, growth, fabrication, characterization”. In: *IEEE Journal of Quantum Electronics* 27.6 (June 1991), pp. 1332–1346.

[19] A. E. Siegman. “Defining, measuring, and optimizing laser beam quality”. In: ed. by A. Bhowmik. Los Angeles, CA, Feb. 5, 1993, pp. 2–12.

[20] K. Otsuka et al. “High-Power Surface-Emitting Photonic Crystal Laser”. In: *LEOS 2007 - IEEE Lasers and Electro-Optics Society Annual Meeting Conference Proceedings.* Lake Buena Vista, FL, USA: IEEE, Oct. 2007, pp. 562–563.

[21] K. Hirose, Y. Liang, Y. Kurosaka, A. Watanabe, T. Sugiyama, and S. Noda. “Watt-class high-power, high-beam-quality photonic-crystal lasers”. In: *Nature Photonics* 8.5 (May 2014), pp. 406–411.

[22] S. Noda, K. Kitamura, T. Okino, D. Yasuda, and Y. Tanaka. “Photonic-Crystal Surface-Emitting Lasers: Review and Introduction of Modulated-Photonic Crystals”. In: *IEEE Journal of Selected Topics in Quantum Electronics* 23.6 (Nov. 2017), pp. 1–7.

[23] M. Imada, S. Noda, A. Chutinan, T. Tokuda, M. Murata, and G. Sasaki. “Coherent two-dimensional lasing action in surface-emitting laser with triangular-lattice photonic crystal structure”. In: *Applied Physics Letters* 75.3 (July 19, 1999), pp. 316–318.

[24] K. Sakai, E. Miyai, T. Sakaguchi, D. Ohnishi, T. Okano, and S. Noda. “Lasing band-edge identification for a surface-emitting photonic crystal laser”. In: *IEEE Journal on Selected Areas in Communications* 23.7 (July 2005), pp. 1335–1340.

[25] Y. Plotnik et al. “Experimental Observation of Optical Bound States in the Continuum”. In: *Physical Review Letters* 107.18 (Oct. 25, 2011).

[26] J. Lee et al. “Observation and Differentiation of Unique High- Q Optical Resonances Near Zero Wave Vector in Macroscopic Photonic Crystal Slabs”. In: *Physical Review Letters* 109.6 (Aug. 8, 2012).

[27] C. W. Hsu, B. Zhen, A. D. Stone, J. D. Joannopoulos, and M. Soljačić. “Bound states in the continuum”. In: *Nature Reviews Materials* 1.9 (Sept. 2016).

[28] L. Ni, Z. Wang, C. Peng, and Z. Li. "Tunable optical bound states in the continuum beyond in-plane symmetry protection". In: *Physical Review B* 94.24 (Dec. 30, 2016).

[29] Y. Kurosaka, K. Sakai, E. Miyai, and S. Noda. "Controlling vertical optical confinement in two-dimensional surface-emitting photonic-crystal lasers by shape of air holes". In: *Optics Express* 16.22 (Oct. 27, 2008), p. 18485.

[30] S. Iwahashi, K. Sakai, Y. Kurosaka, and S. Noda. "Air-hole design in a vertical direction for high-power two-dimensional photonic-crystal surface-emitting lasers". In: *Journal of the Optical Society of America B* 27.6 (June 1, 2010), p. 1204.

[31] C. Peng, Y. Liang, K. Sakai, S. Iwahashi, and S. Noda. "Coupled-wave analysis for photonic-crystal surface-emitting lasers on air holes with arbitrary sidewalls". In: *Optics Express* 19.24 (Nov. 21, 2011), p. 24672.

[32] Y. Kurosaka et al. "On-chip beam-steering photonic-crystal lasers". In: *Nature Photonics* 4.7 (July 2010), pp. 447–450.

[33] T. Okino, K. Kitamura, K. Kitamura, D. Yasuda, Y. Liang, and S. Noda. "Position-modulated Photonic-crystal Lasers and Control of Beam Direction and Polarization". In: *CLEO: 2015 (2015), paper SW1F.1.* Optical Society of America, May 10, 2015, SW1F.1.

[34] S. Noda. "Polarization Mode Control of Two-Dimensional Photonic Crystal Laser by Unit Cell Structure Design". In: *Science* 293.5532 (Aug. 10, 2001), pp. 1123–1125.

[35] M. Yokoyama and S. Noda. "Polarization mode control of two-dimensional photonic crystal laser having a square lattice structure". In: *IEEE Journal of Quantum Electronics* 39.9 (Sept. 2003), pp. 1074–1080.

[36] E. Miyai, K. Sakai, T. Okano, W. Kunishi, D. Ohnishi, and S. Noda. "Lasers producing tailored beams: Photonics". In: *Nature* 441.7096 (June 2006), pp. 946–946.

[37] S. Iwahashi, Y. Kurosaka, K. Sakai, K. Kitamura, N. Takayama, and S. Noda. "Higher-order vector beams produced by photonic-crystal lasers". In: *Optics Express* 19.13 (June 20, 2011), p. 11963.

[38] E. Miyai and S. Noda. "Phase-shift effect on a two-dimensional surface-emitting photonic-crystal laser". In: *Applied Physics Letters* 86.11 (Mar. 14, 2005), p. 111113.

[39] E. Miyai, K. Sakai, T. Okano, W. Kunishi, D. Ohnishi, and S. Noda. "Linearly-Polarized Single-Lobed Beam in a Surface-Emitting Photonic-Crystal Laser". In: *Applied Physics Express* 1 (May 23, 2008), p. 062002.

[40] Y. Yang, C. Peng, Y. Liang, Z. Li, and S. Noda. "Analytical Perspective for Bound States in the Continuum in Photonic Crystal Slabs". In: *Physical Review Letters* 113.3 (July 15, 2014).

[41] X. Gao et al. "Formation mechanism of guided resonances and bound states in the continuum in photonic crystal slabs". In: *Scientific Reports* 6.1 (Oct. 2016).

[42] V. Mocella and S. Romano. "Giant field enhancement in photonic resonant lattices". In: *Physical Review B* 92.15 (Oct. 12, 2015).

[43] J. W. Yoon, S. H. Song, and R. Magnusson. "Critical field enhancement of asymptotic optical bound states in the continuum". In: *Scientific Reports* 5.1 (Nov. 2016).

[44] E. N. Bulgakov and D. N. Maksimov. "Light enhancement by quasi-bound states in the continuum in dielectric arrays". In: *Optics Express* 25.13 (June 26, 2017), p. 14134. arXiv: 1702.05990.

[45] J. Beermann, S. M. Novikov, K. Leosson, and S. I. Bozhevolnyi. "Surface enhanced Raman imaging: periodic arrays and individual metal nanoparticles". In: *Optics Express* 17.15 (July 20, 2009), pp. 12698–12705.

[46] C. J. Chang-Hasnain and W. Yang. "High-contrast gratings for integrated optoelectronics". In: *Advances in Optics and Photonics* 4.3 (Sept. 30, 2012), pp. 379–440.

[47] M. Pu, L. Ottaviano, E. Semenova, and K. Yvind. "Efficient frequency comb generation in AlGaAs-on-insulator". In: *Optica* 3.8 (Aug. 20, 2016), pp. 823–826.

[48] J. Li, D. Fattal, M. Fiorentino, and R. G. Beausoleil. "Strong Optical Confinement between Nonperiodic Flat Dielectric Gratings". In: *Physical Review Letters* 106.19 (May 10, 2011), p. 193901.

[49] Y. Liang, C. Peng, K. Sakai, S. Iwahashi, and S. Noda. "Three-dimensional coupled-wave analysis for square-lattice photonic crystal surface emitting lasers with transverse-electric polarization: finite-size effects". In: *Optics Express* 20.14 (July 2, 2012), p. 15945.

[50] Y. Liang, T. Okino, K. Kitamura, C. Peng, K. Ishizaki, and S. Noda. "Mode stability in photonic-crystal surface-emitting lasers with large $\kappa$ 1DL". in: *Applied Physics Letters* 104.2 (Jan. 13, 2014), p. 021102.

[51] J. Gelleta, Y. Liang, H. Kitagawa, and S. Noda. "Influence of external reflection on the TE mode of photonic crystal surface-emitting lasers". In: *Journal of the Optical Society of America B* 32.7 (July 1, 2015), p. 1435.

[52] S.-L. Chua, L. Lu, J. Bravo-Abad, J. D. Joannopoulos, and M. Soljačić. "Larger-area single-mode photonic crystal surface-emitting lasers enabled by an accidental Dirac point". In: *Optics Letters* 39.7 (Apr. 1, 2014), p. 2072.

[53] A. K. Geim and K. S. Novoselov. "The rise of graphene". In: *Nature Materials* 6.3 (Mar. 2007), pp. 183–191.

[54] T. Ochiai and M. Onoda. "Photonic analog of graphene model and its extension: Dirac cone, symmetry, and edge states". In: *Physical Review B* 80.15 (Oct. 2, 2009).

[55] X. Huang, Y. Lai, Z. H. Hang, H. Zheng, and C. T. Chan. "Dirac cones induced by accidental degeneracy in photonic crystals and zero-refractive-index materials". In: *Nature Materials* 10.8 (Aug. 2011), pp. 582–586.

[56] C. T. Chan, Z. H. Hang, and X. Huang. "Dirac Dispersion in Two-Dimensional Photonic Crystals". In: *Advances in OptoElectronics* 2012 (2012), pp. 1–11.

[57] K. Sakoda. "Proof of the universality of mode symmetries in creating photonic Dirac cones". In: *Optics Express* 20.22 (Oct. 22, 2012), p. 25181.

[58] W.-Y. He and C. T. Chan. "The Emergence of Dirac points in Photonic Crystals with Mirror Symmetry". In: *Scientific Reports* 5.1 (July 2015).

[59] Y. Li et al. "On-chip zero-index metamaterials". In: *Nature Photonics* 9.11 (Nov. 2015), pp. 738–742.

[60] B. Zhen et al. "Spawning rings of exceptional points out of Dirac cones". In: *Nature* 525.7569 (Sept. 2015), pp. 354–358.

[61] M. Berry. "Physics of Nonhermitian Degeneracies". In: *Czechoslovak Journal of Physics* 54.10 (Oct. 2004), pp. 1039–1047.

[62] I. Rotter. "A non-Hermitian Hamilton operator and the physics of open quantum systems". In: *Journal of Physics A: Mathematical and Theoretical* 42.15 (Apr. 17, 2009), p. 153001.

[63] C. E. Rüter, K. G. Makris, R. El-Ganainy, D. N. Christodoulides, M. Segev, and D. Kip. "Observation of parity–time symmetry in optics". In: *Nature Physics* 6.3 (Mar. 2010), pp. 192–195.

[64] N. Moiseyev. *Non-Hermitian Quantum Mechanics*. Cambridge University Press, Feb. 17, 2011.

[65] Z. Lin, H. Ramezani, T. Eichelkraut, T. Kottos, H. Cao, and D. N. Christodoulides. "Unidirectional Invisibility Induced by P T -Symmetric Periodic Structures". In: *Physical Review Letters* 106.21 (May 25, 2011).

[66] J. Gear et al. "Unidirectional zero reflection as gauged parity-time symmetry". In: *New Journal of Physics* 19.12 (2017), p. 123041.

[67] M. Liertzer, L. Ge, A. Cerjan, A. D. Stone, H. E. Türeci, and S. Rotter. "Pump-Induced Exceptional Points in Lasers". In: *Physical Review Letters* 108.17 (Apr. 24, 2012).

[68] L. Feng, Z. J. Wong, R.-M. Ma, Y. Wang, and X. Zhang. "Single-mode laser by parity-time symmetry breaking". In: *Science* 346.6212 (Nov. 21, 2014), pp. 972–975.

[69] H. Hodaei, M.-A. Miri, M. Heinrich, D. N. Christodoulides, and M. Khajavikhan. "Parity-time-symmetric microring lasers". In: *Science* 346.6212 (Nov. 21, 2014), pp. 975–978.

[70] J. Doppler et al. "Dynamically encircling an exceptional point for asymmetric mode switching". In: *Nature* 537.7618 (Sept. 2016), pp. 76–79.

[71] H. Xu, D. Mason, L. Jiang, and J. G. E. Harris. "Topological energy transfer in an optomechanical system with exceptional points". In: *Nature* 537.7618 (Sept. 2016), pp. 80–83.

[72] A. U. Hassan, B. Zhen, M. Soljačić, M. Khajavikhan, and D. N. Christodoulides. "Dynamically Encircling Exceptional Points: Exact Evolution and Polarization State Conversion". In: *Physical Review Letters* 118.9 (Mar. 3, 2017).

[73] L. Lu, J. D. Joannopoulos, and M. Soljačić. "Topological photonics". In: *Nature Photonics* 8.11 (Nov. 2014), pp. 821–829.

[74] B. Zhen, C. W. Hsu, L. Lu, A. D. Stone, and M. Soljačić. "Topological Nature of Optical Bound States in the Continuum". In: *Physical Review Letters* 113.25 (Dec. 18, 2014).

[75] K. Ding, G. Ma, M. Xiao, Z. Q. Zhang, and C. T. Chan. "Emergence, Coalescence, and Topological Properties of Multiple Exceptional Points and Their Experimental Realization". In: *Physical Review X* 6.2 (Apr. 12, 2016).

[76] E. N. Bulgakov and D. N. Maksimov. "Topological Bound States in the Continuum in Arrays of Dielectric Spheres". In: *Physical Review Letters* 118.26 (June 26, 2017).

[77] Y. Guo, M. Xiao, and S. Fan. "Topologically Protected Complete Polarization Conversion". In: *Physical Review Letters* 119.16 (Oct. 18, 2017).

[78] D. Leykam, K. Y. Bliokh, C. Huang, Y. D. Chong, and F. Nori. "Edge Modes, Degeneracies, and Topological Numbers in Non-Hermitian Systems". In: *Physical Review Letters* 118.4 (Jan. 23, 2017).

[79] H. Shen, B. Zhen, and L. Fu. "Topological Band Theory for Non-Hermitian Hamiltonians". In: *Physical Review Letters* 120.14 (Apr. 6, 2018). arXiv: 1706.07435.

[80] A. Taghizadeh and I.-S. Chung. "Quasi bound states in the continuum with few unit cells of photonic crystal slab". In: *Applied Physics Letters* 111.3 (July 17, 2017), p. 031114.

[81] S. Fan, W. Suh, and J. D. Joannopoulos. "Temporal coupled-mode theory for the Fano resonance in optical resonators". In: *JOSA A* 20.3 (Mar. 1, 2003), pp. 569–572.

[82] M. Heuck, P. T. Kristensen, Y. Elesin, and J. Mørk. "Improved switching using Fano resonances in photonic crystal structures". In: *Optics Letters* 38.14 (July 15, 2013), p. 2466.

[83] Y. Yu, W. Xue, E. Semenova, K. Yvind, and J. Mork. "Demonstration of a self-pulsing photonic crystal Fano laser". In: *Nature Photonics* 11.2 (Feb. 2017), pp. 81–84.

[84] U. Bandelow, H. Wunsche, and H. Wenzel. "Theory of selfpulsations in two-section DFB lasers". In: *IEEE Photonics Technology Letters* 5.10 (Oct. 1993), pp. 1176–1179.

[85] H. Wenzel and H.-J. Wunsche. "An equation for the amplitudes of the modes in semiconductor lasers". In: *IEEE Journal of Quantum Electronics* 30.9 (Sept. 1994), pp. 2073–2080.

[86] H.-J. Wuensche, U. Bandelow, H. Wenzel, and D. D. Marcenac. "Self pulsations by mode degeneracy in two-section DFB lasers". In: ed. by M. Osinski and W. W. Chow. San Jose, CA, June 19, 1995, pp. 195–206.

[87] H. Wenzel, U. Bandelow, H.-J. Wunsche, and J. Rehberg. "Mechanisms of fast self pulsations in two-section DFB lasers". In: *IEEE Journal of Quantum Electronics* 32.1 (Jan. 1996), pp. 69–78.

[88] T. J. Milburn, J. Doppler, C. A. Holmes, S. Portolan, S. Rotter, and P. Rabl. "General description of quasiadiabatic dynamical phenomena near exceptional points". In: *Physical Review A* 92.5 (Nov. 30, 2015).

[89] G. Bautista et al. "Nonlinear microscopy using cylindrical vector beams: Applications to three-dimensional imaging of nanostructures". In: *Optics Express* 25.11 (May 29, 2017), p. 12463.

[90] B. J. Roxworthy and K. C. T. Jr. "Optical trapping with $\pi$-phase cylindrical vector beams". In: *New Journal of Physics* 12.7 (2010), p. 073012.

[91] R. Dorn, S. Quabis, and G. Leuchs. "Sharper Focus for a Radially Polarized Light Beam". In: *Physical Review Letters* 91.23 (Dec. 2, 2003).

[92] A. Kodigala, T. Lepetit, Q. Gu, B. Bahari, Y. Fainman, and B. Kanté. "Lasing action from photonic bound states in continuum". In: *Nature* 541.7636 (Jan. 2017), pp. 196–199.

[93] *COMSOL Multiphysics® Modeling Software 5.2a, COMSOL AB, Stockholm, Sweden, https://www.comsol.com/.*

[94] T. Sakaguchi et al. "Surface-Emitting Photonic-Crystal Laser with 35W Peak Power". In: *Conference on Lasers and Electro-Optics/International Quantum Electronics Conference*. Baltimore, Maryland: OSA, 2009, CTuH1.

[95] S. Klaiman, U. Günther, and N. Moiseyev. "Visualization of Branch Points in P T -Symmetric Waveguides". In: *Physical Review Letters* 101.8 (Aug. 21, 2008).

[96] M. V. Berry. "Mode degeneracies and the Petermann excess-noise factor for unstable lasers". In: (), p. 20.

[97] K.-H. Kim, M.-S. Hwang, H.-R. Kim, J.-H. Choi, Y.-S. No, and H.-G. Park. "Direct observation of exceptional points in coupled photonic-crystal lasers with asymmetric optical gains". In: *Nature Communications* 7 (Dec. 21, 2016), p. 13893.

[98] R. Lefebvre, O. Atabek, M. Šindelka, and N. Moiseyev. "Resonance Coalescence in Molecular Photodissociation". In: *Physical Review Letters* 103.12 (Sept. 16, 2009).

[99] M. Lawrence et al. "Manifestation of P T Symmetry Breaking in Polarization Space with Terahertz Metasurfaces". In: *Physical Review Letters* 113.9 (Aug. 28, 2014).

[100] M. Kang, J. Chen, and Y. D. Chong. "Chiral exceptional points in metasurfaces". In: *Physical Review A* 94.3 (Sept. 19, 2016).

[101] T. Stehmann, W. D. Heiss, and F. G. Scholtz. "Observation of exceptional points in electronic circuits". In: *Journal of Physics A: Mathematical and General* 37.31 (Aug. 6, 2004), pp. 7813–7819.

[102] v. Neumann. "Noteworthy discrete eigen values". In: *Physikalische Zeitschrift* 30 (1929), pp. 465–467.

[103] A. G. Every and A. A. Maznev. "Elastic waves at periodically-structured surfaces and interfaces of solids". In: *AIP Advances* 4.12 (Nov. 11, 2014), p. 124401.

[104] R. Porter and D. Evans. "Embedded Rayleigh–Bloch surface waves along periodic rectangular arrays". In: *Wave Motion* 43.1 (Nov. 2005), pp. 29–50.

[105] M. G. Silveirinha. "Trapping light in open plasmonic nanostructures". In: *Physical Review A* 89.2 (Feb. 11, 2014).

[106] F. Monticone and A. Alù. "Embedded Photonic Eigenvalues in 3D Nanostructures". In: *Physical Review Letters* 112.21 (May 29, 2014).

[107] J. D. Joannopoulos, ed. *Photonic crystals: molding the flow of light.* 2nd ed. Princeton: Princeton University Press, 2008.

[108] S. Fan and J. D. Joannopoulos. "Analysis of guided resonances in photonic crystal slabs". In: *Physical Review B* 65.23 (June 7, 2002).

[109] T. Ochiai and K. Sakoda. "Dispersion relation and optical transmittance of a hexagonal photonic crystal slab". In: *Physical Review B* 63.12 (Mar. 12, 2001).

[110] C. W. Hsu et al. "Observation of trapped light within the radiation continuum". In: *Nature* 499.7457 (July 2013), pp. 188–191.

[111] E. Bulgakov, A. Sadreev, and D. Maksimov. "Light Trapping above the Light Cone in One-Dimensional Arrays of Dielectric Spheres". In: *Applied Sciences* 7.2 (Feb. 8, 2017), p. 147.

[112] J. Mork, Y. Chen, and M. Heuck. "Photonic Crystal Fano Laser: Terahertz Modulation and Ultrashort Pulse Generation". In: *Physical Review Letters* 113.16 (Oct. 15, 2014).

[113] Y. Sato, Y. Tanaka, J. Upham, Y. Takahashi, T. Asano, and S. Noda. "Strong coupling between distant photonic nanocavities and its dynamic control". In: *Nature Photonics* 6.1 (Jan. 2012), pp. 56–61.

[114] H. Zheng and H. U. Baranger. "Persistent Quantum Beats and Long-Distance Entanglement from Waveguide-Mediated Interactions". In: *Physical Review Letters* 110.11 (Mar. 12, 2013), p. 113601.

[115] H. Friedrich and D. Wintgen. "Interfering resonances and bound states in the continuum". In: *Physical Review A* 32.6 (Dec. 1, 1985), pp. 3231–3242.

[116] F. Remacle, M. Munster, V. B. Pavlov-Verevkin, and M. Desouter-Lecomte. "Trapping in competitive decay of degenerate states". In: *Physics Letters A* 145.5 (Apr. 16, 1990), pp. 265–268.

[117] J. N. Winn, S. Fan, J. D. Joannopoulos, and E. P. Ippen. "Interband transitions in photonic crystals". In: *Physical Review B* 59.3 (Jan. 15, 1999), pp. 1551–1554.

[118] D. C. Marinica, A. G. Borisov, and S. V. Shabanov. "Bound States in the Continuum in Photonics". In: *Physical Review Letters* 100.18 (May 8, 2008).

[119] S.-L. Chua, Y. Chong, A. D. Stone, M. Soljacic, and J. Bravo-Abad. "Low-threshold lasing action in photonic crystal slabs enabled by Fano resonances". In: *Optics Express* 19.2 (Jan. 17, 2011), p. 1539.

[120] A. A. Yanik et al. "Seeing protein monolayers with naked eye through plasmonic Fano resonances". In: *Proceedings of the National Academy of Sciences* 108.29 (July 19, 2011), pp. 11784–11789.

[121] J. M. Foley, S. M. Young, and J. D. Phillips. "Symmetry-protected mode coupling near normal incidence for narrow-band transmission filtering in a dielectric grating". In: *Physical Review B* 89.16 (Apr. 9, 2014), p. 165111.

[122] H. Matsubara, S. Yoshimoto, H. Saito, Y. Jianglin, Y. Tanaka, and S. Noda. "GaN Photonic-Crystal Surface-Emitting Laser at Blue-Violet Wavelengths". In: *Science* 319.5862 (Jan. 25, 2008), pp. 445–447.

[123] O. Peleg, G. Bartal, B. Freedman, O. Manela, M. Segev, and D. N. Christodoulides. "Conical Diffraction and Gap Solitons in Honeycomb Photonic Lattices". In: *Physical Review Letters* 98.10 (Mar. 6, 2007), p. 103901.

[124] F. D. M. Haldane and S. Raghu. "Possible Realization of Directional Optical Waveguides in Photonic Crystals with Broken Time-Reversal Symmetry". In: *Physical Review Letters* 100.1 (Jan. 10, 2008).

[125] S. Raghu and F. D. M. Haldane. "Analogs of quantum-Hall-effect edge states in photonic crystals". In: *Physical Review A* 78.3 (Sept. 23, 2008), p. 033834.

[126] M. J. Collins, F. Zhang, R. Bojko, L. Chrostowski, and M. C. Rechtsman. "Integrated optical Dirac physics via inversion symmetry breaking". In: *Physical Review A* 94.6 (Dec. 13, 2016).

[127] J. Mei, Y. Wu, C. T. Chan, and Z.-Q. Zhang. "First-principles study of Dirac and Dirac-like cones in phononic and photonic crystals". In: *Physical Review B* 86.3 (July 24, 2012).

[128] Y. Wu, J. Li, Z.-Q. Zhang, and C. T. Chan. "Effective medium theory for magnetodielectric composites: Beyond the long-wavelength limit". In: *Physical Review B* 74.8 (Aug. 15, 2006).

[129] J. Bravo-Abad, J. D. Joannopoulos, and M. Soljacic. "Enabling single-mode behavior over large areas with photonic Dirac cones". In: *Proceedings of the National Academy of Sciences* 109.25 (June 19, 2012), pp. 9761–9765. arXiv: 1204.0500.

[130] W. Heiss. "Exceptional Points – Their Universal Occurrence and Their Physical Significance". In: *Czechoslovak Journal of Physics* 54.10 (Oct. 2004), pp. 1091–1099.

[131] W. D. Heiss. "The physics of exceptional points". In: *Journal of Physics A: Mathematical and Theoretical* 45.44 (Nov. 9, 2012), p. 444016.

[132] C. Dembowski et al. "Experimental Observation of the Topological Structure of Exceptional Points". In: *Physical Review Letters* 86.5 (Jan. 29, 2001), pp. 787–790.

[133] C. Dembowski et al. "Observation of a Chiral State in a Microwave Cavity". In: *Physical Review Letters* 90.3 (Jan. 23, 2003).

[134] W. D. Heiss, M. Müller, and I. Rotter. "Collectivity, phase transitions, and exceptional points in open quantum systems". In: *Physical Review E* 58.3 (Sept. 1, 1998), pp. 2894–2901.

[135] W. Heiss. "Phases of wave functions and level repulsion". In: *The European Physical Journal D - Atomic, Molecular and Optical Physics* 7.1 (Aug. 1, 1999), pp. 1–4.

[136] F. Keck, H. J. Korsch, and S. Mossmann. "Unfolding a diabolic point: a generalized crossing scenario". In: *Journal of Physics A: Mathematical and General* 36.8 (Feb. 28, 2003), pp. 2125–2137.

[137] U. Günther, I. Rotter, and B. F. Samsonov. "Projective Hilbert space structures at exceptional points". In: *Journal of Physics A: Mathematical and Theoretical* 40.30 (July 27, 2007), pp. 8815–8833.

[138] M. Müller and I. Rotter. "Exceptional points in open quantum systems". In: *Journal of Physics A: Mathematical and Theoretical* 41.24 (June 20, 2008), p. 244018.

[139] Y. Chen, J. R. de Lasson, N. Gregersen, and J. Mørk. "Impact of slow-light enhancement on optical propagation in active semiconductor photonic-crystal waveguides". In: *Physical Review A* 92.5 (Nov. 17, 2015).

[140] T. Xu, S. Yang, S. V. Nair, and H. E. Ruda. "Confined modes in finite-size photonic crystals". In: *Physical Review B* 72.4 (July 18, 2005).

[141] A. Taghizadeh, J. Mørk, and I.-S. Chung. "Vertical-cavity in-plane heterostructures: Physics and applications". In: *Applied Physics Letters* 107.18 (Nov. 2, 2015), p. 181107.

[142] P. Bardella and I. Montrosset. "A New Design Procedure for DBR Lasers Exploiting the Photon–Photon Resonance to Achieve Extended Modulation Bandwidth". In: *IEEE Journal of Selected Topics in Quantum Electronics* 19.4 (July 2013), pp. 1502408–1502408.

[143] H. Dalir and F. Koyama. "High-speed operation of bow-tie-shaped oxide aperture VCSELs with photon–photon resonance". In: *Applied Physics Express* 7.2 (Feb. 1, 2014), p. 022102.

[144] A. Taghizadeh, J. Mørk, and I.-S. Chung. "Numerical Investigation of Vertical Cavity Lasers With High-Contrast Gratings Using the Fourier Modal Method". In: *Journal of Lightwave Technology* 34.18 (Sept. 15, 2016), pp. 4240–4251.

[145] H.-Y. Ryu, M. Notomi, and Y.-H. Lee. "Finite-difference time-domain investigation of band-edge resonant modes in finite-size two-dimensional photonic crystal slab". In: *Physical Review B* 68.4 (July 31, 2003).

[146] U. Fano. "Sullo spettro di assorbimento dei gas nobili presso il limite dello spettro d'arco". In: *Il Nuovo Cimento* 12.3 (1935), pp. 154–161.

[147] U. Fano. "Effects of Configuration Interaction on Intensities and Phase Shifts". In: *Physical Review* 124.6 (Dec. 15, 1961), pp. 1866–1878.

[148] C. Ott et al. "Lorentz Meets Fano in Spectral Line Shapes: A Universal Phase and Its Laser Control". In: *Science* 340.6133 (May 10, 2013), pp. 716–720.

[149] M. F. Limonov, M. V. Rybin, A. N. Poddubny, and Y. S. Kivshar. "Fano resonances in photonics". In: *Nature Photonics* 11.9 (Sept. 1, 2017), pp. 543–554.

[150] Y. Yu, H. Hu, L. K. Oxenløwe, K. Yvind, and J. Mork. "Ultrafast all-optical modulation using a photonic-crystal Fano structure with broken symmetry". In: *Optics Letters* 40.10 (May 15, 2015), p. 2357.

[151] Y. Yu, Y. Chen, H. Hu, W. Xue, K. Yvind, and J. Mork. "Nonreciprocal transmission in a nonlinear photonic-crystal Fano structure with broken symmetry: Nonreciprocal transmission in a nonlinear Fano structure". In: *Laser & Photonics Reviews* 9.2 (Mar. 2015), pp. 241–247.

[152] S. Longhi. "Bound states in the continuum in a single-level Fano-Anderson model". In: *The European Physical Journal B* 57.1 (May 2007), pp. 45–51.

[153] S. Weimann et al. "Compact Surface Fano States Embedded in the Continuum of Waveguide Arrays". In: *Physical Review Letters* 111.24 (Dec. 10, 2013).

[154] Q. Xu, S. Sandhu, M. L. Povinelli, J. Shakya, S. Fan, and M. Lipson. "Experimental Realization of an On-Chip All-Optical Analogue to Electromagnetically Induced Transparency". In: *Physical Review Letters* 96.12 (Mar. 27, 2006).

[155] X. Yang, M. Yu, D.-L. Kwong, and C. W. Wong. "All-Optical Analog to Electromagnetically Induced Transparency in Multiple Coupled Photonic Crystal Cavities". In: *Physical Review Letters* 102.17 (Apr. 30, 2009).

[156] B. Peng, Ş. K. Özdemir, W. Chen, F. Nori, and L. Yang. "What is and what is not electromagnetically induced transparency in whispering-gallery microcavities". In: *Nature Communications* 5.1 (Dec. 2014).

[157] N. Caselli et al. "Generalized Fano lineshapes reveal exceptional points in photonic molecules". In: *Nature Communications* 9.1 (Dec. 2018).

[158] B. Maes et al. "Switching through symmetry breaking in coupled nonlinear micro-cavities". In: *Optics Express* 14.22 (2006), p. 10678.

[159] P. Hamel et al. "Spontaneous mirror-symmetry breaking in coupled photonic-crystal nanolasers". In: *Nature Photonics* 9.5 (May 2015), pp. 311–315.

[160] S. Longhi. "Transfer of light waves in optical waveguides via a continuum". In: *Physical Review A* 78.1 (July 10, 2008).

[161] F. Dreisow et al. "Adiabatic transfer of light via a continuum in optical waveguides". In: *Optics Letters* 34.16 (Aug. 15, 2009), p. 2405.

[162] *Lumerical FDTD Solutions 8.16.903, Lumerical Inc, Vancouver, BC, Canda, https://www.lumerical.com/.*

[163] Z. Zhang and M. Qiu. "Small-volume waveguide-section high Q microcavities in 2D photonic crystal slabs". In: *Optics Express* 12.17 (2004), p. 3988.

[164] K. Srinivasan and O. Painter. "Momentum space design of high-Q photonic crystal optical cavities". In: *Optics Express* 10.15 (July 29, 2002), p. 670.

[165] K. Srinivasan and O. Painter. "Fourier space design of high-Q cavities in standard and compressed hexagonal lattice photonic crystals". In: *Optics Express* 11.6 (Mar. 24, 2003), p. 579.

[166] Y. Akahane, T. Asano, B.-S. Song, and S. Noda. "High-Q photonic nanocavity in a two-dimensional photonic crystal". In: 425 (2003), p. 4.

[167] Y. Akahane, T. Asano, B.-S. Song, and S. Noda. "Fine-tuned high-Q photonic-crystal nanocavity". In: *Optics Express* 13.4 (2005), p. 1202.

[168] A. R. A. Chalcraft et al. “Mode structure of the L3 photonic crystal cavity”. In: *Applied Physics Letters* 90.24 (June 11, 2007), p. 241117.

[169] A. R. A. Chalcraft et al. “Mode structure of coupled L3 photonic crystal cavities”. In: *Optics Express* 19.6 (Mar. 14, 2011), pp. 5670–5675.

[170] J. Vuckovic, M. Loncar, H. Mabuchi, and A. Scherer. “Q Optimization of the Factor in Photonic Crystal Microcavities”. In: *IEEE JOURNAL OF QUANTUM ELECTRONICS* 38.7 (2002), p. 7.

[171] M. Heuck, P. T. Kristensen, and J. Mørk. “Dual-resonances approach to broadband cavity-assisted optical signal processing beyond the carrier relaxation rate”. In: *Optics Letters* 39.11 (June 1, 2014), p. 3189.

[172] T. S. Rasmussen, Y. Yu, and J. Mork. “Theory of Self-pulsing in Photonic Crystal Fano Lasers: Theory of Self-pulsing”. In: *Laser & Photonics Reviews* 11.5 (Sept. 2017), p. 1700089.

[173] A. Andrae. “Total Consumer Power Consumption Forecast”. In: *Nordic Digital Business Summit* (2017).

[174] L. A. Coldren, S. W. Corzine, and M. L. Mashanovitch. *Diode Lasers and Photonic Integrated Circuits*. 2 edition. Hoboken, N.J: Wiley, Mar. 20, 2012.

[175] S. Noda. “Seeking the Ultimate Nanolaser”. In: *Science* 314.5797 (Oct. 13, 2006), pp. 260–261.

[176] S. Matsuo et al. “High-speed ultracompact buried heterostructure photonic-crystal laser with 13 fJ of energy consumed per bit transmitted”. In: *Nature Photonics* 4.9 (Sept. 2010), pp. 648–654.

[177] T. Alexoudi et al. “III–V-on-Si Photonic Crystal Nanocavity Laser Technology for Optical Static Random Access Memories”. In: *IEEE Journal of Selected Topics in Quantum Electronics* 22.6 (Nov. 2016), pp. 295–304.

[178] A. Sakanas et al. “Fabrication and experimental demonstration of photonic crystal laser with buried heterostructure”. In: *2017 Conference on Lasers and Electro-Optics Europe European Quantum Electronics Conference (CLEO/Europe-EQEC)*.. June 2017, pp. 1–1.

[179] S. Matsuo et al. “Ultralow Operating Energy Electrically Driven Photonic Crystal Lasers”. In: *IEEE Journal of Selected Topics in Quantum Electronics* 19.4 (July 2013), pp. 4900311–4900311.

[180] Wonjoo Suh, Zheng Wang, and Shanhui Fan. “Temporal coupled-mode theory and the presence of non-orthogonal modes in lossless multimode cavities”. In: *IEEE Journal of Quantum Electronics* 40.10 (Oct. 2004), pp. 1511–1518.

[181] W. Govaerts, Y. A. Kuznetsov, and B. Sijnave. “Numerical Methods for the Generalized Hopf Bifurcation”. In: *SIAM Journal on Numerical Analysis* 38.1 (Jan. 2000), pp. 329–346.

[182] Y. Kuznetsov. *Elements of Applied Bifurcation Theory*. 3rd edition. New York: Springer, June 29, 2004.

[183] A. I. Magunov, I. Rotter, and S. I. Strakhova. “Fano resonances in the overlapping regime”. In: *Physical Review B* 68.24 (Dec. 8, 2003).

[184] W. D. Heiss and G. Wunner. “Fano-Feshbach resonances in two-channel scattering around exceptional points”. In: *The European Physical Journal D* 68.10 (Oct. 2014).

[185] L. Schwarz, H. Cartarius, G. Wunner, W. D. Heiss, and J. Main. “Fano resonances in scattering: an alternative perspective”. In: *The European Physical Journal D* 69.8 (Aug. 2015).

[186] N. B. Abraham, L. A. Lugiato, and L. M. Narducci. "Overview of instabilities in laser systems". In: *Journal of the Optical Society of America B* 2.1 (Jan. 1, 1985), p. 7.

[187] D. D. Nolte. "The tangled tale of phase space". In: *Physics Today* 63.4 (Apr. 2010), pp. 33–38.

[188] S.-B. Lee et al. "Observation of an Exceptional Point in a Chaotic Optical Microcavity". In: *Physical Review Letters* 103.13 (Sept. 25, 2009), p. 134101.

[189] T. Gao et al. "Observation of non-Hermitian degeneracies in a chaotic exciton-polariton billiard". In: *Nature* 526.7574 (Oct. 2015), pp. 554–558.

[190] H. Cartarius, J. Main, and G. Wunner. "Exceptional Points in Atomic Spectra". In: *Physical Review Letters* 99.17 (Oct. 26, 2007).

[191] O. Atabek, R. Lefebvre, M. Lepers, A. Jaouadi, O. Dulieu, and V. Kokoouline. "Proposal for a Laser Control of Vibrational Cooling in $Na_2$ Using Resonance Coalescence". In: *Physical Review Letters* 106.17 (Apr. 29, 2011), p. 173002.

[192] R. Uzdin, A. Mailybaev, and N. Moiseyev. "On the observability and asymmetry of adiabatic state flips generated by exceptional points". In: *Journal of Physics A: Mathematical and Theoretical* 44.43 (2011), p. 435302.

[193] I. Gilary, A. A. Mailybaev, and N. Moiseyev. "Time-asymmetric quantum-state-exchange mechanism". In: *Physical Review A* 88.1 (July 25, 2013).

[194] E.-M. Graefe, A. A. Mailybaev, and N. Moiseyev. "Breakdown of adiabatic transfer of light in waveguides in the presence of absorption". In: *Physical Review A* 88.3 (Sept. 25, 2013), p. 033842.

[195] H. Menke, M. Klett, H. Cartarius, J. Main, and G. Wunner. "State flip at exceptional points in atomic spectra". In: *Physical Review A* 93.1 (Jan. 4, 2016).

[196] S. N. Ghosh and Y. D. Chong. "Exceptional points and asymmetric mode conversion in quasi-guided dual-mode optical waveguides". In: *Scientific Reports* 6 (Apr. 22, 2016), p. 19837.

[197] M. Born and V. Fock. "Beweis des Adiabatensatzes". In: *Zeitschrift für Physik* 51.3 (Mar. 1928), pp. 165–180.

[198] B. Tromborg, H. Olesen, X. Pan, and S. Saito. "Transmission line description of optical feedback and injection locking for Fabry-Perot and DFB lasers". In: *IEEE Journal of Quantum Electronics* 23.11 (Nov. 1987), pp. 1875–1889.

[199] C. Henry. "Theory of the linewidth of semiconductor lasers". In: *IEEE Journal of Quantum Electronics* 18.2 (Feb. 1982), pp. 259–264.

[200] Y. Lumer, Y. Plotnik, M. C. Rechtsman, and M. Segev. "Nonlinearly Induced P T Transition in Photonic Systems". In: *Physical Review Letters* 111.26 (Dec. 27, 2013).

[201] L. Ge. "Anomalous parity-time–symmetry transition away from an exceptional point". In: *Physical Review A* 94.1 (July 19, 2016).

[202] P. Glendinning. *Stability, Instability and Chaos: An Introduction to the Theory of Nonlinear Differential Equations*. 1 edition. Cambridge England ; New York: Cambridge University Press, Nov. 25, 1994.

[203] C. M. Bender, M. V. Berry, and A. Mandilara. "Generalized PT symmetry and real spectra". In: *Journal of Physics A: Mathematical and General* 35.31 (Aug. 9, 2002), pp. L467–L471.

[204] L. Feng, R. El-Ganainy, and L. Ge. "Non-Hermitian photonics based on parity–time symmetry". In: *Nature Photonics* 11.12 (Dec. 2017), pp. 752–762.

[205] R. El-Ganainy, K. G. Makris, M. Khajavikhan, Z. H. Musslimani, S. Rotter, and D. N. Christodoulides. "Non-Hermitian physics and PT symmetry". In: *Nature Physics* 14.1 (Jan. 5, 2018), pp. 11–19.

[206] C. M. Bender and S. Boettcher. "Real Spectra in Non-Hermitian Hamiltonians Having P T Symmetry". In: *Physical Review Letters* 80.24 (June 15, 1998), pp. 5243–5246.

[207] A. Szameit, M. C. Rechtsman, O. Bahat-Treidel, and M. Segev. "P T -symmetry in honeycomb photonic lattices". In: *Physical Review A* 84.2 (Aug. 19, 2011).

[208] Wolfram Research, Inc. "Mathematica 11.1.1". Version 1.1.1.1. In: (2017).

[209] W. D. Heiss. "Repulsion of resonance states and exceptional points". In: *Physical Review E* 61.1 (Jan. 1, 2000), pp. 929–932.

[210] G. Iooss and D. D. Joseph. *Elementary Stability and Bifurcation Theory*. 2nd edition. New York: Springer, Oct. 30, 1997.

[211] R. Seydel. *Practical bifurcation and stability analysis*. 3rd ed. Interdisciplinary applied mathematics 5. New York: Springer, 2010.

[212] A. Leclerc, D. Viennot, and G. Jolicard. "The role of the geometric phases in adiabatic population tracking for non-Hermitian Hamiltonians". In: *Journal of Physics A: Mathematical and Theoretical* 45.41 (Oct. 19, 2012), p. 415201.

[213] S. Ibáñez and J. G. Muga. "Adiabaticity condition for non-Hermitian Hamiltonians". In: *Physical Review A* 89.3 (Mar. 4, 2014).

[214] E. Istrate and E. H. Sargent. "Photonic crystal heterostructures resonant tunnelling, waveguides and filters". In: *Journal of Optics A: Pure and Applied Optics* 4.6 (Nov. 1, 2002), S242–S246.

[215] E. Istrate, M. Charbonneau-Lefort, and E. H. Sargent. "Theory of photonic crystal heterostructures". In: *Physical Review B* 66.7 (Aug. 29, 2002).

[216] E. Istrate and E. H. Sargent. "Photonic crystal heterostructures and interfaces". In: *Reviews of Modern Physics* 78.2 (May 16, 2006), pp. 455–481.

[217] R. Faggiani, J. Yang, R. Hostein, and P. Lalanne. "Implementing structural slow light on short length scales: the photonic speed bump". In: *Optica* 4.4 (Apr. 20, 2017), p. 393.

[218] S. Campione et al. "Broken Symmetry Dielectric Resonators for High Quality Factor Fano Metasurfaces". In: *ACS Photonics* 3.12 (Dec. 21, 2016), pp. 2362–2367.

[219] P. E. Landreman, H. Chalabi, J. Park, and M. L. Brongersma. "Fabry-Perot description for Mie resonances of rectangular dielectric nanowire optical resonators". In: *Optics Express* 24.26 (Dec. 26, 2016), p. 29760.

**www.elektro.dtu.dk**

Department of Electrical Engineering
Electromagnetic Systems Group
Technical University of Denmark
Ørsteds Plads
Building 348
DK-2800 Kgs. Lyngby
Denmark
Tel: (+45) 45 25 38 00
Fax: (+45) 45 93 16 34
Email: info@elektro.dtu.dk